Magnetic correlations in high temperature superconductivity ⋆

Arno P. Kampf

Institut für Festkörperforschung, Forschungszentrum Jülich, D-52425 Jülich, Germany
Institut für Theoretische Physik, Universität zu Köln, Zülpicher Str. 77, D-50937 Köln, Germany [1]

Contents:

⋆ Research performed within the program of the Sonderforschungsbereich 341 supported by the Deutsche Forschungsgemeinschaft.

[1] Present address.

Abstract

Many experimental findings in the materials family of cuprate superconductors are converging towards an electronic picture which involves strong local Coulomb correlations. Characteristic normal state properties appear to be beyond the conventional framework of Landau's Fermi liquid theory. Spin correlations among the charge carriers are discussed as a possible source for the intricate electronic properties. The low energy physics is determined by the charge and spin dynamics in CuO_2 layers which all cuprate superconductors have in common despite their otherwise complex composition. Strong short range Coulomb repulsion between the charge carriers in these planar units imply magnetic ordering phenomena among the Cu spins. Depending on the doping controlled carrier concentration the cuprate compounds are either antiferromagnetic (AF) insulators or correlated metals with short range spin correlations extending also into the superconducting state.

The purpose of this article is twofold: In the first part we review results of basic experiments which probe the magnetic correlations in the CuO_2 planes. Particular emphasis is given on neutron and Raman scattering, nuclear magnetic relaxation, and a selected set of experiments which contain information about the nature of the superconducting state. Based on these experiments the evolution of the spin dynamics from the AF insulator into the doped metallic regime will be discussed. On the other hand we give an overview of current phenomenological and microscopic approaches in the context of purely electronic Hubbard type models which focus on the role of AF spin fluctuations. This includes the results for single particle properties as well as for the dynamic spin susceptibility. Special attention is given to the discussion of spin fluctuation exchange as the possible mechanism underlying high temperature superconductivity.

1. Introduction

Most noticeable in last years' research on high temperature superconductors (HTSC) has been the continuing convergence of experimental data. Improved sample quality and thin film techniques have allowed for the isolation of many of the key intrinsic physical properties. Also the comparison among the compounds in the still growing family of cuprate superconductors has helped to discriminate between sample specific and general physical properties. For example the discovery of the p- [402] or n-type [478] infinite layer materials with T_c near 90 K has once more supported the notion that the important physics is entirely determined by two dimensional CuO_2 layers common to all cuprates, although it may still be regarded as an open question whether the superconductivity is a single plane property or essentially a three dimensional phenomenon.

The 2D physics of mobile charge carriers with strong Coulomb interactions has attracted an enormous amount of theoretical work since the (by that time unexpected) discovery of layered high-T_c superconductors [36]. First principles calculations [167,386,262] have yielded microscopic parameter sets for the cuprate compounds which have revealed the need to deal with strong electronic correlations. Unusual frequency and temperature dependences of susceptibilities or transport quantities [221,306] and the low dimensionality seem to require new or modified theoretical concepts No consensus has yet been reached on the framework which allows a consistent description of the normal metallic state – a prerequisite to address the mechanism responsible for superconductivity.

All of the cuprate high-T_c materials have in common the existence of a perovskite parent compound which is insulating and has long range antiferromagnetic (AF) order among local Cu d^9 magnetic moments. Changing the carrier concentration by ionic substitution or increase of the oxygen content turns these compounds into correlated metals leaving finite range AF spin correlations still intact which is suggestive to picture the perovskite derived cuprates as doped magnetic insulators. This, however, has to be reconciled with a series of data from angular resolved photoemission (ARPES), positron annihilation, and de Haas–van Alphen measurements unambiguously verifying the existence of a Fermi surface in the metallic compounds which has turned out to be closely in accordance with band theory predictions [309]. The dispute whether the correlated metallic state is to be described as a Fermi liquid or in terms of a novel concept is still left undecided.

Conventional electron–phonon coupling has been widely rejected to be the only origin for HTSC or the unconventional behavior in the normal state. Still, there is evidence that the phonons probe the superconducting condensate and alter its properties. But in particular the observed rapid increase of the quasiparticle lifetime below T_c [47] has been interpreted in favour of a dominantly electronic scattering mechanism in the normal state, since electron–phonon scattering would leave the quasiparticle lifetime unchanged across T_c.

The often quoted notion of unconventional properties, however, requires some care. If the definition of a conventional Fermi liquid is based on the existence of a Boltzmann transport equation [10] then e.g. the temperature dependence of the Hall effect ($\propto 1/T$) [300] or the resistivity ($\propto T$) [185] provide examples of transport quantities which are not understood in this framework. Still, many of the characteristic features of HTSC's are not unique and have been found in other oxide or layered materials as well [10].

What is special to the cuprate superconductors is that they continuously evolve from magnetic insulators by changing the concentration of doped carriers. It is the purpose of this article to review the accompanying evolution of the magnetic correlations and the corresponding theoretical concepts.

The related theoretical work starts from the observation that the low doped compounds are close to a magnetic instability. On the other hand it is expected that more heavily doped materials – although limited to the regime of chemical stability – should behave more like a weakly correlated Fermi liquid. All experimental results appear consistent with a smooth crossover between these two regimes by continuous variation of the carrier density.

In chapter 2 we start with some basic notions on the different materials, their structure, and phase diagrams. Chapter 3 is intended to collect some of the presently available experimental results for the magnetic properties. Special emphasis is given to neutron scattering, nuclear magnetic resonance (NMR), magnetic susceptibility, Raman scattering and other selected experiments. We will in chapter 4 continue with phenomenological descriptions which attempt to correlate some of the experimental results into a coherent picture of the normal state. In the same chapter we will consider effective microscopic Hubbard models intended to describe the electronic properties of CuO_2 layers. All subsequent theoretical results are obtained from different versions of these Hubbard models.

The theoretical analyses for the normal state are centered around the problem of holes doped into an AF correlated environment. Separately, we will discuss magnetic ordering phenomena for the insulators as well as for the doped systems in the presence of static or mobile holes. Selected theoretical results for the dynamic spin susceptibility are reviewed in chapter 5 in comparison with experimental data. The results for the magnetic correlations are used to discuss their influence on the dynamics of the doped charge carriers. Both, analytical and numerical results will be presented with particular emphasis on single particle properties and the application to the optical conductivity.

The exchange of spin fluctuations is reviewed in chapter 6 as the possible source for pairing and superconductivity. A lot of theoretical work has been devoted to the search of a possible superconducting ground state for the Hubbard Hamiltonians with purely repulsive Coulomb interactions. No conclusive answer has yet been reached, but it has become clear that a magnetic pairing mechanism will favorably lead to a superconducting order parameter with $d_{x^2-y^2}$ symmetry. We will discuss some of the related implications from numerical calculations combined with phenomenological attempts to determine the pairing state which compares favorably with the experimental data.

2. Materials and structure

2.1. Antiferromagnetic parent compounds

We start with some basic notions on the cuprate materials, their crystal structure, and chemistry. Rough counting shows that by now about 35 different high T_c cuprate superconductors have been synthesized. Most recently a $HgBa_2CuO_{4+x}$ compound was added to the cuprate family [317]. One of its descendants has raised the confirmed record T_c at ambient pressure to 156 K [349]. The continuing materials science activities make it natural to expect further HTSC compounds to follow.

Despite their compositional complexity all cuprate HTSC materials have in common a layered structure with different stacking sequences of CuO_2 planes. Fig. 1 shows the structure of the parent compounds for three examples of the most extensively studied materials. In La_2CuO_4 (henceforth we will use the common short notation 214 for this material) the unit cell contains a single CuO_2 plane while $YBa_2Cu_3O_6$ ($123\,O_6$) has a double layer structure with a two-layer spacing of ~ 3.2 Å. Even three or four closely spaced layers are realised in some of the Bi and Tl based cuprate materials.

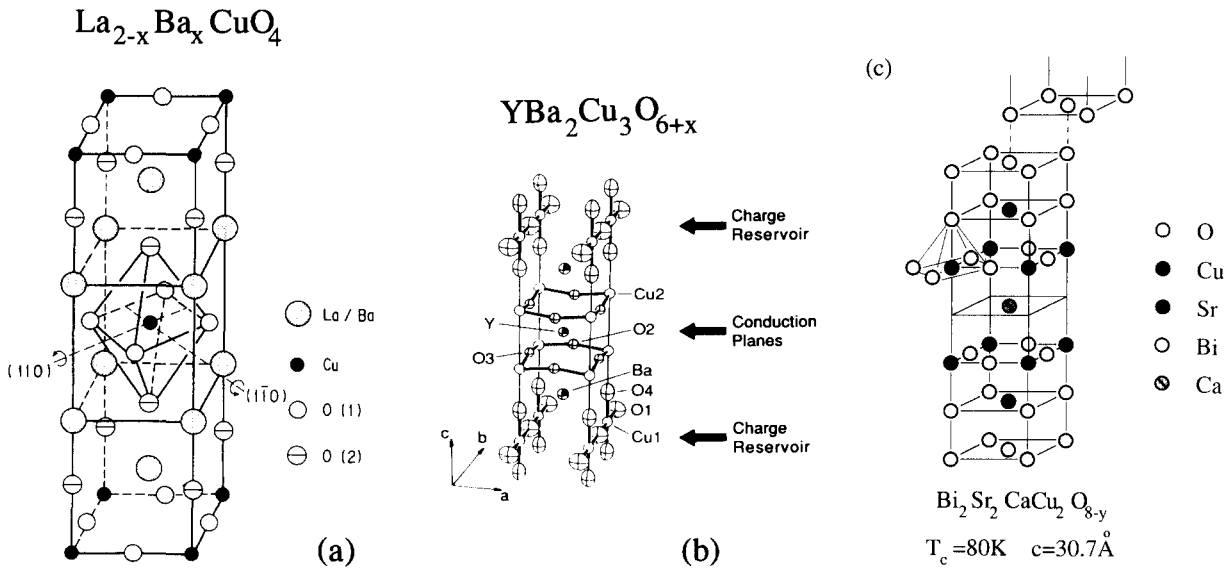

Fig. 1. (a) Schematic diagram of the crystal structure of tetragonal $La_{2-x}(Sr,Ba)_xCuO_4$. Structural phase transitions are caused by cooperative rotations of CuO_6 octahedra around the [110] and [1$\bar{1}$0] axes. (From Ref. [203].) (b) Structure of $YBa_2Cu_3O_{6+x}$. The arrows indicate the conduction plane regions and the charge reservoir in CuO chains. For the insulating and antiferromagnetic O_6 compound there is no oxygen (O1) on the chains. (From Ref. [189].) (c) Crystal structure of one of the Bi HTSC compounds. The two-layer $Bi_2Sr_2CaCu_2O_{8+y}$ material is often abbreviated as BSCCO 2212. (From Ref. [415].)

Layers in between the CuO_2 planes are believed to play a minor role for the low energy electronic properties serving simply as a reservoir to provide additional charge carriers to the CuO_2 planes.

The Cu ions in the CuO_2 planes form a square lattice with a Cu–Cu distance of ~ 3.8 Å. Each Cu has a bond to four neighboring O ions sitting half-way in between the Cu ions. In many cuprates the planar Cu ions have additional O ions located right above or below them at a distance of ~ 2.4 Å. These so called apex oxygens are therefore more weakly bound to the Cu ions as compared to the planar oxygens. In 214 the oxygens form somewhat elongated octahedra with the Cu ions in their center. In $123\,O_6$ a distinct Cu site is also present between the double layers. As we will see below, adding oxygen to this compound leads to the formation of Cu–O chains along these out of plane Cu sites.

Cuprates generally have a tetragonal crystal structure. At low temperatures many of these materials undergo transformation towards an orthorhombic structure. In 214 this structural transformation involves a slight tilting of CuO_6 octahedra of about 4° into an alternating pattern [462], and in $123\,O_{6+x}$ the structural transformation leads to a buckling of the CuO_2 planes. Structural changes have been found in some cases to have a subtle influence on the electronic properties. For the sake of the intended focus of this review article we will not discuss these issues here and refer instead to recent proceedings articles e.g. in Ref. [343].

The one aspect for which consensus has been reached is the nature of the long range AF order in the insulating parent compounds La_2CuO_4 [437,361], $YBa_2Cu_3O_6$ [430], or also $Bi_2Sr_2YCu_2O_8$ [391]. Contrary to one electron band structure calculations, which predict that these materials are nonmagnetic metals [260], the correlated ionic limit is the more appropriate starting point. Consid-

ering e.g. La_2CuO_4 valence counting arguments immediately tell us that Cu is expected to be in a 2+ state. The configuration of the Cu^{2+} ion in the solid is $[Ar]3d^9$, and therefore contains a single $3d^9$ hole. Crystal fields lift the degeneracy of the orbitals in the d-shell and $3d_{x^2-y^2}$ is the only remaining partially filled orbital [307]. The uncompensated spin of this orbital is responsible for the local magnetic moment of the Cu^{2+} ion. Due to the superexchange mechanism [322] as mediated across the neighboring oxygen ions the Cu spins are coupled antiferromagnetically. As we will discuss in more detail in section 4.2 this is effectively described by an $S = \frac{1}{2}$ Heisenberg model

$$H = J \sum_{\langle ij \rangle} \boldsymbol{S}_i \cdot \boldsymbol{S}_j, \tag{2.1}$$

with an exchange constant J. Since the Heisenberg Hamiltonian is restricted to the square lattice of Cu spins in the planes, a finite albeit small interplanar coupling J' is required for the appearance of a three dimensional AF transition at the Néel temperature T_N, e.g. for La_2CuO_4 at about 300 K [437]. However, since the interplanar coupling is very small [336], the spin correlations are dominantly two dimensional until a crossover to three dimensional behavior occurs on cooling down to temperatures very close to T_N [74].

While the spin dynamics is governed by the pure Heisenberg model [81], differences in T_N and also in the magnon spectrum arise from anisotropies and different numbers of CuO_2 planes per unit cell in each material. For example the AF coupled bilayers in $123\,O_6$ lead to slightly modified magnetic properties [45] as compared to the single layer 214 compound. The dominant source for in-plane anisotropy and in- and out-of plane spin wave gaps is the antisymmetric Dzyaloshinskii–Moriya (DM) interaction [107]

$$H_{\mathrm{DM}} = \sum_{\langle ij \rangle} \boldsymbol{D}_{ij} \cdot \boldsymbol{S}_i \times \boldsymbol{S}_j, \tag{2.2}$$

which arises from spin–orbit coupling effects on the superexchange mechanism. The pattern of the DM vectors $\boldsymbol{D}_{ij}$ is sensitive to deviations from the ideal tetragonal La_2CuO_4 structure [84]. For example in the orthorhombic phase with an alternating pattern of the CuO_6 octahedra tilted along the (110) direction the DM interaction induces spin canting out of the CuO_2 planes leading to a net weak ferromagnetic moment [84,418,85,79].

2.2. *Phase diagrams*

Metals are derived from the insulating compounds by a random partial substitution of out-of-plane ions or by adding further oxygens. Trivalent La is replaced by divalent Sr or Ba in La_2CuO_4 (or Y by Ca in $Bi_2Sr_2YCu_2O_8$). To realize a 2+ state for the Sr dopants charge neutrality requires that electrons are removed from the CuO_2 planes thereby effectively creating mobile holes in the planes. As we will discuss in more detail in section 4.2 this is realized by changing an equivalent amount of planar O^{2-} ions into an O^- state [116]. Similarly, substituting Nd^{3+} in Nd_2CuO_4 by Ce^{4+} ions transfers excess electrons into the planes [424]. In this case, it is generally believed that the electrons transferred into the planes create locally Cu^+ which has a closed d-shell configuration and therefore carries no magnetic moment. Hole and electron doping processes are therefore different microscopically. The different nature of the charge carriers has been confirmed by the observed sign of the Hall coefficient in metallic $La_{2-x}Sr_xCuO_4$ and $Nd_{2-x}Ce_xCuO_4$ [300].

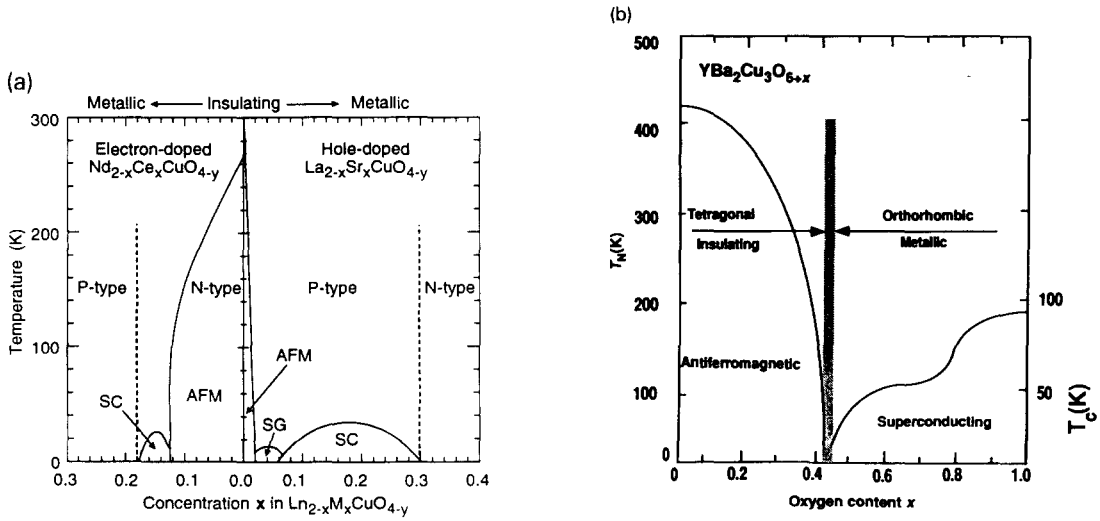

Fig. 2. (a) T–x phase diagram for $La_{2-x}Sr_xCuO_4$ and $Nd_{2-x}Ce_xCuO_4$ (taken from Ref. [15] as reproduced in Ref. [103]). (b) Schematic temperature versus oxygen content phase diagram for $YBa_2Cu_3O_{6+x}$. Both diagrams show insulating–metallic, magnetic–nonmagnetic and structural boundaries together with the regime of high-temperature superconductivity. (From Ref. [309].)

In $123\,O_{6+x}$ hole doping is achieved by increasing the oxygen content continuously from O_6 to O_7. In this material a peculiarity arises in that initially Cu–O chains start to form in between the CuO_2 bilayers. In order to create n O^{2-} ions along the chains $2n$ electrons have to be removed from other parts of the crystals. Most likely these electrons are removed from the CuO_2 planes. Due to subtle details in the chain formation the amount of electronic charge removed from the planes does not increase linearly with the oxygen content. This gives rise in the T versus x phase diagram of $123\,O_{6+x}$ to a so called "60 K plateau" where T_c changes only little with the oxygen content. This is clearly displayed in the phase diagram in Fig. 2b. The highest T_c is reached near the O_7 compound. At this oxygen content the Cu–O chains are completed and no further oxygen can be added. Estimates put the hole doping concentration near 20% in the O_7 material [423]. With respect to the value of T_c 123 compounds with oxygen contents near O_7 are often referred to as *optimally* doped while the compounds with $T_c \sim 60$ K are referred to as *underdoped*.

As the phase diagrams in Fig. 2 show holes doped into the CuO_2 planes appear to be very efficient in destroying the AF state and already a low hole concentration is sufficient to suppress the Néel temperature T_N. In a simplified picture the extra spins of the added holes frustrate the AF exchange interaction between the Cu moments forming a singlet state with either of the two adjacent Cu^{2+} spins [6,474]. With the disappearance of antiferromagnetism metallic behavior evolves continuously accompanied by essentially no changes in the Cu–O bonding pattern. This argues to view the metallic cuprates as doped Mott insulators [330]. Yet, no well defined boundary can be drawn in the phase diagram between the insulating and metallic phases [234]. Beyond the critical hole concentration where Néel order disappears high temperature superconductivity emerges.

The phase diagram in Fig. 2a for the 214 materials is drawn symmetrically for both hole and electron doping. In these compounds the superconducting transition temperature has a maximum at

intermediate doping values disappearing again for higher dopings. This defines an optimum composition at which the highest T_c is reached, as well as an under- or overdoped doping region, respectively. Despite the qualitative similarity between hole and electron doping there is obviously a noticeable quantitative difference: the electron-doped compounds sustain AF order over a much larger doping range. This is in part due to the different microscopic doping mechanism as outlined above.

3. Experiments probing magnetic correlations

Since this article focusses on the magnetic properties and AF spin fluctuations in the metallic cuprates we select in the experimental overview the subset of data which probe specifically the magnetic correlations. This selection by no means underestimates the importance of the data available from other experiments such as e.g. photoemission spectroscopy, tunneling, or measurements of the optical conductivity which will only briefly be addressed at some instances. They have been summarized in a series of comprehensive review articles (see e.g. Refs. [33,34,144–146]). Rather we concentrate here on the magnetic phenomena which underly and motivate the theoretical approaches that will be discussed in subsequent chapters.

3.1. Static magnetic susceptibility

We start by reviewing experimental results for the magnetic susceptibility $\chi(T)$ in undoped and doped compounds. Fig. 3 shows the temperature dependence for series of samples of the 214 and $123\,O_{7-x}$ compounds [418,296,187,188]. The Sr free 214 sample in Fig. 3a clearly exhibits a peak at around 240 K signalling the transition to a long range ordered AF state. This peculiar susceptibility peak at T_N is not a general feature of an isotropic Heisenberg antiferromagnet and rather must be attributed to result from the Dzyaloshinskii–Moriya interaction [418]. For all the doped samples this peak is absent. In Fig. 3b the 214 samples with Sr contents $0.15 < x < 0.2$ show instead a broad smooth maximum which moves to higher temperatures with decreasing x until it is no longer detectable in the temperature range of the experiments.

This general behavior is actually known to occur in the square lattice spin 1/2 Heisenberg antiferromagnet where $\chi(T)$ has a maximum at around a temperature of the order of the exchange coupling J [299]. However, J is as large as 1500 K for the cuprate materials (see Tab. 1) which is of course inaccessible to experiment since around these temperatures La_2CuO_4 starts to decompose. So the theoretical result for the 2D Heisenberg model unfortunately cannot be verified by a measurement of $\chi(T)$ in the undoped antiferromagnets. With increasing Sr doping, however, it appears that $\chi(T)$ preserves its general shape and the maximum moves with growing x to lower temperatures when it becomes visible in the experimental temperature range (see also [465]). The results for the magnetic susceptibility can therefore be qualitatively understood if one assumes that the Heisenberg exchange energy is reduced by the presence of doped holes. Furthermore, for the Heisenberg antiferromagnet $\chi \propto 1/J$ at $T = 0$, [218] and if the effective exchange coupling is reduced by the doped holes the magnetic susceptibility should increase with x, at least at low temperatures. This is indeed what the data show for the 214 material [426]. For $x > 0.2$ $\chi(T)$ grows monotonously with decreasing temperature. In this doping range the maximum is presumably masked by a Curie term which gets stronger with increasing x. [296]

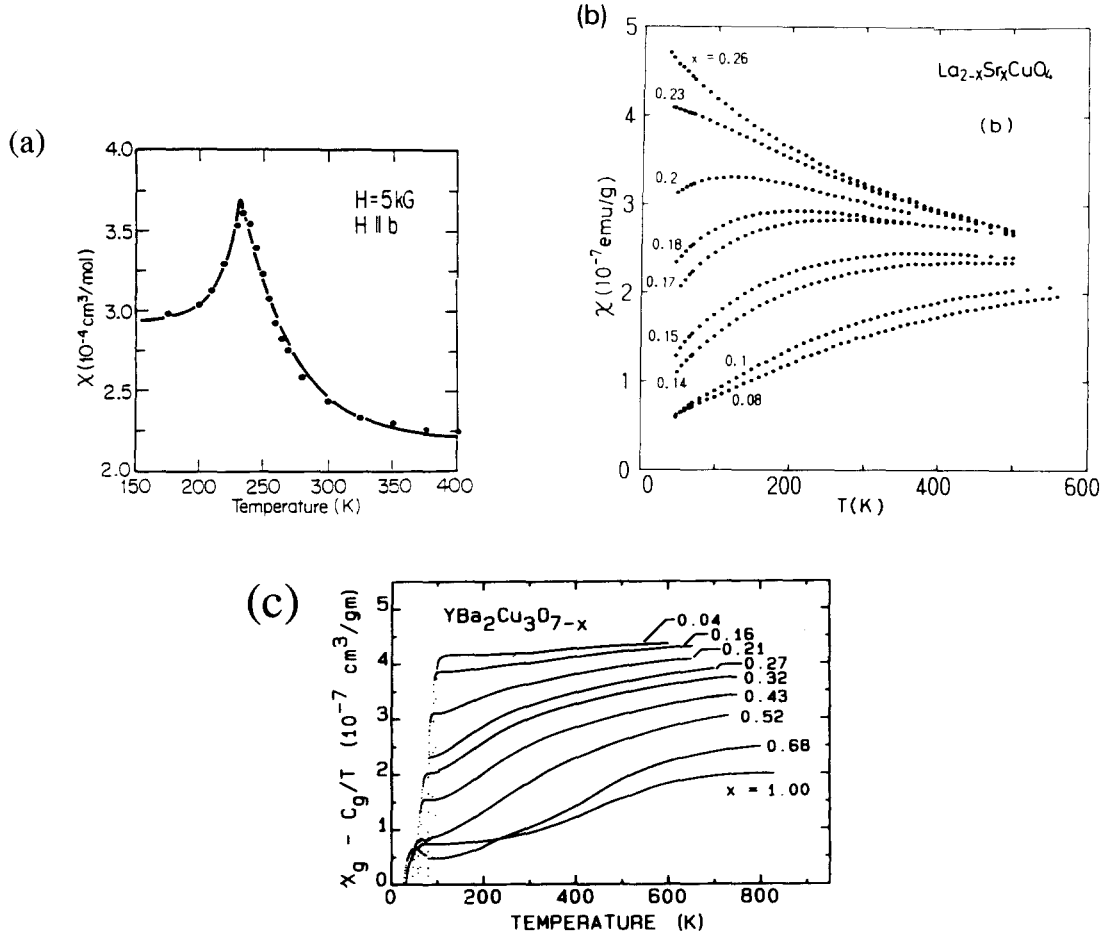

Fig. 3. Magnetic susceptibility for (a) undoped La_2CuO_4 (corrected for core susceptibility) (from Ref. [418]) and sample series of (b) $La_{2-x}Sr_xCuO_4$ (from Ref. [296]), and (c) $YBa_2Cu_3O_{7-x}$ (from Ref. [187]).

The 123 compounds show a similar evolution of the magnetic susceptibility with decreasing oxygen content as shown in Fig. 3c. The highest T_c samples near O_7, however, have an essentially T-independent Pauli like susceptibility [187,293]. One may be tempted to conclude that AF correlations are no longer important in this material, but the flattening may be due to other contributions to $\chi(T)$ e.g., contributions from the Cu–O chains [188]. The exchange energy in 123 materials is comparably large as in the 214 compounds (see Tab. 1) and the temperature range for which $\chi(T)$ data are available may be to small for a conclusive answer. Complementary information is needed from other experiments.

3.2. *Magnetic neutron scattering*

The method of choice for the investigation of magnetic ordering phenomena and the spin dynamics is magnetic neutron scattering. Among various experimental tools neutron scattering experiments are

unique in the sense that they allow in principle to determine the full frequency, momentum and temperature dependence of the spin structure factor

$$S^{\alpha\beta}(\boldsymbol{q},\omega) = \frac{1}{2\pi}\int_{-\infty}^{\infty} dt\, e^{i\omega t}\sum_{\boldsymbol{R}} e^{i\boldsymbol{q}\cdot\boldsymbol{R}}\langle S_0^{\alpha}(0)S_{\boldsymbol{R}}^{\beta}(t)\rangle. \tag{3.1}$$

$S_{\boldsymbol{R}}^{\alpha}$ is a component of the local spin density operator at the spatial position $\boldsymbol{R}$ with $\alpha \in \{x, y, z\}$. The cross section measured in a magnetic neutron-scattering experiment is related to the spin-structure factor by [238]

$$\frac{\partial^2\sigma}{\partial\Omega_f\partial\omega_f} \propto \frac{k_f}{k_i}\sum_{\alpha\beta}(\delta_{\alpha\beta} - \hat{q}_{\alpha}\hat{q}_{\beta})\, S^{\alpha\beta}(\boldsymbol{q},\omega), \tag{3.2}$$

where $\omega = \omega_f - \omega_i$ and $\boldsymbol{q} = \boldsymbol{k}_f - \boldsymbol{k}_i$ are the energy and momentum transfer of the scattered neutron, respectively. In isotropic spin systems and of course also in the paramagnetic state only the diagonal components $S^{\alpha\alpha}(\boldsymbol{q},\omega)$ are finite. For a system with long range magnetic order the Bragg scattering is given by the $\omega = 0$ response to Eq. (3.2) for $\boldsymbol{q}$ equal to the magnetic reciprocal lattice vector. The directional prefactor $(1 - \hat{q}_{\alpha}^2)$ allows to determine the ordered spin direction. The fluctuation–dissipation theorem relates the spin structure factor to the corresponding dynamical spin susceptibility by

$$S(\boldsymbol{q},\omega) = (1/\pi)[1 + n(\omega)]\,\mathrm{Im}\,\chi(\boldsymbol{q},\omega), \quad n(\omega) = [1 + \exp(-\hbar\omega/k_BT)]^{-1}, \tag{3.3}$$

where $n(\omega)$ is the Bose function. The neutron-scattering cross section therefore allows one to determine the structure of the spin order as well as the electronic spin dynamics. In the following we collect some of the experimental results obtained for undoped and doped cuprate materials.

3.2.1. Spin order and magnons in the AF compounds

While already the bulk susceptibility measurements have shown the Néel like transition [418], the occurence of a magnetic Bragg peak in neutron scattering experiments on La_2CuO_4 (as shown in Fig. 4) and $123\,O_6$ has proven convincingly the long range AF order [119,430]. The direction of the ordered Cu spins has been found to be perpendicular to the crystal c-axis [70,430]. In the basal plane the Cu spins are oriented at a 45° angle to the Cu–O bonds [132,430] which in the orthorhombic phase of La_2CuO_4 is the direction of the tilt axis for the buckling pattern of the CuO_2 layer [42]. The tilting of the octahedra leads to an additional feature unique to the 214 compounds in the cuprate family: The induced Dzyaloshinskii–Moriya interaction enforces a spin canting in the direction perpendicular to the basal plane. The canting angle has been determined [418,202] to be as small as 0.2° but gives rise to a weak planar ferromagnetic moment. The overall AF spin structure in La_2CuO_4 is shown in Fig. 5a. No spin canting occurs in the AF compound $123\,O_6$. The magnetic ordering wave vector within a CuO_2 plane is in this compound in the $(1, 1)$ direction and the Cu spins in adjacent CuO_2 planes are coupled antiferromagnetically as well [430] (see Fig. 5b).

Inelastic neutron scattering measurements of the spin wave spectrum in La_2CuO_4 [158] and antiferromagnetic $123\,O_{6+x}$ [336] have shown that the spin ordering is well described by the $S = \frac{1}{2}$ Heisenberg model. Linear spin wave theory with added quantum corrections proved to be sufficient to describe the measured spin wave dispersion [158] and the magnitude of the ordered Cu moment

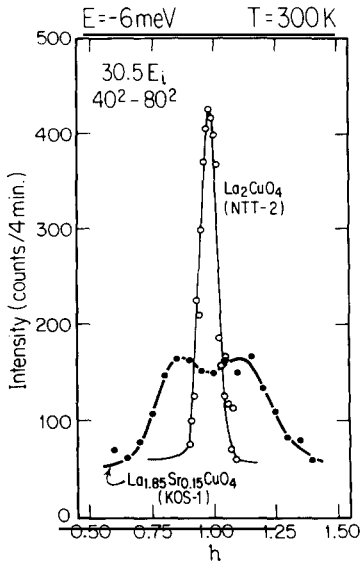

Fig. 4. Inelastic neutron scattering spectra in La_2CuO_4 and $La_{1.85}Sr_{0.15}CuO_4$ for an energy transfer of 6 meV at $T = 300$ K. The solid lines are guides for the eye. (From Ref. [363].)

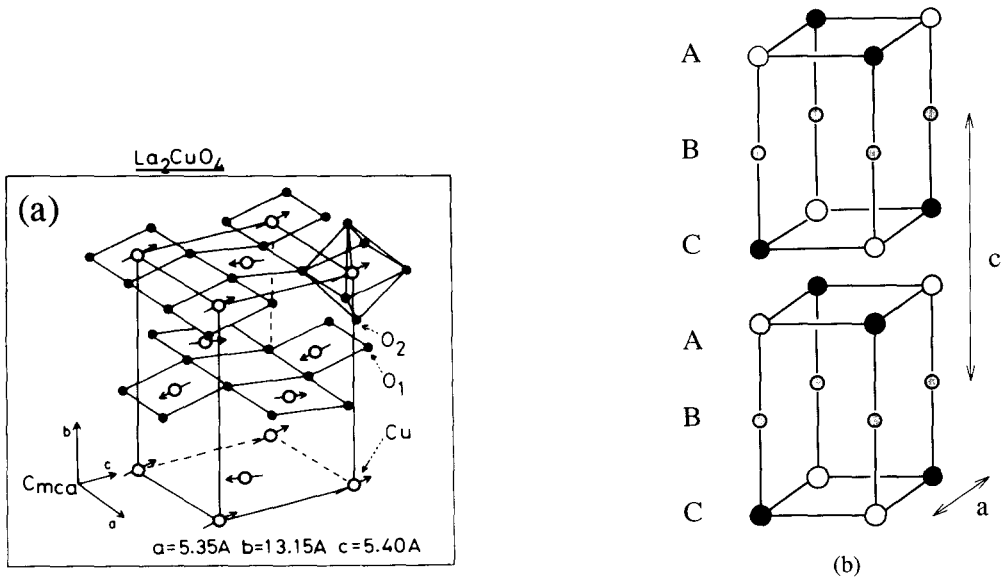

Fig. 5. (a) Spin structure in antiferromagnetic La_2CuO_4 (from Ref. [462]). (b) Spin structure in $YBa_2Cu_3O_{6+x}$ with x near zero. In the planes only copper atoms are shown for clarity. Small shaded circles represent nonmagnetic Cu^{1+} ions in the chains, while filled and open circles indicate antiparallel spins at planar Cu^{2+} sites. Solid lines connect pairs of sites bridged by oxygen atoms. Two full chemical unit cells are shown stacked vertically. The magnetic unit cell has the same height as the chemical one, but it has double the area in the basal plane. (Reproduced from Ref. [430].)

Table 1
Experimental values for two different antiferromagnetic cuprate materials. Note that there is a considerable discrepancy in the results for $YBa_2Cu_3O_{6.15}$ between the most recent results of [357] and earlier reported numbers. The Cu–Cu exchange energy has been obtained from the spin-wave velocity using the linear spin wave theory results for the 2D Heisenberg model, i.e $c = 1.18\sqrt{2}Ja$ (see section 5.1.1).

	$YBa_2Cu_3O_{6.15}$ [336,339]	La_2CuO_4
Ordered moment	$(0.64 \pm 0.03)\mu_B$, $(0.47 \pm 0.03)\mu_B$ [357]	$\sim 0.6\mu_B$ [119,205]
T_N	(415 ± 5) K, (410 ± 3) K [357]	325 K [205]
Spin wave velocity	(1.0 ± 0.05) eV Å	(0.85 ± 0.03) eV Å[3]
J_{Cu-Cu}	(100 ± 20) meV [357]	(136 ± 5) meV [3]

of $\approx 0.6\mu_B$. In particular the agreement of the values for the exchange coupling constant determined independently from neutron and Raman scattering, analysed on the basis of the 2D Heisenberg model, gives convincing evidence for the applicability of this model. Still, more recent neutron data suggest that AF 123 materials may be more appropriately described in terms of an anisotropic 3D system [357].

The measured anisotropy gap for zone boundary magnons also allows an estimate for the weak planar XY anisotropy of the order [336] $\Delta J/J \approx 10^{-4}$. For the bilayer system $123\,O_{6+x}$ the coupling between the two closest layers has been roughly estimated to be $J_b \approx 10^{-2}J$ to $10^{-1}J$ while the AF coupling between bilayers is very weak $J' \approx 10^{-5}J$ [336,339]. The bilayer coupling causes the 2D-like spin waves to be split into acoustic and optical branches. A search for the optical spin wave modes in antiferromagnetic $123\,O_{6.15}$ at excitation energies up to 60 meV has so far been unsuccessful [357]. The reason for this is still unresolved.

For further reference we collect in Tab. 1 some numbers for the 214 and 123 antiferromagnetic compounds obtained from neutron scattering experiments.

The magnon spectrum has also been monitored in the slightly doped AF state of $123\,O_{6+x}$ compounds. Upon doping the spin wave velocity c softens considerably. Magnons become strongly overdamped and c vanishes at a critical hole concentration of about 2% holes in the CuO_2 planes [336] indicating a complete loss of 3D long range magnetic order.

3.2.2. *Spin correlations in doped compounds*

Neutron scattering experiments on $123\,O_{6+x}$ [337,362] and $La_{2-x}(Ba, Sr)_xCuO_4$ [420,157] show that for small doping ($x \leq 0.04$ in doped 214) the AF long range order is replaced by commensurate short range spin correlations. For metallic samples at larger doping concentrations magnetic scattering has been detected also near optimum compositions, e.g. even in stoichiometric $123\,O_7$ magnetic scattering has been identified using polarised neutrons [278]. The propagating spin wave excitations are replaced by a broad excitation spectrum which is found to extend up to energies of about 45 meV. [337] Remarkably, experiments have proved that dynamical AF correlations persist even into the superconducting state [431].

For metallic doping concentrations $x > 5\%$ the magnetic Bragg peaks in $La_{2-x}Sr_xCuO_4$ broaden and develop a two-peak structure [420,363] at low temperatures $T < 100$ K. Representative scans are shown in Fig. 6. This indicates the persistence of finite range AF order in the metallic compounds but also an incommensuration of the magnetic correlations. Interestingly, in the electron doped

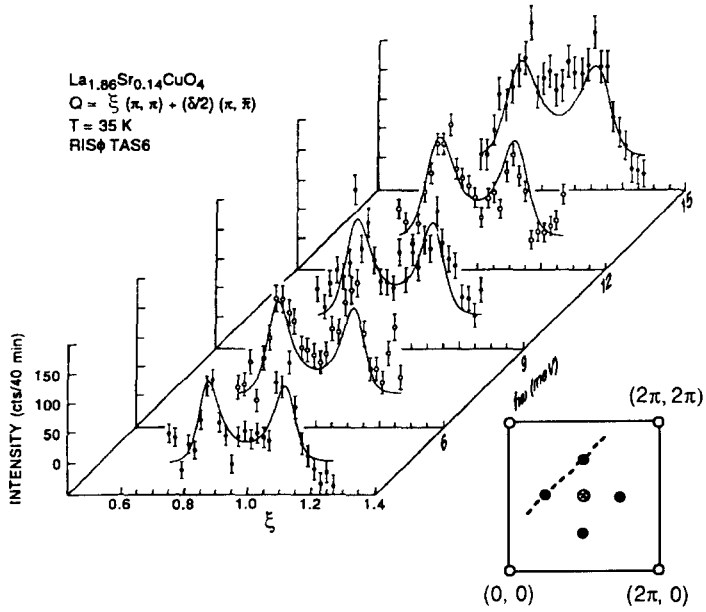

Fig. 6. Magnetic scattering at T = 35 K for a sample of $La_{1.86}Sr_{0.14}CuO_4$ with T_c = 33 K. The main figure consists of a series of constant energy scans collected along the momentum trajectory indicated by the dashed line in the inset. (From Ref. [257].)

214 compounds $(Nd, Pr)_{2-x}Ce_xCuO_4$ the magnetic correlations remain commensurate at least for samples with x up to 10% for which neutron scattering data are available [421]. So far, no clean discommensuration effect has been observed in $123\,O_{6+x}$. Although, the flat topped magnetic peak observed in a superconducting sample with x = 0.6 has been suggested to indicate that the same phenomenon occurs in this material as well [432]. These different behaviors nevertheless show subtle differences in the spin dynamics in both materials. Unanswered by neutron experiments remains the issue whether the incommensurate signals arise from an intrinsic change of the spatial magnetic structure or whether they result from the formation of domains inside which the magnetism remains commensurate. An alternative explanation relates the different behaviors of doped 214 and $123\,O_{6+x}$ to band structure effects [226,235]. So it is possible that the incommensurate peak in doped 214 merely reflects the topology of the Fermi surface.

A thorough investigation of q scans with improved resolution [80] has revealed that the incommensurate modulation wave vector moves with increasing doping level away from the (π, π) point (in the square lattice notation) along the directions $(0, 1)$ or $(1, 0)$. $\mathrm{Im}\,\chi(q, \omega)$ in doped metallic 214 samples is therefore peaked at the points $(\pi, \pi) \pm \delta(\pi, 0)$ and its equivalent points in the Brillouin zone. The deviation from the commensurate wave vector scales roughly as [80] $\delta \cong 2x$. On cooling the incommensurate peaks get sharper and remain sharp also below T_c. [257] However, for low energy transfers $\hbar\omega$ = 3.5 meV the incommensurate modulations disappear almost entirely below T_c. In the normal state, the peaks considerably broaden as the energy is increased [257], e.g. as shown in Fig. 6 in the range from 3.5 meV to 15 meV. Provided that the structure factor $S(q, \omega)$ in the metallic samples of $La_{1.86}Sr_{0.14}CuO_4$ is dominated by particle–hole excitations near the Fermi level

this indicates an unusually rapid energy dependence of the quasiparticle lifetimes [234] consistent with results obtained from angular resolved photoemission experiments [301].

3.2.3. Doping and temperature dependence of the correlation length $\xi(x,T)$

The momentum width of the magnetic Bragg peaks is a direct measure for the spin–spin correlation length. Conveniently, the energy integrated measurements of the dynamical spin structure function yield the instantaneous spin–spin correlation function

$$S^{\alpha\alpha}(\boldsymbol{q}) = \int d\omega S^{\alpha\alpha}(\boldsymbol{q},\omega) = \frac{1}{2\pi}\sum_{R} e^{i\boldsymbol{q}\cdot\boldsymbol{R}}\langle S_0^{\alpha} S_R^{\alpha}\rangle . \tag{3.4}$$

Due to the experimentally limited finite energy cutoffs of the integrated spectra, presumably more reliable data analysis is based on energy resolved spectra. In particular, for metallic samples data are fit assuming a diffusive spin dynamics and a two dimensional Lorentzian lineshape around the momentum $\boldsymbol{Q}_{\mathrm{AF}}$ of the magnetic Bragg peak [257]

$$\chi(\boldsymbol{q},\omega) = \frac{\Gamma_0\chi_0}{i\omega + \Gamma_0[\xi^{-2} + (\boldsymbol{q}-\boldsymbol{Q}_{\mathrm{AF}})^2]} . \tag{3.5}$$

This form is applied to the commensurate (π,π) peak or to each split peak at the incommensurate wave vectors in $La_{2-x}Sr_xCuO_4$ and allows one to obtain the correlation length $\xi(T)$. In some cases a Gaussian line profile has been found to provide better fits to the data [432].

Empirically the instantaneous correlations in the so called *spin glass* regime, intermediate between long range antiferromagnetism and superconductivity, are well described by the simple relation [204,120]

$$\xi^{-1}(x,T) = \xi^{-1}(x,0) + \xi^{-1}(0,T). \tag{3.6}$$

As shown in Fig. 7a this relation holds in low doped $La_{2-x}Sr_xCuO_4$ with $x \leq 5\%$, where the magnetic peak is commensurate. In Eq. (3.6) $\xi(0,T)$ is the temperature dependent correlation length of the undoped system. The doping dependence of the correlation length in this regime behaves roughly as $1/\sqrt{x}$ corresponding to the average separation between the holes in the CuO_2 plane as introduced by the Sr doping [42].

The simple relation Eq. (3.6), however, no longer holds in the metallic regime for $x > 5\%$. Instead, the magnetic correlation length ξ as established at low $\hbar\omega \sim 1$ meV becomes considerably larger than the mean spacing $a_0/\sqrt{x}$ between the carriers where $a_0 = 3.8$ Å is the distance between nearest neighbor Cu atoms in the planes. The deviation from the $1/\sqrt{x}$ behavior gets larger faster with increasing x. This conclusion is drawn from the Lorentzian fit to a single incommensurate magnetic peak. The enhancement over the $1/\sqrt{x}$ behavior has been interpreted to indicate an excellent screening of the donor impurities by the charge carriers in the CuO_2 planes [4], but it remains puzzling that the correlation length is increasing with hole concentration.

Still, there is a discrepancy between the numbers quoted for ξ in $La_{2-x}Sr_xCuO_4$ as reported from different groups (see Table 2 and Figs. 7b,c). A complication arises from the frequency dependence of the correlation length as revealed from energy resolved data analysis [432]. This presumably explains the different results in Fig. 7b and Fig. 7c: $\bar{\xi}$ in Fig. 7b is obtained for $\hbar\omega \cong 1$ meV and describes the inverse q-width of the peak in $\mathrm{Im}\,\chi(\boldsymbol{q},\omega)$ while ξ in Fig. 7c is the equal time

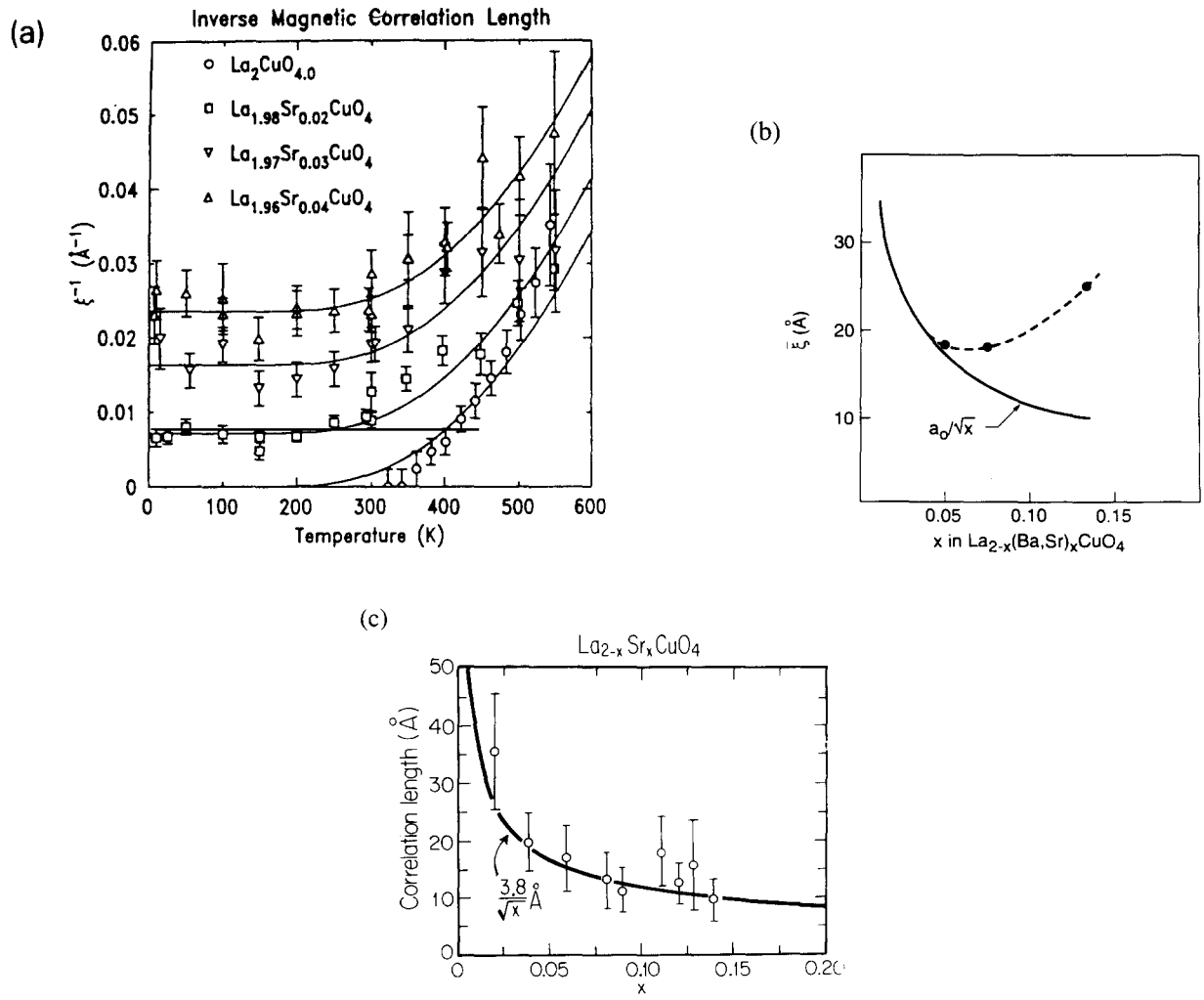

Fig. 7. (a) Inverse magnetic correlation length of four $La_{2-x}Sr_xCuO_4$ samples in the low doping regime. The solid lines are calculated from Eq. (3.6). (From Ref. [206].) (b) Doping dependence of the correlation length $\bar{\xi}$ in $La_{2-x}(Sr, Ba)_xCuO_4$. $\bar{\xi}$ corresponds to best estimates of full-width at half-maximum of peaks in $\chi''(\boldsymbol{q}, \omega)$ at the lowest possible energy ($\hbar\omega \cong 1$ meV) in the normal state $T \geq T_c$. The solid line represents $a_0/\sqrt{x}$, the mean distance between Ba or Sr dopant ions. (From Refs. [4,258].) (c) Magnetic correlation length ξ versus Sr concentration x obtained from two-Lorentzian fits to the incommensurate magnetic peaks of energy integrated data. (From Ref. [420].)

spin–spin correlation length. But generally ξ is found to be of the order of a few lattice spacings in moderately doped materials. From constant energy scans of the $\boldsymbol{q}$-width of the susceptibility peak, ξ has been demonstrated to be essentially temperature independent between 20 K and room temperature [56,336].

3.2.4. ω/T scaling

Quite remarkable results have been obtained for the frequency and temperature dependence of the dynamical susceptibility in low doped samples. The data have been analysed in terms of the

Table 2
Correlation lengths as obtained from the width of the magnetic Bragg peaks (commensurate or incommensurate) at low energies. For comparison: the Cu–Cu distance in the planes is 3.8 Å. (Note, e.g. that the result for the 214 sample with $x = 0.15$ has been obtained from the energy integrated structure factor, while ξ for the $x = 0.14$ sample was determined by the half-width half-maximum of inelastic scans at low energies.)

$La_{2-x}Sr_xCuO_4$	Sr content x	Correlation length ξ
	0.04	42 Å [206]
	0.075	(18 ± 1) Å [80]
	0.14	25 Å [257]
	0.15	12 Å [261]
$YBa_2Cu_3O_{6+x}$	Oxygen content x	Correlation length ξ
	0.50	(9 ± 2) Å [43]
	0.51	8.5 Å [336,56]
	0.60	7.6 Å [390]
	0.69	5.5 Å [336]
	0.92	3.3 Å [338]

relaxational dynamics Eq. (3.5) where the frequency scale is set by $\Gamma = \Gamma_0/\xi^2$. Below room temperature Γ_0 is found to increase linearly with temperature [157]. This in turn implies that the local susceptibility obtained from the momentum integral around the AF zone center is a homogeneous function of ω/T

$$I(\omega, T) = \int_{(\pi,\pi)} d^2q \, \mathrm{Im}\,\chi(q, \omega) = f(\omega/T). \tag{3.7}$$

The scaling behavior Eq. (3.7) has been verified in the energy range $4.5\,\mathrm{meV} < \omega < 12\,\mathrm{meV}$ between 10 K and 500 K for nearly metallic $La_{1.96}Sr_{0.04}CuO_4$ [204] and similarly in $La_{1.95}Ba_{0.05}CuO_4$ [157]. Local susceptibility data have been demonstrated to follow the simple heuristic form (see Fig. 8a)

$$I(\omega, T) = I(\omega, 0)(2/\pi) \arctan\,(a_1\omega/T + a_3\omega^3/T^3 + \cdots). \tag{3.8}$$

While this behavior is strikingly simple it is equally important to recognize its limitations: the scaling relation holds in the regime where $I(\omega, 0)$ is approximately constant, that is for energies $10\,\mathrm{meV} < \omega < 40\,\mathrm{meV}$ [43] and $T > 100$ K. At higher energy the magnetic signal drops sharply [336,338], while below 100 K the generic behavior breaks down at low energies where the appearance of a gap in the spin excitation spectrum starts to interfere. The ω/T scaling is clearly an interesting feature of the spin dynamics in low doped 214 samples, but it has not been found to apply to the superconducting 214 samples.

Similar scaling has also been observed in superconducting $123\,O_{6+x}$ samples with T_c near 50 K [43,390]. However, here the temperature dependence of the susceptibility converges to a universal function of ω/T only at high temperatures. The temperature at which the scaling sets in increases with decreasing energy transfer as shown in Fig. 8b. The appearance of the temperature as the relevant energy scale for the spin dynamics may be very significant because of its possible relation to other normal state properties. Linear temperature dependences of NMR relaxation rates and electronic

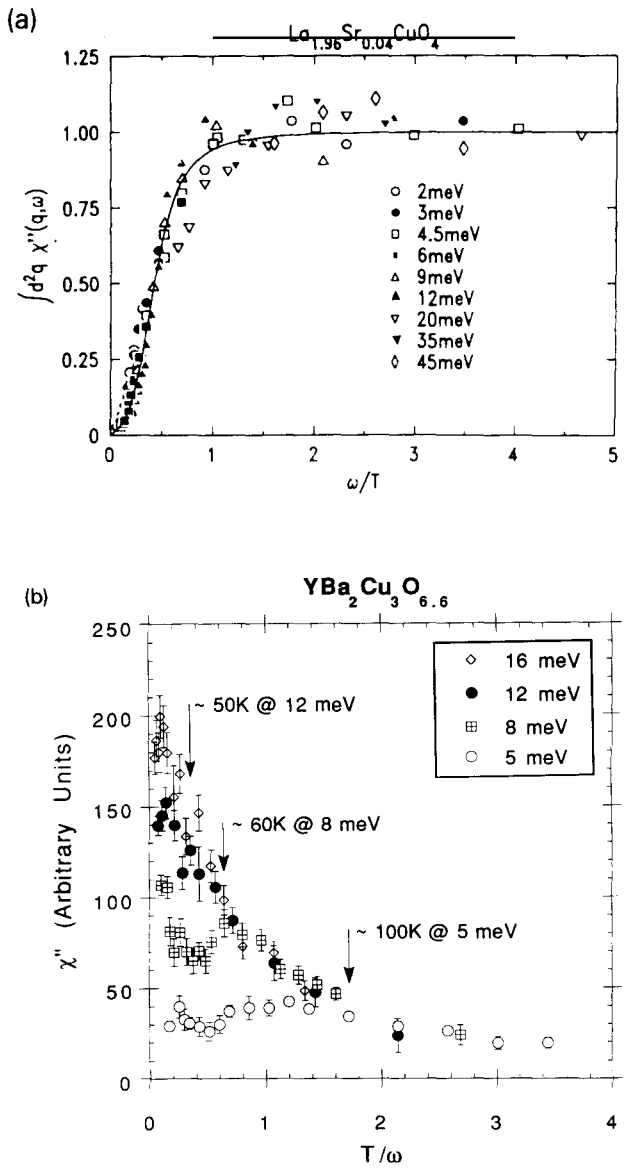

Fig. 8. (a) Normalized q integrated spin susceptibility (χ'') in $La_{1.96}Sr_{0.04}CuO_4$ as a function of the scaling variable ω/T. The solid line results from a fit to the function Eq. (3.8) with $a_1 = 0.43$ and $a_3 = 10.5$. (From Ref. [206].) (b) The temperature dependence of the momentum integrated dynamical susceptibility Im χ in $123O_{6.6}$ at a fixed energy transfer converges to a universal function at high temperatures. The arrows mark the temperature at which the generic behavior sets in with decreasing energy. (From Ref. [390].)

scattering rates have become hallmark examples of anomalous properties in cuprate materials. For example the Drude part of the optical conductivity and the dc resistivity have been interpreted in this way providing a possible basis for a successful normal state phenomenology [130].

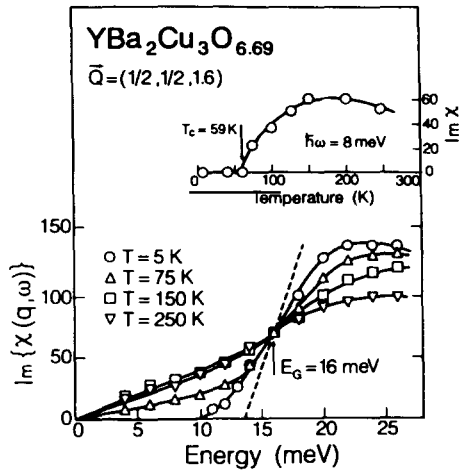

Fig. 9. Low energy part of the spin excitation spectrum $\mathrm{Im}\,\chi(q,\omega)$ in $YBa_2Cu_3O_{6.69}$ below (T = 5 K) and above (T = 75, 150, 250 K) the superconducting transition temperature T_c = 59 K. A spin-excitation energy gap E_g = 16 meV clearly persists above T_c (from Ref. [337]).

3.2.5. Spin excitation gap

On entering the superconducting state we have noted already that the AF spin correlations continue to persist. To be more precise this does not hold for low neutron energy transfers where the magnetic scattering gets suppressed [257]. Well below T_c the low energy neutron scattering intensity is shifted to higher energies opening a spin excitation gap E_g of a few meV. For example a gap value of $E_g = 16\,\mathrm{meV} = 3.2k_BT_c$ has been determined in $123\,O_{6.69}$ [336]. The apparent gap energies increase gradually with increasing oxygen content but are always less than the BCS value for the superconducting energy gap. Such small gap values have been consistently observed also in superconducting $La_{2-x}Sr_xCuO_4$ [420,363]. This deserves special attention since from other experimental data and in particular from optical conductivity measurements [350] consistently much larger gap values have been reported. Not understood is also the rapid change in the gap size for relatively small changes in T_c in underdoped 123 [142]. But the available energy resolution appears to be sufficient to show that the spin excitation gap is not sharp in the sense that $\mathrm{Im}\,\chi(Q_{AF}, E_g)$ has a finite slope at the deduced gap energy [336]. This is in accordance with other experiments which detect low energy magnetic scattering below T_c. It may either imply a pairing state which is different from conventional s-wave pairing [422], or it may equally well result from localised magnetic impurities which have been detected at least in $La_{1.85}Sr_{0.14}CuO_4$ by specific heat measurements [259].

The gap feature in the spin excitation spectrum starts to develop already well above T_c [336,142] in underdoped 123 material (see Fig. 9). It is unlikely to be a superconducting precursor effect because it affects the spectrum up to temperatures as high as $2T_c$ [336]. More likely, the data indicate the development of a normal state spin excitation gap in underdoped 123. This spin pseudogap will also reappear in the subsequent discussion of nuclear resonance experiments. A comparable feature has not been reported from neutron scattering experiments in doped 214 samples.

3.3. Nuclear magnetic resonance

While the neutron scattering experiments have the virtue to provide functional dependences of dynamical susceptibilities on frequency and momentum, it is the special advantage of nuclear resonance techniques, i.e. nuclear magnetic resonance (NMR) and nuclear quadrupolar resonance (NQR), to give local, atomic site specific information. The magnetic hyperfine interaction of distinct nuclei at different crystallographic sites couples the nuclear moments to the spins of the conduction electrons as well as to the unpaired valence electrons. This leads to shifts in NMR resonance frequencies as a measure of the uniform susceptibility, and the coupling to the local electron spin dynamics determines the relaxation of the field aligned nuclear moments in NMR. The availability of several nuclear sites and the different field directions have provided a large number of complementary data (for recent reviews see [304,444]).

The analysis of nuclear resonance experiments has commonly adopted the standard hyperfine Hamiltonian of Mila and Rice [264] for the planar ^{63}Cu (or ^{65}Cu) and ^{17}O isotopes' nuclear spins $^{63}\boldsymbol{I}$ and $^{17}\boldsymbol{I}$, respectively. The result of their quantum chemical analysis is written in the form

$$H_{\mathrm{hf}} = \sum_{i,\alpha} {}^{63}I_{i,\alpha} A_{\alpha\alpha} S_{i,\alpha} + B \sum_{\langle ij \rangle} {}^{63}\boldsymbol{I}_i \cdot \boldsymbol{S}_j + C \sum_{\langle ij \rangle} {}^{17}\boldsymbol{I}_i \cdot \boldsymbol{S}_j. \tag{3.9}$$

The first term follows from a direct hyperfine interaction between the Cu nucleus and Cu d-orbitals at the same site and it is anisotropic, $A_{\parallel} \equiv A_{xx} = A_{yy} \neq A_{zz} \equiv A_{\perp}$. The second and the third term describe transferred hyperfine couplings to nearest neighbor electronic Cu spins. B is assumed isotropic as it arises from a Fermi contact interaction. The oxygen part contains in principle a tensorial coupling [358] but with the exception of [271] most of the analyses have taken C to be isotropic [62,272]. Couplings to other nuclei, like e.g. ^{89}Y in the 123 compounds, can be added in a similar way.

The hyperfine Hamiltonian Eq. (3.9) has proven to be a successful starting point for a consistent description of NMR experiments. Its applicability implies already two important features for the spin dynamics in the cuprates: firstly, a one component picture of a local Cu^{2+} moment strongly hybridised with neighboring oxygen orbitals applies [265]. This is supported by the similar temperature dependences of the different Knight shift in the normal state as well as by the simultaneous disappearance of the relaxation rates on planar Cu and O sites – and on chain sites in the 123 compounds – below T_c [407]. It is therefore sufficient to consider a single spin degree of freedom per unit cell, i.e. a single hybridised band of oxygen $p_{x,y}$ and copper $d_{x^2-y^2}$ orbitals is relevant for the low energy physics of the electronic spins. The success of the one component picture has led us to discard earlier suggestions of two component models for itinerant O holes and localized Cu moments [288,287,92].

Secondly, there is no evidence that the itinerancy of the charge carrier spin needs to be incorporated in the hyperfine Hamiltonian. Although it has been found [403] that the itinerancy of the carriers gives rise to additional terms in the Hamiltonian comparable in strength to the transferred hyperfine coupling, they apparently do not lead to observable deviations from the localised picture. Additional support has come from experiments which indicate that the hyperfine couplings are almost doping independent [30,443,464]. This may be due to form factor effects [274], but a thorough investigation of these issues is still lacking. However, Millis and Monien have also derived expressions for the Knight shift and the relaxation rates in terms of a band theory model [271]. They have concluded that these expressions do not differ essentially from the predictions of the Mila–Rice Hamiltonian.

There are basically three different sets of nuclear resonance experiments providing information about the spin susceptibility. One of them is the Knight shift ${}^aK_\alpha$ of the nuclear Larmor frequency in an applied magnetic field. In this experiment the external field polarizes the electronic spins leading to an additional field at the nuclear site. The corresponding shift in the resonance frequency therefore measures the product of the hyperfine coupling and the static susceptibility

$$ {}^aK_\alpha = \frac{1}{2\mu_B\gamma_n\hbar} \lim_{q\to 0} {}^aF_\alpha(q)\, \chi(q, \omega = 0). \tag{3.10} $$

In Eq. (3.10) α denotes the direction of the applied field, i.e. parallel or perpendicular to the c-axis, and the superscript indicates the nucleus, γ_n is its nuclear gyromagnetic ratio. The q-dependence of the form factors is determined by geometry and their magnitude follows from the coupling constants of the hyperfine Hamiltonian Eq. (3.9). Explicitly, for planar oxygen and copper sites they are given by [272,62,358]

$$ {}^{63}F_{\|,\perp}(q) = A_{\|,\perp} - 2B(\cos q_x + \cos q_y), \tag{3.11a} $$

$$ {}^{17}F_\alpha(q) = 2C \cos \tfrac{1}{2} q_x. \tag{3.11b} $$

Zero field NQR studies have also been used to confirm the long range AF order in the undoped compounds by detecting a finite static hyperfine field of the ordered planar copper moments [463].

The second experimental quantity is the spin lattice relaxation rate $T_{1\alpha}^{-1}$. This is the rate at which the nuclear spin magnetization decays due to the coupling to the conduction electrons. $T_{1\alpha}^{-1}$ thereby measures the local spin fluctuation response at the nucleus for very low Larmor precession energies of the order of 10^{-7} eV . This is orders of magnitude smaller than the characteristic energy scale for the spin dynamics and can safely be taken to zero. The spin lattice relaxation rate follows from the golden rule formula [285], and e.g. for a field applied perpendicular to the c-axis it is given by [272]

$$ \hbar\, {}^aT_{1\perp}^{-1} = \frac{3}{8\mu_B^2} \lim_{\omega\to 0} \frac{k_B T}{\hbar\omega} \sum_{q,\alpha'} [{}^aF_{\alpha'}(q)]^2\, \mathrm{Im}\, \chi_s(q, \omega), \tag{3.12} $$

where the sum on α' is over directions perpendicular to the applied magnetic field. Since NMR is a local probe the response is averaged over all momenta. In this averaging the form factors for the different nuclear sites filter out different parts of momentum space. The same quantity is also measured by NQR without the necessity of applying an external magnetic field.

A magnetic peak in $\mathrm{Im}\, \chi_s(q, \omega)$ at large momenta near the AF wave vector $Q = (\pi, \pi)$ enhances the relaxation rate on Cu while the form factor ${}^{17}F_\alpha(Q)$ vanishes for oxygen and the corresponding relaxation rate ${}^{17}T_\alpha^{-1}$ is not enhanced and insensitive to commensurate (or nearly commensurate) AF fluctuations. This is indeed plausible from the location of the O atoms in between two essentially oppositely aligned Cu moments so that the transferred hyperfine fields cancel at the planar oxygen sites [151,358,264]. A similar geometrical cancellation occurs at the ^{89}Y nucleus as well [272,62]. The relaxation rates at the Y and the O sites are therefore governed by the long wavelength $q \sim 0$ part of the spin susceptibility.

Complementary information on the spin susceptibility is provided by a separate relaxation rate $1/T_{2G}$ which arises from an indirect coupling between the Cu nuclear spins. The local magnetic field

of a nuclear copper spin $\boldsymbol{I}_1$ couples to an electronic spin located at, say, $\boldsymbol{R}_i$, resulting in the spatially varying spin polarization

$$\langle S_\alpha(\boldsymbol{R}_i)\rangle = \frac{I_1^\alpha}{(\hbar\gamma_e)^2}\frac{1}{N}\sum_{\boldsymbol{q}} \exp(-i\boldsymbol{q}\cdot\boldsymbol{R}_i)\,\chi_S^\alpha(\boldsymbol{q})A_{\boldsymbol{q}}^{\alpha\alpha}\,. \tag{3.13}$$

The spin polarization likewise interacts with another nuclear spin $\boldsymbol{I}_2$ giving rise to an indirect RKKY coupling. This coupling leads to a transverse relaxation rate for the nuclear Cu spins given by [403,417]

$$\left(\frac{1}{T_{2G}}\right)^2 = \frac{c}{8\hbar^2}\frac{1}{(\hbar\gamma_e)^2}\left[\frac{1}{N}\sum_{\boldsymbol{q}}|A_{\boldsymbol{q}}^{zz}|^4\chi_S^2(\boldsymbol{q}) - \left(\frac{1}{N}\sum_{\boldsymbol{q}}|A_{\boldsymbol{q}}^{zz}|^2\chi_s(\boldsymbol{q})\right)^2\right]. \tag{3.14}$$

The factor $c = 0.69$ is the natural abundance fraction of the ^{63}Cu isotope. $1/T_{2G}$ is determined from the real-time Gaussian decay in a spin-echo experiment [305,181,410], and allows an independent measurement of the static, momentum dependent spin susceptibility.

3.3.1. Knight shift

Together with the anisotropy of the Cu relaxation rates the Knight shift experiments have been used to fix all the relevant hyperfine coupling constants [272]. They can be found tabulated e.g. in [289]. All data are consistent with the assumption of doping independent coupling constants [445]. With the knowledge of these constants Knight shift data allow to determine the temperature dependence of the uniform static susceptibility. However, the total experimentally observed susceptibility is the sum of various contributions: the spin susceptibility χ_s, a paramagnetic van Vleck orbital term (referred to as the chemical shift), and a core diamagnetic contribution [304,444]. But since only the spin part of χ is commonly expected to be temperature dependent it can be obtained from the total Knight shift by subtracting its $T = 0$ value, $K_S(T) = K(T) - K(0)$. In addition, only the spin part K_S of the Knight shift is related to the density of states at the Fermi energy and hence affected by the transition to the superconducting state [304]. For example the observed constancy of $^{63}K_{\|}$ across the superconducting transition implies that the spin part of the Knight shift $^{63}K_{S\|}$ vanishes. This allows us to conclude that there is a coincidental cancellation of two hyperfine coupling constants, i.e. $A_{\|} + 4B = 0$, [449,30,404].

As we have noted already for the bulk susceptibility data, in the normal state of the $T_c = 90$ K 123 material and also in other optimum doped materials [326] χ_s is Pauli like and temperature independent (see Fig. 10). In the superconducting state the spin Knight shift for planar Cu sites has been found [30] not to follow the simple Yosida function [467]

$$Y(T) = \int_{-\infty}^{\infty} dE\left(-\frac{\partial f}{\partial E}\right)N(E) \tag{3.15}$$

as it does in a weak-coupling BCS singlet superconductor. In Eq. (3.15) $N(E)$ is the density of states and f is the Fermi distribution function. Rather, the Knight shift below T_c is better described by strong coupling behavior [311]. Testing various assumptions for the gap symmetry and its temperature dependence, the data are compatible with both, s- or d-wave symmetry [287] or a mixed s+id state [227,228] which is also allowed from symmetry arguments [216]. The data cannot discriminate

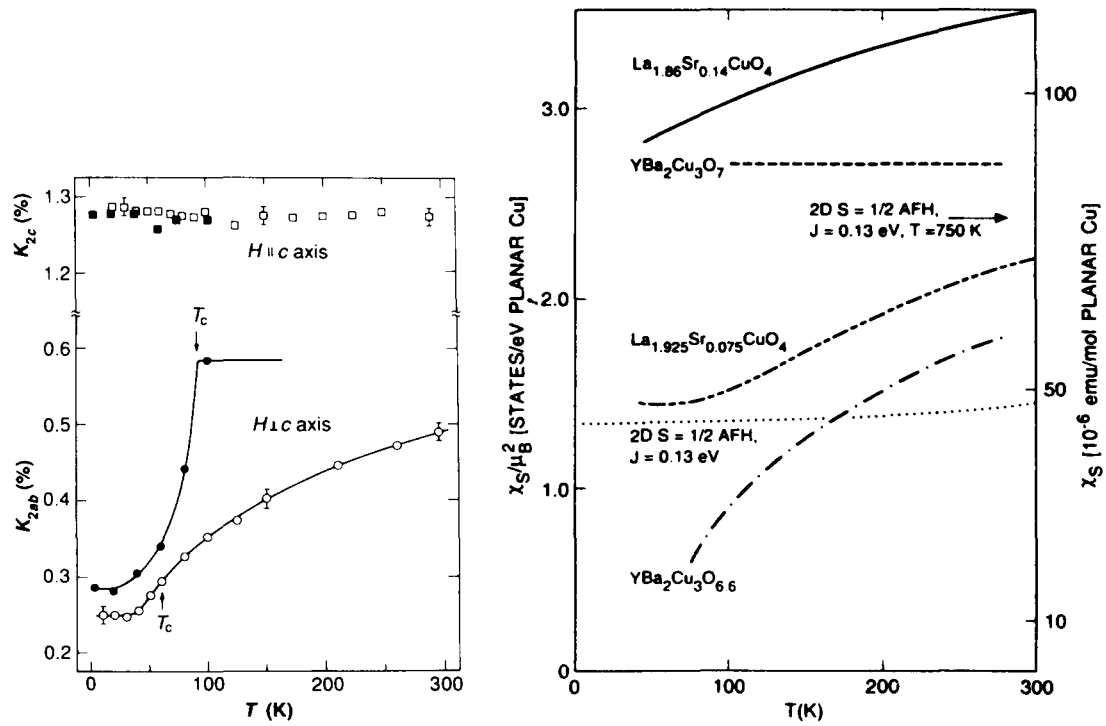

Fig. 10. The closed symbols show the temperature dependence of the planar Cu(2) NMR Knight shift ^{63} K for $123O_7$ [data from [30]], with the magnetic field parallel (K_{2c}, solid squares) and perpendicular (K_{2ab}, •) to the c-axis. The solid line is a guide to the eye showing the very nearly constant Knight shift K_{2ab} in the normal state. The open symbols show corresponding data for the 60 K material $123O_{6.64}$ (open squares, ○) [data from [445]]. (Figure taken from Ref. [444].)

Fig. 11. Temperature dependences for the spin susceptibility in different HTSC materials, along with the theoretical susceptibility of the 2D $S = 1/2$ Heisenberg model (from Ref. [268]).

between these possibilities, although K_S appears to have a nonvanishing slope at low T. Left open remains the possibility for another temperature dependent, possibly orbital contribution. Generally, for all fits the zero temperature value of the energy gap exceeds the BCS weak coupling limit. One important result of the Knight shift measurements is the rapid drop below T_c since this has allowed us to identify the spin pairing to occur in a singlet state [406,30].

In striking contrast χ_s, as obtained from the copper Knight shift, is dramatically suppressed in oxygen depleted $123O_{6.64}$ [445,407] (see Fig. 10). Similar behavior is observed on the other nuclear sites as well [11,407]. In fact, when appropriately scaled ^{17} K and ^{63} K have even identical temperature dependences [407], once again emphasizing the validity of the one-component spin-fluid picture. Furthermore, there is little or no change in K_S at T_c. Above T_c the decrease in χ_s with decreasing T agrees with the bulk susceptibility measurements [293], which in turn then proves to be dominated by the physics of the electron liquid in the CuO_2 planes. This is also supported by the scaling of the ^{89}Y Knight shift with the bulk susceptibility [11].

Spin susceptibility data from the Knight shift as well as bulk susceptibility measurements have

been collected by Millis and Monien [268] as shown in Fig. 11. The plot underlines that underdoped 123 is special, in the sense that its spin susceptibility χ_s extrapolates to zero at zero temperature. This may be viewed as the signature for the opening of a spin excitation gap at low temperatures. It is also noteworthy that χ_s in doped 214 compounds apparently extrapolates to a finite zero temperature value. Clearly, there are differences in the magnetic properties of 123 and 214 materials, and as concluded in [268] there is presumably no spin-gap phenomenon in $La_{2-x}Sr_xCuO_4$.

3.3.2. Spin–lattice relaxation rate

Since the hyperfine couplings are known from the Knight shift measurements direct quantitative information on $\mathrm{Im}\,\chi_s(\boldsymbol{q},\omega)$ at low frequencies is obtained from the relaxation rates. We first consider the relaxation rate at the planar oxygen sites. The marked differences in the magnetic properties that are observed for the Knight shift between $123\,O_7$ and $O_{6.63}$ material continue to hold for the relaxation rates, too. For the O_7 compounds as well as in all other near optimum T_c compounds [326] the Korringa behavior T_1T = const – valid for noninteracting electrons – holds on the oxygen sites (see Fig. 12). This has been naturally explained above by form-factor filtering of large-momentum AF spin fluctuations growing with decreasing temperature.

For noninteracting electrons and with isotropic and $\boldsymbol{q}$ independent hyperfine coupling constants a universal relation between $(T_1T)^{-1}$ and the spin Knight shift is satisfied,

$$1/T_1TK_S^2 = \pi h\gamma_n^2 k_B/\mu_B^2 \equiv S. \tag{3.16}$$

This so-called Korringa relation is verified to hold in all optimally doped compounds for the planar oxygen nuclei [151,165,166], albeit with an enhanced value for the Korringa ratio S. This follows from the temperature independence in the normal state of both, $^{17}T_1T$ and ^{17} K. The temperature dependences of Cu and O relaxation rates are found to be identical between 20 K and 110 K in $123\,O_7$, i.e. up to a temperature well above T_c demonstrating the existence of another characteristic temperature T^* [151]. The susceptibilities below this temperature and also in the superconducting state are therefore suppressed with the same temperature dependence at all $\boldsymbol{q}$, since otherwise the scaling between $^{17}T_1$ and $^{63}T_1$ would be disturbed.

In the oxygen deficient T_c = 60 K 123 compound the planar oxygen spin–lattice relaxation rate develops the same temperature dependence as the spin susceptibility obtained from the oxygen Knight shift [11,13]. This implies that the Korringa relation is no longer satisfied. Instead, the different behavior $^{17}T_1T\,^{17}K_S$ = const holds down to the superconducting transition temperature [466,407]. As is true for the spin Knight shift, the relaxation rate traverses the vicinity of T_c smoothly and nearly featureless [449], as shown in Fig. 12a. The striking temperature dependence of $(^{17}T_1T)^{-1}$ is again a signature for the development of a spin-excitation gap at low temperatures, following an argument given by Millis and Monien [271]. This argument is based on the total-moment sum rule which implies that

$$\langle \boldsymbol{S}^2\rangle \sim \sum_{\boldsymbol{q}} \int d\omega \frac{1}{1-e^{-\omega/T}}\,\mathrm{Im}\,\chi(\boldsymbol{q},\omega) \tag{3.17}$$

is close to $S(S+1)$ and cannot be strongly temperature dependent. The sum rule requires that the loss in low frequency spectral weight of $\mathrm{Im}\,\chi(\boldsymbol{q},\omega)$ as inferred from the decrease of $^{17}T_1^{-1}$ with decreasing temperature has to be compensated by shifting spectral weight to higher frequencies. This spectral weight shift leads to the opening of a spin pseudogap.

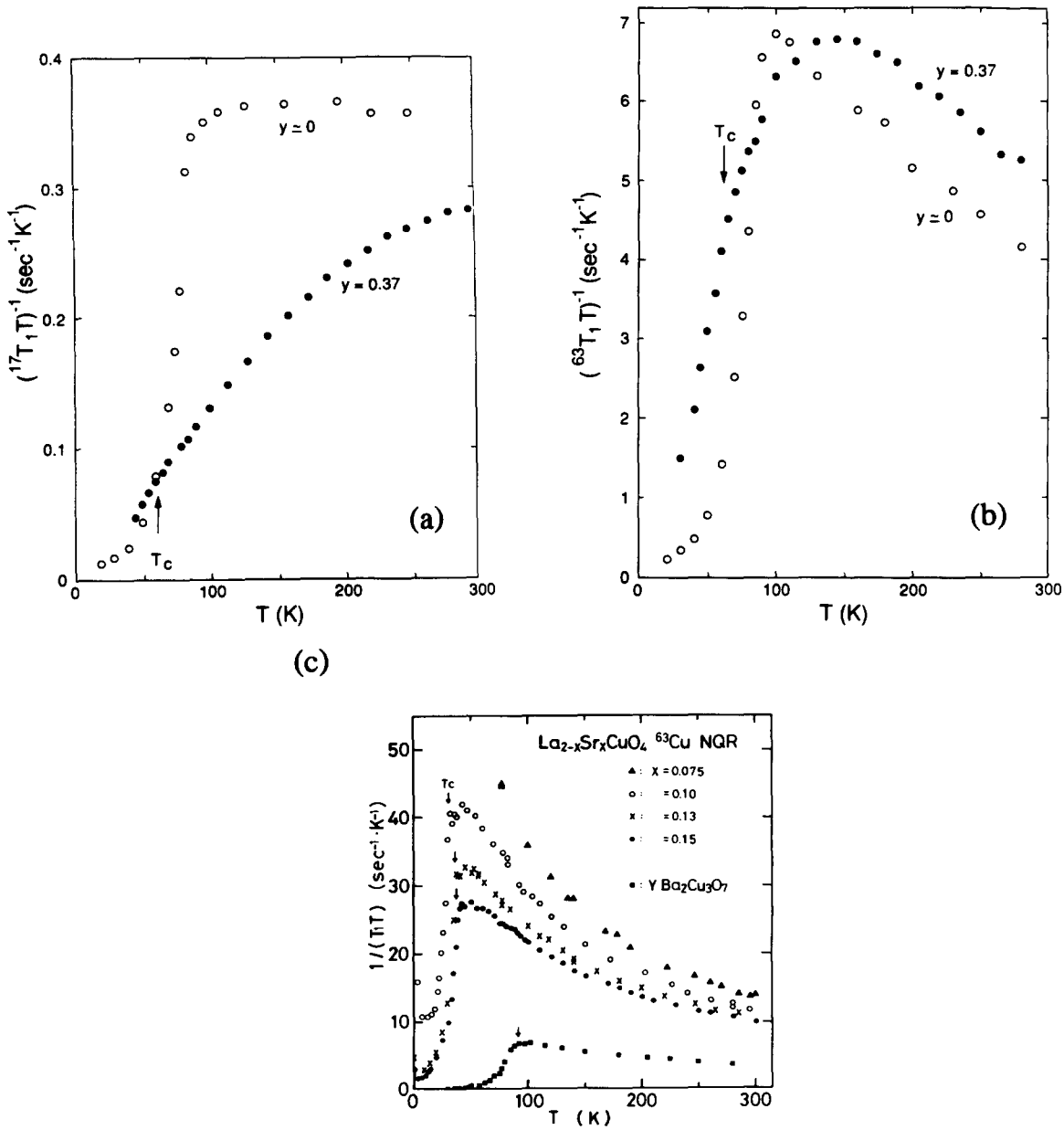

Fig. 12. Temperature dependence of (a) $1/(^{17}T_1T)$ and (b) $1/(^{63}T_1T)$ for $123O_7$ (○) and $123O_{6.63}$ (•). The magnetic field is applied along the c-axis. (From Ref. [407], data for $123O_7$ from [151].) (c) NQR temperature dependence of $1/T_1T$ of ^{63}Cu in $La_{2-x}Sr_xCuO_4$ for $x = 0.075$ (filled triangles), $x = 0.10$ (○), $x = 0.13$ (×), and $x = 0.15$ (•) plotted in linear scale together with that of $YBa_2Cu_3O_7$ (filled squares). (From Ref. [298].)

The planar Cu relaxation rates are similar in all materials and they are strikingly different from the oxygen rates discussed above. As a result of the strong local spin fluctuations on the copper sites the Cu relaxation rate is enhanced by an order of magnitude over the oxygen rate and its temperature

dependence does not follow the Korringa law [407,151,449,464]. In $123\,O_7$, $1/(^{63}T_1T)$ continues to rise with decreasing temperature until T_c is reached where the rate sharply drops. As shown in Fig. 12b the behavior is again different in the 60 K 123 superconductor. Here, $1/(^{63}T_1T)$ goes through a broad maximum at around 150 K and continues to drop with decreasing temperature showing only a weak anomaly at T_c. Once again, this is consistent with the opening of a spin-excitation gap in the underdoped 123 material.

Early on it was suggested that for all superconducting cuprates high-temperature relaxation rate data, i.e. for T well above T_c, are best fit by the linear relation [464,178,179]

$$(^{63}T_1)^{-1} = a + bT, \tag{3.18}$$

with temperature independent constants a and b. Deviations from this behavior start to develop below about 150 K. Eq. (3.18) indeed seems to hold in double layer materials, but for the single-layer $La_{2-x}Sr_xCuO_4$ superconductor the relaxation rate has subsequently been found to be closer to a Curie–Weiss like temperature dependence [212,298],

$$(^{63}T_1T)^{-1} = C/(T + \theta), \tag{3.19}$$

with constants C and θ varying with the Sr concentration. Also, the data for the Cu spin–lattice relaxation rate in $La_{2-x}Sr_xCuO_4$ for various dopings x do not allow an unambiguous identification of a maximum close above T_c [298] as a possible signature for a spin-excitation gap (see Fig. 12c). This is an indication that there are possibly subtle differences in the spin dynamics between the multi- and single-layer materials. Similar evidence arises from the different high-temperature behaviors of the Cu relaxation rate: while $1/^{63}T_1$ continues to grow linearly with T in $123\,O_7$ [179] it saturates in $La_{2-x}Sr_xCuO_4$ to a constant, doping independent value around 300 K [180].

In the superconducting state the copper relaxation rate in 123 compounds approaches an approximate T^3 behavior below 40 K [211,177], clearly distinct from an exponential temperature dependence expected for an s-wave BCS superconductor. Both $^{63}T^{-1}$ and $^{17}T^{-1}$ depend on magnetic-field strength in the NMR experiments but low-field data have confirmed the T^3 behavior at low temperatures [254] which is expected for an orbital pairing state with d-wave symmetry.

3.3.3. Absence of coherence peaks

A separate important feature in the spin lattice relaxation rate data on all nuclear sites is the absence of a coherence Hebel–Slichter peak [159] in the superconducting state [448,177,151,251]. Instead of rising, as it does in conventional low T_c superconductors [159], the relaxation rate is rapidly suppressed below T_c [177]. The Hebel–Slichter peak has been a common signature of conventional BCS singlet, s-wave superconductors. It is essentially an effect of the singular nature of the superconducting density of states which is not suppressed by the type II coherence factors associated with nuclear relaxation [352].

In the light of its importance for our understanding of conventional superconductors the absence of the coherence peak in cuprate superconductors bears an important clue to the electronic correlations and the pairing. An s-wave superconductor can yield T_1^{-1} similar to the ones observed in the cuprates provided that a large temperature dependent pair-breaking mechanism is active and the gap ratio $2\Delta(0)/k_BT_c$ is large [87,162,219]. In Eliashberg strong coupling theory the coherence peak – in NMR as well as in the optical conductivity – may disappear for sufficiently strong coupling to

phonons [9,7] or a featureless bosonic mode suggested in the phenomenological hypothesis of the marginal Fermi-liquid [219,232,233] (see the brief discussion in section 4.1.1). While also a d-wave gap function leads to a substantially reduced coherence peak the peak feature itself is still present [287,65]. Also for this pairing state inelastic pair-breaking processes and enhanced gap ratios are necessary to explain the abrupt drop of the relaxation rate on entering the superconducting state in the near-optimum T_c compounds.

3.3.4. Spin gap

The spin gap phenomenon has attracted a lot of attention in the literature and we may add here a few more comments. The magnetic susceptibility decreasing with decreasing temperature and the normal-state maximum in the temperature dependence of Cu relaxation rates are characteristic anomalies in underdoped 123 materials (as well as in the similarly underdoped but stoichiometric $YBa_2Cu_4O_8$ compound [477] and in $BiSr_2Ca_2Cu_2O_8$ [446]). As discussed above this is taken as evidence for a gap to low-lying spin excitations developing in the normal state. The same phenomenon of a spin-pseudogap has also been observed in neutron scattering (see section 3.2.5). When first mentioned in the literature [449] suggestions have been made that the spin gap which appears already significantly above T_c results from precursive superconducting pair formation [449,445]. A scenario, however, where the superconducting transition is viewed as Bose condensation of preformed Cooper pairs is not supported by experiment. Measurements of the work function have shown that the behavior of the chemical potential at and below T_c is not compatible with what is expected for Bose condensation [332]. The nature of the transition is in fact much closer to BCS behavior with modifications arising from the anomalously short coherence length in the cuprate superconductors.

Further conclusive evidence against a superconducting precursor effect as the origin for the anomalous spin gap has come from measurements on Zn substituted $123\,O_{6+x}$ [12]. While the Zn substitution for Cu substantially reduces the superconducting transition temperature, the homogeneous spin susceptibility χ_s and hence the spin gap feature is only weakly modified proving that it is of a different origin.

It is important to stress again that the spin-gap behavior disappears for the optimally doped $123\,O_7$ compound and does not occur for overdoped 123 materials [164]. In these compounds the gap for charge and spin excitations opens at the same temperature T_c. The existence of apparently two different temperatures for the onsets of the gaps for spin and charge excitations in the underdoped region has been speculated to result from the separation of spin and charge [292].

However, another possible hint to the origin of the spin gap in underdoped 123 compounds may be inferred from the similar features observed in other underdoped double- [152] and triple-layer Bi and Tl based cuprates [166] and a comparison to the single layer $La_{2-x}Sr_xCuO_4$ superconductors. All double layer compounds show a common magnetic behavior which is implied by the ^{89}Y NMR data [152]. Neutron scattering has already provided evidence for strong AF bilayer correlations [432]. A detailed comparison of the relaxation rates at Y and O sites in $YBCO_{6.63}$ [409] has shown distinct temperature dependences. The ^{89}Y relaxation rate decreases more steeply than the ^{17}O rate with decreasing temperature: Since Y nuclei are located in between the two adjacent CuO_2 planes of a bilayer this result suggests that the AF bilayer correlations become stronger at lower temperatures. If this is the correct interpretation then the origin of the spin gap is not an intrinsic property of the planar spin dynamics but rather results from the AF coupling of layers which is stronger in the

oxygen-deficient compounds closest to the composition of the insulator [268,269]. The open question remains whether the intra-bilayer coupling is strong enough to explain the observed spin-pseudogap feature.

We mention that a different point of view has been taken by Sokol and Pines who argue that the appearance of a spin gap is not related to the presence of CuO_2 bilayers. Rather it is suggested to reflect a crossover in the spin dynamics from an overdamped to a quantum disordered regime [380].

3.3.5. *Anisotropy of* $1/T_1$ *below* T_c

Another set of experiments has employed the anisotropies of the relaxation rates with respect to the direction of the applied magnetic field. For Cu one distinguishes $^{63}T_{1\|}^{-1}$ and $^{63}T_{1\perp}^{-1}$ for magnetic field directions parallel or perpendicular to the crystal c-axis, respectively. For planar oxygen sites two different rates T_a and T_b are considered when the field is in the CuO_2 planes parallel or perpendicular to the Cu–O–Cu bond, respectively [405]. While the anisotropy ratio of Cu relaxation rates $^{63}R = {}^{63}T_{1\perp}^{-1}/{}^{63}T_{1\|}^{-1}$ is temperature [31,407] and field [27,253] independent in the normal state, a nonmonotonic temperature dependence has been found in the superconducting state of $123\,O_7$ [31,408,253].

Low field experiments have proven that the anisotropy is not an artifact resulting from the presence of the applied magnetic field [408,253]. As the temperature is lowered through T_c an initial drop of the anisotropy ratio is followed by a rise at lower temperatures eventually exceeding the ratio in the normal state (see Fig. 13). Isotopic substitution of ^{63}Cu has allowed to identify the relaxation mechanism above 30 K to be almost purely magnetic and not electric quadrupolar in origin [408]. At lower temperature additional relaxation mechanisms appear – most likely caused by oxygen motion [408] or impurities [176]. The unusual temperature dependence of the anisotropy ratio and the magnetic origin of the nuclear relaxation suggest a temperature dependent anisotropy of $\chi_s(\boldsymbol{q}, \omega)$ below T_c indicative of an anisotropic gap function favoring a $d_{x^2-y^2}$ symmetry of the superconducting state [65,242] (see also section 6.3.2).

3.3.6. *Transverse spin–spin relaxation rate* $1/T_{2G}$

The complementary measurements of $1/T_{2G}$ for the Cu nuclear moment have provided further insights into the different spin dynamics of underdoped and fully oxygenated 123 materials. With respect to the Cu spin–lattice relaxation rate the underdoped 123 and similarly also the two-layer compound $YBa_2Cu_4O_8$ [477] have appeared to be special because of the development of a spin-excitation gap well above T_c. But as has been revealed by the $1/T_{2G}$ data, the spin dynamics in the underdoped compounds is distinctly different also above the spin gap temperature when compared to the data for $123\,O_{6.9}$. Most noticeable, the ratio T_1T/T_{2G}^2 is approximately constant in $123\,O_7$ above $\sim$ 150 K [181,380]. On the contrary, in $123\,O_{6.63}$ it is the ratio T_1T/T_{2G} which is nearly constant above $\sim$ 200 K [410]. This difference has recently received special attention [380]. It has been interpreted to indicate that the spin dynamics in underdoped and fully oxygenated 123 are to be described with two different dynamical exponents[2], $z = 1$ and $z = 2$, respectively [380].

Finally, we mention another significant result for the transverse relaxation rate in the superconducting state. The data for $YBa_2Cu_4O_8$ in Fig. 14 show that the absolute value of $1/T_{2G}$ barely changes below T_c [184]. This is consistent with the prediction of an RPA like theory of AF spin fluctuations

[2] The dynamical exponent z relates the characteristic energy and length scales for the spin dynamics according to $\omega \sim \xi^{-z}$.

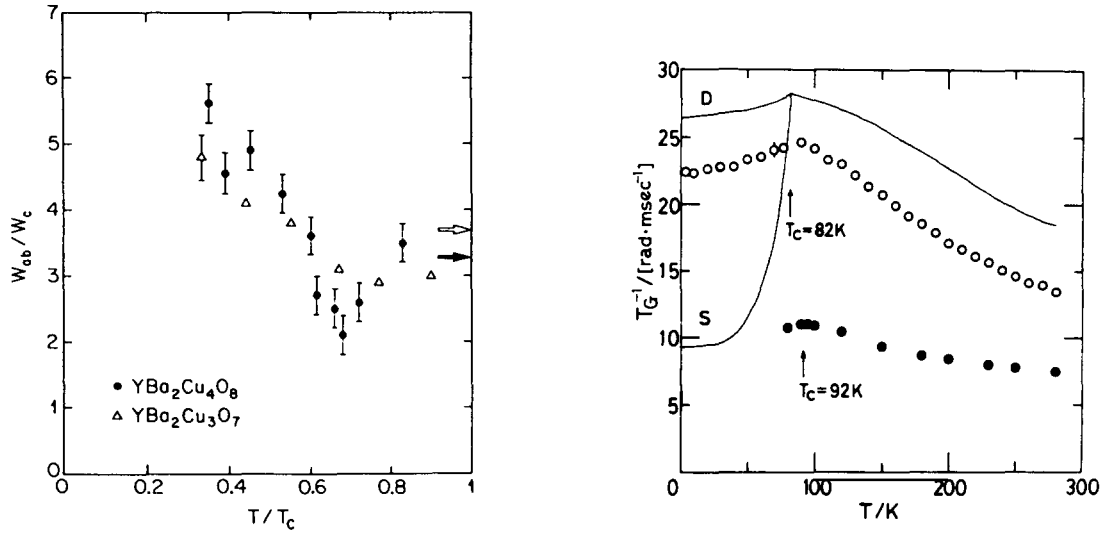

Fig. 13. Planar Cu spin–lattice relaxation rate anisotropy ratio ^{63}R (in the figure denoted by W_{ab}/W_c) versus reduced temperature T/T_c in a weak magnetic field: $YBa_2Cu_4O_8$ in $B = 0.58T$ (•) and $YBa_2Cu_3O_7$ in $B = 0.44T$ (△). The arrows indicate the value of ^{63}R above T_c. (Figure taken from Ref. [27], the data for $YBa_2Cu_3O_7$ are from Ref. [407].)

Fig. 14. Temperature dependence of the transverse spin–spin relaxation rate $1/^{63}T_{2G}$ in $YBa_2Cu_4O_8$ (○) and $YBa_2Cu_3O_{9.98}$ (•). The solid curves are the results of an RPA like calculation of Bulut and Scalapino [64] for a s- and d-wave superconducting gap function, respectively (S and D in the figure). (Figure reproduced from [184].)

for a superconducting gap function with $d_{x^2-y^2}$ symmetry [64]. The inverse transverse relaxation rate squared, Eq. (3.14), measures a momentum average of $\chi^2(q)$ which is dominated by momenta $q \sim Q$. Contrary to an s-wave gap, a d-wave gap will not suppress $\chi(q)$ around (π, π) [64] which offers a possible explanation for the barely reduced $1/T_{2G}$ below T_c.

3.4. Raman scattering

In this chapter we will selectively discuss results for electronic and magnetic light scattering in doped and undoped cuprates. Although detailed information has been collected by Raman scattering techniques about the lattice dynamics we will not discuss phonon properties in this article and refer instead to the recent review articles on this topic in [71,419]. In passing we mention that phonon frequency shifts between the normal and the superconducting state have allowed accurate measurements of the energy gap yielding gap ratios $2\Delta(0)/k_BT_c$ near 4.95 in the $YBa_2Cu_3O_7$ system [136]. In addition, as recently suggested, phonon linewidths do offer an as yet unexplored opportunity to test the symmetry of the gap function in the superconducting state [129].

Certainly, the distinction between a wide variety of origins for features in the Raman intensity is not clear in many cases and offers a pertinent problem for the understanding and correct interpretation of the light scattering data. As is true for the results from other experiments, well established is the Raman light scattering in the insulating and antiferromagnetic materials. Raman techniques have proven to be a valuable tool in exploring the collective spin excitations in support of the

picture obtained from the neutron scattering experiments we have discussed in section 3.2. On the other hand the Raman background continuum observed in metallic as well as insulating cuprates has received special attention since it appeared to contain valuable information on the electronic excitation spectrum. Despite many efforts to resolve the origin of the Raman continuum no consensus has yet been reached on whether it is an intrinsic property of the charge carriers in cuprate materials.

Before we discuss experimental results we will briefly outline some basics for electronic Raman scattering. In the light scattering process incoming photons couple to the charge or current density of the electronic system. The coupling to the electrons leads internally to the creation of particle–hole or collective charge- or spin-excitations. Information about the electronic excitations is contained in the frequency shift and the polarization of the reemitted photon. Light scattering probes the $q \sim 0$ response so that only single long-wavelength or multiple excitations with total momenta summing to zero are accessible.

Microscopically it is the vector potential A of the transverse electromagnetic photon field which couples to the motion of the electrons by introducing a Peierls phase factor into the kinetic energy

$$H_{\mathrm{kin}}^{A} = -t \sum_{\langle ij\rangle,\sigma} \left[\exp\left(i\frac{e}{\hbar c} \int_{i}^{j} \boldsymbol{A}\cdot d\boldsymbol{l} \right) c_{i\sigma}^{+} c_{j\sigma} + \mathrm{h.c.} \right] + H_{\mathrm{int}}. \tag{3.20}$$

$c_{i\sigma}^{+}(c_{i\sigma})$ destroys (creates) an electron of spin σ on site i of the lattice and H_{int} represents the interaction term of the correlated electron system which is probed in the light scattering experiment. Since the photon field is a weak perturbation H_{kin}^{A} can be expanded to second order in A. In performing the spatial Fourier transformation we introduce the components of the current operator

$$j_{q}^{\alpha} = \sum_{k,\sigma} \frac{\partial \epsilon_{k}}{\partial k_{\alpha}} c_{k+q/2,\sigma}^{+} c_{k-q/2,\sigma}, \tag{3.21}$$

and the components of the "inverse mass tensor"

$$\tau_{q}^{\alpha\beta} = \sum_{k,\sigma} \frac{\partial^{2} \epsilon_{k}}{\partial k_{\alpha}\, \partial k_{\beta}} c_{k+q/2,\sigma}^{+} c_{k-q/2,\sigma}. \tag{3.22}$$

Both, j_{q}^{α} and $\tau_{q}^{\alpha\beta}$ are here written for simplicity for a single band with dispersion ϵ_{k}. For a free electron dispersion $\tau_{q}^{\alpha\beta}$ is proportional to the familiar density operator. To second order in A we then obtain the effective Hamiltonian

$$H_{\mathrm{kin}}^{A} = H_{\mathrm{kin}}^{A=0} - \frac{e}{\hbar c} \sum_{q\alpha} j_{q}^{\alpha} A_{-q}^{\alpha} + \frac{1}{2} \left(\frac{e}{\hbar c}\right)^{2} \sum_{q_1,q_2,\alpha,\beta} \tau_{q_1+q_2}^{\alpha\beta} A_{-q_1}^{\alpha} A_{-q_2}^{\beta}. \tag{3.23}$$

The Raman scattering cross section is proportional to the transition rate R which is obtained by applying Fermi's Golden Rule. The inelastic scattering rate R is obtained from second order perturbation theory for transitions with energy and momentum transfer $\Delta\omega = \omega_i - \omega_f$ and $q = k_i - k_f$, respectively, between the incoming and outgoing photon. Following the derivation of Shastry and Shraiman a convenient way to express the transition rate R in terms of a susceptibility may be obtained in the form [359]

$$R(q, \Delta\omega) = [1 + n(\Delta\omega)] \frac{c^{2}}{\Omega\sqrt{\omega_i \omega_f}} \left(\frac{e}{\hbar c}\right)^{4} \int dt\, e^{-it\Delta\omega} \langle [\hat{M}^{+}(q,0), \hat{M}(-q,t)] \rangle, \tag{3.24}$$

where $n(\Delta\omega) = (e^{\Delta\omega/T} - 1)^{-1}$ is the Bose distribution function. Since the wavelength of light in the optical range is large compared to the lattice spacing of the crystal and all length scales of the electronic system, the momentum transfer $\boldsymbol{q}$ of the photon to the electrons can safely be neglected.

The matrix elements of the effective Raman scattering operator $\hat{M}(\boldsymbol{q})$ between initial and final eigenstates $|i\rangle$ and $|f\rangle$ with energy eigenvalues ϵ_i and ϵ_f, respectively, of the correlated electron system are given by [359]

$$\langle f|\hat{M}(\boldsymbol{q})|i\rangle = \sum_{\alpha,\beta} e_i^{\alpha} \bar{e}_f^{\beta} \langle f|\tfrac{1}{2}\tau_{\boldsymbol{q}}^{\alpha\beta} + \hat{M}_R^{\alpha\beta}(\boldsymbol{q})|i\rangle, \tag{3.25}$$

$$\langle f|\hat{M}_R^{\alpha\beta}(\boldsymbol{q})|i\rangle = \sum_{\nu} \left(\frac{\langle f|j_{\boldsymbol{k}_f}^{\beta}|\nu\rangle\langle\nu|j_{-\boldsymbol{k}_i}^{\alpha}|i\rangle}{\epsilon_\nu - \epsilon_i - \omega_i} + \frac{\langle f|j_{-\boldsymbol{k}_i}^{\alpha}|\nu\rangle\langle\nu|j_{\boldsymbol{k}_f}^{\beta}|i\rangle}{\epsilon_\nu - \epsilon_i + \omega_f} \right). \tag{3.26}$$

From the electron–photon coupling Eq. (3.23) there are two contributions to $\hat{M}(\boldsymbol{q})$, a direct scattering term from the coupling to the "inverse mass tensor" and a resonant contribution $\hat{M}_R^{\alpha\beta}(\boldsymbol{q})$ from the coupling to the current, which involves virtual intermediate states $|\nu\rangle$ with energy ϵ_ν of the correlated electron system. $\boldsymbol{e}_i$ and $\boldsymbol{e}_f$ are unit vectors for the polarizations of the incoming and outgoing photon, respectively.

For further reference we fix the notation for the photon polarizations in different scattering geometries. Since the notations in the literature for the polarizations in 123 and BSCCO 2212 materials are rotated by 45° with respect to each other [384] it is convenient to relate the polarization vectors of the incoming and outgoing photons to the Cu–O bonds in the CuO_2 planes. The different combinations of $\boldsymbol{e}_i$ and $\boldsymbol{e}_f$ shown in Fig. 15 define the three major scattering geometries with A_{1g}, B_{1g} and B_{2g} symmetry.

Eqs. (3.25) and (3.26) demonstrate the complexity of the Raman response of an itinerant correlated electron system. Generally, the Raman intensity involves density–density, four-current and mixed current–density correlations and it is difficult to disentangle specific contributions, e.g. the magnetic contributions from spin fluctuations. Due to the general form Eq. (3.24) Raman data are frequently analysed in terms of the Bose factor and the imaginary part of an appropriate response function

$$R(\Delta\omega) = [1 + n(\Delta\omega)]\,\mathrm{Im}\,\chi(\boldsymbol{q} \sim 0, \Delta\omega, T). \tag{3.27}$$

3.4.1. Two-magnon scattering

In the AF insulators the electric field of the incoming photon can couple to a two-spin flip process [114] exciting two magnons of opposite momenta $\boldsymbol{q}$ and $-\boldsymbol{q}$, respectively. The standard scattering Hamiltonian describing the interaction of the spin pairs with the photon pairs is given by [303]

$$H_R = \sum_{\langle ij\rangle} (\boldsymbol{E}_{\mathrm{inc}} \cdot \boldsymbol{n}_{ij})(\boldsymbol{E}_{\mathrm{sc}} \cdot \boldsymbol{n}_{ij}) \boldsymbol{S}_i \cdot \boldsymbol{S}_j, \tag{3.28}$$

where $\boldsymbol{E}_{\mathrm{inc}}$ and $\boldsymbol{E}_{\mathrm{sc}}$ are the electric field vectors for the incident and scattered photons, respectively. $\boldsymbol{n}_{ij}$ is a unit vector connecting lattice sites i and j. If the coupling H_R allows only for two-spin flips on nearest-neighbor sites $\langle ij\rangle$ then Raman light-scattering intensity from this process will appear in B_{1g} symmetry only for a spin system described by the spin 1/2 square lattice Heisenberg antiferromagnet. In this symmetry and within linear spin-wave (LSW) theory the excitation of a pair of zone-boundary magnons leads to a high frequency peak at $\omega_{2m} \cong 2.7J$ [303]. Strong two-magnon scattering has

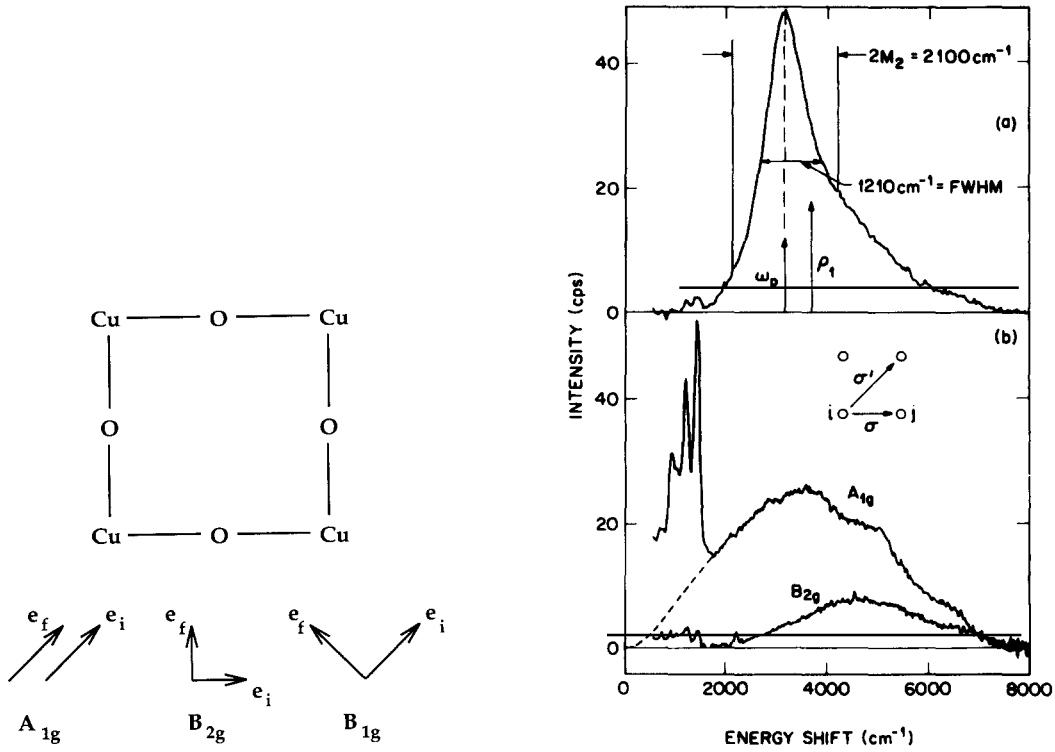

Fig. 15. Polarizations of the incoming (e_i) and outgoing (e_f) photons in different scattering geometries. The orientation of the photon polarization vectors is shown relative to the Cu–O bonds in the planes.

Fig. 16. Light scattering spectra for La_2CuO_4 in B_{1g}, A_{1g} and B_{2g} geometries. All spectra were excited with 4880 Å laser light. (From Ref. [373].)

indeed been observed in B_{1g} geometry for cuprate antiferromagnets. With the LSW theory results values for the exchange coupling energy have been extracted from the energy of the two-magnon peak. For example $J = 1100\,\mathrm{cm}^{-1} = 136\,\mathrm{meV}$ for La_2CuO_4 [243] and $J = 950\,\mathrm{cm}^{-1} \sim 117\,\mathrm{meV}$ for $123\,O_6$ [244], reasonably close to the numbers obtained in neutron scattering experiments (see Tab. 1).

Weaker two-magnon Raman scattering is also observed in A_{1g} and B_{2g} scattering geometries [373,393,376]. The nonvanishing A_{1g} intensity implies that in terms of the square lattice Heisenberg model finite exchange couplings exist also between diagonal next-nearest-neighbor (nnn) sites. The weak but finite B_{2g} intensity possibly results from nnn two-spin flip pairs created by longer range terms which are missing in the spin–photon coupling Hamiltonian Eq. (3.28) [256]; nnn two-spin flip terms are also made possible by the quantum fluctuations in the two-sublattice antiferromagnetic state which are strong due to the low dimensionality and the small spin 1/2. Quantum fluctuations lead to a spectral lineshape of the two-magnon peak whose width is significantly broader and whose tails extend up to energies $\sim 8J$ – very different from the spectra of the two-magnon approximation in LSW theory [245,373]. Singh et al. have taken quantum fluctuations into account by expansions around the Ising limit of the 2D Heisenberg model [373]. The resulting moments of the two-magnon

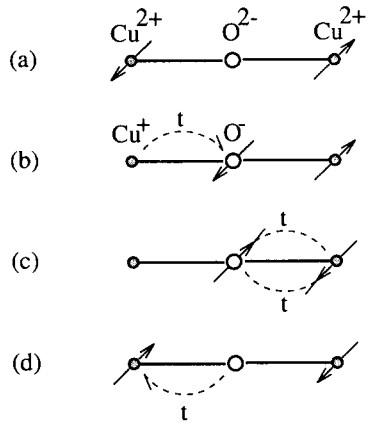

Fig. 17. Schematic picture for the two-spin flip light scattering process in a CuO_2 plane: (a) Initial configuration. (b) The incoming photon is absorbed creating a charge transfer excitation from a Cu to an O orbital. (c) Exchange process. (d) Charge transfer from O to Cu emitting the outgoing photon. (Figure reproduced from [256].)

spectra have been found to agree very well with experiments and have allowed a more accurate determination of the exchange coupling constants, e.g. $J = (1030 \pm 50)\text{cm}^{-1}$ is found from this analysis applied to the data for La_2CuO_4 [373].

A simple picture for the two-spin flip scattering in a CuO_2 plane can be obtained if the microscopic process is decomposed into individual electron hoppings as visualized in Fig. 17. The incoming photon couples to, say, an up-spin electron on a Cu site inducing a charge transfer to a neighboring oxygen orbital. This is followed by an exchange process with a separate neighboring Cu spin. Finally, a down-spin electron hops back to the initial Cu site emitting the outgoing photon. Altogether this sequence has created a pair of flipped nearest-neighbor Cu spins while the photon has in fact been coupled to the charge transfer excitation from a Cu to an oxygen orbital.

When holes are doped into the antiferromagnet the two-magnon feature in the Raman intensity rapidly weakens and the peak's center of gravity moves to lower energy [243] as might be expected from the spin disordering effect of the doped carriers [246]. A sequence of $123\,O_{6+x}$ samples with different oxygen contents has shown that a remnant of the magnetic spin-fluctuation component of the light scattering is still present in the metallic and superconducting samples (see Fig. 18). Local spin correlations on some short time scale do therefore coexist with superconductivity [246]. In particular, a two-spin fluctuation peak has been observed by Lyons et al. in a $T_c = 60$ K sample simultaneously with a superconducting gap opening at low energies [246]. A more rapid disappearance of the two-magnon peak has been reported by Reznik et al. but it has been confirmed to be still present in superconducting samples with lower T_c values [329]. Stronger two-magnon peaks in metallic 123 samples are argued to arise from oxygen deficient surface layers [329].

The sensitive dependence on the frequency of the incoming photon has shown that the two-magnon scattering is of resonant nature [237,329]. Only when the incident photons are at resonance with the charge-transfer gap energy of the insulators (see section 4.1.1) is the two-magnon peak observed in Raman scattering. This indicates that it arises from the resonant coupling of the light to the current density Eq. (3.26) and hence the resonance is an effect of intermediate transitions to high-energy states [91]. The disappearance of the two-magnon peak upon doping in the metallic regime therefore does not necessarily imply the disappearance of short range AF spin correlations. Rather, it may be

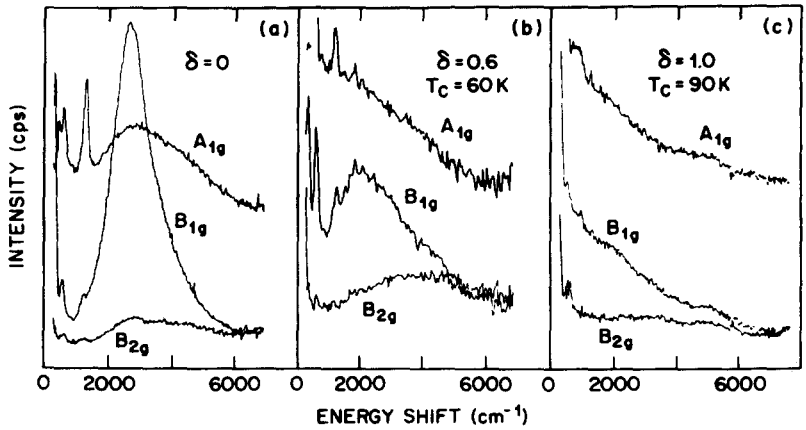

Fig. 18. Light scattering spectra for $123O_{6+\delta}$ obtained in the three relevant scattering geometries B_{1g}, A_{1g} and B_{2g}. (a) Antiferromagnetic insulator with $\delta = 0$, (b) $T_c = 60$ K superconductor with $\delta = 0.6$, and (c) $T_c = 90$ K superconductor with $\delta = 1$. (From Ref. [246].)

caused by the weakening of the resonant enhancement at finite doping concentrations due to the loss of spectral intensity for charge-transfer excitations [91,329]. As schematically shown in Fig. 17 this excitation involves a hole hopping from a Cu d-orbital to a nearest-neighbor oxygen p-orbital.

The change with doping in the two-magnon scattering intensity is different in the electron doped superconductor $Nd_{2-x}Ce_xCuO_4$ where the two-magnon peak clearly does not disappear in a wider metallic composition range [425,395]. This is consistent with the previously discussed observation that the long range antiferromagnetism persists to considerably larger doping concentrations in the electron doped 214 materials as compared to hole doped 214 (see section 2.2).

3.4.2. Electronic background continuum

Although probably not related to the magnetic properties a discussion of the Raman experiments has to include the large background intensity observed in all high T_c cuprates. This most notable feature in the normal state of superconducting samples has been found to be nearly frequency and also temperature independent in stoichiometric compounds [392,383]. It extends from very low energy transfers $\hbar\omega < k_BT$ [379] up to ~ 1 eV at all major plane polarised symmetries [383]. The large energy range of the featureless Raman background suggests that it is electronic in origin but cannot purely result from magnetic or two-phonon excitations. Additional evidence for the electronic origin comes from asymmetric Fano lineshape of certain phonons since electron–phonon coupling leads to an antiresonance only if both the continuum and the phonons are Raman active. However, the Raman continuum is not restricted to the metallic and superconducting compounds and it is observed to be comparably strong in the insulating antiferromagnets [327,328]. So it is unlikely that the Raman continuum in its entire range is caused by the scattering of light from conduction electrons which would suggest a close resemblance in its doping dependence to the infrared conductivity; however, this is not observed. In fact, the background intensity does not scale with the concentration of doped holes [213].

If the Raman intensity is divided by the Bose factor from Eq. (3.27) the response function responsible for the Raman background is found to behave as

$$\mathrm{Im}\,\chi(q \sim 0, \omega, T) \propto \begin{cases} \omega/T & \text{for } \omega \ll T, \\ \text{const} & \text{for } \omega \gg T, \end{cases} \tag{3.29}$$

in A_{1g} and B_{2g} scattering geometries [384,329]. So in these symmetries the temperature is the only relevant energy scale for the response function, reminiscent of the ω/T scaling behavior in the magnetic neutron scattering in low doped compounds (compare section 3.2.4). Again, the appearance of the temperature as the relevant low energy scale is distinct from a conventional metal where the Fermi energy sets this scale. The ω/T scaling behavior of the Raman response has been taken as the starting point for the marginal Fermi liquid phenomenology [130] (see section 4.1.1). A different behavior is, however, observed in B_{1g} geometry with a temperature independent slope in the linear low frequency part of the response function [384,248,329]. It is interesting that the Raman continuum persists also in the overdoped $La_{2-x}Sr_xCuO_4$ compound with $x = 0.34$ [394] which is not superconducting and more likely behaves as a conventional metal [401]. The Raman background continuum can therefore not serve to answer the question whether the charge carriers in the cuprates form a Fermi liquid or not.

So far there is no satisfactory explanation of the Raman background in optimally doped as well as insulating compounds. The insensitivity to doping and also the incomplete low frequency gap-like redistribution below T_c may favour an interpretation in terms of defect induced localised states more or less present at all doping concentrations [329]. Nevertheless conduction electrons do contribute to the low energy continuum intensity where gap like structures are formed in the superconducting state.

3.4.3. Energy gap

Raman gap spectroscopy in $123\,O_7$ has generally found a distribution of gap values for different scattering geometries [149,89,248]. They have been assigned to a large gap anisotropy with mean gap energies ranging from $\Delta \sim 3k_BT_c$ to $\Delta \sim 5.5k_BT_c$ [149]. Another intriguing result is the almost ideal superconducting spectrum found in BSCCO 2212 at B_{1g} symmetry while in all other symmetries low energy scattering extending to zero frequency is observed suggesting a continuum of electronic states inside the gap [385,89]. The incompleteness of the gap formation and the polarization dependence of the gap feature may require both, an anisotropic gap function and additional localised states not participating in the pairing.

3.5. Transport, impurity effects

While the experimental techniques we have focused on so far are direct probes for the magnetic correlations we will in the present chapter collect some examples for other distinguished properties of the cuprates which are related to the presence of AF spin fluctuations. Not all of them are rigorous but nevertheless suggestive to be of magnetic origin. They indicate that some of the normal state properties which are referred to as *unconventional* are most likely related to short range spin correlations in the doped compounds.

3.5.1. Spin gap and resistivity

One of the anomalous properties found in NMR and neutron scattering experiments is the apparent spin-excitation gap in underdoped 123 compounds. Interestingly, the maximum in $(^{63}T_1T)^{-1}$, which

we may refer to for our convenience as a spin-gap phenomenon, is directly accompanied by features in the dc-resistivity and the optical conductivity. In the material $YBa_2Cu_4O_8$ (referred to as YBCO 124) – which is a stoichiometric, metallic compound with a planar hole content comparable to the 60 K 123 superconductor – the in-plane resistivity ρ_{ab} decreases faster than linear below the spin-gap temperature T_D = 160 K [59]. This temperature is obtained from the Cu spin–lattice relaxation rate [477] shown in Fig. 19. Above T_D the resistivity increases linearly with temperature in a temperature range of several hundred K; this is one of the most intriguing transport properties observed in essentially all optimally doped cuprate superconductors [33]. Since $(^{63}T_1T)^{-1}$ is governed by the AF spin fluctuations near $\boldsymbol{Q} = (\pi, \pi)$ the connection between the spin gap and the drop in the resistivity suggests that a major part of the resistivity results from large-$\boldsymbol{q}$ magnetic scattering. Because of a loss in spectral weight for the spin fluctuations due to the spin-excitation gap the magnetic scattering is reduced below T_D and the resistivity therefore decreases. An analogous correlation of the appearance of the spin-excitation gap with deviations from the T-linear resistivity as well as deviations from the often observed $1/T$ dependence of the Hall coefficient [300] has been recently reported for underdoped 123 compounds [183].

A similar phenomenon is observed in the planar infrared conductivity of underdoped 123 compounds. Here, $\sigma(\omega)$ shows a remarkably similar temperature dependence to the ^{17}O NMR relaxation rate for frequencies in the region of the superconducting energy gap [88,340]. With these closely related temperature dependences of both charge and spin degrees of freedom the spin gap opening in the underdoped compounds has its counterpart in the development of a 500 cm^{-1} absorption threshold in the real part of $\sigma(\omega)$ well above T_c. While the similarities in the superconducting state between the $\omega \to 0$ quantity $1/T_1T$ and $\sigma_1(\omega)$ for frequencies $\omega \sim \Delta$ are also well known in BCS theory – in particular both quantities have the same coherence factors – the remarkable feature in $123\,O_{6.6}$ is that the same single temperature dependence appears for all relevant frequencies $\omega \leq 2\Delta$ [88] tying spin and charge dynamics close together. Theoretical concepts which rely on the separation of spin and charge excitations are not supported by these experimental results.

3.5.2. *Impurity doping with nonmagnetic ions*

Ionic substitution serves as another experimental tool to obtain information about the magnetic correlations and their relation to superconductivity. Local defects can be created on the Cu sites in particular by the replacements with nonmagnetic Zn or Ga ions. In 123 compounds Ga^{3+} favourably replaces Cu^{2+} ions on the CuO chains which has only a minor effect on the superconductivity [458] proving that the chains do not play an essential role for the electronic properties. Zn ions, however, do preferentially enter the CuO_2 planes without adding an excess of charge carriers [12,459]. Zn ($3d^{10}4s^2$) is divalent and its d-shell is completely filled. Zn therefore creates local static vacancies when doped into the AF parent compounds and the antiferromagnetism is weakened by diluting the number of magnetic moments. Accordingly the Néel transition temperature is initially suppressed linearly with increasing Zn concentration [460,205] as shown in Fig. 20. This physical situation is appropriately described by a randomly diluted 2D Heisenberg antiferromagnet. As we will see in section 5.1.3 in linear spin wave theory the spin wave velocity softens linearly with the (small) vacancy concentration [50] at a rate comparable to the experimentally observed reduction in T_N.

It is also remarkable that the rate of the suppression of the Néel temperature with Zn substitution is very similar to the situation when electrons are doped into the antiferromagnet Pr_2CuO_4 [205] by

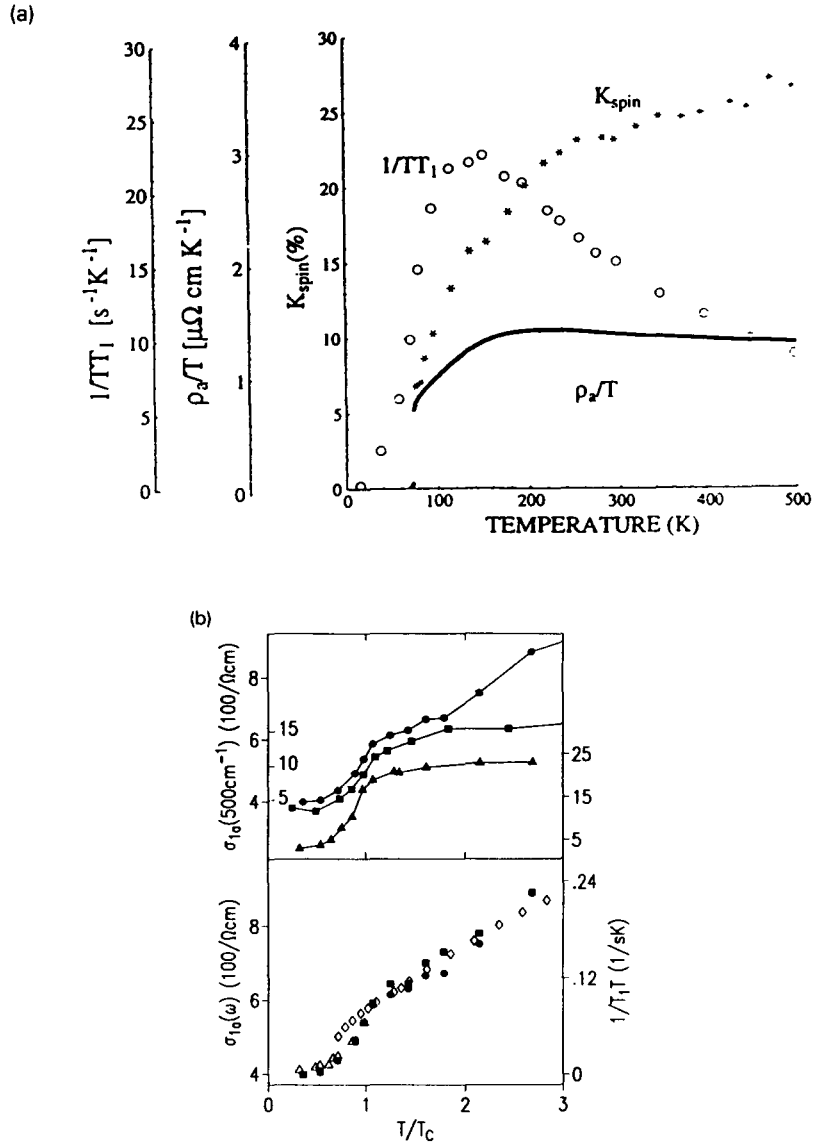

Fig. 19. (a) Connection of NMR magnetic probes, Cu Knight shift and $1/T_1T$, to the planar resistivity in $YBa_2Cu_4O_8$. (From Ref. [59].) (b) Comparison between the CuO_2 plane conductivity $\sigma_{1a}(\omega)$ in the gap region [ω = 250 cm^{-1} (squares) and 500 cm^{-1} (•)] and the NMR Korringa product, $1/T_1T$ for ^{17}O in a T_c = 62 K $123O_{6+x}$ sample (△◇). (Figure taken from Ref. [340].)

substituting Ce for Pr as is also shown in Fig. 20. The doped electrons presumably create locally nonmagnetic Cu^+ with a $3d^{10}$ configuration, i.e. the same d-shell configuration as for a doped Zn^{2+} ion. This leads to the same magnetic dilution effect for low electron doping concentrations.

A nonmagnetic dopant like Zn creates locally a static vacancy in the antiferromagnet which has total spin $\langle S^z_{tot}\rangle = 0$ and hence the vacancy creates a net uncompensated spin $S = 1/2$. This generates an

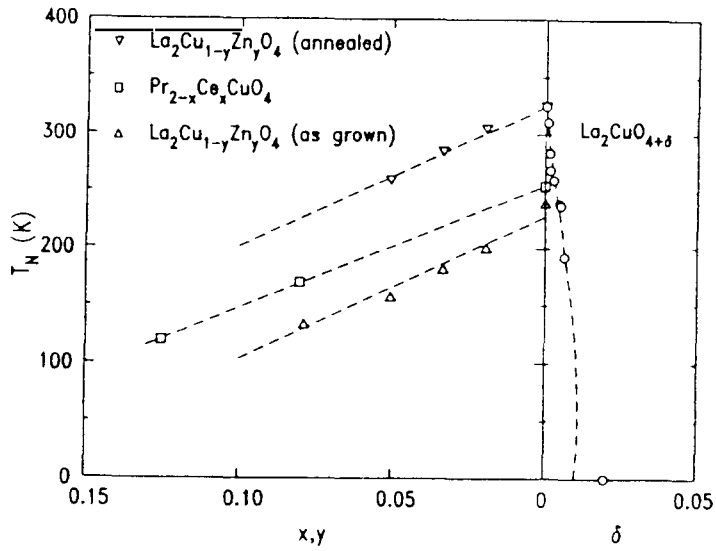

Fig. 20. Néel temperature as a function of the concentration of doped electrons or holes in 214 samples, together with the dependence on the Zn concentration in Zn doped La_2CuO_4. (From Ref. [205].)

effective local moment. Zn doped materials therefore exhibit a Curie–Weiss behavior in the magnetic susceptibility as observed in $La_{2-x}Sr_xCu_{1-y}Zn_yO_4$ [461]. This local moment may be viewed to be localized on a small number of Cu sites surrounding the static vacancy.

Zn doping also has a detrimental effect on the superconductivity. T_c is suppressed to zero in $La_{1.85}Sr_{0.15}Cu_{1-y}Zn_yO_4$ by the substitution of less than $y = 3\%$ Zn on the Cu sites [458,461,229]. Even more striking is that as little as 0.31% Zn substitution makes the superconductor $YBa_2Cu_3O_{6.95}$ gapless [49]. Because of the Zn-doping induced local moment it has been suggested that the suppression of superconductivity arises from a magnetic pair breaking effect [460,12]. However, an analysis of the ^{63}Cu NMR linewidth in Zn doped $123\,O_7$ [447] has shown that the Abrikosov–Gorkov magnetic pair-breaking mechanism [1] is too weak to account quantitatively for the rapid T_c suppression. Alternatively, the effect may arise dominantly from strong potential scattering from the Zn impurity sites [447]. In order for this mechanism to be an effective pairbreaker the orbital pair wave function is required to have a symmetry different from s-wave according to Anderson's theorem [16].

3.5.3. Quasiparticle lifetime

It is generally agreed that the normal state conductivity of high-temperature superconductors (HTSC) in the frequency range below $\sim 300\,\mathrm{cm}^{-1}$ can be described by a Drude term $\sigma(\omega) = (\omega_p^2/4\pi)/(\tau^{-1} - i\omega)$ with a roughly constant plasma frequency $\omega_p = (4\pi ne^2/m^*)^{1/2}$ and an inelastic scattering rate τ^{-1} that decreases fairly linearly with temperature [350,131,190]. In ω_p, n is the density of conduction electrons with effective mass m^*. The behavior of τ^{-1} has emerged as one of the characteristic features in phenomenological descriptions of the normal state charge dynamics. High-quality microwave surface-impedance measurements have subsequently been performed by Bonn et al. [47,48] to determine the temperature dependence of the inelastic scattering rate also in the superconducting state. A rapid suppression of τ^{-1}, much faster than a linear temperature dependence,

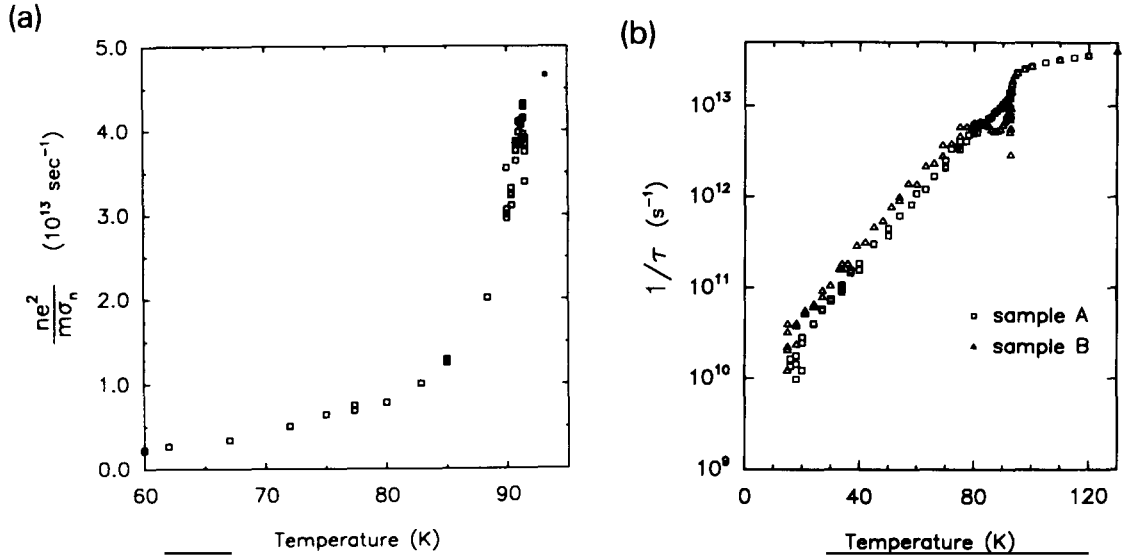

Fig. 21. (a) Estimate for the quasiparticle scattering rate in $YBa_2Cu_3O_7$ as obtained from the quantity $ne^2/m^*\sigma_n$ close below T_c. The open circles are extracted from microwave data and the solid square at 95 K is derived from the normal state resistivity. (From Ref. [47].) (b) The temperature dependent part of the quasiparticle scattering rate obtained by subtracting a low temperature limiting value of $7 \times 10^{10} s^{-1}$. Here, the temperature dependence of the normal-fluid has been taken into account. The nearly straight line on a semi-log scale indicates that the scattering rate varies as $\exp(T/T_0)$. (From Ref. [48].)

has been observed in $123\,O_7$ below T_c.

An estimate for the quasiparticle scattering rate has been obtained from a two-fluid model analysis of the low-frequency conductivity [47–49]. In the two-fluid model the real part of the conductivity is divided into the two terms

$$\mathrm{Re}\,\sigma(\omega,T) = \sigma_s(T) + \sigma_n(T) = \frac{\omega_p^2}{4\pi}\left(x_s(T)\delta(0) + x_n(T)\frac{\tau(T)}{1+\omega^2\tau^2}\right). \tag{3.30}$$

The first term is the superfluid response which is related to the London penetration depth λ via $x_s(T) = \lambda^2(0)/\lambda^2(T)$. The second term in Eq. (3.30) is the normal fluid component which has been modeled here by a simple Drude response [49]. $x_s(T) + x_n(T) = 1$ in the clean limit, which is appropriate for HTSC where the electronic mean-free path is large compared to the coherence length in the superconducting state. An estimate for τ^{-1} is therefore provided by plotting $ne^2/m^*\sigma_n(T)$ versus temperature for the low-frequency microwave data in the few GHz range. Fig. 21a shows the corresponding result obtained by Bonn et al. [47].

Even though the neglect of the temperature dependence of the normal-fluid density $x_n(T)$ leads to an uncertainty in identifying the ratio $ne^2/m^*\sigma_n(T)$ with the quasiparticle scattering rate the rapid drop in this quantity below T_c evidently tells that τ^{-1} falls much faster than linearly with temperature. In a subsequent analysis the temperature dependence of $x_n(T)$ has been taken into account and the scattering rate has been found to follow an approximate exponential law, $\tau^{-1} \propto \exp(T/T_0)$ in the temperature range between 15 and 84 K with $T_0 \approx 12$ K [48] (see Fig. 21b). Quinlan and Scalapino have noted that the temperature dependence of τ^{-1} may also be viewed to be close to a power law

T^3 behavior between $T_c/2$ and T_c [323]. The significance of the rapid decrease of τ^{-1} below T_c is that it strongly argues for an electronic origin of the dominant scattering process in the normal state. Below T_c the superconducting gap opens up in the excitation spectrum and the electronic scattering process is considerably suppressed explaining the drop in the quasiparticle scattering rate.

3.6. Gap anisotropy: hints for $d_{x^2-y^2}$ symmetry

As we will discuss in chapter 6 a pairing interaction mediated by the exchange of AF spin fluctuations will most likely lead to an anisotropic gap function with $d_{x^2-y^2}$ symmetry. The line nodes in this gap function imply observable consequences for the properties of the superconducting state. A number of experiments have been found compatible with a $d_{x^2-y^2}$ pairing state. A direct experimental proof for line nodes is not yet available. But a conclusive experiment with a SQUID arrangement for a cuprate superconductor in contact with a conventional superconductor known to have an s-wave gap has been suggested recently [370]. First results from this difficult experiment have been reported and are found to support the d-wave hypothesis [457]. A refinement of these experimental results is still needed for a conclusive answer. Without this explicit test for nodes in the gap function on the Fermi surface a distinction from a highly anisotropic yet nodeless gap may remain ambiguous. However, an interpretation in terms of a d-wave gap appears very natural for recent penetration depth [153], thermal conductivity [469] and photoemission data [360] and also for a recently discovered, very peculiar phenomenon which has been called the paramagnetic Meissner effect [57]. Some of these data will be discussed in the next three chapters.

3.6.1. Angular resolved photoemission spectroscopy (ARPES)

Due to recent remarkable progress in photoemission spectroscopy with energy resolution down to ~ 10 meV an angular resolved gap spectroscopy has become possible in HTSC materials. The high transition temperature is accompanied by energy gap values around 20 meV so that a measurement at least of bounds for the energy gap by photoemission techniques has become meaningful. This possibility is unique to HTSC and is inapplicable to low T_c superconductors where the gap is an order of magnitude smaller.

In the Bi 2212 superconductor ARPES experiments have been able to demonstrate a large planar anisotropy of the energy gap in the superconducting state [450,360]. Spectra for two momenta, chosen to lie on the Fermi surface of the normal state, are shown in Fig. 22. One $\boldsymbol{k}$ value is chosen along the diagonal of the Brillouin zone ($\boldsymbol{k}_B$), the other along the (1,0) direction ($\boldsymbol{k}_A$). The opening of the energy gap at $\boldsymbol{k}_A$ is clearly observed on cooling through T_c while only minor changes are observed at $\boldsymbol{k}_B$. This suggests that the energy gap is strongly anisotropic and very small – if finite at all – along the diagonal of the Brillouin zone. The observed anisotropy agrees with what is expected for a $d_{x^2-y^2}$ gap function of the form $\Delta_k = \Delta_0[\cos(k_x a) - \cos(k_y a)]$. The photoemission data, however, cannot tell whether or not Δ_k has line nodes on the Fermi surface.

A separate feature visible in Fig. 22 is the appearance of a dip below T_c in the data for momentum $\boldsymbol{k}_A$. Similar features are observed in other cuprates in the superconductor–insulator–superconductor (S–I–S) tunneling conductance where the energy of the dip is found to scale roughly as 3Δ if the energy gap Δ is identified with the peak voltage in the conductance [472]. An explanation for this dip feature has been suggested by Coffey and Coffey in terms of quasiparticle decay effects in the

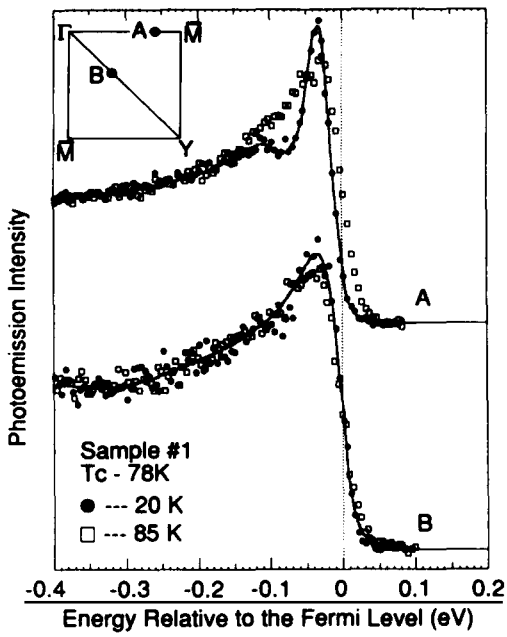

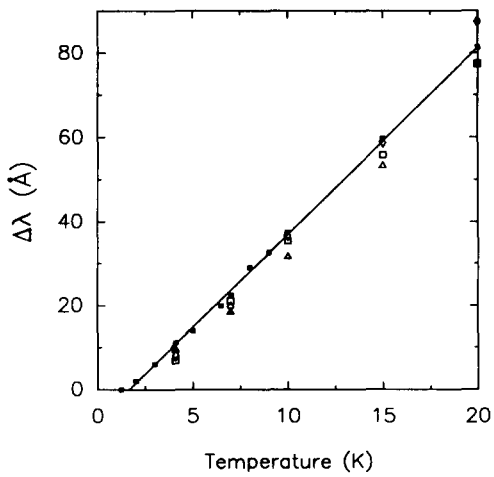

Fig. 22. ARPES spectra for $Bi_2Sr_2CaCu_2O_{8+\delta}$ recorded at k-space locations as illustrated in the inset. The spectral changes below T_c are caused by the opening of the superconducting gap. The change at A is clearly visible (large gap) while the change at B is hardly visible (small or null gap). (From Ref. [360].)

Fig. 23. Temperature dependence of the penetration depth $\lambda(T)$ for a clean single crystal of $123\,O_{6.95}$. Plotted is $\Delta\lambda(T) = \lambda(T) - \lambda(1.3\,K)$ in the low temperature regime. The strong linear behavior is what is expected for a superconductor with line nodes in the gap function. (From Ref. [153].)

superconducting state [86]. These decay effects are sensitive to the order parameter symmetry and a 3Δ scaling is predicted for a $d_{x^2-y^2}$ state in ARPES as well as S–I–S tunneling data.

3.6.2. Penetration depth

In a d-wave superconductor the density of states has a linear energy dependence in the gap region. This gives rise to characteristic power law behaviors in thermodynamic properties instead of the exponential low temperature dependence of a nodeless s-wave superconductor. But in the search for the power laws which could identify a d-wave superconductor the intrinsic temperature dependences are often masked by impurity or other extrinsic effects which prevent an unambiguous conclusion for the gap symmetry. High precision experiments on very clean samples are therefore needed.

One such measurement may have been performed by Hardy et al. for the penetration depth λ using microwave techniques for a high-quality single crystal of the $T_c = 90$ K superconductor $123\,O_{6.95}$ [153]. A strong linear temperature dependence has been found for $\Delta\lambda(T) = \lambda(T) - \lambda(0)$ extending from approximately 3 to 25 K as shown in Fig. 23. This is particularly remarkable because all possible non-s-wave singlet pairing states with line nodes in the gap function have this linear temperature dependence. This has been proved by Annett et al. [20] for a superconductor with tetragonal or orthorhombic symmetry and a spherical or cylindrical Fermi surface topology.

The results of Hardy et al. differs from earlier reported results on thin films for which a T^2 dependence has been obtained at low temperatures (see e.g. Refs. [20,19]). The linear temperature dependence in the high-quality single crystal data of Hardy et al. is suggestive of line nodes in a clean d-wave superconductor. The T^2 term observed in thin films is most likely due to the influence of defects. The possible defect origin of the T^2 term has been nicely demonstrated by doping a $123\,O_{6.95}$ single crystal with 0.15% Zn [2]. In the Zn doped sample a T^2 contribution has been found to appear at the lowest temperature. This suggests that the linear temperature dependence of $\Delta\lambda(T)$ is intrinsic to pure crystals whereas the T^2 behavior would be due to defects [2].

3.6.3. Paramagnetic Meissner effect (Wohlleben effect)

In some polycrystalline Bi based HTSC the very peculiar but reproducible effect has been observed that in low fields of about 10–100 mOe the dc field-cooling Meissner signal becomes *paramagnetic* [57,58] as shown in Fig. 24. In the same samples which show this paramagnetic Meissner effect[3] (PME) anomalies in the low-field microwave absorption occur. Since there is no evidence in these samples for magnetic impurities the PME must be due to the appearance of orbital magnetic moments. Granularity is a general characteristic of the samples and suggests that the PME is related to the network of weak links between individual superconducting grains. It is known that a network of Josephson junctions can lead locally to spontaneous circular currents provided that the Josephson coupling energy is *negative* at some Josephson contacts between the grains. This means that the Cooper pairs acquire a phase shift π in the tunneling process between two linked superconducting grains. Spontaneous orbital currents are created in loops which contain an odd number of contacts with a negative Josephson coupling [220]. The existence of these so-called π-junctions would therefore naturally explain the PME in granular Bi-based compounds; also the anomalies in the microwave absorption have been shown to find a simple explanation presuming the existence of π-junctions in a network of weak links [370].

As proposed by Sigrist and Rice π-junction contacts can arise if d-wave superconductivity is realised in the individual grains [370]. In a tunneling junction the tunneling probability is strongly peaked for electron wavevectors perpendicular to the junction interface, and the Josephson supercurrent depends on the phase difference of the superconducting order parameter across the junction. Due to the sign change of the $d_{x^2-y^2}$ order parameter around the Fermi surface in the 1st Brillouin zone 0- or π-junctions can be realised depending on the position of the tunneling contact with respect to the axis of an appropriately aligned single crystal of the superconducting material [143,370]. Based on this idea the experimental setup shown in Fig. 25a has been used by Wollman et al. [457] for the first attempt of a direct test of the orbital pairing state in a $YBa_2Cu_3O_7$ single crystal.

Maintaining phase coherence around the SQUID loop in Fig. 25 requires the constraint condition

$$\phi_a - \phi_b + 2\pi\Phi/\Phi_0 + \delta_{ab} = 0 \tag{3.31}$$

to be satisfied for the gauge-invariant phase differences ϕ_a and ϕ_b across the junctions on the a and b faces of the $123\,O_7$ crystal, respectively. $\Phi = \Phi_{ext} + LJ$ is the total flux in the loop with self-inductance L, which includes both, the externally applied flux Φ_{ext} and the flux from the circulating supercurrent density J. Since Pb has an s-wave gap function the shift parameter δ_{ab} determines whether the phase

[3] In honour of the late Dieter Wohlleben the paramagnetic Meissner effect is now frequently referred to as the Wohlleben effect.

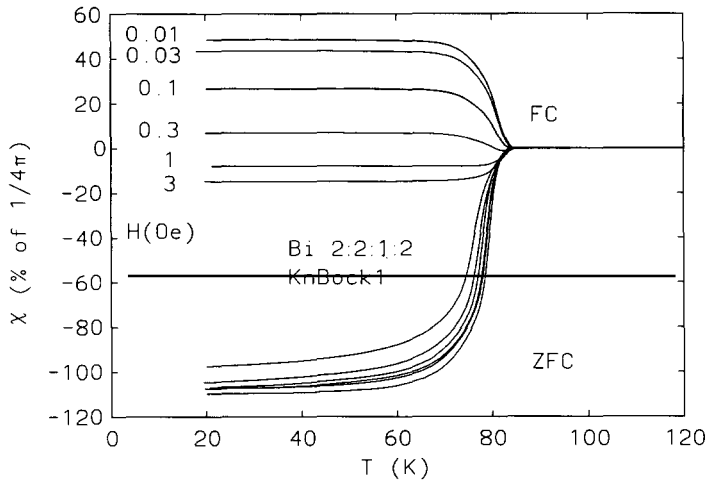

Fig. 24. Zero-field-cooled (ZFC) and field-cooled (FC) susceptibilities as a function of temperature for a melt-processed Bi 2212 sample exhibiting the paramagnetic Meissner effect in very low fields. (From Ref. [58].)

of the 123 order parameter is the same or different at the junction faces a and b. If the $123\,O_7$ superconductor has an s-wave gap, too, then $\delta_{ab} = 0$. But for a $d_{x^2-y^2}$ symmetry the gap function has the form $\Delta(\boldsymbol{k}) = \Delta_0[\cos(k_x a) - \cos(k_y a)]$ which changes sign between the junction faces a and b. This would lead to an intrinsic phase shift $\delta_{ab} = \pi$. The modulation of the maximum supercurrent I_c with the external flux is sensitive to the phase shift as shown in Fig. 25b. For example in the limit of a vanishing self-inductance I_c is given by

$$I_c = 2I_0|\cos(\pi\Phi_{\text{ext}}/\Phi_0 + \delta_{ab})|. \tag{3.32}$$

The measurements by Wollman et al. [457] of the resistance versus applied magnetic flux at different bias currents have given preliminary evidence that the phase shift δ_{ab} in the $123\,O_7$ single crystal is of order π consistent with the hypothetical $d_{x^2-y^2}$ pairing state. Further refinements of this difficult experiment will certainly give the opportunity for an unambiguous determination of the pairing state in high-temperature superconducting cuprates bearing an important hint for the pairing mechanism.

4. Phenomenological concepts and microscopic models

While the antiferromagnetism in the insulating parent compounds is well understood in terms of a Heisenberg model and its material specific extensions, the various experiments described in chapter 3 have furthermore provided evidence for the presence of AF spin fluctuations persisting also in the doped, metallic and superconducting compounds. In this chapter we will outline some of the theoretical concepts which have led to consider microscopic Hubbard like models for the correlated electrons and their magnetic correlations in cuprate materials. These are the models for which we will review in chapter 5 some of the results and theories attempting to understand selected normal state

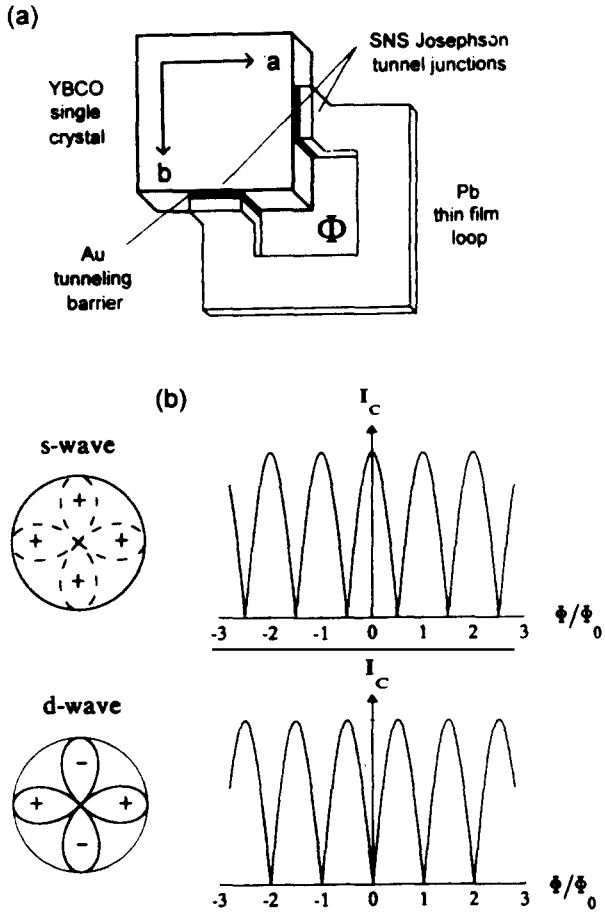

Fig. 25. (a) Experimental configuration of $YBa_2Cu_3O_7$–Pb corner dc-SQUIDS. (b) Predicted modulation of the SQUID's critical current versus applied magnetic flux Φ (in units of the flux quantum Φ_0) for the s-wave and $d_{x^2-y^2}$-wave pairing states. The two principal axes for the two order parameters are also indicated in a polar graph. (From Ref. [457].)

properties. However, for a smooth transition from the experimental to the more theoretical chapters we start by discussing some phenomenological aspects first.

4.1. Phenomenologies of the normal state

4.1.1. Marginal Fermi liquid phenomenology

As a guiding idea for a consistent picture of the normal state properties it was recognized early on that a number of experimental data can be explained by an anomalous linear frequency and temperature dependence of the quasiparticle scattering rate. For example a linear dependence for the imaginary part of the self-energy has been the central part of the marginal Fermi-liquid (MFL) phenomenology [130]. It follows from the key assumption that the quasiparticles scatter from an unspecified boson[4]

[4] The boson in the MFL phenomenology has been called "marginon" by some authors.

with an excitation spectrum which is structureless over an energy range $T < \omega < \omega_c$ [130], where ω_c is an ultraviolet frequency cutoff. Explicitly, a simple model for the boson spectrum of the form [232]

$$B_{\rho,\sigma} = \frac{\tanh(\omega/T)}{1 + (\omega/\omega_c)^2} \tag{4.1}$$

has been assumed – originating from either charge or spin excitations. A one-loop calculation for the self-energy from the coupling to the "marginon" with the spectrum Eq. (4.1) leads to a result which is conveniently approximated by [232]

$$\Sigma_{\mathrm{MFL}}(\omega, T) = \pi\lambda \left[\frac{2\omega}{\pi} \ln\left(\frac{\pi T + i\omega}{\omega_c} \right) + i\pi T \right]. \tag{4.2}$$

λ is a coupling constant. The imaginary part of Σ_{MFL} has the desired asymptotic forms

$$\mathrm{Im}\, \Sigma_{\mathrm{MFL}}(\omega, T) \sim \begin{cases} \pi^2 \lambda T & \text{for } \omega \ll T, \\ \pi\lambda\omega & \text{for } T \ll \omega \ll \omega_c. \end{cases} \tag{4.3}$$

Most importantly, the energy scale for particle–hole fluctuations is set by the temperature only and in particular, the "marginon" spectrum and the resulting self-energy are momentum independent. However, charge and spin density are conserved quantities and their response functions require therefore a q^2 dependence at low momentum. To account for this requirement the boson spectrum needs to be modified for long wavelengths and Eq. (4.1) is valid only for $v_F q > [\omega \max(\omega, T)]^{1/2}$ [217]. But this restriction does not lead to important consequences for the self-energy [217].

The microscopic origin has not been specified in the original MFL hypothesis, but it has pointed to a common electronic origin of different normal state phenomena. Some of the immediate consequences of the hypothesis for the normal state include [439,234]

(i) the quasiparticle peak width in the single-electron spectral function should vary linearly in $|\epsilon_k - E_F|$ near the Fermi energy E_F as approximately verified in angular resolved photoemission experiments within the available energy resolution [301],
(ii) a linear tunneling conductance, and
(iii) a linear temperature dependence of the resistivity.

The last two features are indeed observed in the corresponding normal state experiments. (See e.g. Ref. [33] for a discussion of resistivity data and e.g. Refs. [148,210] for the tunneling conductance.)

The Raman background continuum in metallic cuprates was one of the basic motivations for the flat and featureless "marginon" spectrum but, as discussed in chapter 3, its appearance in the insulators as well as in overdoped non-superconducting materials has raised doubts whether the Raman continuum is an intrinsic feature which is connected to the dynamics of the metallic charge carriers.

Since the MFL hypothesis does not assume any momentum dependence for the response functions there is no obvious way how to consistently explain the NMR data whose interpretation has naturally been based on large $\boldsymbol{q}$ AF spin fluctuations. In particular, it is not clear whether a plausible alternative explanation can be offered for the different spin dynamics at the Cu and at the O nucleus. For the understanding of the neutron scattering data, however, the MFL picture has been extended to include band structure effects [235]. It has been recognized that band structure alone, especially in two dimensions, can give rise to strong momentum dependence in the magnetic structure factor [240,368,308,62]. A combination with MFL frequency dependence for the response function [235]

has been offered as an explanation for neutron scattering data as an alternative to magnetic correlations for a system near an ordered AF phase.

An extension of the MFL phenomenology has been proposed by Zimanyi and Bedell to include large q momentum structure into the theory arising from antiferromagnetic spin fluctuations [476]. In the spirit of the original MFL hypothesis the AF–MFL theory is based on an anomalous spin correlator

$$\mathrm{Im}\,\chi(q,\omega) \approx \chi_0 \left(\frac{\omega}{\omega_0} + \frac{B}{[1+(q-Q)^2\xi^2]^2} \tanh(\omega/T)\,\theta(\omega-\omega_c) \right). \tag{4.4}$$

Here it is assumed that anomalous spin fluctuations in the vicinity of the AF wavevector $Q = (\pi, \pi)$ are the origin of the "marginon". The strength of the spin correlations is measured by the numerical constant B, while ξ indicates their correlation length. When compared to the original MFL ansatz Eq. (4.4) has been suggested to provide an improved correspondence with experimental data, in particular with Cu and O relaxation times in NMR experiments. By applying renormalization-group techniques this extended MFL scheme has been found to be capable of interpreting qualitatively further experimental results, including the doping dependence of the resistivity and the magnetic susceptibility [476].

It has clearly been the merit of the MFL phenomenology to recognize for the first time that a number of the unusual normal state properties in cuprate materials can be qualitatively understood in terms of a single correlated electron fluid which differs from the conventional low temperature properties of a Fermi liquid. All what appeared left to do was to search for the origin of the "marginon" with a bosonic spectrum as in Eq. (4.1). Many experimental and theoretical results continue to be interpreted in this way. But the question whether or not the normal state in metallic cuprates can be described in a Fermi liquid framework with appropriate modifications has not yet found a commonly accepted answer.

An entirely novel concept for the normal state of the HTSC's has been proposed by Anderson [14,17]. In this picture the electrons are supposed to form a Luttinger liquid in which the excitations decompose into holons, carrying charge e and spin $S = 0$, and spinons, carrying charge 0 and spin $S = 1/2$. This phenomenon of the separation of charge and spin excitations is known to occur e.g. in the 1D Hubbard model or in soliton excitations in polyacetylene [382]. To the knowledge of the author virtually all calculations to date on the Hubbard, t–J or related models in 2D have shown no evidence for the deconfinement of charge and spin of the elementary excitations (see, however, the recent high-temperature expansion results of [319] for the t–J model) and the excitations are most likely the conventional ones, carrying charge $\pm e$ *and* spin $S = 1/2$. For an extended discussion of the Luttinger liquid picture for HTSC we refer the reader to the announced forthcoming book by P.W. Anderson.

4.1.2. Nearly antiferromagnetic Fermi liquid

In a more conventional framework and originally intended to explain the NMR experiments in $123\,O_7$ Millis, Monien and Pines (MMP) [272] have developed a phenomenological model for the low energy spin dynamics in the normal state. Their phenomenology has provided a useful model form to parametrise the data from Knight shift and spin lattice relaxation rate measurements and it has allowed even quantitative fits to the available experimental data. The NMR phenomenology relies on a spin susceptibility strongly peaked at the commensurate AF wavevector $Q = (\pi, \pi)$. Based on

this assumption Pines [311] has introduced the concept of a *nearly AF Fermi liquid* (NAFL). Very low frequency, diffusive paramagnon modes required by MMP to explain the NMR experiments are suggested to be strongly coupled to the quasiparticles and thereby also responsible for the unusual charge response of the metallic cuprates. Since the NMR based NAFL concept has found a wider extension to other normal state properties and the pairing mechanism for superconductivity we will outline below in detail the original NMR analysis.

MMP start with the assumption that for the understanding of the magnetic relaxation phenomena it is sufficient to consider the coupling of the nuclei to a one-component spin fluid with strong AF correlations. The central part of the MMP analysis of NMR data is a model form for the imaginary part of the spin susceptibility

$$\mathrm{Im}\,\chi(\boldsymbol{q},\omega) = \pi(\omega/\Gamma)\chi_0(T) + \mathrm{Im}\,\chi_{\mathrm{AF}}(\boldsymbol{q},\omega). \tag{4.5}$$

χ is decomposed into a long wavelength part containing the uniform susceptibility χ_0 of Fermi-liquid-like quasiparticles and a short wavelength contribution from commensurate AF correlations between spins located on the copper sites. Due to the proximity to an AF ordered phase a mean field expression is argued to be a reasonable ansatz for χ_{AF},

$$\chi_{\mathrm{AF}}(\boldsymbol{q},\omega) = \frac{\hat{\chi}(\boldsymbol{q},\omega)}{1 - J_{\boldsymbol{q}}\hat{\chi}(\boldsymbol{q},\omega)}, \tag{4.6}$$

where $\hat{\chi}(\boldsymbol{q},\omega)$ is the susceptibility of a noninteracting spin system and $J_{\boldsymbol{q}}$ a momentum dependent exchange coupling. The ultrasmall energy probed by NMR experiments and the short wavelength of AF spin correlations centered around $\boldsymbol{Q}$ allow to expand $\chi(\boldsymbol{q},\omega)$ to lowest order in ω and in $\hat{\boldsymbol{q}} = \boldsymbol{q} - \boldsymbol{Q}$. Assuming that the real and imaginary part of $\hat{\chi}$ are at low energy related by

$$\lim_{\omega\to 0} \mathrm{Im}\,\hat{\chi}(\boldsymbol{q},\omega) = \pi\frac{\omega}{\Gamma_{\hat{\boldsymbol{q}}}}\,\mathrm{Re}\,\hat{\chi}(\hat{\boldsymbol{q}},\omega=0) \equiv \pi\frac{\omega}{\Gamma_{\hat{\boldsymbol{q}}}}\hat{\chi}_{\hat{\boldsymbol{q}}} \tag{4.7}$$

with a characteristic energy $\Gamma_{\hat{\boldsymbol{q}}}$ of spin fluctuations at wavevector $\hat{\boldsymbol{q}}$, MMP obtain the small $\omega, \hat{\boldsymbol{q}}$ expansion in the form

$$\mathrm{Im}\,\chi_{\mathrm{AF}}(\hat{\boldsymbol{q}},\omega\to 0) = \pi\frac{\omega}{\Gamma_{\hat{\boldsymbol{q}}}}\,\hat{\chi}_{\hat{\boldsymbol{q}}}\,\frac{(\xi/\xi_0)^4}{(1+[\xi\hat{\boldsymbol{q}}]^2)^2 + (\omega/\omega_{\mathrm{SF}})^2}. \tag{4.8}$$

Here, ξ is the spin–spin correlation length and $1/\xi_0$ roughly sets the wave vector at which the AF part starts to dominate the spin susceptibility over the quasiparticle contribution [289]. ω_{SF} is a typical energy scale for the AF paramagnons,

$$\omega_{\mathrm{SF}} = (\Gamma_{\boldsymbol{Q}}/\pi)(\xi_0/\xi)^2. \tag{4.9}$$

Combined with the quasiparticle part of the spin susceptibility, $\mathrm{Im}\,\chi$ may be written in the form – dropping the $\hat{\boldsymbol{q}}$ dependences of $\Gamma_{\hat{\boldsymbol{q}}}$ and $\hat{\chi}_{\hat{\boldsymbol{q}}}$

$$\mathrm{Im}\,\chi(\hat{\boldsymbol{q}},\omega\to 0) = \pi\frac{\chi_0\omega}{\Gamma}\left(1 + \beta\frac{(\xi/a)^4}{(1+[\xi\hat{\boldsymbol{q}}]^2)^2}\right). \tag{4.10}$$

Eq. (4.10) displays explicitly the four unknown quantities to be adjusted to the NMR experiments: the uniform spin susceptibility of the CuO_2 planes, an electronic energy scale Γ for spin fluctuations,

an amplitude factor β as a measure for the enhancement of the susceptibility at $\boldsymbol{q} \sim \boldsymbol{Q}$ over its long wavelength value, and the AF correlation length ξ/a in units of the lattice constant. MMP have further chosen to postulate a specific temperature dependence for the correlation length,

$$\left(\frac{\xi(T)}{a}\right)^2 = \left(\frac{\xi(0)}{a}\right)^2 \frac{T_x}{T+T_x}, \tag{4.11}$$

giving a complete framework for a quantitative description of NMR experiments.

Using the Mila–Rice Hamiltonian [264] Eq. (3.9) for the coupling between the electronic spins and the nuclear moments the MMP analysis has been applied to NMR data obtained in $123\,O_7$ [272], $123\,O_{6.63}$ [289] and $La_{1.85}Sr_{0.15}CuO_4$ [273]. We collect some of the implications following from the quantitatively consistent description of the data in terms of the MMP ansatz:

(i) The characteristic energy scale $\hbar\omega_{SF}$ for spin fluctuations is very small, $\hbar\omega_{SF} < k_B T$, and the more antiferromagnetic the system is, the lower is the paramagnon energy. Over a substantial temperature range ω_{SF} varies linearly with temperature. The remarkably small ω_{SF} has been argued to define the energy region near the Fermi surface where the thermal lifetime τ_{qp} of the quasiparticles from the scattering by paramagnons varies like $\sim 1/T^2$ as in a conventional Fermi liquid, while above this energy the lifetime behaves as $\tau_{qp} \sim 1/T$.

(ii) A huge enhancement of $\chi_{AF}(\boldsymbol{Q})/\chi_0$ is required even in the stoichiometric $123\,O_7$ material and the enhancement is as large as 50 in $123\,O_{6.63}$ and larger than 100 in $La_{1.85}Sr_{0.15}CuO_4$ at temperatures closely above T_c [273] (see Fig. 26c).

(iii) The correlation length as modeled by Eq. (4.11) is found to be strongly temperature dependent from room temperature down to near T_c when it starts to saturate.

Generally, the AF spin correlations are found to be much stronger in $La_{1.85}Sr_{0.15}\,CuO_4$ than in the metallic 123 compounds. At T_c the MMP analysis stops and modifications are required below T_c. An application of the MMP equations to the superconducting state is found to be not consistent with available experimental data [31]. Also, we note that below room temperature, the MMP parametrisation form of the peak in $\chi(\boldsymbol{q}, \omega)$ near $\boldsymbol{q} \approx \boldsymbol{Q}$ breaks down in underdoped 123 since there is a spin gap rather than Lorentzian behavior [330]. In the normal state the MMP phenomenology is nevertheless quantitatively successful. The magnitude and the temperature dependence of the quantities introduced to parametrise the phenomenological MMP susceptibility have, however, also pointed to its limitations. In this respect, a comparison to the results obtained in neutron scattering experiments on the same compounds is instructive. Although, it has to be kept in mind that the MMP analysis addresses only the $\omega \to 0$ limit of the susceptibility and cannot straightforwardly be extended to finite frequencies, say ~ 10 meV, typically probed by the neutrons.

The most noticeable discrepancy between the MMP analysis of NMR data and the neutron scattering experiments concerns the correlation length. The magnitude of ξ obtained from the NMR phenomenology is larger than the lengths observed in magnetic neutron scattering [42,339,157]. Also the temperature dependence shown in Fig. 26a contradicts the neutron results which indicate the temperature independence of ξ below room temperature [120,206]. Furthermore, from the application to relaxation rate data in $La_{2-x}Sr_xCuO_4$ [326] it has been concluded that any appreciable departure from the commensurability of the AF fluctuations can be ruled out on the basis of the MMP description; yet, the neutrons have found the AF correlations to be clearly incommensurate [80,257] in moderately doped 214 compounds. Another difference between the MMP analysis and neutron scattering data concerns the frequency dependence of the susceptibility. Neutron data observe

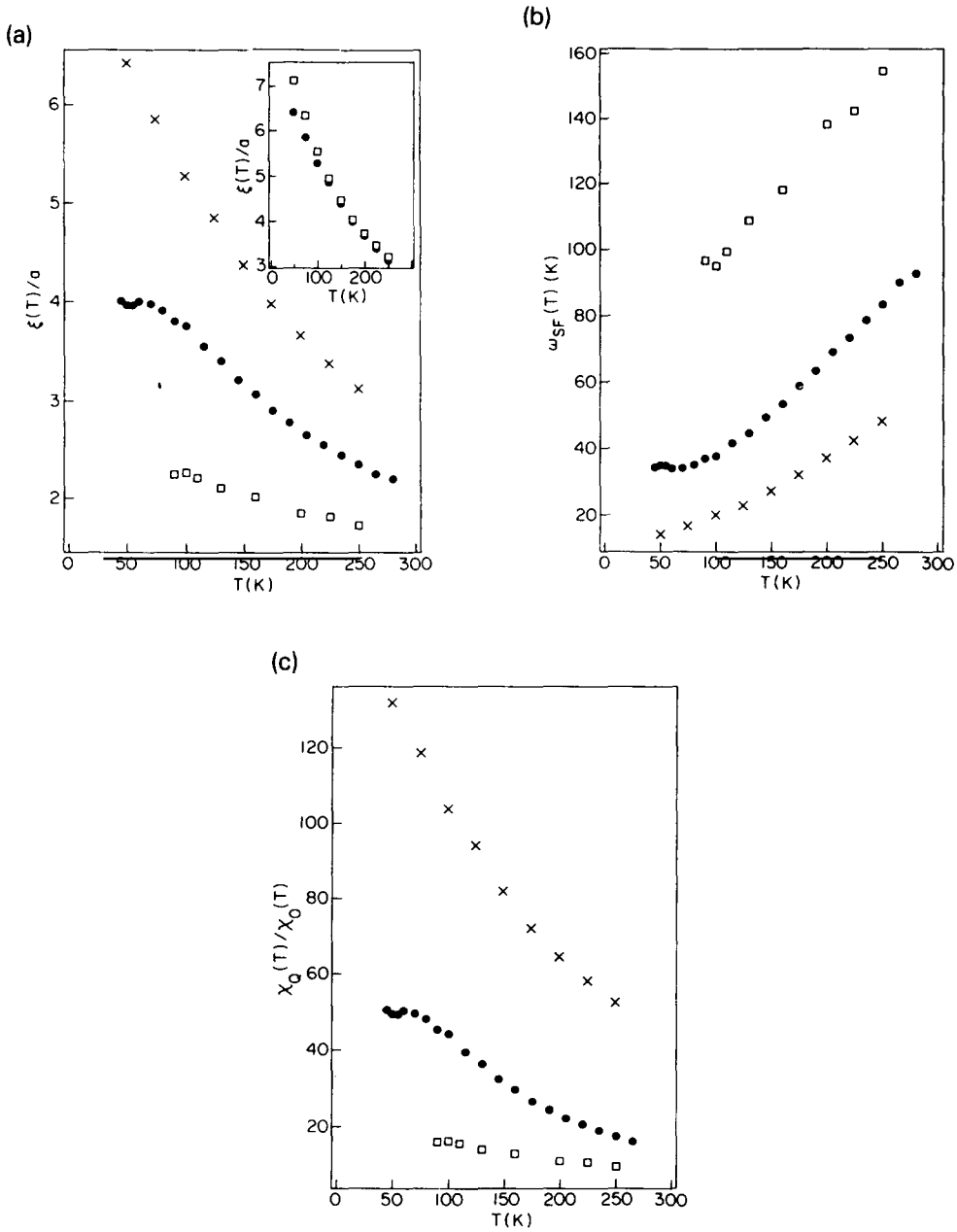

Fig. 26. Results from the MMP analysis of NMR data for (a) the temperature dependence of the correlation length ξ, (b) the spin fluctuation frequency ω_{SF}, and (c) the AF enhancement $\chi_{AF}(Q)/\chi_0$ in $123O_7$ (squares), $123O_{6.63}$ (•), and $La_{1.85}Sr_{0.15}CuO_4$ (×). (From Ref. [273].)

a peak in the frequency dependence of $\mathrm{Im}\,\chi$ which is at an order of magnitude larger energy than the results of the MMP analysis [432].

In order to examine if and how some of the discrepancies can be removed Millis and Monien (MM) have reanalysed the NMR phenomenology in more detail [271] also testing a Gaussian for the AF enhancement peak in $\mathrm{Im}\,\chi(\boldsymbol{q},\omega)$ which leads to considerably smaller values of the correlation length. But they have also concluded that data for relaxation rate ratios still favour a temperature dependent correlation length over a constant ξ instead of a temperature dependent AF enhancement factor β. This attempt has left the disagreement with neutron data unresolved. Still the possibility remains that neutron scattering experiments have not been performed at low enough frequency to detect the temperature changes in ξ required to fit the NMR measurements. Equally possible is that the MMP form of the spin susceptibility does not apply to the frequency range probed in neutron scattering experiments. A possible way out may be the AF–MFL model for the spin correlator Eq. (4.4) which combines the anomalous frequency dependence of the marginal-Fermi-liquid phenomenology with the spin-fluctuation enhancement near $\boldsymbol{Q} = (\pi,\pi)$ [476]. Also, for an analysis of NMR data in underdoped 123 the spin excitation gap needs to be built into a phenomenological ansatz for the spin susceptibility.

Given a model form for the spin susceptibility which accounts for the NMR data one may go one step further and use it as input for calculations of transport properties which rely on magnetic scattering. Moriya et al. have calculated the contribution to the electrical resistivity from quasiparticle – spin fluctuation scattering [286]. Their result – originally derived for an s–d exchange interaction [435] – has been provided in a very convenient form which involves the convolution of spectral densities for particle–hole and spin excitations ($\mathrm{Im}\,\chi$) [286]. Monien et al. [273] have combined the formula of Moriya et al. with the results of the NMR phenomenology. The knowledge of the dynamical spin susceptibility from experimental data then allows one to calculate the quasiparticle–paramagnon scattering contribution to the *dc* resistivity from

$$R(T) \sim \frac{1}{T}\sum_{\boldsymbol{q}}\int_{-\infty}^{\infty} d\omega\, \frac{\omega\, e^{\omega/T}}{\left(e^{\omega/T}-1\right)^2}\,\mathrm{Im}\,\chi_{\mathrm{AF}}(\boldsymbol{q},\omega). \tag{4.12}$$

This result for the resistivity is appropriate for a direct insertion of the low frequency MMP model for $\mathrm{Im}\,\chi_{\mathrm{AF}}$ of the NMR phenomenology. The result implies that as long as the characteristic energy ω_{SF} for AF paramagnons varies linearly with temperature the resistivity is linear in T, too [273]. Still, the MMP analysis has found significant deviations from linearity of $\omega_{\mathrm{SF}}(T)$ at low temperatures as shown in Fig. 26b. But since $k_B T_c > \hbar\omega_{\mathrm{SF}}$ at these temperatures the authors argue that the corresponding crossover to quadratic behavior of $R(T)$ will not be seen in the normal state resistivity data. So the precise form of $R(T)$ in this formulation depends on the variation of ω_{SF} or equivalently of the correlation length ξ with temperature. If the mean field form for $\xi(T)$ Eq. (4.11) holds the linear temperature dependence of the resistivity follows [273,286]. The caveat remains that the MMP temperature dependence of ξ is not in agreement with the neutron data.

An extension to calculate also the optical conductivity $\sigma(\omega)$ from the phenomenological MMP description has been performed by Arfi within the memory function formalism [21]. While the experimental data of Ref. [350] can be roughly fitted within this scheme below $\omega \sim 30$ meV, modifications to the phenomenological susceptibility are clearly required at higher frequencies. Separately, quasiparticle lifetime effects have been found to markedly influence the frequency dependence of the

conductivity and their inclusion considerably improves the comparison to the data [277].

A similar attempt to correlate the experimental result for $\chi(q,\omega)$ with the resistivity has been based on the magnetic neutron scattering data [43]. Using again the Moriya et al. formula Eq. (4.12) it is obvious that the ω/T scaling behavior found for the local susceptibility in lightly doped materials (see chapter 3.2.4) implies a linear resistivity. Though very suggestive, so far the ω/T scaling has been reported for low doped materials only and the connection between the dynamic susceptibility and the cleanest linear resistivities in optimally doped compounds [33] still needs to be established.

4.2. Microscopic models

Without doubt, phenomenologies serve as a valuable guide to correlate the various intricate normal state properties. The unresolved challenge remains to derive the essential features from a minimal microscopic model which also contains all the ingredients to capture the mechanism for the superconducting pairing instability itself. The rapid suppression of the quasiparticle lifetime below T_c [47] has supported the belief that the origin of superconductivity and the dominant scattering source of the charge carriers result from purely electronic interactions. In this chapter we describe the corresponding microscopic, correlated electron models that most of the subsequent theoretical calculations are based on.

4.2.1. Three-band-Hubbard model

Already early on it was suggested that a good starting point to describe the CuO_2 planes is a three-band model composed of $3d_{x^2-y^2}$ orbitals on the Cu sites and $2p_{x,y}$ orbitals on the O sites [116,438]. In an ionic picture for the parent compounds Cu^{2+} is in a $[Ar]3d^9$ configuration and the single d-shell hole is in a $d_{x^2-y^2}$ orbital which is highest in energy among the five d-orbitals due to crystal field effects [127]. Oxygen p_x and p_y orbitals directed along the x and y axis of the CuO_2 planes (see Fig. 27) are filled with two electrons each in the $2p^6$ configuration of the O^{2-} ions. Hence, the CuO_2 unit cell is considered to have three orbitals containing altogether five electrons in the undoped insulating compounds.

Starting from a picture of itinerant electrons or holes their kinetic energy may be represented by the hopping Hamiltonian (in hole notation)

$$H_0 = \sum_{i\sigma}(\epsilon_d - \mu)\, n^d_{i\sigma} + \sum_{j\sigma}(\epsilon_p - \mu) n^p_{j\sigma} + \sum_{\langle i,j\rangle\sigma} t^{pd}_{ij}(d^+_{i\sigma}p_{j\sigma} + \text{h.c.})$$
$$+ \sum_{\langle j,j'\rangle\sigma} t^{pp}_{jj'}(p^+_{j\sigma}p_{j'\sigma} + \text{h.c.}). \tag{4.13}$$

Here, the index i denotes the Cu sites and j the O sites. $d^+_{i\sigma}$ ($d_{i\sigma}$) and $p^+_{j\sigma}$ ($p_{j\sigma}$) are the creation (annihilation) operators for holes with spin σ in the copper $d_{x^2-y^2}$- and oxygen $p_{x,y}$-orbitals, respectively. ϵ_p and ϵ_d are the local energy levels in these orbitals, μ is the chemical potential, and $n^p_{j\sigma} = p^+_{j\sigma}p_{j\sigma}$ and $n^d_{i\sigma} = d^+_{i\sigma}d_{i\sigma}$ are the number operators for holes in the given orbital. The Cu–O and O–O hybridizations are determined by the hopping matrix elements

$$t^{pd}_{ij} = -t_{\text{Cu–O}}(-1)^{\alpha_{ij}}, \qquad t^{pp}_{jj'} = t_{\text{O–O}}(-1)^{\beta_{jj'}}, \tag{4.14}$$

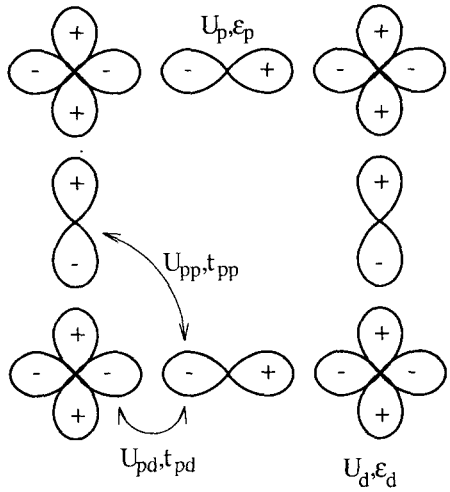

Fig. 27. A simplified view of the electronic structure of the CuO_2 planes showing the orbitals, hopping transitions and interactions for a Hubbard model Hamiltonian. The appropriate phase factors (+−) for the hopping are also indicated. (Figure reproduced from Ref. [167].)

where the phase factors with the exponents α_{ij} and $\beta_{jj'}$ take into account the d- and p-symmetry of the Cu and O orbitals, respectively, between which the holes hop [474] as indicated in Fig. 27. The hopping Hamiltonian Eq. (4.13) gives rise to three bands and with five electrons per unit cell two bands are filled and one band is left half-filled. A large hybridization t_{pd} splits these bands into a filled bonding band with mainly Cu character, a filled nonbonding band, and a half-filled antibonding band with mainly O character.

The simple band picture would imply that e.g. stoichiometric La_2CuO_4 has a half-filled antibonding band and therefore should be a metal as is found in LDA bandstructure calculations [307]. Instead, as we know, La_2CuO_4 is an antiferromagnetic insulator underlining that it is crucial to include strong local Coulomb repulsions – in particular on the localized d-orbitals. This is described by the additional Hubbard coupling terms in

$$H_1 = \sum_i U_d\, n^d_{i\uparrow} n^d_{i\downarrow} + \sum_{\langle i,j\rangle\sigma\sigma'} U_{pd}\, n^p_{j\sigma} n^d_{i\sigma'} + \sum_j U_p\, n^p_{j\uparrow} n^p_{j\downarrow}\,. \tag{4.15}$$

Besides the Coulomb repulsion on the Cu sites also the equivalent term on the O sites is included together with a nearest-neighbor Coulomb repulsion between holes on adjacent Cu and O orbitals. Typical numbers for the parameters of the three-band Hubbard Hamiltonian $H = H_0 + H_1$ as obtained from quantum chemical, constrained density functional methods [167,263] and multiband cluster calculations [121] are given in Tab. 3.

From Tab. 3 we find that the largest Coulomb interaction is the on-site interaction between d-holes on Cu-sites, U_d, and the largest hopping integral is t_{pd} (for the σ bond) between a Cu $3d_{x^2-y^2}$ and a neighboring O $2p_x$ or O $2p_y$ orbital. With respect to the excitation spectra exact diagonalization studies have shown [122] that for low hole doping concentrations the Coulomb repulsion within oxygen orbitals is of minor importance. U_{pd} is found to be small and does not appear to have an important influence on the physics of the CuO_2 planes [320] at least for the parameter set of Tab. 3.

Table 3
Typical parameter values (taken from Refs. [167,121,263]) for the three-band Hubbard Hamiltonian. Energies are given in eV.

	Hybertsen et al. [167]	Eskes–Sawatzky [121]	McMahan et al. [263]
$\epsilon_p - \epsilon_d$	3.6	2.75–3.75	3.5
t_{pd}	1.3	1.5	1.5
t_{pp}	0.65	0.65	0.6
U_d	10.5	8.8	9.4
U_p	4.0	6.0	4.7
U_{pd}	1.2	< 1.0	0.8

(For a different point of view see e.g. Refs. [438,341].)

The two key parameters of the three-band Hubbard model are U_d and the charge-transfer (CT) energy $\Delta = \epsilon_p - \epsilon_d$. For cuprate materials $U_d \gg \Delta > t_{pd}$ and the parent compounds fall into the class of the so-called CT insulators [470,471]. As a consequence of the large Hubbard U_d the antibonding band of the noninteracting CuO_2 tight binding band structure is split into a lower Hubbard band (LHB) pushed below the oxygen level ϵ_p and a high energy upper Hubbard band (UHB) which corresponds to states involving Cu $d_{x^2-y^2}$ orbitals doubly occupied with two holes [163].

Besides the Hubbard U_d splitting there is another important correlation effect which modifies also the bonding band of the tight-binding band structure. Photoemission spectroscopies have shown that holes doped into the antiferromagnetic insulators preferentially occupy the oxygen orbitals in the CuO_2 planes [295,127]. The created oxygen hole and the nearest local Cu spin interact by a strong Kondo exchange coupling. In perturbation theory with respect to the small parameter t_{pd}/Δ the corresponding exchange energy is given by (neglecting the effects of U_p and U_{pd})

$$J_{\mathrm{Cu-O}} = t_{pd}^2 \left(\frac{1}{\Delta} + \frac{1}{U_d - \Delta} \right) . \tag{4.16}$$

The oxygen hole may be viewed to be localised on the four oxygen ions surrounding a given Cu moment and the exchange interaction $J_{\mathrm{Cu-O}}$ splits the oxygen hole state entering the bonding band into triplet and singlet states. Since the latter state is found to be higher in energy and pushed above the nonbonding states [389], doped holes tend to form singlet states with Cu moments as has been proposed originally by Zhang and Rice [474]. As a consequence of this picture the bonding band splits into a triplet and a so-called *Zhang–Rice singlet* band leading to the qualitative band scheme shown in Fig. 28. In undoped La_2CuO_4 the filled Zhang–Rice singlet band is separated from the upper Hubbard band by an effective CT insulating gap of about $E_{\mathrm{CT}}^g \simeq 1.7$ eV [333].

Antiferromagnetism of the Cu moments arises by the superexchange mechanism via the intermediate oxygen orbitals. In terms of the three-band Hubbard model parameters the exchange coupling constant between the Cu moments is given by [123]

$$J_{\mathrm{Cu-Cu}} = \frac{4t_{pd}^4}{(\Delta + U_{pd})^2} \left(\frac{1}{U_d} + \frac{2}{2\Delta + U_p} \right) . \tag{4.17}$$

In the case of exactly one hole per Cu and for strong Hubbard U Coulomb repulsions the low energy Hamiltonian of the three-band model reduces to a Heisenberg spin Hamiltonian with exchange

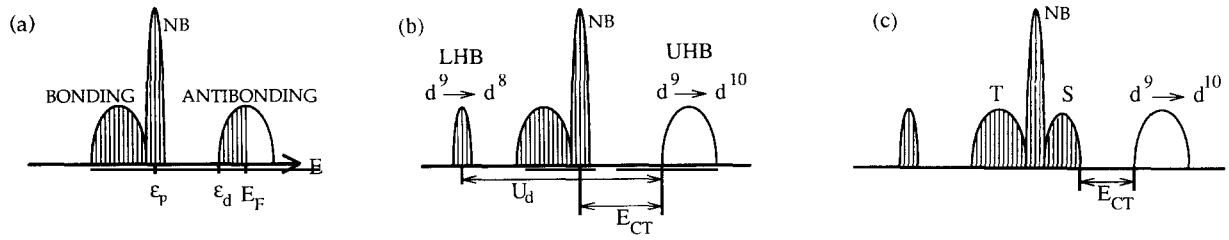

Fig. 28. Qualitative picture for the density of states in the three-band Hubbard model: (a) band structure results in the half-filled case, (b) charge-transfer insulator with and (c) without singlet–triplet splitting. NB, LHB and UHB denote the non-bonding, lower and upper Hubbard band, respectively. T and S indicate the triplet and the Zhang–Rice singlet bands, respectively. (Figure reproduced from Ref. [163].)

coupling J_{Cu-Cu}, since the charge excitations have a gap E^g_{CT}. By fitting the results of exact small cluster diagonalizations of $H_0 + H_1$ to a Heisenberg model, Hybertsen et al. [168] have extracted a value $J_{Cu-Cu} \sim 0.13$ eV agreeing favorably with the experimental value as obtained from neutron or two-magnon Raman scattering.

4.2.2. *One-band Hubbard and t–J model*

Due to its several parameters the three-band Hubbard model is a complicated starting point for the study of the electronic properties in the CuO_2 planes. Many theoretical studies have considered instead the simpler one-band Hubbard model to get insight into the low energy physics of the electronic states in the vicinity of the charge-transfer gap. In this sense the effective parameters of the one-band Hubbard model serve to model the charge-transfer gap in terms of a Mott–Hubbard picture with $U \sim E^g_{CT}$. The one-band Hubbard model contains only one orbital per site and is defined by

$$H = -t \sum_{\langle ij \rangle \sigma} (c^+_{i\sigma} c_{j\sigma} + \text{h.c.}) - t' \sum_{\langle ii' \rangle \sigma} (c^+_{i\sigma} c_{i'\sigma} + \text{h.c.}) + U \sum_i n_{i\uparrow} n_{i\downarrow} . \tag{4.18}$$

The hopping term t is restricted to the nearest-neighbor (nn) sites of a square lattice while an additional t' hopping process is also included between next-nearest-neighbor (nnn) sites. A parameter set with $t = 0.43$ eV, $t' = -0.06$ eV and $U = 4.1$ eV (i.e. $U/t \sim 9.5$ and $t'/t = -0.16$) has been found to reproduce approximately the low energy spectrum of the three-band model [169] with parameters as given in Tab. 3. The parameter set for the one-band model is appropriate for $La_{2-x}Sr_xCuO_4$ and approximately valid also for the electron doped 214 compounds. The tight-binding band parameters alone are able to reproduce the Fermi surface of this material (see Fig. 29a) through the dispersion relation $\epsilon_k = -2t(\cos k_x + \cos k_y) - 4t' \cos k_x \cos k_y$.

In the $123\,O_{6+x}$ system, band structure calculations indicate that the Fermi surface shape is rotated by 45° relative to that of the 214 material. This rotation has been claimed to be associated with the hybridisation between the apical O and the planar Cu [18]. Also the Cu–O chains do play a role in the more complex band structure of the 123 compounds [307,168]. Within the t–t' tight binding scheme this situation can be effectively modeled by choosing $t' \sim 0.45t$ [468] leading to the Fermi surfaces shown in Fig. 29b.

By means of the on-site Coulomb U the single band of the Hubbard model Eq. (4.18) is split into a lower (LHB) and an upper Hubbard band (UHB) where the LHB is meant to represent the

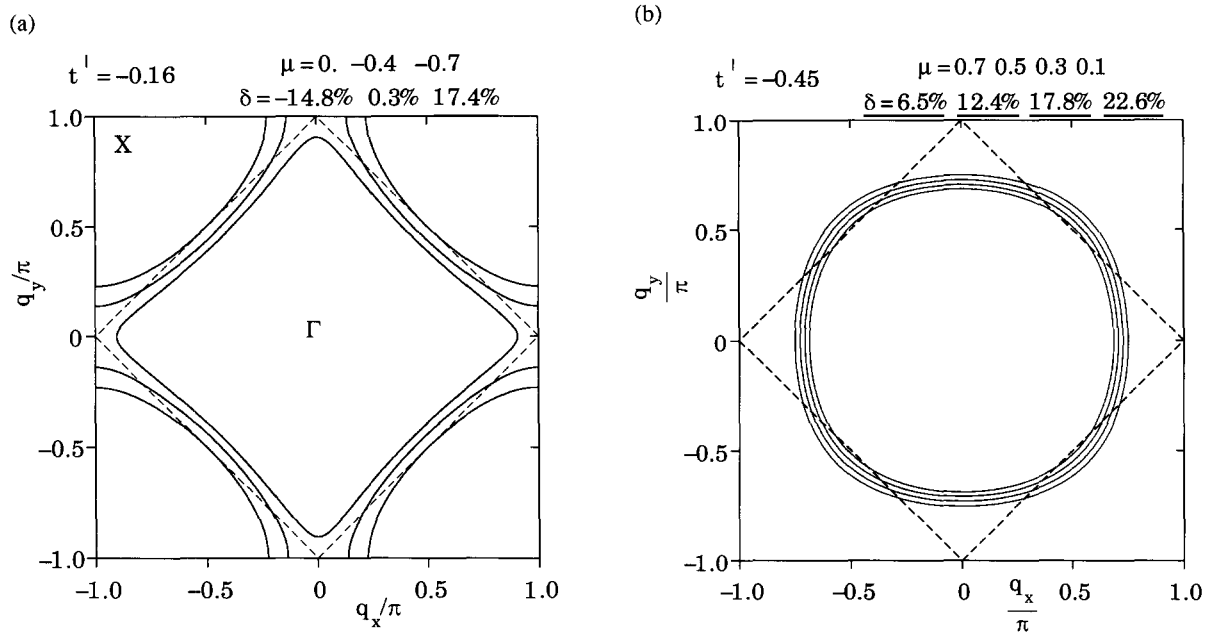

Fig. 29. Tight-binding Fermi surfaces for the square lattice with nearest- and next-nearest neighbor hopping t and t', respectively. (a) for $t'/t = -0.16$, appropriate for 214 materials. The Fermi surface is shown for three different fillings: $\delta = -14.8\%$ corresponds to electron doping, $\delta = 0.3\%$ is near half-filling, and $\delta = 17.4\%$ corresponds to hole doping. (b) Fermi surfaces for $t'/t = -0.45$ appropriate for 123 compounds. Here, the Fermi surfaces are shown for four different hole concentrations.

"Zhang–Rice singlet band" of the original three-band model. The validity, however, of the reduction of three-band model to the single-band Hubbard model is still controversial. The ongoing discussion [117,475] on this issue has focused on the question whether a strong coupling version of the Hubbard Hamiltonian, i.e. the t–J model, is appropriate to describe correctly the low-energy physics of the original three-band model. The t–J model is in the strong coupling limit $U/t \gg 1$ obtained by a canonical transformation which eliminates configurations with doubly occupied sites [154,160]. To leading t^2/U-order the single-band Hubbard model reduces by this transformation to

$$H_{tt'J} = -t \sum_{\langle ij\rangle\sigma} [(1 - n_{i-\sigma}) c^+_{i\sigma} c_{j\sigma} (1 - n_{j-\sigma}) + \text{h.c.}] + H_{t'} + J \sum_{\langle ij\rangle} (\boldsymbol{S}_i \cdot \boldsymbol{S}_j - \tfrac{1}{4} n_i n_j), \tag{4.19}$$

with an exchange coupling energy $J = 4t^2/U$. $\boldsymbol{S}_i = c^+_{i\alpha} \underline{\sigma}_{\alpha\beta} c_{i\beta}$ is the spin operator at site i for $S = \frac{1}{2}$, where $\underline{\sigma}_{\alpha\beta}$ denotes the components of the Pauli spin matrices. The hopping term explicitly excludes the double occupancy of sites due to the projection operators $(1 - n_{i-\sigma})$ and only states with a single up- or down-spin electron or a hole are allowed at each lattice site. In addition to the exchange interaction between neighboring spins, there is another hopping term $H_{t'}$ of the same order in t^2/U, i.e. $t' = 2t^2/U$. $H_{t'}$ involves three distinct sites $\langle ijk\rangle$ where i and k are nearest-neighbor sites of site j. Explicitly, $H_{t'}$ is given by

$$H_{t'} = -t' \sum_{\langle ijk\rangle\sigma} (\hat{c}^+_{i\sigma} \hat{c}_{k\sigma} n_{j-\sigma} - \hat{c}^+_{i\sigma} \hat{c}_{k-\sigma} \hat{c}^+_{j-\sigma} \hat{c}_{j\sigma}). \tag{4.20}$$

Here, we have used $\hat{c}_{i\sigma} = c_{i\sigma}(1 - n_{i-\sigma})$ which already incorporates the projection operator to exclude double occupancy. The $H_{t'}$ hopping is commonly dropped in t–J model calculations, and its importance has so far not been explored in detail.

4.2.3. Spin-Fermion model

The simplified t–J model or the one-band Hubbard model serve as minimal models to study the correlated motion of holes in an environment with antiferromagnetic spin fluctuations. Still, their applicability to the real cuprate materials requires further discussion. A justification may be given a posteriori from comparison of model-specific results to the experimental data. In the subsequent chapters we will present evidence that some of the experimentally established electronic properties are indeed at least qualitatively captured by the simple one-band models.

Yet, some groups have argued that it may be necessary to start from the more realistic three-band Hubbard model itself. Considering the strong coupling limit in this case [116,438] leads to the so called spin–fermion model [316,471,290,297] defined by the Hamiltonian

$$H_{\mathrm{SF}} = \sum_{\langle jj'\rangle\sigma} t_{jj'}(c^{+}_{j\sigma}c_{j'\sigma} + \mathrm{h.c.}) + \sum_{\langle jj'i\rangle\alpha\beta} J_K^{ijj'}\, \boldsymbol{S}_i \cdot c^{+}_{j\alpha}\underline{\sigma}_{\alpha\beta}c_{j'\beta} + J_{\mathrm{Cu-Cu}} \sum_{\langle ii'\rangle} \boldsymbol{S}_i \cdot \boldsymbol{S}_{i'} \,. \tag{4.21}$$

The site indices i and j denote the Cu and O sites, respectively, in the CuO_2 plane. The hopping term in Eq. (4.21) contains both, a direct O–O hopping as well as an effective hopping between O sites mediated by a nearest-neighbor Cu site. The second term in Eq. (4.21) is a nonlocal Kondo like interaction between the spin on the Cu site and the holes on the surrounding O sites. Not only pure exchange parts are present in the spin-fermion model, but also the possibility of a spin-exchange process with hopping appears. Orbital phase factors are included in $t_{jj'}$ as well as in $J_K^{ijj'}$. In the following we will, however, not consider this model further and focus instead on the Hubbard and the t–J model. For recent results on the spin-fermion model we refer the reader e.g. to Refs. [139,291] and the references therein.

5. Theoretical results for the magnetically ordered and the metallic state

5.1. Magnetic order in the insulators

In this chapter we briefly summarize some results for electronic densities with exactly one hole per CuO_2 unit where long range AF order is known to occur. This is the case for which the most firmly established results are available. We will consider both the weak coupling itinerant limit where antiferromagnetism arises from the formation of a spin density wave (SDW) and the strong coupling limit with localised spins as described by the Heisenberg model. Both limits have been argued to serve as a valid starting point for model studies with a small concentration of doped carriers. The arguments are derived from the effective parameters for the cuprates as described by the three-band Hubbard model [169] and the truncated one-band models which may place these models rather into the intermediate coupling regime than into the truely strong coupling limit.

5.1.1. Heisenberg antiferromagnet

Considering e.g. the strong coupling t–J Hamiltonian, at half-filling, i.e. for precisely one electron per site, this model contains only the Heisenberg exchange coupling

$$H = -J \sum_{\langle ij \rangle} \boldsymbol{S}_i \cdot \boldsymbol{S}_j \tag{5.1}$$

for localised spins on a square lattice – apart from a constant energy shift. The charge excitations have a gap (in fact, an infinitely large gap in this model) and the low energy physics is entirely determined by the spin degrees of freedom. Extensive analytical and numerical studies have given evidence that the ground state of the square lattice AF Heisenberg model has long range order at zero temperature (for recent reviews see e.g. Refs. [74,249,29] and references therein) although a rigorous proof is still lacking. More exotic spin liquid scenarios like the resonating valence bond (RVB) or the flux phase state have been suggested but they have not been found to be realised in this model [96].

The magnetization $\langle S_z \rangle$ of a given sublattice serves as a staggered order parameter for the ground state. The approximate ground state from linear spin wave (LSW) theory is the quantum Néel state (see e.g. Ref. [255])

$$|qN\rangle = \exp\left(\sum_q \frac{v_q}{u_q} a_q^+ a_{-q}^+\right)|N\rangle \tag{5.2}$$

with the usual expressions for the coherence factors

$$u_q = \left(\frac{1+\nu_q}{2\nu_q}\right)^{1/2}, \qquad v_q = -\mathrm{sgn}\ \gamma_q \left(\frac{1-\nu_q}{2\nu_q}\right)^{1/2}. \tag{5.3}$$

The spin-wave operators a_q^+ in Eq. (5.2) act on the classical Néel state $|N\rangle$, and the magnon dispersion in LSW theory is given by $\omega_q = 2J\nu_q = 2J(1-\gamma_q)^{1/2}$ with $\gamma_q = \frac{1}{2}(\cos k_x + \cos k_y)$. As we outline below LSW theory has proven to provide an even quantitatively reasonable approximation to the ground state properties of the Heisenberg model.

Most accurate estimates for $\langle S_z \rangle$ have been obtained from series expansions [372] ($\langle S_z \rangle = 0.3025$) or asymptotic $1/S$ expansions [73,173] up to $O(1/(2S)^2)$ where S is the length of the spin. Quantitative calculations of static $T = 0$ properties have focused on the renormalization factors Z_c, Z_χ and Z_ρ for the spin wave velocity c, the uniform magnetic susceptibility $\chi_\perp$ in the direction perpendicular to the staggered magnetization and the spin-stiffness constant ρ_s, respectively. ρ_s is determined by the response to a twist of the staggered order parameter [128]. The renormalization factors are defined through the relations (in units where $\hbar = 1$ and the lattice constant has been set to unity)

$$c = 2S\sqrt{2}\, JZ_c, \qquad \chi_\perp = (1/8J)Z_\chi, \qquad \rho_s = JS^2 Z_\rho. \tag{5.4}$$

These "Z factors" contain the effects of quantum fluctuations present in the ground state which are expected to be large due to the smallness of the spin $S = 1/2$ and the low dimension $D = 2$. They are in fact not independent quantities due to the hydrodynamic Halperin–Hohenberg relation [150] $\rho_s = c^2 \chi_\perp$.

Table 4
Renormalization factors for the spin wave velocity Z_c, the perpendicular susceptibility Z_χ and the spin stiffness constant Z_ρ as well as the sublattice magnetization $\langle S_z \rangle$ for the square lattice Heisenberg spin-$\frac{1}{2}$ antiferromagnet.

Theory	Z_c	Z_χ	Z_ρ	$\langle S_z \rangle$
$1/S$ expansion (Holstein–Primakoff) [173]	1.1794	0.514	0.724	0.3069
$1/S$ expansion (Dyson–Maleev)	1.1765 [72]			0.30069 [73]
Series expansion [372]	1.176	0.52	0.72	0.3025
Schwinger bosons (mean field theory) [25]	1.159	0.53		
Quantum Monte Carlo	1.14 [433]		0.796 [247]	0.31 [433]

Some numbers for the renormalization factors as obtained by different techniques are collected in Tab. 4 giving an example for the achieved accuracy of quantitative results for the Heisenberg model. Generally it is found that already linear spin-wave theory (LSW), i.e. the leading order of the asymptotic $1/S$ expansion, gives quantitatively satisfying results. The result for the spin-wave velocity in Eq. (5.4) and with $Z_c \simeq 1.18$ has e.g. been used in the analysis of the neutron scattering data on the spin-wave excitations [158] to extract the bare value for the exchange coupling J.

A separate important quantity, also for the comparison to experimental data, is the temperature dependence of the dynamic structure factor and in particular of the spin–spin correlation length ξ. The decay at finite T of the spin–spin correlation function $\langle \boldsymbol{S}_0 \cdot \boldsymbol{S}_r \rangle$ at long distances is represented in the general form

$$\langle \boldsymbol{S}_0 \cdot \boldsymbol{S}_r \rangle \propto r^{-\lambda} \exp(-r/\xi) . \tag{5.5}$$

The best fit to Monte Carlo data has been obtained with the power law exponent [106] $\lambda \approx 0.4$ which is close to the result $\lambda = 0.5$ obtained for the classical nonlinear σ-model [82]. The correlation length ξ has an exponential temperature dependence [25,81] at low T. We quote the result of Ref. [81] for the asymptotic low temperature behavior $T \leq \pi\rho_s$ obtained on the basis of a dynamical scaling ansatz (we set $k_B = 1$)

$$\xi = 0.27 \frac{\hbar c}{2\pi\rho_s} \frac{\exp(2\pi\rho_s/T)}{1 + T/2\pi\rho_s} . \tag{5.6}$$

In the low temperature regime $T \leq \pi\rho_s$ the correlation length is determined predominantly by classical thermal fluctuations while quantum fluctuations only renormalize the values of c and ρ_s. The magnetic neutron scattering data [462] on La_2CuO_4 have been fitted quite well by Eq. (5.6).

The correlation length ξ also enters the expression for the NMR relaxation rate which has been calculated for the Cu site with a field applied along the c-direction. Explicitly, it is given by [75]

$$\frac{1}{^{63}T_1} = \frac{A^2}{\hbar} \frac{\sqrt{\pi}}{J} \frac{\xi}{a} \frac{0.2}{Z_c} \left(\frac{T}{2\pi\rho_s} \right)^{3/2} \left(\frac{1}{1 + T/2\pi\rho_s} \right)^2 \tag{5.7}$$

where A is the hyperfine coupling and a is the lattice constant. This form for $1/^{63}T_1$ has been found to properly describe the observed temperature dependence [180] in undoped La_2CuO_4 giving confidence that indeed the AF insulating cuprates are well described in terms of the $2D$ Heisenberg model (or more precisely its description in terms of the nonlinear σ-model for which the results Eqs. (5.6), (5.7) have been derived). Still, in the comparisons to the experimental data one has to keep in mind

that the model considered is in $D = 2$ for which $T_N = 0$. The successful comparison to the data for the cuprate insulators above their Néel temperature of a few hundred degrees K therefore implies that their spin correlations are dominantly two-dimensional.

Long range AF spin order has also been established in the half-filled one-band Hubbard model for weak and intermediate coupling values of U/t [161,456,381] as well as in the three-band model [347,108,348] for a density of one hole per CuO_2 unit. The long range spin order in the one-band model has been convincingly demonstrated by evaluating the spin–spin correlation function

$$C(\boldsymbol{r}) \equiv C(\boldsymbol{r}_i - \boldsymbol{r}_j) = (-1)^{i_x+i_y+j_x+j_y} \langle S_i^z S_j^z \rangle \tag{5.8}$$

on finite size systems with quantum Monte Carlo (QMC) [283] as well as Lanczos diagonalization techniques [125,99]. In Eq. (5.8) a notation has been used where $\boldsymbol{r}_i = (i_x, i_y)$ indicates the coordinates of a site on the square lattice. $C(\boldsymbol{r})$ clearly extrapolates to a finite value near 0.13 for the largest distances on increasingly larger clusters with up to 8×8 lattice sites [283,103]. These results have supported the belief that the ground state of the one-band Hubbard model at half-filling is magnetically ordered for all finite values of U/t.

5.1.2. Weak coupling spin density wave analysis

The magnetic ordering at small or intermediate values of the Hubbard U is more appropriately described in terms of a spin density wave (SDW) with itinerant electrons rather than localised spins. This situation is conceptually simple described in the Hartree–Fock scheme originally introduced by Schrieffer, Wen and Zhang [398] for the half-filled one-band Hubbard model. We will describe this scheme in detail below because in subsequent chapters we will use it again several times to discuss results in the weak coupling limit.

The mean-field treatment of the SDW state starts by introducing the spin density operator

$$\boldsymbol{S}_q = \frac{1}{2N} \sum_{k,\sigma} c^+_{k+q,\alpha} \underline{\sigma}_{\alpha\beta} c_{k,\beta}. \tag{5.9}$$

Antiferromagnetism or equivalently the formation of the SDW amounts to a finite expectation value of the staggered magnetization

$$S_z(\boldsymbol{Q}) = \frac{1}{2N} \sum_{k,\sigma} \sigma c^+_{k+Q,\sigma} c_{k,\sigma} \tag{5.10}$$

which we assume to be polarised along the z-direction. Here, $\boldsymbol{Q} = (\pi, \pi)$ and $\sigma = \pm 1$ for up and down spins, respectively. $m = \langle S_z(\boldsymbol{Q}) \rangle$ serves as the magnetic order parameter which accounts for the two-sublattice spin structure. Spin-up electrons reside mainly on the, say, even sites while down-spin electrons reside primarily on the odd sites of the square lattice. Introducing $S_z(\boldsymbol{Q})$ into the interaction part of the Hubbard Hamiltonian allows a straightforward mean-field decoupling and the Hartree–Fock factorised form of the Hamiltonian follows as

$$H_{\mathrm{MF}} = \sum_{k,\sigma} \epsilon_k c^+_{k,\sigma} c_{k,\sigma} - Um \sum_{k,\sigma} \sigma c^+_{k,\sigma} c_{k+Q,\sigma}\,. \tag{5.11}$$

Here, $\epsilon_k = -2t(\cos k_x + \cos k_y)$ is the tight-binding dispersion for nearest-neighbor hopping on the square lattice. The two-sublattice structure of the SDW state doubles the unit cell and the extended

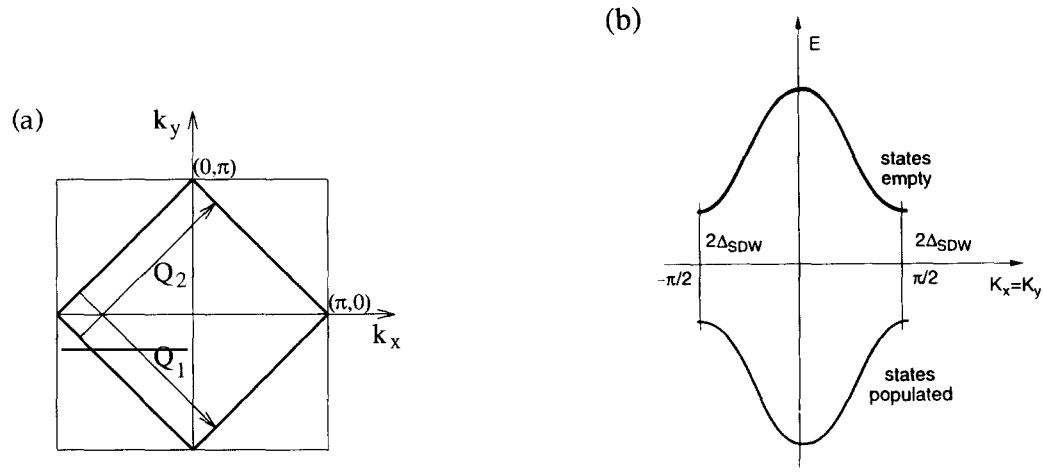

Fig. 30. (a) The first Brillouin zone and the reduced magnetic Brillouin zone (inner square) of the square lattice with the two nesting vectors $\boldsymbol{Q}_1 = (\pi, -\pi)$ and $\boldsymbol{Q}_2 = (\pi, \pi)$. (b) Quasiparticle spectrum in the Hartree–Fock description of the SDW state in the half-filled Hubbard model. The lower valence band is filled and the upper conduction band is empty.

first Brillouin zone is reduced to the magnetic Brillouin zone (MBZ) given by the momenta for which $\epsilon_k < 0$ as shown in Fig. 30a.

Very reminiscent of the weak-coupling BCS theory, the quadratic Hamiltonian Eq. (5.11) is diagonalized by means of a transformation to valence and conduction band quasiparticle operators [398]

$$\gamma^c_{k,\sigma} = u_k c_{k,\sigma} + v_k \sigma c_{k+Q,\sigma}, \tag{5.12a}$$

$$\gamma^v_{k,\sigma} = v_k c_{k,\sigma} - u_k \sigma c_{k+Q,\sigma}. \tag{5.12b}$$

The momenta of $\gamma^c_{k,\sigma}$ and $\gamma^v_{k,\sigma}$ are restricted to the MBZ to avoid double counting. The coherence factors u_k and v_k are given by

$$u_k = \sqrt{\tfrac{1}{2}(1 + \epsilon_k/E_k)}, \qquad v_k = \sqrt{\tfrac{1}{2}(1 - \epsilon_k/E_k)}. \tag{5.13}$$

The diagonalised mean-field Hamiltonian Eq. (5.11) following from this linear transformation then reads

$$H_{MF} = \sum_{k,\sigma}{}' E_k(\gamma^{c+}_{k,\sigma}\gamma^c_{k,\sigma} - \gamma^{v+}_{k,\sigma}\gamma^v_{k,\sigma}), \quad E_k = \sqrt{\epsilon_k^2 + (mU)^2}, \tag{5.14}$$

where the single particle energies of the new valence (γ^v) and conduction (γ^c) band quasiparticles are determined by E_k giving rise to the split band structure schematically shown in Fig. 30b. The primed sum indicates the restriction of the momenta to the MBZ. The self-consistency condition for the magnetization requires that $\langle S_z(\boldsymbol{Q})\rangle = \frac{1}{N}\sum_k{}' u_k v_k$ which leads to the "gap equation"

$$1/U = (1/N)\sum_k{}' 1/E_k. \tag{5.15}$$

$\Delta_{SDW} = |mU|$ is the energy gap which splits the lower filled valence band and the upper conduction band which is empty for a filling of one electron per site. In this weak coupling scheme the gap

arises from the umklapp scattering in the static periodic potential provided by the two-sublattice spin structure. For $U \ll t$ the gap is exponentially small, $\Delta_{SDW} \sim t\exp(-2\pi\sqrt{t/U})$, while for $t \ll U$ the solution of the gap equation approaches the Mott–Hubbard value $2\Delta_{SDW} = U$.

The two limits are therefore smoothly connected within the Hartree–Fock SDW scheme. This allows a continuous crossover from the itinerant to the localised regime where it is the large on-site Coulomb repulsion that suppresses the charge fluctuations and leads to the Mott insulating state. There is, however, an important difference between the weak and the strong coupling regime. For weak U, well above the Néel temperature (assuming for the moment the three-dimensional situation) the gap will essentially vanish with the disappearance of the magnetic SDW order. The gap will, however, persist for large U in the spin disordered regime since the charge fluctuations remain suppressed due to the large Coulomb repulsion.

In the two-sublattice structure of the SDW state, the single particle c electron propagator $G_\sigma(\boldsymbol{k}, \boldsymbol{k}', \omega)$ as well as the response functions depend on two momenta where the umklapp scattering allows $\boldsymbol{k}$ and $\boldsymbol{k}'$ either to be equal or to differ by $\boldsymbol{Q}$. This is taken into account by using a 2×2 matrix formulation with respect to the momentum arguments. In matrix form the Hartree–Fock c-electron propagator is written as (using $\epsilon_{k+Q} = -\epsilon_k$)

$$\boldsymbol{G}^{0c}_\sigma(\boldsymbol{k}, \omega) \equiv \begin{bmatrix} G^{0c}_\sigma(\boldsymbol{k}, \boldsymbol{k}, \omega) & G^{0c}_\sigma(\boldsymbol{k}, \boldsymbol{k}+\boldsymbol{Q}, \omega) \\ G^{0c}_\sigma(\boldsymbol{k}+\boldsymbol{Q}, \boldsymbol{k}, \omega) & G^{0c}_\sigma(\boldsymbol{k}+\boldsymbol{Q}, \boldsymbol{k}+\boldsymbol{Q}, \omega) \end{bmatrix}$$

$$= \frac{1}{\omega^2 - E_k^2 + i\delta} \begin{bmatrix} \omega + \epsilon_k & \sigma\Delta_{SDW} \\ \sigma\Delta_{SDW} & \omega - \epsilon_k \end{bmatrix}. \tag{5.16}$$

Before we proceed we take a closer look at the origin for the appearance of the SDW in the itinerant weak coupling limit. For this purpose we consider the spin-density correlation function

$$\chi^{ij}(\boldsymbol{q}, t) = (i/2N)\langle TS^i_{\boldsymbol{q}}(t) S^j_{-\boldsymbol{q}}(0)\rangle \tag{5.17}$$

assuming the absence of any broken symmetry. Summing the infinite series of bubble diagrams in the random phase approximation (RPA) leads to the well known result

$$\chi^{ij}_{RPA}(\boldsymbol{q}, \omega) = \frac{\chi_0(\boldsymbol{q}, \omega)}{1 - U\chi_0(\boldsymbol{q}, \omega)}\delta_{ij} \tag{5.18}$$

where $\chi_0(\boldsymbol{q}, \omega)$ is the zeroth order $U = 0$ particle–hole bubble as given by

$$\chi_0(\boldsymbol{q}, \omega) = \frac{1}{N}\sum_{\boldsymbol{k}} \left(\frac{f_{k+q}(1 - f_k)}{\omega + \epsilon_k - \epsilon_{k+q} + i\delta} - \frac{f_k(1 - f_{k+q})}{\omega + \epsilon_k - \epsilon_{k+q} - i\delta} \right). \tag{5.19}$$

f_k is the Fermi function for the electron occupation number. At half-filling the Fermi surface of the tight binding band is a perfect square (see Fig. 30a) which has the nesting property, i.e. the wave vectors $\boldsymbol{Q} = (\pm\pi, \pm\pi)$ span opposite, parallel sides of the Fermi surface. As a consequence $\chi_{RPA}(\boldsymbol{Q}, \omega = 0)$ at half-filling is logarithmically singular at $T = 0$ in 2D for arbitrarily weak U, signaling an instability of the normal Fermi surface. Thus, it is the nesting instability for weak U that leads to a ground state with commensurate (i.e. with wavevector $\boldsymbol{Q}$) static SDW order [398].

Taking the broken symmetry state for granted we recalculate the spin density correlation functions. We define $|SDW\rangle$ as the vacuum for the γ-quasiparticles, i.e. $\gamma^{v+}_{k,\sigma}|SDW\rangle = \gamma^{c}_{k,\sigma}|SDW\rangle = 0$ and evaluate

$$\bar{\chi}^{ij}(\boldsymbol{q},\boldsymbol{q}',t) = (i/2N)\langle SDW|TS^{i}_{\boldsymbol{q}}(t)S^{j}_{-\boldsymbol{q}'}(0)|SDW\rangle\,. \tag{5.20}$$

Due to the broken spin rotation invariance we have to distinguish between the longitudinal and transverse susceptibilities with respect to the direction of the staggered magnetization. In the matrix notation both susceptibilities – in the absence of the residual interactions between the γ-quasiparticles – are obtained as [398,374,442]

$$\bar{\chi}^{zz}_{0}(\boldsymbol{q},\omega) = \frac{1}{N}{\sum_{k}}'\left(\frac{1}{\omega + E_{k} + E_{k+q} - i\delta} - \frac{1}{\omega - E_{k} - E_{k+q} + i\delta}\right)\begin{bmatrix} p^{2}_{k,k+q} & 0 \\ 0 & n^{2}_{k,k+q}\end{bmatrix}, \tag{5.21a}$$

$$\bar{\chi}^{-\sigma\sigma}_{0}(\boldsymbol{q},\omega) = \frac{1}{N}{\sum_{k}}'\left(\frac{1}{\omega + E_{k} + E_{k+q} - i\delta} \mp \frac{1}{\omega - E_{k} - E_{k+q} + i\delta}\right) \times \begin{bmatrix} m^{2}_{k,k+q} & -\sigma l_{k,k+q}m_{k,k+q} \\ -\sigma l_{k,k+q}m_{k,k+q} & l^{2}_{k,k+q}\end{bmatrix}, \tag{5.21b}$$

where the upper (lower) sign in the transverse susceptibility Eq. (5.21b) refers to the diagonal (off-diagonal) matrix elements. The superscripts in the transverse susceptibility distinguish between χ^{+-}_{0} and χ^{-+}_{0} which differ in the sign of the off-diagonal matrix elements. In Eqs. (5.21a), (5.21b) we have introduced the combinations of coherence factors

$$\begin{aligned} l_{k,k'} &= u_k u_{k'} + v_k v_{k'} & p_{k,k'} &= u_k v_{k'} - v_k u_{k'} \\ m_{k,k'} &= u_k v_{k'} + v_k u_{k'} & n_{k,k'} &= u_k u_{k'} - v_k v_{k'}\,. \end{aligned} \tag{5.22}$$

Gaussian fluctuations around the SDW state resulting from the residual interaction between the γ-quasiparticles are included by summing the RPA diagram series as shown in Fig. 31 for the transverse and longitudinal susceptibility, respectively, leading to

$$\bar{\chi}^{-\sigma\sigma}_{\mathrm{RPA}}(\boldsymbol{q},\boldsymbol{q}',\omega) = \sum_{\tilde{q}} \bar{\chi}^{-\sigma\sigma}_{0}(\boldsymbol{q},\tilde{\boldsymbol{q}},\omega)\left[1 - U\bar{\chi}^{-\sigma\sigma}_{0}(\tilde{\boldsymbol{q}},\boldsymbol{q}',\omega)\right]^{-1}, \tag{5.23a}$$

$$\chi^{zz}_{\mathrm{RPA}}(\boldsymbol{q},\boldsymbol{q}',\omega) = \delta_{q,q'}\frac{\chi^{zz}_{0}(\boldsymbol{q},\boldsymbol{q},\omega)}{1 - U\chi^{zz}_{0}(\boldsymbol{q},\boldsymbol{q},\omega)}. \tag{5.23b}$$

$\left[1 - \bar{\chi}^{-\sigma\sigma}_{0}(\boldsymbol{q},\boldsymbol{q}',\omega)\right]^{-1}$ is a 2×2 matrix inverse with respect to the momentum indices. The broken spin rotation invariance in the SDW state implies the presence of gapless Goldstone spin wave modes which are determined by the poles in the transverse susceptibility. Explicitly, the spin wave dispersion is obtained from

$$\det\left[1 - U\bar{\chi}^{-\sigma\sigma}_{0}(\boldsymbol{q},\boldsymbol{q}',\omega)\right] = 0. \tag{5.24}$$

The condition that the spin wave spectrum is gapless as required by the Goldstone theorem is found to be identical to the gap equation showing the internal consistency of the RPA calculation [398].

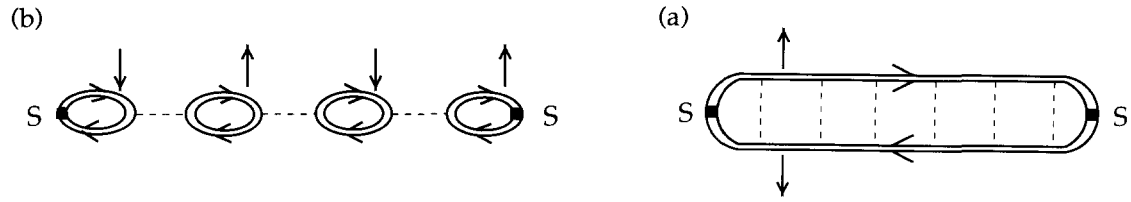

Fig. 31. RPA diagrams for the calculation of the (a) transverse (ladder diagrams) and (b) longitudinal (bubble diagrams) spin susceptibility. The double fermion lines represent Hartree–Fock propagators in the presence of the static SDW order and the dashed lines the Hubbard interaction U.

It is instructive to consider formally the large U limit, $U \gg \omega, t$. This may appear unjustified since the RPA is considered to be valid in the weak coupling regime only. However, as we noted already for the gap equation, also the RPA transverse susceptibility connects smoothly to known results for the large U limit which justifies a posteriori the extension to large U. For $U \gg \omega, t$, $\bar{\chi}^{+-}_{\mathrm{RPA}}$ takes the very transparent form

$$\bar{\chi}^{+-}_{\mathrm{RPA}}(q,\omega) \overset{U/t\gg 1}{\longrightarrow} \frac{1}{\omega^2-\omega_q^2+i\delta}\begin{bmatrix} -2J(1+\epsilon_q/4t) & \omega \\ \omega & -2J(1-\epsilon_q/4t)\end{bmatrix}, \tag{5.25}$$

displaying explicitly propagating spin wave modes. The spin wave dispersion is given by $\omega_q = 2J[1-(\epsilon_q/4t)^2]^{1/2}$. This is a remarkable result, since it is identical to the result from linear spin wave (LSW) theory for the Heisenberg antiferromagnet with an exchange coupling $J = 4t^2/U$ as it also appears in the t–J limit of the Hubbard model. Thus, there is a smooth crossover for the spin excitations from the weak coupling SDW to the strong coupling Heisenberg limit. This is shown in Fig. 32 for the spin wave dispersion and the velocity c obtained from the small q limit where $\omega_q \sim cq$. For weak U we have [83] $c = (2/\sqrt{\pi})(U/t)^{1/4}t$ and for large U we recover the LSW result $c = \sqrt{2}\,J$.

An interesting result is also obtained when the same analysis is performed with an additional t' hopping between next-nearest neighbor sites. For a finite t' it is known that antiferromagnetism in the half-filled Hubbard model sets in above a finite critical value of U [230]. In this case we obtain again the spin wave dispersion from the poles in $\bar{\chi}^{+-}_{\mathrm{RPA}}$. In the large U limit the result is [198]

$$\omega_q = 2J\left[\left(1-\frac{t'^2}{t^2}\left(1-\cos q_x\cos q_y\right)\right)^2-\left(\frac{\epsilon_q}{4t}\right)^2\right]^{1/2}. \tag{5.26}$$

Introducing the exchange coupling $J' = 4t'^2/U$ the small q expansion of Eq. (5.26) reads

$$\omega_q \simeq \sqrt{2}Jq\sqrt{1-2J'/J}. \tag{5.27}$$

The spin wave velocity vanishes for $J' = J/2$ and no propagating Goldstone spin wave exists for correspondingly larger values of t' indicating the loss of AF order. We therefore recover the result for the classical frustrated Heisenberg J–J' model on a square lattice

$$H_{JJ'} = J\sum_{nn} S_i\cdot S_j + J'\sum_{nnn} S_i\cdot S_j, \tag{5.28}$$

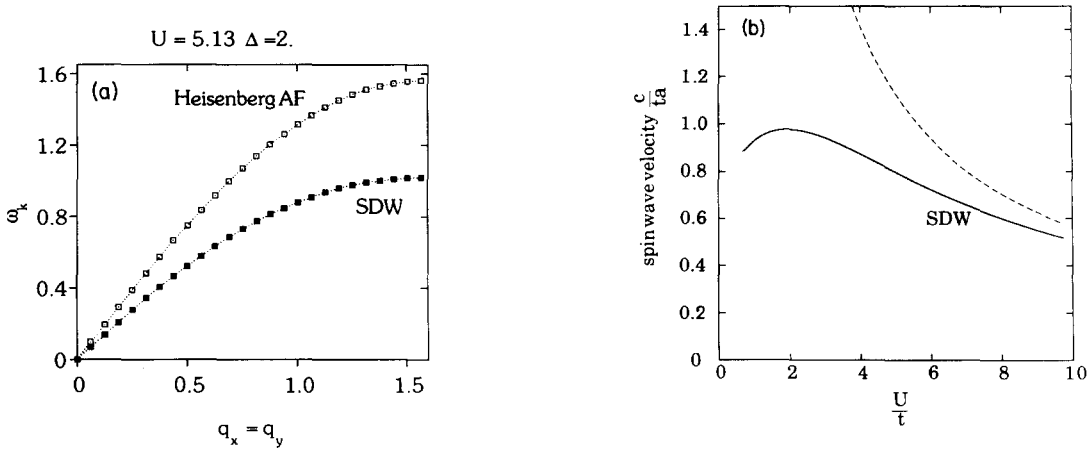

Fig. 32. (a) SDW spin-wave dispersion for $U/t = 5.13$ for which $\Delta_{SDW}/t = 2$, compared to the linear-spin-wave theory result for the Heisenberg antiferromagnet with exchange coupling $J = 4t^2/U$. In the strong coupling limit both curves smoothly merge. (b) SDW spin wave velocity as a function of the coupling strength U/t. The dashed line shows the strong coupling limit $c = \sqrt{2}J$.

where the nearest-neighbor sublattice Néel state is known to survive until $J' = J/2$ (see e.g. Refs. [96,266] and references therein).

We return to the Hubbard model in the absence of t' hopping and evaluate the self-energy correction to the quasiparticle propagator from the coupling to transverse and longitudinal spin fluctuations. On the one-loop level the self-energy is calculated by summing the diagrammatic series shown in Fig. 33. Using the original c-electron representation of the Hubbard model the elements of the 2×2 self-energy matrix are readily expressed as

$$\Sigma^c_\sigma(\boldsymbol{k}, \boldsymbol{k}', \omega) = -iU^2 \frac{1}{N} \sum_{\boldsymbol{q}} \int \frac{d\nu}{2\pi} \Big(G^{0c}_{-\sigma}(\boldsymbol{k} - \boldsymbol{q}, \boldsymbol{k}' - \boldsymbol{q}, \omega - \nu) \chi^{-\sigma\sigma}_{\mathrm{RPA}}(\boldsymbol{q}, \boldsymbol{q}, \nu)$$

$$+ G^{0c}_{-\sigma}(\boldsymbol{k} + \boldsymbol{Q} - \boldsymbol{q}, \boldsymbol{k}' - \boldsymbol{q}, \omega - \nu) \chi^{-\sigma\sigma}_{\mathrm{RPA}}(\boldsymbol{q} + \boldsymbol{Q}, \boldsymbol{q}, \nu)$$

$$+ G^{0c}_{\sigma}(\boldsymbol{k} - \boldsymbol{q}, \boldsymbol{k}' - \boldsymbol{q}, \omega - \nu) \frac{U^2 [\chi^{zz}_0(\boldsymbol{q}, \boldsymbol{q}, \nu)]^3}{1 - [U\chi^{zz}_0(\boldsymbol{q}, \boldsymbol{q}, \nu)]^2} \Big). \tag{5.29}$$

The first two terms result from the coupling to the transverse spin fluctuations contained in the ladder series of the self-energy diagrams Fig. 33b, including the umklapp contribution from the off-diagonal matrix elements of the transverse susceptibility. The third term arises from the odd-bubble-number diagram series Fig. 33a which contains longitudinal spin as well as charge fluctuations.[5]

The corresponding elements for the self-energy matrix of the γ SDW-quasiparticles is then obtained by the linear transformation

$$\Sigma^\gamma_\sigma = U \Sigma^c_\sigma U^{-1}, \tag{5.30}$$

[5] Note that the lowest order single-bubble diagram in Fig. 33a is already included in the first two terms and has to be omitted in the third term in order to avoid double counting.

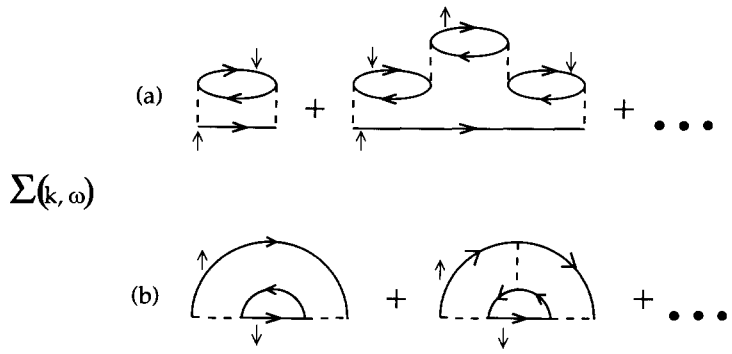

Fig. 33. Self-energy diagrams from the coupling to (a) transverse spin and (b) longitudinal spin and charge fluctuations. Note that the first diagrams in each series are identical and have to be included only once in the expression for the self-energy. The broken lines represent the Hubbard interaction U and the fermion lines the c-electron propagators in the SDW state.

$$\boldsymbol{U} \equiv \boldsymbol{U}(\boldsymbol{k}, \sigma) = \begin{bmatrix} u_{\boldsymbol{k}} & \sigma v_{\boldsymbol{k}} \\ v_{\boldsymbol{k}} & -\sigma u_{\boldsymbol{k}} \end{bmatrix}. \tag{5.31}$$

With $\boldsymbol{G}^{0\gamma} = \boldsymbol{U}\boldsymbol{G}^{0c}\boldsymbol{U}^{-1}$ we obtain the γ-quasiparticle propagator from the Dyson equation

$$\left[\boldsymbol{G}_{\sigma}^{\gamma}\right]^{-1} = \left[\boldsymbol{G}_{\sigma}^{0\gamma}\right]^{-1} - \boldsymbol{\Sigma}_{\sigma}^{\gamma}. \tag{5.32}$$

We postpone the discussion of the renormalized single particle properties contained in the self-energy correction Eq. (5.29) to chapter 5.4.2. Instead, we use here the single particle propagator to calculate the reduction of the sublattice magnetization which arises from the self-energy correction.

A simple derivation shows that the staggered magnetization $\langle S_z(\boldsymbol{Q})\rangle$ is obtained from [398]

$$\langle S_z(\boldsymbol{Q})\rangle = -\frac{i}{N}\sum_{\boldsymbol{k}}{}' \int \frac{d\omega}{2\pi}\left[G_{\uparrow}^{c}(\boldsymbol{k}, \boldsymbol{Q}-\boldsymbol{k}, \omega) - G_{\downarrow}^{c}(\boldsymbol{k}, \boldsymbol{Q}-\boldsymbol{k}, \omega)\right]. \tag{5.33}$$

The Hartree–Fock result for $m = \langle S_z(\boldsymbol{Q})\rangle$ is directly related to the SDW energy gap by $m = -\Delta_{\mathrm{SDW}}/U$. In the large U limit, m therefore approaches $1/2$ as expected for the localised spin system. On the one-loop level for the self-energy Eq. (5.29) the Gaussian spin fluctuations reduce the sublattice magnetization from its Hartree–Fock value as shown in Fig. 34. Extending the results again to the large U limit one finds [374]

$$|m| \overset{U\gg t}{\longrightarrow} 1 - \frac{1}{N}\sum_{\boldsymbol{q}}{}' \frac{1}{\sqrt{1-(\epsilon_{\boldsymbol{q}}/4t)^2}} = 0.3035. \tag{5.34}$$

The crossover from weak to large U for the magnetization is represented in Fig. 34 as well. The result Eq. (5.34) agrees with the linear spin wave analysis [321] and the Schwinger boson mean-field theory [25] of the 2D Heisenberg model. It is also in good agreement with the QMC results [325,433] (see Tab. 4), a further example that the weak coupling RPA calculation for the SDW state leads to meaningful results when U is formally increased into the strong coupling regime.

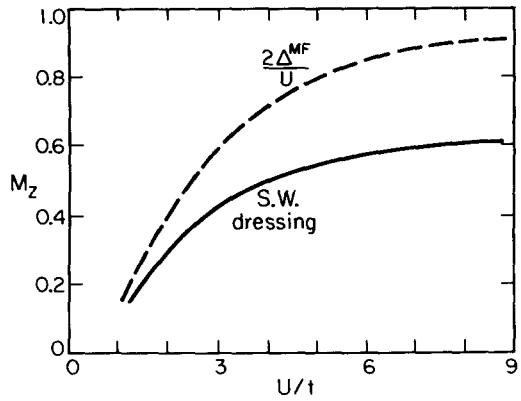

Fig. 34. Sublattice magnetization as a function of U/t in the Hartree–Fock approximation (dashed line) and with the RPA spin-fluctuation correction (solid line). (Note that in this plot M_z is minus two times the magnetization m as used in the text.) (From Ref. [195].)

5.1.3. Static vacancies in a Heisenberg antiferromagnet

As we know, the important physics of weakly doped metallic cuprates arises from the correlated motion of holes or electrons in an environment with short range AF spin correlations. Before we consider this central issue it is worthwhile to consider first the simpler problem of static vacancies in a Heisenberg antiferromagnet. The creation of vacancies can be modeled by adding the impurity term [61]

$$H_{\mathrm{IMP}} = -J \sum_{\boldsymbol{R}_l} \sum_{j(l)} \boldsymbol{S}_l \cdot \boldsymbol{S}_j \tag{5.35}$$

to the Heisenberg Hamiltonian. H_{IMP} effectively cuts all bonds to the spins located at the randomly distributed positions $\{\boldsymbol{R}_l\}$ and $j(l)$ denotes the corresponding nearest neighbor sites on the lattice. The isolated spins therefore act for the host system like a static vacancy. Propagating spin waves are scattered from these impurity vacancies and the same techniques can be applied as for impurity scattering of electrons in metals.

It is instructive to solve first the case of a single vacancy. This problem can be treated exactly within linear-spin-wave (LSW) theory since the impurity potential is local. Bulut et al. [61] have solved for the renormalized spin-wave Green's functions which allows one to obtain the spin correlation functions in the neighborhood of a vacancy. One interesting result of this calculation is that the local staggered magnetization on the next-nearest neighbor sites of the vacancy is actually found to be enhanced by 3.5% relative to the host value in the absence of the vacancy [61]. This follows from the suppressed zero-point fluctuations on these sites due to the absence of the S^+S^- terms which involve the nearest-neighbor vacancy site.

In the limit of a small vacancy concentration one may resort to the standard many-body techniques for impurity scattering. Applying these techniques for the spin-wave Green's functions in LSW theory, the renormalized spin-wave properties are obtained from the single-impurity scattering T-matrix [50]. In the dilute limit it is sufficient to consider the diagram series for the self-energy as shown in Fig. 35. In this limit only the diagrams to lowest, linear order in the vacancy concentration $n_V = (1/N) \sum_{\boldsymbol{R}_l}$ have to be included within the averaging procedure over the impurity positions. This is equivalent

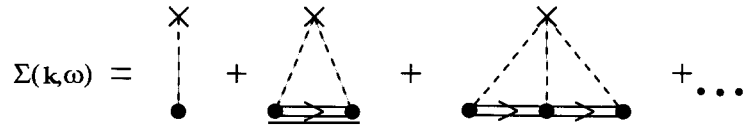

Fig. 35. Diagrams for the self-energy of the spin-wave propagator. Scattering off a specific impurity vacancy is represented by a full circle attached to a dashed line. Configurational averaging over the positions of the static vacancies is symbolised by a cross. (From Ref. [50].)

to treating the single-site scattering process exactly and neglecting all correlations between different vacancy sites.

Given the self-energy from the diagram series in Fig. 35 it is straightforward to evaluate the renormalized spin-wave properties. Due to the impurity scattering the spin wave excitations acquire a finite lifetime, and the spin-wave dispersion is softened at long wavelengths [50]. For a comparison to experimental results it is useful to obtain a quantitative estimate for the reduction of the spin-wave velocity c. To leading linear order in the vacancy concentration this reduction of c is approximately given by

$$c = \sqrt{2}J(1 - 3.1n_V)\,. \tag{5.36}$$

Interestingly, a similar magnitude for the slope is found experimentally [205,206] for the reduction of the Néel temperature in the electron doped material $Nd_{2-x}Ce_xCuO_4$ where a finite Néel temperature T_N is still observed for x as high as 0.14 [421]. Also the temperature dependence of the spin correlation length in this material has been found to be properly described by a "diluted" Heisenberg model [250]. This supports the view that at small x the doped electrons seem to be favorably localised on the Cu ions creating locally a $Cu^+ d^{10}$ configuration which carries no magnetic moment. Vacancies of magnetic moments are similarly created by Zn doping in La_2CuO_4 where they have a comparably weak effect on T_N [205,206] (see the more detailed discussion of experimental results in chapter 3.5.2).

The situation is different in $La_{2-x}Sr_xCuO_4$ where the mobility of the holes doped primarily into the oxygen orbitals leads to a much more effective disruption of the magnetic order. A description in terms of localised static holes is clearly inappropriate in this case. The considerably more involved situation of hole doping in 214 and other cuprate materials will be the central subject of the next chapters.

5.2. Spin correlations in the doped metallic state

Two central questions arise when a small concentration of mobile holes is doped into an antiferromagnet: The first question addresses the magnetic properties, in particular, how are the static and dynamic spin correlations affected due to the presence of mobile holes? The second question is related to the single particle properties and the charge dynamics of the doped holes themselves as they move in an AF correlated environment. We will in the following chapters discuss the magnetic properties first. Before the discussion of the dynamic spin susceptibility in chapter 5.3, we start by illustrating some of the intuitive pictures for the hole motion and discuss magnetic structures which have been suggested to replace the Néel order in the presence of a small amount of holes.

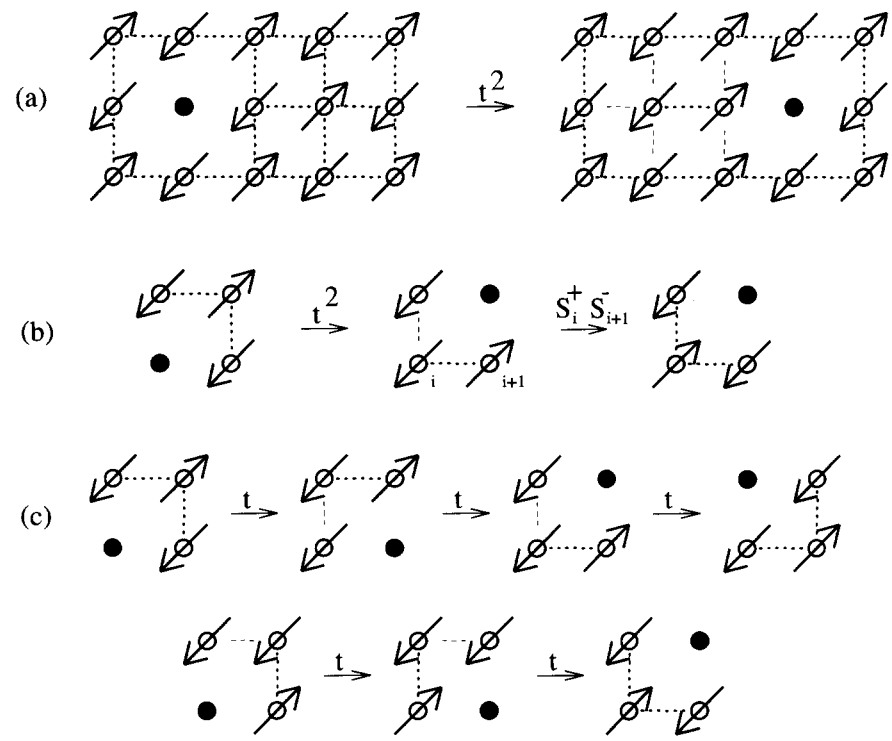

Fig. 36. (a) Schematic figure of hole motion in an antiferromagnetically ordered spin background. In this example the hole hops twice along the x-axis creating a string of five misaligned spin pairs (indicated by the thin broken lines) along its path. (b) Sublattice hole motion accompanied by a two-spin flip process from $S_i^+ S_{i+1}^-$ acting on the spin pair at sites i and $i+1$ on the hole's path. (c) The Trugman loop [427,428]: with six individual hops the hole moves around a plaquette $1\frac{1}{2}$ times and finds itself translated to the next-nearest neighbor site without disturbing the spin background. In between two adjacent plaquettes the hole has performed one counter-clockwise hop to a next-nearest-neighbor site on the plaquette.

5.2.1. Spin disorder from hole motion

Numerical evidence for the Hubbard model seems to indicate that for any finite amount of hole doping AF long range order is immediately lost [161]. In the strong coupling limit of localised spins doped, mobile holes create misaligned spins along their hopping paths and thereby disrupt the spin order [60,55]. This is shown schematically in Fig. 36a where a single hole hops two lattice spacings away from its originally position in an ordered antiferromagnet. The hole leaves behind a string of misaligned, i.e. ferromagnetically aligned, spin pairs. The number of misaligned spin pairs grows linearly with the number of hoppings leading to a competition between the kinetic energy gain of the hole and the cost in magnetic energy. Nearest-neighbor pairs of disordered spins, however, are eventually repaired by transverse quantum spin-fluctuations (see Fig. 36b). In the t–J model these processes arise naturally from the S^+S^- terms acting on the misaligned spin pair. Spin fluctuations therefore prevent the holes from being localised and allow for coherent hole propagation [351,200,113,255].

Even in an Ising spin background where transverse spin fluctuations are absent the hole can move along a spiraling path without destroying the AF spin order. As has been first pointed out by Trugman

[427,428] a hole can travel around a plaquette $1\frac{1}{2}$ times without disturbing the AF spin alignment and finds itself translated to the next-nearest neighbor site as shown in Fig. 36c. This means that the hole can "unwind" the string of misaligned spins it leaves behind on its path and self-generate a next-nearest neighbor hopping.

Ideally, a hole moving on the same given sublattice of a quantum antiferromagnet would leave the AF order perfectly intact. In fact, as we will see below in chapter 5.4.3, the effective motion of holes doped into a quantum antiferromagnet appears to generate indeed a dispersion which closely resembles the sublattice hopping motion along the next-nearest neighbor sites of the square lattice [255,236]. Since there are two sublattices, the hole motion in an AF spin background gives rise to two degenerate hole bands. Any spatial modulation of the commensurate spin order will lift the degeneracy of the two hole bands, offering a possible way to gain further energy by occupying dominantly the lower one of the two hole bands [171]. This is the origin for the instability of commensurate AF order under doping. Within mean-field theory spin textures with a spiral pattern are indeed found to have a lower energy in the presence of a finite amount of doped holes [186,201,26]. In these spiral states the staggered magnetization is not fixed along a certain direction but rather it slowly rotates with a wavenumber proportional to the density of doped holes [366].

5.2.2. *Spiral spin patterns*

The concept of a spiral phase has originally been discussed for the t–J model by Shraiman and Siggia [364–366]. Most of their results have been derived in the quasiclassical limit $J \gg t$. The spin background is assumed to be classical but the distortion of this background due to the hole motion is taken into account. In their picture the motion of a hole doped into an antiferromagnet creates a long range dipolar distortion of the staggered magnetization [364]. The associated dipole moment $\boldsymbol{P}_a$ is found to be related to the direction of the staggered magnetization $\hat{\boldsymbol{\Omega}}$ by

$$\langle \hat{\boldsymbol{\Omega}} \times \partial_a \hat{\boldsymbol{\Omega}} \rangle = \boldsymbol{P}_a, \tag{5.37}$$

where $\partial_a = \hat{\boldsymbol{a}} \cdot \nabla$ is a discrete gradient along the direction $\hat{\boldsymbol{a}}$. The dipole moment is proportional to the density of doped holes and Eq. (5.37) tells that it induces a slow twisting of the direction of the order parameter $\hat{\boldsymbol{\Omega}}$. In the spiral state the staggered magnetization rotates in a plane with a spiral pitch scaling inversely proportional to the density of holes [366]. Quantum spin fluctuations have not been included by Shraiman and Siggia and the spin distortion discussed by them is the long distance behavior, i.e. far away from the hole location.

A conceptually transparent formulation for the spiral state can be achieved within a Hartree–Fock scheme for the one-band Hubbard model. For each lattice site i we assign a unit vector $\hat{\boldsymbol{n}}_i$ pointing in the direction, or opposite direction, of the on-site magnetization, depending on the different sublattices. $\hat{\boldsymbol{n}}_i$ is chosen as the local spin quantisation axis and can be specified by the two spherical angles $\Omega_i = (\theta_i, \phi_i)$. With the unitary transformation [452,22]

$$d_{i\sigma} \equiv \sum_{\sigma'} [\mathcal{R}(\Omega_i)]_{\sigma\sigma'} = \sum_{\sigma'} \left[\exp(i(\theta_i/2)\sigma_y)\, \exp(i(\phi_i/2)\sigma_z)\right]_{\sigma\sigma'} c_{i\sigma'}, \tag{5.38}$$

the Hubbard Hamiltonian then takes a form which explicitly accounts for the new set of local spin quantization axes,

$$H(\{\Omega_i\}) = -t \sum_{\langle ij\rangle\sigma_1\sigma_2} \{d^+_{i\sigma_1}[\mathcal{R}(\Omega_i)\mathcal{R}^+(\Omega_j)]_{\sigma_1\sigma_2} d_{j\sigma_2} + \text{h.c.}\} + U\sum_i d^+_{i\uparrow} d_{i\uparrow} d^+_{i\downarrow} d_{i\downarrow}. \tag{5.39}$$

The Hubbard U term is naturally invariant under the unitary transformation Eq. (5.38). The subset of homogeneous spiral phases which preserve the discrete translational symmetry of the lattice is selected by the choice of the angles

$$\phi_i = 0, \qquad \theta_i = \boldsymbol{q}^S \cdot \boldsymbol{R}_i, \tag{5.40}$$

where the wavenumber $\boldsymbol{q}^S$ characterizes the pitch of the spiral. This choice restricts the spiral arrangements of the magnetic moments into the x–z plane, i.e. $\langle \boldsymbol{S}_i\rangle = m[\sin(\boldsymbol{q}_S \cdot \boldsymbol{R}_i), 0, \cos(\boldsymbol{q}_S \cdot \boldsymbol{R}_i)]$.

In the new local set of spin quantisation axes the interaction term can be decoupled in the standard way. Introducing $\langle n^d_{i\sigma}\rangle = \frac{1}{2}n + \sigma m$, we may look for solutions with a uniform hole density. The diagonalised Hartree–Fock Hamiltonian leads to two quasiparticle bands with the dispersion

$$E^{\pm}(\boldsymbol{k}) = \epsilon^+_{\boldsymbol{k}} \pm \sqrt{(\epsilon^-_{\boldsymbol{k}})^2 + (Um)^2}, \tag{5.41}$$

$$\epsilon^{\mp}_{\boldsymbol{k}} = -t \sum_{\alpha=x,y} [\cos(k_\alpha - \tfrac{1}{2}q^S_\alpha) \mp \cos(k_\alpha + \tfrac{1}{2}q^S_\alpha)]. \tag{5.42}$$

The corresponding free energy has to be minimised with respect to the magnetization m and the spiral wave vector $\boldsymbol{q}^S$ for fixed density n. The SDW-quasiparticle dispersion derived in chapter 4.3.2 is included in Eq. (5.41) for $\boldsymbol{q}^S = (\pi, \pi)$. The mean-field U/t vs. filling phase diagram turns out to have a series of transitions between different spiral phases characterised by the wavenumber $\boldsymbol{q}^S$ (for the one-band Hubbard model see e.g. Ref. [112], for the three-band Hubbard model see Ref. [23]). For arbitrarily small hole (or electron) doping the commensurate antiferromagnetic state is generally found to be unstable against the diagonal spiral with $\boldsymbol{q}^S$ along the $(1,1)$ direction. The deviation of $\boldsymbol{q}^S$ from (π,π) starts out linearly with the dopant concentration. At a critical, U dependent doping $n_c(U)$, a first order transition occurs to a $(1,0)$ spiral for which $\boldsymbol{q}^S = (\pi,\pi) - \delta q(1,0)$. A pictorial view for the $(1,1)$ and $(1,0)$ spiral is given in Fig. 37.

It is tempting to relate the incommensurate spin modulation of the spiral states with the splitting of the magnetic peak seen in the neutron scattering data for $La_{2-x}Sr_xCuO_4$ [80]. The experimentally observed discommensuration would correspond to the wavenumber of the $(1,0)$ spiral state. This connection has been made on the basis of a more sophisticated slave boson treatment [135]. The obtained energies for the spiral states in the slave boson formulation agree within 2% with QMC results indicating that spiral states are good approximate candidates for the ground state of the Hubbard model near half-filling and at intermediate to large values of U/t [134]. Further possible spin textures have been suggested which include spin canted states, double spirals [201], or soliton lattice states [170].

A separate interesting observation is made when a t' next-nearest-neighbor hopping is included in the kinetic energy of the Hubbard Hamiltonian to model more closely the bandstructure and the Fermi surface of the 214 materials. In this case the commensurate antiferromagnetic state is found to be stabilised against spiral distortions for a finite range of electron doping [197]. A $(1,1)$ spiral state is instead immediately favored if holes are added. This asymmetry between hole and electron doping arises here obviously from a bandstructure effect due to the inclusion of t' hopping. This result provides another possible origin for the robustness of the Néel state in the electron doped materials.

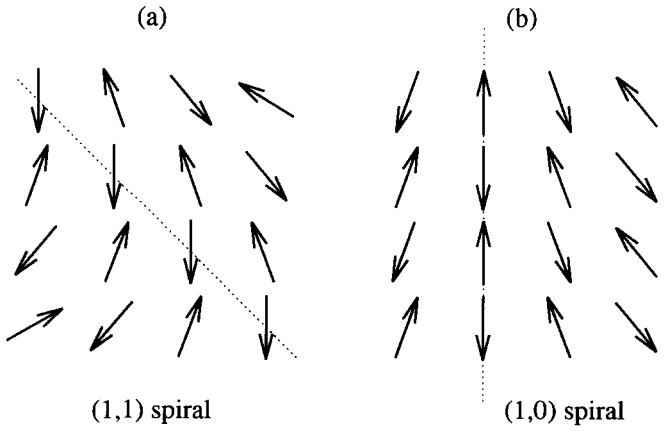

Fig. 37. Schematic figure for the two spiral spin states with q_S along the (1,1) direction (a) and along the (1,0) direction (b). The dotted line indicates the spins whose directions remain untwisted.

It also agrees with the neutron scattering data which show that the magnetic correlations in Pr_2CuO_4 remain commensurate under Ce doping [421] which adds electrons to the CuO_2 planes.

There is, however, a caveat concerning the stability of homogeneous spiral states. In the t–J model they show a tendency to a local increase of the hole density as is signalled by a negative mean-field compressibility [26]. This implies phase separation into hole rich and hole pure domains [118]. For the t–J model it is known that in the unphysical large J/t limit the holes will cluster in order to minimise the number of broken antiferromagnetic bonds [331]. For smaller values $J/t < 1$ the issue is still controversial. For the one-band Hubbard model no evidence for phase separation has been found in quantum Monte Carlo studies. (For an extensive discussion see Ref. [103].)

5.3. *Dynamic spin susceptibility* $\chi(\boldsymbol{q}, \omega)$

Calculations of the dynamic spin susceptibility allow one to test the applicability of the Hubbard models for the magnetic correlations in the metallic cuprates. In particular the neutron scattering and NMR data have provided detailed information on $\chi(\boldsymbol{q}, \omega)$ to be compared with theory. On the one hand the validity of the models themselves is in question. In particular, do the Hubbard Hamiltonians provide the minimal models which contain the essential physics of cuprate superconductors? To answer this question rigorous results are needed which are so far available mainly from numerical calculations on small clusters. This topic has been extensively discussed in a recent review article by Dagotto [103]. Separately, different levels of approximation schemes have been developed which are not limited to finite size systems. Their quality can often be tested against QMC and exact diagonalization results. As we will see below it is generally found that the single-band Hubbard model does very well in describing the magnetic properties of the cuprates. More detailed comparisons with experiment, however, show that also band structure effects do play a role, e.g. for the understanding of the different neutron scattering results obtained for the 214 and 123 materials.

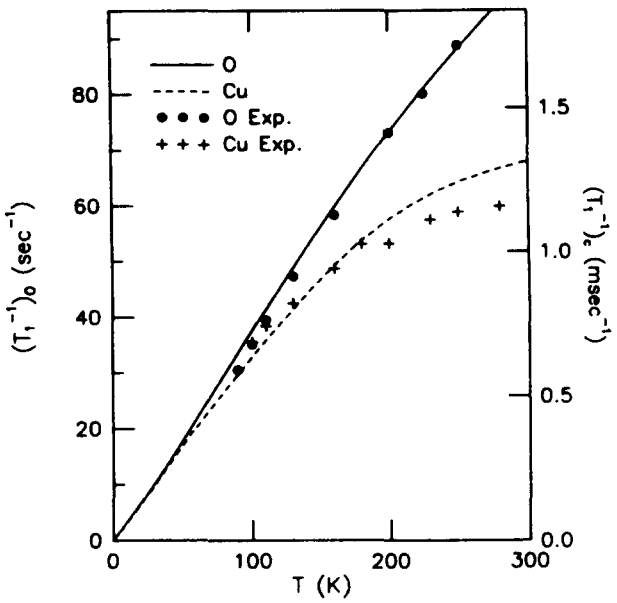

Fig. 38. RPA fit of the spin-lattice relaxation rates $^{63}T^{-1}$ and $^{17}T^{-1}$ with the Hubbard model parameters $U/t = 2$, filling $\langle n \rangle = 0.86$ and $8t = 1.2$ eV. (From Ref. [62].) The data points for $123\,O_7$ are from Refs. [151,405].

5.3.1. RPA in the normal state: application to NMR and Raman scattering

The weak-coupling RPA treatment for the paramagnetic state of the one-band Hubbard model provides the simplest parametrisation of $\chi(q, \omega)$ in the form of Eq. (5.18) which includes strong AF spin fluctuations. Within this approach a very exhaustive quantitative analysis has been performed for the NMR relaxation rate and the neutron scattering intensity [62,37]. Using the form factors of Mila and Rice [264] and the experimentally determined hyperfine coupling constants [405,30] the spin lattice relaxation rate $1/T_1$ at the oxygen and copper sites has been fitted with a weak-coupling $U = 2t$ and a filling $\langle n \rangle = 0.86$ as shown in Fig. 38. The large AF spin fluctuations which are implied by the enhancement for the Korringa ratio at the Cu site (see chapter 3.3.2) require a tuning of the parameters right on the boundary of the magnetic instability. Thus, for the chosen value of $U/t = 2$ the critical filling is $\langle n \rangle = 0.865$ which is only 0.5% larger than the filling used to fit the NMR data. Yet, if one accepts to view U/t and the filling as adjustable parameters and not to be fixed a priori for the considered material, then the RPA with this delicately balanced parameter set allows a reasonable fit of the experimental data.

The RPA analysis is straightforwardly extended to the three-band model as well [62]. If on-site oxygen and intersite copper–oxygen Coulomb repulsions are ignored the result for the spin susceptibility is written in terms of partial susceptibilities in the form,

$$\chi^{\mathrm{RPA}}_{rr'}(q, \omega) = \chi^0_{rr'}(q, \omega) + \chi^0_{rd}(q, \omega) \frac{U_d}{1 - U_d \chi^0_{dd}(q, \omega)} \chi^0_{dr'}(q, \omega). \tag{5.43}$$

Here, $r, r' \in \{d, p_1, p_2\}$ denote the Cu and O orbitals within the three-site unit cell of the CuO_2 lattice. The noninteracting $U = 0$ partial susceptibilities are calculated by transforming to the energy band basis in which the kinetic energy of the three-band Hamiltonian is diagonal:

$$\chi^0_{rr'}(\boldsymbol{q},\omega) = \frac{1}{N}\sum_{k;\nu,\nu'=0\pm} \alpha^{\nu}_{rr'}(\boldsymbol{k}+\boldsymbol{q})\alpha^{\nu'}_{rr'}(\boldsymbol{k})\frac{f(E^{\nu}_{k+q}) - f(E^{\nu'}_{k})}{\omega - (E^{\nu}_{k+q} - E^{\nu'}_{k}) + i\eta}. \tag{5.44}$$

E^{ν}_{k} are the energies of the bonding and antibonding Cu(3d)–O(2pσ) bands as given by

$$E^{\pm}_{k} = \tfrac{1}{2}\epsilon_p \pm [\tfrac{1}{4}\epsilon^2_p + 4t^2_{pd}(\cos^2\tfrac{1}{2}k_x + \cos^2\tfrac{1}{2}k_y)]^{1/2}. \tag{5.45}$$

$E^0_k = \epsilon_p$ is the energy of the nonbonding oxygen band. For simplicity the results here apply in the absence of oxygen–oxygen hopping $t_{pp} = 0$ and energies are measured relative to the Cu 3d level $\epsilon_d = 0$. In Eq. (5.44) $\alpha^{\nu}_{rr'}$ are the coherence factors with band index ν introduced in order to diagonalise the kinetic energy term [62,226]. In the NMR analysis the partial susceptibilities χ_{dd} and χ_{pp} have to be inserted for the Cu and O Knight shift and relaxation rates, respectively. Generally, the RPA three- and one-band analyses give qualitatively similar results [62].

As we know, the RPA susceptibility contains an unphysical instability of the paramagnetic phase at any finite hole doping as signalled by the Stoner condition, i.e. by $1 - U\chi_0(\boldsymbol{q},0,T) = 0$ in the one-band model. Purely as a consequence of the tight-binding band structure $\chi_0(\boldsymbol{q},0)$, at zero temperature has degenerate maxima at $\boldsymbol{Q}_1 = (\pi \pm \delta, \pi)$ and $\boldsymbol{Q}_2 = (\pi, \pi \pm \delta)$. The instability is therefore towards incommensurate antiferromagnetism with the modulation wavevectors $\boldsymbol{Q}_1$ or $\boldsymbol{Q}_2$ in the weak U approximation [354]. At $T = 0$ the magnitude of the discommensuration is determined by the chemical potential, $\delta = \mu/t$.

Naively, one might have expected that the maximum occurs somewhere along the diagonal of the Brillouin zone. But it is in fact the wavevectors $\boldsymbol{Q}_1$ or $\boldsymbol{Q}_2$ which favourably connect flat parts of the Fermi surface for the 2D tight binding band [354]. At finite but low temperatures the discommensuration occurs above a critical concentration of doped holes as shown in Fig. 39. While the instability is itself an artifact of the RPA, the discommensuration wavevectors $\boldsymbol{Q}_1$ and $\boldsymbol{Q}_2$ are in qualitative accordance with the magnetic neutron scattering experiments on $La_{2-x}Sr_xCuO_4$ [80,257]. However, the magnitude of the discommensuration obtained within RPA is much smaller than experimentally observed. This can be remedied in part by the inclusion of a t' next-nearest neighbor hopping term which effectively modifies the tight binding Fermi surface. For $t' = -0.16t$ the Fermi surface for the tight binding dispersion is found to be consistent with local-density-approximation (LDA) calculations and comparisons with X-ray-absorption experiments [169] (see Fig. 29 in chapter 4.2.2). Still, the positions of the peaks in the magnetic structure factor cannot agree quantitatively with the neutron results if the band structure parameters are assumed to be independent of the concentration of doped holes [37].

In view of the qualitatively reasonable results the RPA is able to provide for the NMR experiments a similar calculation has been applied to Raman scattering from AF spin fluctuations. Due to the persisting short range AF order in the doped metallic materials local two-spin flip processes will still contribute to the Raman scattering intensity. In order to separate this magnetic contribution a diagrammatic repesentation as shown in Fig. 40 is more appropriate [196] instead of the general calculational scheme outlined in chapter 3.4.

The diagram in Fig. 40A has two separate parts: a scattering vertex V_q describing the coupling of the photon to the electron, and two spin-fluctuation propagators carrying momenta $\boldsymbol{q}$ and $-\boldsymbol{q}$, respectively. Specifically for the one-band Hubbard model this gives a spin-fluctuation contribution to the total Raman scattering intensity of the form [196]

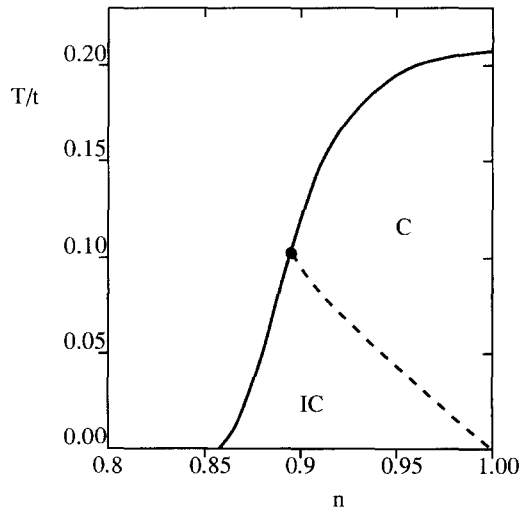

Fig. 39. Phase diagram in the temperature versus density (n) plane for $U = 2t$ with commensurate (C) and incommensurate (IC) antiferromagnetic phases, and the paramagnetic state. Most of the C–IC line is drawn only schematically. (Reproduced from Ref. [354].)

$$I(\omega,T) = [1 + n(\omega)]\frac{1}{N}\sum_{q}\int d\omega' \, |V_q(\omega_i + i\delta, \omega, \omega')|^2 [n(\omega') - n(\omega' - \omega)]$$

$$\times \, U^2 \operatorname{Im}\chi(q, \omega' + \omega)\, U^2 \operatorname{Im}\chi(-q, \omega'), \tag{5.46}$$

Here, $\omega = \omega_i - \omega_o$ is the shift between the frequencies of the incoming and outgoing photon ω_i and ω_o, respectively. The structure of the vertex function V_q is shown diagrammatically in Fig. 40B. V_q contains four different contributions from the coupling of the photon to the current operator and the "inverse mass tensor" (i.e. the density). The elementary scattering vertices (represented by black dots in Fig. 40) contain the photon polarization vectors for the different scattering geometries[6] of A_{1g}, B_{1g} and B_{2g} symmetry.

For the calculation of the spin susceptibility which enters into Eq. (5.46) we apply the weak coupling RPA approximation and sum the standard ladder and bubble diagrams for the Hubbard model. The different lowest order contributions are shown in Fig. 41. Spin constraints impose an even (odd) number of closed particle–hole loops between the fermion lines of opposite (parallel) spin which are part of the scattering vertex. The two separate contributions are given by

$$U^2\chi^{\uparrow\downarrow}(q,\omega) = U + \frac{U^2\chi_0(q,\omega)}{1 - U\chi_0(q,\omega)} + \frac{U^3\chi_0^2(q,\omega)}{1 - U^2\chi_0^2(q,\omega)}, \tag{5.47a}$$

$$U^2\chi^{\uparrow\uparrow}(q,\omega) = -\frac{U^2\chi_0(q,\omega)}{1 - U^2\chi_0^2(q,\omega)}. \tag{5.47b}$$

[6] See Fig. 15 in chapter 3.4 for the definition of the different symmetries and Ref. [196] for a table of the different scattering vertices.

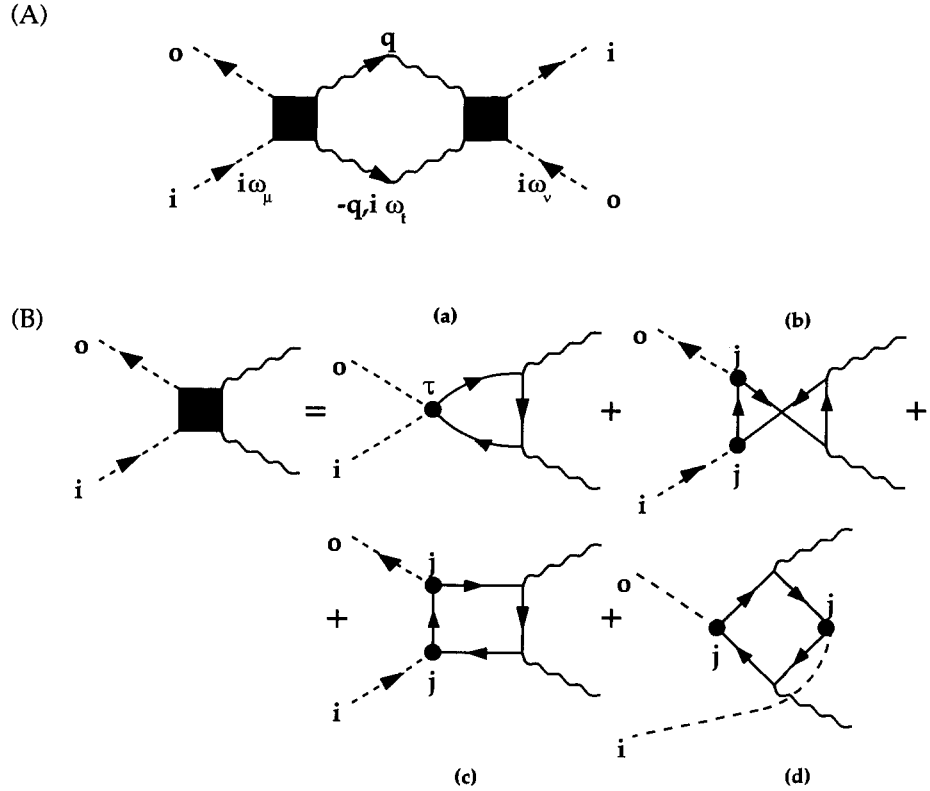

Fig. 40. (A) General diagram for the Raman intensity from two-spin fluctuation scattering. The broken lines represent the incoming (i) and outgoing (o) photon and the wiggly line the propagator (susceptibility) for the spin fluctuation. (B) Scattering-vertex function V_q from the coupling to the "inverse mass tensor" τ (a) and the current operator [j (b),(c) and (d)] for different time orderings. (For the definition of τ and j see chapter 3.4). Full lines represent the single electron propagator. (From Ref. [196].)

The elementary bubble $\chi_0(q,\omega)$ is the Lindhard function Eq. (5.19) for $U = 0$. Due to the spin constraints only the combination $2(\mathrm{Im}\,\chi^{\uparrow\uparrow}\,\mathrm{Im}\,\chi^{\uparrow\uparrow} + \mathrm{Im}\,\chi^{\uparrow\downarrow}\,\mathrm{Im}\,\chi^{\uparrow\downarrow})$ enters into the Raman intensity formula Eq. (5.46).

A difficulty arises from a proper treatment of the vertex function which has a complicated frequency and momentum dependence. As a first step free tight-binding electron propagators have been used for the evaluation of V_q together with the RPA form of the spin susceptibility [196]. The large spectral weight of χ_{RPA} near $Q = (\pi,\pi)$ in the vicinity of the magnetic instability leads to a peaked contribution to the Raman scattering intensity $I(\omega,T)$ even in the paramagnetic phase (see Fig. 42). This two-spin fluctuation contribution is the analog of the two-magnon Raman scattering in the ordered antiferromagnet. The relative strength of the intensities in the different scattering geometries roughly corresponds to the intensity ratios in the doped cuprates. Similar results have been obtained in the more phenomenogical analysis of Brenig and Monien [52].

The magnitude and shape of the two-spin fluctuation peak in this one-band model calculation bears unfortunately only little resemblance with the experimental Raman data. As discussed in chapter 3.4 the strength of the two-magnon peak is enhanced by a resonance effect with the incoming light frequency. An inclusion of these effects into a model calculation requires an improved treatment

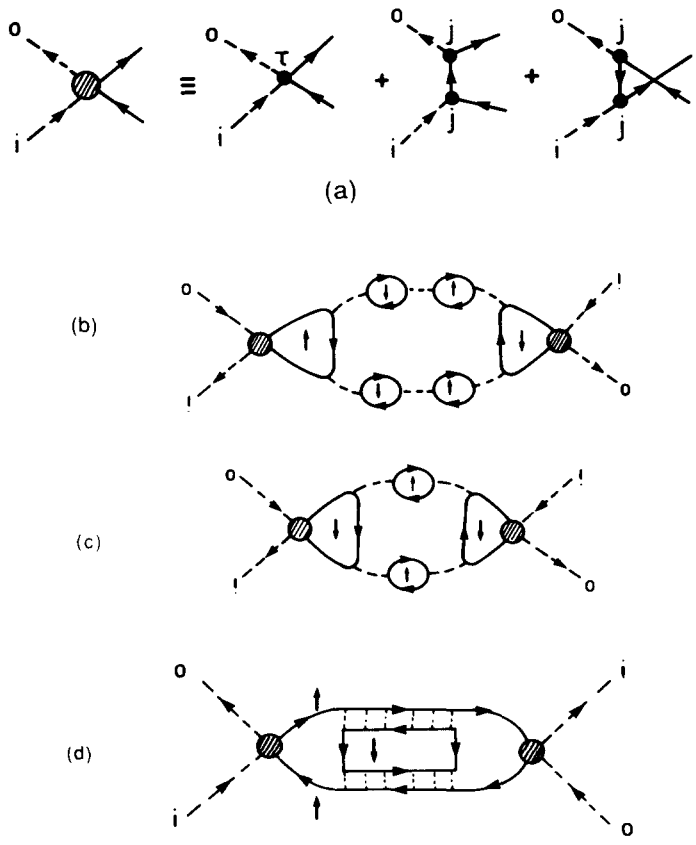

Fig. 41. (a) Effective vertex used in (b), (c) and (d). (Note that these elementary photon–electron scattering vertices also appear as part of the vertex function in Fig. 40.) (b)–(d): lowest order diagrams in U which are summed in the RPA series for the susceptibility, separated into (b) the "even-bubble", (c) the "odd-bubble", and (d) the ladder contributions. (From Ref. [196].)

of the Raman vertex function which has to account for interband transitions to intermediate states. This could appropriately be done within the three-band Hubbard model. No attempt has, however, so far been made in this direction. We have also learned from the experimental data that the resonant enhancement of the two-magnon peak rapidly weakens with increasing hole content. This points to the necessity of using dressed propagators in the Raman vertex function to account for doping dependent changes in the electronic spectrum. A formidable task for future work!

5.3.2. Beyond RPA

So far, we have used the simple RPA form of the dynamic spin susceptibility to describe the spin fluctuations in the doped Hubbard model. Naturally, we have to ask how good an approximation the RPA really is, in particular whether it is still approximately valid when the Hubbard U is increased into the intermediate to strong coupling regime. For this purpose a quantitative comparison has been performed to the magnetic structure factor obtained from Monte Carlo simulations on Hubbard clusters with 8×8 lattice sites [76,63,66]. In these comparisons the RPA susceptibility has been found to

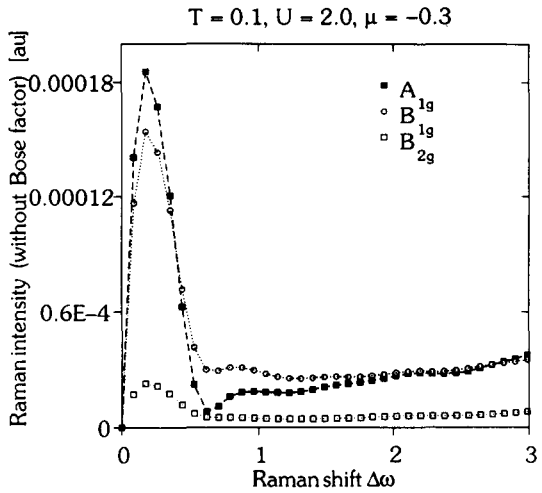

Fig. 42. Raman intensity (divided by the Bose factor) from two-spin fluctuation scattering evaluated with the vertex function V_q of Fig. 40 for different scattering geometries of A_{1g}, B_{1g} and A_{2g} symmetry. The dashed and dotted lines are a guide to the eye connecting data points of the same symmetry. (From Ref. [196].)

provide a surprisingly, even quantitatively accurate parametrisation of the Monte Carlo results if the Hubbard U in χ_{RPA} is replaced by the particle–particle scattering T-matrix. This renormalization of U was originally introduced by Kanamori [199], and has recently been renamed the *generalised* RPA (GRPA) [76,37].

The renormalized interaction $\bar{U}$ in this extension of the RPA has been found by Chen et al. [76] to be only weakly temperature dependent, in particular when the temperature scale is much less than the Fermi energy. $\bar{U}$ can be approximately obtained from the simple formula

$$\bar{U} = U/(1 + U\Lambda). \tag{5.48}$$

in terms of a renormalization parameter Λ. For example with $U = 4t$ the renormalized U decreases monotonously from $2.5t$ to $1.9t$ with increasing band-filling, and with $\bar{U} \sim 2.2t$ the QMC data for the dynamic spin susceptibility are fitted within 15% accuracy [76]. Near the magnetic instability at half-filling mode–mode coupling effects are found to become important and the GRPA is less accurate. The renormalization in the GRPA arises from summing the ladder diagrams in the particle–particle channel. Physically, it accounts for short range electron–electron correlations which reduce the probability for two electrons with antiparallel spins to occupy the same site. This effectively weakens the Hubbard interaction reducing U from the bare value by roughly a factor of 2 at intermediate values of U. Similar conclusions have been reached by Bulut et al. [63,66]. As a consequence, weak coupling approaches can still give accurate results for $\chi(\boldsymbol{q}, \omega)$ even for the intermediate coupling regime if the bare U is replaced by its renormalized value. This shifts e.g. the RPA Stoner-instability closer to half-filling.

A similar shift of the instability is found when the RPA is extended to include the effects of anharmonic local-moment-fluctuations [51]. These fluctuations are expected to be important in the intermediate coupling regime when local magnetic moments begin to develop. One way to investigate

local-moment fluctuations is to consider the functional integral representation for the partition function of the Hubbard model [124]. In this approach an interesting trick is commonly used to isolate the effects of spin fluctuations by rewriting the Hubbard interaction in terms of the identity

$$Un_{i\uparrow}n_{i\downarrow} = \tfrac{1}{2}U(n_{i\uparrow} + n_{i\downarrow}) - \tfrac{1}{2}U(n_{i\uparrow} - n_{i\downarrow})^2. \tag{5.49}$$

The second term can be decoupled by introducing an imaginary-time dependent auxiliary field in a Hubbard–Stratonovich transformation for the partition function Z. Then, one is left with the following functional integral [124]

$$Z = \int D[x]\,\mathrm{Tr}\left\{T_\tau \exp\left[-\int_0^{1/T}\left(\tfrac{1}{2}U\sum_i x_i^2(\tau) + H(\{x\})\right)d\tau\right]\right\}, \tag{5.50a}$$

$$H(\{x\}) = -t\sum_{\langle ij\rangle\sigma} c_{i\sigma}^{+}c_{j\sigma} - U\sum_{i\sigma}\sigma x_i(\tau)n_{i\sigma} - (\mu - \tfrac{1}{2}U)\sum_{i\sigma} n_{i\sigma}. \tag{5.50b}$$

This equation represents a one-particle problem in which the auxiliary fields $x_i(\tau)$ play the role of fluctuating site-diagonal exchange fields. Taking the trace in Eq. (5.50) over the fermion degrees of freedom leads to

$$Z = Z_0 \int D[x]\, e^{A(\{x\})}, \tag{5.51}$$

with the action functional

$$A(\{x\}) = -(U/2T)\sum_{j,\omega_n} |x_j(i\omega_n)|^2 + \mathrm{Tr}\,\ln(\underline{1} - \underline{M}). \tag{5.52}$$

Z_0 is the partition function of the noninteracting system for $U = 0$, and $x_j(i\omega_n)$ is the Fourier transform of the auxiliary field. The trace in $A(\{x\})$ refers to a matrix in real, frequency and spin space where the matrix elements of $\underline{M}$ are defined as [51]

$$M^{\sigma\sigma'}_{\omega_m+\nu_n,\nu_n|i,j} = -\sigma\delta_{\sigma\sigma'}Ux_i(i\omega_m)G_{ij}(\nu_n). \tag{5.53}$$

In Eq. (5.53) G_{ij} denotes the lattice Green's functions for the 2D tight-binding model [284] and $\omega_n = 2\pi mT$ and $\nu_n = (2n+1)\pi T$ are bosonic and fermionic Matsubara frequencies, respectively. Considering only Gaussian fluctuations of the x_j-fields around the saddle point of the action Eq. (5.52) is equivalent to the RPA approximation. This is sufficient in the weak-coupling limit when the action is dominated by harmonic fluctuations around a single minimum with respect to the auxiliary-field configurations.

With increasing U/t the static, zero-frequency part of the action develops a double-well structure with respect to the static exchange fields x_j [209]. This is the signature of local-moment-formation. Short range AF correlations between the local moments can be treated in the functional integral scheme by cluster coherent-potential methods [194]. As a consequence of the double well structure of the action, anharmonic and slow mode fluctuations with large amplitude of the x_j-fields become important, and non-Gaussian terms in $A(\{x\})$ have to be retained in the expansion of the logarithm in Eq. (5.52) [51]. The simplest such extension includes a fourth-order quartic term in $x_j(i\omega_n)$

in the action. As expected, the quartic term counteracts the RPA instability [51]. The quartic term is, however, even more sensitive to nesting features than the Gaussian RPA term of the action. The local moment scenario is physically appealing, yet, the approximation scheme is unfortunately not controlled by a small parameter. Preliminary results have been obtained by Monte Carlo sampling techniques for the partition function with a quartic term included in the action [54], but a detailed analysis stills waits for further improvements.

An extension along these lines has been obtained within the self-consistent renormalization (SCR) scheme of Moriya et al. [155]. The SCR method has originally been developed for the description of itinerant electron ferro- and antiferromagnets and includes mode–mode coupling effects near the magnetic instability. As applied to two-dimensional metallic systems in the vicinity of antiferromagnetism the SCR theory suggests the existence of a small crossover temperature scale T^* from low-temperature Fermi liquid behavior to anomalous temperature dependences above T^* [436]. SCR results in this anomalous regime have been compared to the normal state resistivity and optical conductivity of the cuprates with some success [286], but no specific results for the dynamic spin susceptibility of the Hubbard model are so far available which allow a direct comparison with the other schemes mentioned above.

5.3.3. $\chi(\boldsymbol{q}, \omega)$ *in an almost-localised Fermi liquid*

The RPA theories and their extensions we have discussed so far are based on the vicinity to a magnetic instability. A separate concept has been put forward by the Chicago group of Levin et al. which emphasizes that the underlying insulating state of the cuprates should be more appropriately described in terms of Mott localisation (for recent reviews on this approach see Refs. [226,369] and references therein). In this picture the transition to the insulating state is driven by a diverging effective mass of the charge carriers, rather than by a vanishing number of carriers as in the Mott–Hubbard picture.

Based on the idea of "almost localised" d-electrons a large U mean-field theory has been chosen as the starting point to obtain a renormalized band structure for the three-band Hubbard model. Introducing auxiliary bosons by the transformation [294]

$$d_{i\sigma}^{+} = s_{i\sigma}^{+} e_i + \sigma s_{i-\sigma} f_i^{+} \tag{5.54}$$

the three possible valence states Cu^{3+}, Cu^{2+}, and Cu^{1+} are explicitly represented by the creation operators e_i^{+}, $s_{i\sigma}^{+}$ and f_i^{+}, respectively. The first and last of these are boson operators while $s_{i\sigma}$ is a fermion operator which creates a Cu^{2+} state with spin index σ. In terms of e, s and f operators and using otherwise the notation of Eqs. (4.15) and (4.13) the three-band Hubbard Hamiltonian is rewritten as

$$\begin{aligned} H = & \sum_{i\sigma} \epsilon_d s_{i\sigma}^{+} s_{i\sigma} + \sum_{i} (2\epsilon_d + U_d) f_i^{+} f_i + \sum_{j\sigma} \epsilon_p p_{j\sigma}^{+} p_{j\sigma} \\ & + \sum_{\langle jj' \rangle \sigma} t_{pp} (p_{j\sigma}^{+} p_{j'\sigma} + \text{h.c.}) + \sum_{\langle ij \rangle \sigma} t_{pd} [(s_{i\sigma}^{+} e_i + \sigma s_{i-\sigma} f_i^{+}) p_{j\sigma} + \text{h.c.}], \end{aligned} \tag{5.55}$$

where the index i (j, j') refers to a copper (oxygen) site in the CuO_2 plane. In order for this Hamiltonian to be equivalent to the original three-band model the auxiliary operators have to satisfy the local constraint equation

$$\sum_{\sigma} s_{i\sigma}^{+} s_{i\sigma} + e_i^{+} e_i + f_i^{+} f_i = 1. \tag{5.56}$$

This constraint is imposed by introducing a Lagrange multiplier λ_i at each lattice site. In mean-field approximation the boson and constraint fields are replaced by static uniform c-numbers whose values have to be determined self-consistently. In this way a renormalized band structure is obtained which closely resembles the result Eq. (5.45) of the RPA calculation for the three-band Hubbard model. The important difference is that the hybridisation t_{pd} and the Cu d-level are renormalized due to the large Coulomb repulsion in the Cu d-orbitals. In the limit $U \to \infty$, in the "electron picture" the Cu^{1+} valence state is removed from the Hilbert space and t_{pd} and ϵ_d are renormalized as [208,226]

$$t_{pd} \longrightarrow \langle e \rangle t_{pd}, \qquad \epsilon_d \longrightarrow \epsilon_d + \lambda_0. \tag{5.57}$$

A systematic extension beyond mean-field theory is obtained by allowing formally for a large spin degeneracy N of the copper and oxygen orbitals and performing an expansion in $1/N$. To order $1/N^2$ the quasiparticle exchange interaction – in the following denoted as J_H – contains both, a superexchange contribution as well as a RKKY-type interaction [367,239]. To the $1/N^2$ level the RPA-like series for the partial dynamic spin susceptibilities are resummable as

$$\chi_{rr'}(\boldsymbol{q}, \omega) = \chi^0_{rr'}(\boldsymbol{q}, \omega) + \chi^0_{rd}(\boldsymbol{q}, \omega) \frac{-J_H(\boldsymbol{q})}{1 + J_H(\boldsymbol{q}) \chi^0_{dd}(\boldsymbol{q}, \omega)} \chi^0_{dr'}(\boldsymbol{q}, \omega), \tag{5.58}$$

where, as before in the discussion of Eq. (5.43), r, r' refer to the p- and d-orbitals, respectively. Implicitly, J_H depends on the band-filling, but in a moderate hole doping range the momentum dependence of $J_H(\boldsymbol{q})$ is argued to be well approximated by the tight-binding form [367]

$$J_H(\boldsymbol{q}) = J_0 \left(\cos q_x + \cos q_y \right). \tag{5.59}$$

$J_H(\boldsymbol{q})$ is negative, i.e. antiferromagnetic around $\boldsymbol{q} = (\pi, \pi)$ but has also a ferromagnetic part at long wavelengths. The susceptibility Eq. (5.58) has been used to investigate and contrast the spin dynamics in 214 and 123 materials [241,473,368]. For a given set of three-band Hubbard model parameters only the J_0 has been used as a single adjustable parameter to model the data. Fixing J_0 once for a single selected stoichiometry the same parameter set has been applied to the compounds with other hole concentrations as well. In this way, the different band structures and the related Fermi surface geometries have been found to naturally explain the temperature independent commensurate peaks in the magnetic structure factor of 123 materials. In the same approach, temperature dependent incommensurate peaks are found in the 214 compounds for comparable hole concentrations as observed in the neutron scattering experiments. Two examples of the corresponding theoretical results for the magnetic structure factor $S(\boldsymbol{q}, \omega)$ are shown in Fig. 43.

Three important low energy scales appear in this fermiology scheme: a characteristic spin-fluctuation frequency, a crossover coherence temperature below which coherent Fermi liquid behavior sets in, and the third scale is associated with the vicinity to a van Hove singularity in the band-structure density of states. All three energy scales are comparable in magnitude to the superconducting transition temperature T_c. The existence of the different low energy scales arises in this formalism from the band narrowing effects of strong Coulomb interactions combined with spin fluctuations of moderate strength. In particular, the vicinity to the van Hove singularity is offered as an explanation for the low energy peak appearing in the magnetic structure factor of the neutron scattering data in 123

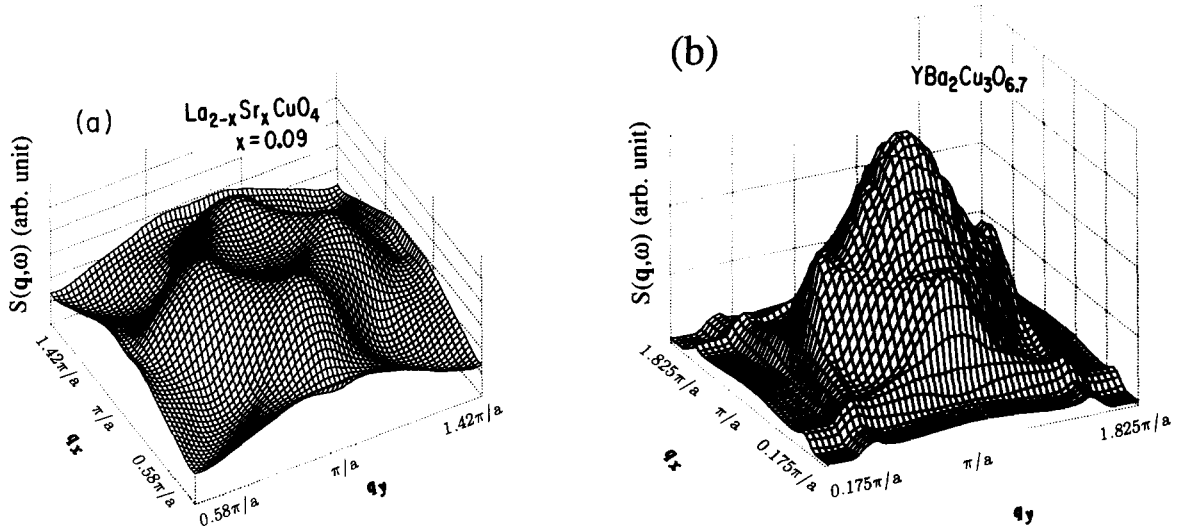

Fig. 43. Plots of the magnetic structure factor $S(\boldsymbol{q},\omega)$ versus momentum $\boldsymbol{q} = (q_x, q_y)$ for (a) $La_{1.91}Sr_{0.09}CuO_4$ and for (b) $YBa_2Cu_3O_{6.7}$. The temperature and frequency are 1 and 10 meV, respectively. (From Ref. [368].)

materials. This scheme of an almost-localised Fermi liquid has been quite successful in modeling the neutron scattering data. However, Korringa behavior of the oxygen NMR relaxation rate and the origin for the temperature dependent Knight shift and the related spin-gap effects remain problems so far unresolved within this Fermi-liquid scheme [473,368].

5.3.4. *Spin susceptibility in the t–J model*

A spin susceptibility with a $\boldsymbol{q}$-dependent exchange interaction has also been derived on a mean-field level for the t–J Hamiltonian by Tanamoto et al. [411]. The method of choice has been the slave-boson technique in which the electron operators $c_{i\sigma}$ are decomposed into the so-called spinon $f_{i\sigma}$ and holon operators b_i by $c_{i\sigma} = b_i^+ f_{i\sigma}$. $f_{i\sigma}$ removes a spin σ at site i and b_i^+ creates a hole. The spinons carry zero charge and spin $1/2$ while the holons have charge e and spin 0. Since in the t–J model there is either a hole or an electron with spin σ at a given site the constraint $b_i^+ b_i + \sum_\sigma f_{i\sigma}^+ f_{i\sigma} = 1$ has to be enforced locally. In terms of holon and spinon operators the t–J model Hamiltonian – including the constraint condition with a Lagrange multiplier – is written as

$$H = -t\sum_{\langle ij\rangle}(b_j^+ b_j \chi_{ij} + \text{h.c.}) - \tfrac{1}{2}J\sum_{\langle ij\rangle}\chi_{ij}^+\chi_{ij} - \mu\sum_{i\sigma} f_{i\sigma}^+ f_{i\sigma}$$

$$-\sum_i \lambda_i\left(b_i^+ b_i + \sum_\sigma f_{i\sigma}^+ f_{i\sigma} - 1\right). \tag{5.60}$$

[Note, that in this version the term $-\frac{1}{4}n_i n_j$ has been dropped from the t–J Hamiltonian Eq. (4.19).] $\chi_{ij} = \sum_\sigma f_{i\sigma}^+ f_{j\sigma}$ is a bond operator for spinons, defined similarly as the valence bond operators in the gauge theory of Affleck and Marston [5]. For the mean-field decoupling scheme the spin and charge degrees of the electrons are treated separately and the local constraint is replaced by a

global constraint. Two sets of order parameters are introduced [411,138]: "diagonal" order parameters $\langle f^+_{i\sigma} f_{j\sigma}\rangle$ and $\langle b^+_i b_j\rangle$ for the coherence of holons and spinons, and an "off-diagonal" order parameter $(1/\sqrt{2})\langle f_{i\uparrow} f_{j\downarrow} - f_{i\downarrow} f_{j\uparrow}\rangle$. Various forms of mean-field approximations have been studied in this framework with different kinds of solutions depending on the parameters in the model (see e.g. Refs. [396,5,147,137,222]). Fluctuations around mean-field solutions have been systematically investigated by Wen, Wilczek, and Zee [451] and Ioffe and Larkin [182] based on the original gauge-field approach of Baskaran and Anderson [32].

In the so-called singlet resonating-valence-bond (RVB) state all three order parameters introduced above are assumed to be finite. The magnetic properties of this state have been analysed on the basis of the RPA form for the dynamical susceptibility given by

$$\chi(\boldsymbol{q},\omega) = \frac{\chi_0(\boldsymbol{q},\omega)}{1 + J_{\boldsymbol{q}}\chi_0(\boldsymbol{q},\omega)}, \quad J_{\boldsymbol{q}} = J(\cos q_x + \cos q_y), \tag{5.61}$$

where $\chi_0(\boldsymbol{q},\omega)$ is the Lindhard function of free spinons in which the order parameters for nearest-neighbor sites $\langle i, j\rangle$ enter the spinon dispersion $\epsilon^S_{\boldsymbol{k}}$ by [411]

$$\epsilon^S_{\boldsymbol{k}} = -2(t\langle b^+_i b_j\rangle + \tfrac{1}{2}J\langle\chi_{ij}\rangle)(\cos k_x + \cos k_y). \tag{5.62}$$

The spin susceptibility Eq. (5.61) has been applied and compared to the data from NMR measurements [411,413]. Distinct differences between the magnetic properties at low and moderate hole doping have been obtained and it is argued that these differences explain part of the NMR data in fully oxygenated and underdoped 123 compounds. In particular, the spin-gap phenomenon is suggested to arise from subtle dependences on temperature and energy of the single-plane magnetic excitations near $\boldsymbol{Q} = (\pi,\pi)$. Similarly to the analysis in the almost-localised Fermi liquid scheme, for the detailed comparison to the NMR and neutron scattering data it has been found necessary to include band structure effects in terms of longer range hoppings into the starting Hamiltonian [412]. Yet, it still remains open whether the mean-field decoupling of spinons and holons – which amounts to the assumption of the separation of spin and charge excitations – is a valid concept for the t–J model in two dimensions.

An analytic calculation for the t–J model which does not rely on a mean-field decoupling scheme has been performed by Singh and Glenister for the static $\boldsymbol{q}$-dependent magnetic structure factor using a high-temperature expansion technique [378], i.e. an expansion in powers of J/T. More specifically, a series expansion is obtained for the spin–spin correlation function $S(\boldsymbol{r}) = 4\langle S^z_0 S^z_{\boldsymbol{r}}\rangle$ in the form

$$S(\boldsymbol{r}) = \frac{1}{4g}\sum_n \frac{(J/4T)^n}{n!}\sum_{m,p} s(n,m,p)\rho^m(4t/J)^{2p}, \tag{5.63}$$

where g counts the number of lattice vectors $\boldsymbol{r}$, which are equivalent by symmetry, and $\rho = (1/N)\sum_i\langle n_i\rangle$ is the density of electrons. The expansion has been performed up to 9^{th} order in J/T. The corresponding expansion coefficients $s(n,m,p)$ are tabulated in Ref. [378]. Padé approximants have been used to extrapolate $S(\boldsymbol{r})$ and the static magnetic structure factor $S(\boldsymbol{q}) = \sum_{\boldsymbol{r}} S(\boldsymbol{r})\exp(i\boldsymbol{q}\cdot\boldsymbol{r})$ to low temperatures. This controlled high-temperature series expansion is not limited to calculations on small clusters and provides results which are valid in the bulk limit. Only the uncertainties in the low temperature extrapolations limit the application to couplings $J/t > 1/2$ and temperatures $T/J > 2$ [378].

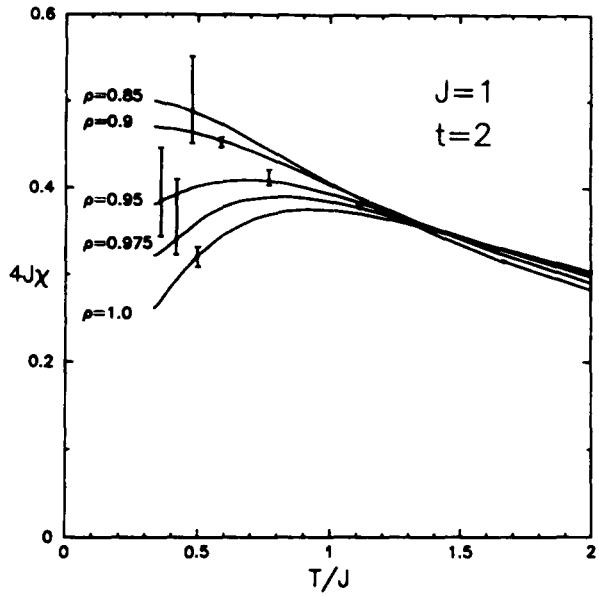

Fig. 44. Temperature dependence of the uniform susceptibility $\chi = S(q = 0)/4T$ obtained from high-temperature series expansions for the t–J model at different electron densities. (From Ref. [378].)

Fig. 44 shows the temperature dependence of the uniform susceptibility for $t/J = 2$, a value smaller than suggested by microscopic calculations [168] which put t/J around 3. Plotted in Fig. 44 is $4J\chi = JS(q = 0)/T$. Evidently, the peak in χ shifts to lower temperatures with doping away from its position at $T = J$ in the 2D Heisenberg model or, equivalently, the half-filled t–J model [299,375]. Moreover, the uniform susceptibility increases with doping at low temperatures and reaches a maximum around a density $\rho = 0.85$. At higher dopings, not shown in Fig. 44, the susceptibility decreases and $\chi(T)$ is essentially flat, i.e. Fermi-liquid like. This is qualitatively the behavior observed in the bulk-susceptibility measurements of doped 214 compounds (see chapter 3.1). It is explained in terms of a weakening of the effective exchange interaction J_{eff} in the presence of holes and a susceptibility χ which scales as $1/J_{\text{eff}}$. The increase of χ with doping is absent in RPA calculations for the one-band Hubbard model [62,240]. One may suspect that this is a genuine difference between the weak and strong coupling regime. But instead, it is rather a shortcoming of the RPA approximation [78].

5.3.5. Numerical results

Complementary to the above approximation schemes we finally review a few numerical results for the magnetic spin susceptibility in the Hubbard model. These results are unbiased against any approximation scheme and help to identify intrinsic properties of the model itself. We resume the discussion of the static spin susceptibility as started in the preceding chapter by comparing it to QMC results.

In the numerical simulations of the one-band Hubbard model the maximum of χ is observed for a filling near $\langle n \rangle = 0.85$ in the strong coupling regime with $U/t = 10$ at a fixed temperature $T = 0.25t$ [283] (Fig. 45a). The maximum persists also into the intermediate coupling regime $U/t = 4$ where the

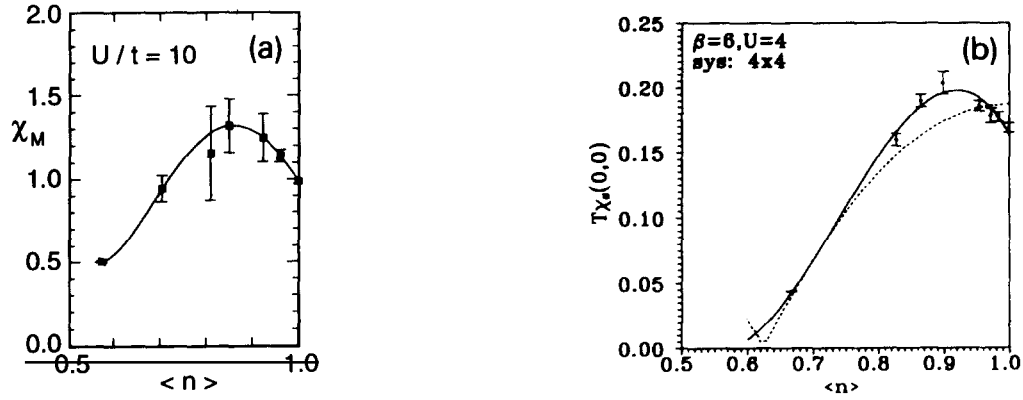

Fig. 45. QMC results for the uniform magnetic susceptibility for the one-band Hubbard model on a 4×4 lattice as a function of electron filling: (a) $U/t = 10$ and $T/t = 1/4$ (from Ref. [279]), (b) $U/t = 4$ and $T/t = 1/6$ (from Ref. [78]).

same feature is observed at the lower temperature $T = t/6$ [78] (Fig. 45b). Although no QMC data have so far been reported for weaker couplings these results suggest that most likely the maximum persists to even smaller U/t at lower temperatures. Furthermore, no indication has been found for a spin-excitation gap in the susceptibility and the available data support the expectation that χ remains finite at low temperatures for the half-filled as well as the doped case.

QMC simulations for the Hubbard model [279,140] and Lanczos exact diagonalization studies [281] have also clearly established the incommensurate structure of the equal-time spin correlations in the doped case. One example is shown in Fig. 46. The corresponding QMC data have been analysed by assuming a single-peak Lorentzian around the incommensurate wavenumber $\boldsymbol{Q}^*$ which means that the spin correlations are assumed to decay exponentially as

$$\langle \boldsymbol{S}_0 \cdot \boldsymbol{S}_r \rangle \propto \exp(i\boldsymbol{Q}^* \cdot \boldsymbol{r})\, e^{-r/\xi}. \tag{5.64}$$

From a least square fit to the QMC data the doping dependence of the spin–spin correlation length ξ for the exponential decay Eq. (5.64) is deduced to be approximately given by [140]

$$\xi = a/(\delta - \delta_c)^{\lambda/2}, \tag{5.65}$$

with $\lambda \sim 0.96 \pm 0.03$. δ_c has been found to be very small and could not be resolved to be nonzero in the finite size systems studied so far. This means that a diverging ξ and hence a long range ordered magnetic state is realized at half-filling, i.e. $\delta = 0$, only. The behavior Eq. (5.65) is very close to the inverse square root dependence on the hole doping δ found in the magnetic neutron scattering data in lightly doped 214 compounds [42]. This is a very convincing agreement with the experiments and suggests that the magnetic correlations in the doped cuprates are well represented by the one-band Hubbard model.

5.4. Single particle properties

In the previous chapter we have reviewed results and concepts developed to describe the magnetic susceptibility in the doped materials. In the present chapter we switch to the properties of the doped charge carriers themselves and discuss how their dynamics is in turn affected by the AF spin

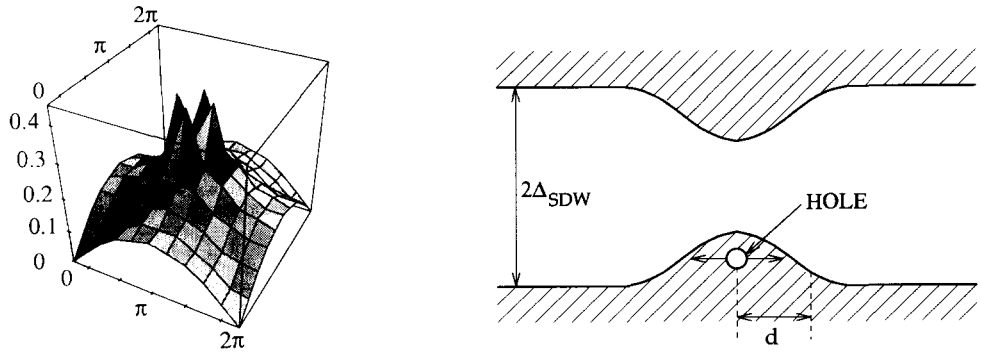

Fig. 46. QMC results for the equal-time spin–spin correlation function $S(q)$ of the one-band Hubbard model on a 10×10 lattice for a filling of 41 up and down spin electrons each. (From Ref. [140].)

Fig. 47. Schematical picture of a spin bag. A hole inserted into a spin-density-wave (SDW) state suppresses locally the amplitude of the SDW in a "bag region" of size $d = \xi_{SDW} = \hbar v_F / \pi \Delta_{SDW}$ leaving the magnetic order essentially intact in the bag's environment.

correlations in their environment. A pictorial view on the motion of holes in an antiferromagnet has already been given in chapter 5.2.1. In the present chapter we will be more specific and review results for the single particle properties arising from the coupling to AF spin fluctuations. As an application to an experimentally accessible quantity we will give particular emphasis to the optical conductivity as a direct probe for the carrier dynamics in the CuO_2 planes.

5.4.1. SDW quasiparticles, spin bags

Following the same route as we have done in the previous chapter on the dynamic spin susceptibility we start again with the weak-coupling limit of the single-band Hubbard model. As we have outlined before, in this limit the antiferromagnetism is appropriately described in terms of a spin-density-wave (SDW). In chapter 5.1.2 we have described already in detail the RPA calculation for the self-energy correction of the Hartree–Fock γ-quasiparticles of the SDW state arising from the coupling to transverse (χ^{+-}) as well as longitudinal (χ^{zz}) spin fluctuations. We emphasize that this one-loop calculation for the self-energy matrix is strictly valid only at half-filling where the ground state is known to have a broken symmetry due to the long range magnetic order of the SDW. It should be noted, however, that contrary to the common expectation of an immediate instability of the commensurate SDW order upon doping [26,377] this point of view has been challenged recently by Chubukov and Frenkel [83]. They have argued that the vacuum renormalization of the effective interaction between doped holes together with Fermi surface effects prevent an immediate instability of commensurate antiferromagnetism until a finite concentration of holes is reached. While this issue remains to be clarified the assumption of a persisting commensurate SDW should still serve as a proper approximation for weak U and very low doping.

For the weak coupling SDW regime Schrieffer, Wen and Zhang [397] have originally invented the idea to describe the quasiparticle excitations in terms of *spin bag* entities. Intuitively, an added hole or electron locally weakens antiferromagnetism and leads to a dressing of the fermion with a cloud of spin fluctuations. The dressed excitation is called a spin bag or a one-band polaron. It is important to note that the dressings with longitudinal or transverse spin fluctuations have distinct

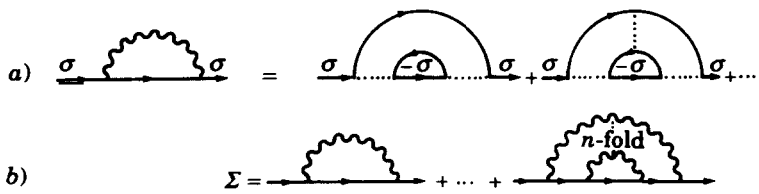

Fig. 48. (a) One-loop self-energy correction from the coupling to transverse spin fluctuations in the RPA ladder series. (b) "Rainbow" (polaron) scheme for the self-energy in the self-consistent non-crossing approximation. The wiggly line represents the RPA ladder series of Fig. (a). (From Ref. [53].)

effects: The coupling to χ^{zz} fluctuations leads to a local reduction of the amplitude for the staggered magnetization, i.e. within the bag of size $\xi_{SDW} = \hbar v_F/\pi\Delta_{SDW}$ (see the schematic picture in Fig. 47). The coupling to χ^{+-} fluctuations on the other hand creates a long range dipolar spin distortion around the bag with the spatial variation given by an inverse power law falloff [364,133]. In its original formulation the spin-bag concept has focused on the longitudinal spin-amplitude fluctuations in the SDW environment. But soon afterwards it has been demonstrated that transverse fluctuations are equally important [133], even in the weak coupling limit. The spin-bag or one-band polaron idea serves as an appealing physical picture for the quasiparticles moving in an AF background. In subsequent chapters we discuss the properties of these quasiparticles, as they arise more generally from the spin-fluctuation dressing.

5.4.2. Polaron scheme in the SDW limit

We start from the weak-coupling SDW limit and discuss the propagator of a single hole inserted into the SDW state at half-filling. We consider specifically the effects from the coupling to transverse spin fluctuations as described by the RPA spin susceptibility $\bar{\chi}^{+-}_{RPA}$ (see chapter 5.1.2). The coupling to the low energy spin-wave modes is assumed to be the dominant source for the renormalization of the single particle properties. The distortive motion of holes or electrons in the SDW is accompanied by the continuous emission and absorption of spin wave excitations. In order to account for these multiple spin-wave shakeoffs we go beyond the lowest order one-loop corrections to the self-energy as given by Eq. (5.29). Diagrammatically, this procedure is equivalent to a summation of all non-crossing (NC) diagrams for the self-energy as shown in Fig. 48. The evaluation of the NC diagram series amounts to using fully dressed Green's functions in the calculation of the self-energy, and in the 2×2 matrix formulation of the split-band SDW state a set of four nonlinear coupled integral equations for the elements of the single particle propagator matrix has to be solved [53].

To reduce the mathematical complexity of the non-crossing equations we use $\bar{\chi}^{+-}_{RPA}$ in the limit $U \gg t$ – which we denote by χ^{+-}_s – with the same arguments outlined in chapter 5.1.2. The strong coupling version of the NC equations represented by the diagram series of Fig. 48 then takes the following simple form for the self-energy matrix elements of the γ-quasiparticles [53]

$$\Sigma^{ll}_{\sigma}(\boldsymbol{k},\omega) = -iU^2(1/N)\sum_{\boldsymbol{q}}{}' \int (d\nu/2\pi)$$
$$\times [\chi_S^{-\sigma\sigma}(\boldsymbol{q},\boldsymbol{q},\nu) + \chi_s^{-\sigma\sigma}(\boldsymbol{q}+\boldsymbol{Q},\boldsymbol{q}+\boldsymbol{Q},\nu) + l\sigma 2\chi_s^{-\sigma\sigma}(\boldsymbol{q}+\boldsymbol{Q},\boldsymbol{q},\nu)]$$
$$\times G^{-l-l}_{-\sigma}(\boldsymbol{k}-\boldsymbol{q},\omega-\nu), \tag{5.66a}$$

$$\Sigma_\sigma^{-ll}(\boldsymbol{k},\omega) = -iU^2(1/N)\sum_{\boldsymbol{q}}{}' \int (d\nu/2\pi)$$

$$\times [\chi_S^{-\sigma\sigma}(\boldsymbol{q},\boldsymbol{q},\nu) - \chi_s^{-\sigma\sigma}(\boldsymbol{q}+\boldsymbol{Q},\boldsymbol{q}+\boldsymbol{Q},\nu)] G_{-\sigma}^{l-l}(\boldsymbol{k}-\boldsymbol{q},\omega-\nu). \tag{5.66b}$$

$\Sigma_\sigma^{ll'}(\boldsymbol{k},\omega)$ and $G_\sigma^{ll'}(\boldsymbol{k},\omega)$ are the momentum diagonal components of the γ-quasiparticle self-energy and the *dressed* γ-Green's function for band indices $l, l' = \pm 1$ refering to the SDW valence and conduction band, respectively.

The virtue of the limit $U/t \gg 1$ is that, starting from the Hartree–Fock SDW propagator, the iterative solution of Eqs. (5.66b) and (5.66b) leads to a vanishing *interband* self-energy and a vanishing *interband* Green's function. This leaves only the two equations (5.66b) for the *intraband* Green's functions to be solved. Both Green's functions are related by particle–hole symmetry at half-filling as is reflected by the symmetry relation $A_\sigma^{-1-1}(\boldsymbol{k},\omega) = A_\sigma^{11}(\boldsymbol{k},-\omega)$ for the spectral functions $A_\sigma^{ll}(\boldsymbol{k},\omega) = \mathrm{Im}\,[G_\sigma^{ll}(\boldsymbol{k},\omega+i\delta)]/\pi$. Due to the particle–hole symmetry relation we are left with a single integral equation. For the valence band the retarded self-energy has to be determined self-consistently from [53]

$$\Sigma_\sigma^{-1-1}(\boldsymbol{k},\omega+i\delta) = U^2 \sum_{\boldsymbol{q}\neq 0}{}' \left[\left(1+\frac{2J}{\omega_{\boldsymbol{q}}}\right) \int_0^\infty d\omega' \frac{A_\sigma^{-1-1}(\boldsymbol{k}-\boldsymbol{q},\omega')}{\omega_{\boldsymbol{q}}+\omega'+\omega+i\delta} \right.$$

$$\left. + \left(1-\frac{2J}{\omega_{\boldsymbol{q}}}\right) \int_{-\infty}^0 d\omega' \frac{A_\sigma^{-1-1}(\boldsymbol{k}-\boldsymbol{q}],\omega')}{\omega_{\boldsymbol{q}}-\omega'-\omega-i\delta} \right]. \tag{5.67}$$

We discuss the iterative solution of this equation by showing in Fig. 49 the resulting spectral function for fixed momenta $\boldsymbol{k} = (\pi/2,\pi/2)$ and $\boldsymbol{k} = (0,0)$ as obtained on a 16×16 sites lattice. Besides the renormalized quasihole peak, the figures display a considerable shift of spectral weight into a spin wave shakeoff structure below the quasihole energy as well as into the upper conduction band. The loss of spectral weight into the incoherent part is much stronger for the zone center holes than for holes on the boundary of the MBZ.

This behavior is made more explicit in Fig. 50 which shows the quasihole's spectral weight factor $z(\boldsymbol{k})$ together with its dispersion for momenta along a closed path in the MBZ. $z(\boldsymbol{k})$ is obtained from the area under the quasihole peak in the spectral function. A comparison to the Hartree–Fock SDW dispersion demonstrates the significant band narrowing of the polaron band, i.e. the effective mass enhancement from the multiple spin-wave dressing. Most striking is the result that the degeneracy of the Hartree–Fock band dispersion along the MBZ boundary is barely lifted. This means that the Fermi surface shape is hardly changed when compared to the Fermi surface of the non-interacting tight-binding band. The same conclusion has been drawn from the results of QMC simulations [279] and Lanczos diagonalization studies on 4×4 Hubbard clusters [224,100,279].

Although not clearly visible in the figures, the energy maximum of the quasiparticle band occurs at $\boldsymbol{k} = (\pi,0)$. This is a result which arises only on the multi-loop level since for the one-loop calculation of the self-energy the maximum does appear at $\boldsymbol{k}_p = (\pi/2,\pi/2)$. The same result for the one-loop level has also been obtained Singh and Tešanović [374]. The dispersion maximum also remains at $\boldsymbol{k}_p$ when longitudinal χ^{zz} spin and charge fluctuations are included in the one-loop self-energy [442]. Besides the substantial quantitative difference which is demonstrated in Fig. 51

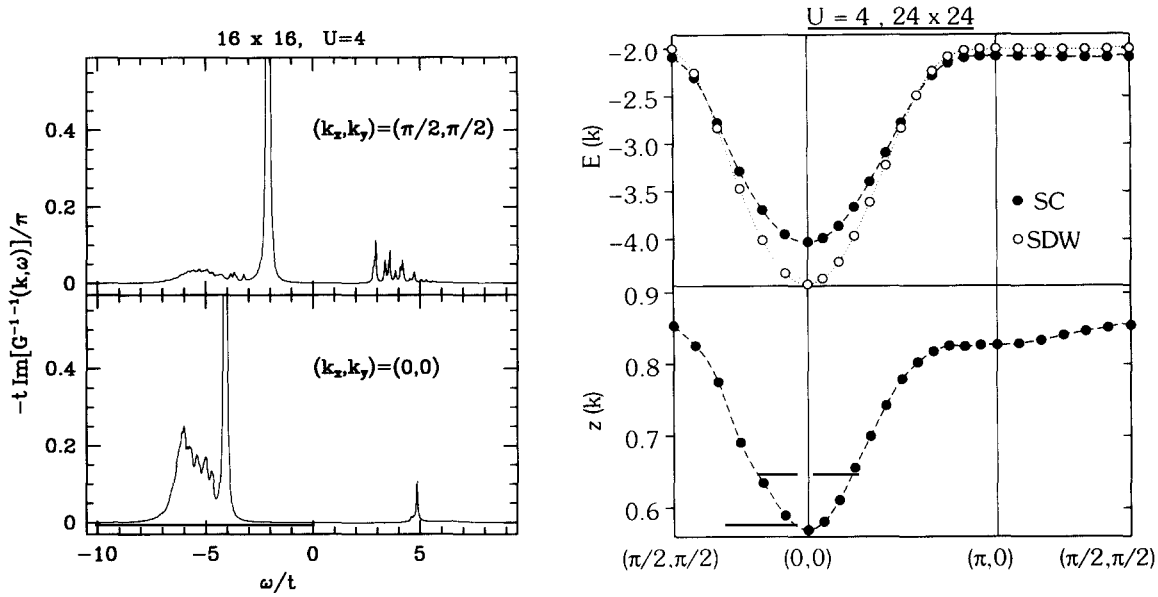

Fig. 49. Single hole spectral function for a moderate value of $U/t = 4$ and the two momenta $\boldsymbol{k} = (\pi/2, \pi/2)$ and $\boldsymbol{k} = (0,0)$ obtained from the self-consistent non-crossing approximation on a 16×16 lattice. Energies are given in units of t. (From Ref. [53]).

Fig. 50. Quasiparticle properties for $U = 4$ on a 24×24 lattice along a closed triangular path in the magnetic Brillouin zone. The upper panel shows the valence band dispersion for the self-consistent non-crossing calculation as compared to the Hartree–Fock SDW dispersion $E(\boldsymbol{k}) = [\epsilon^2(\boldsymbol{k}) + \Delta^2]^{1/2}$ for $2\Delta = U$. The lower panel shows the corresponding quasihole spectral weight factor $z(\boldsymbol{k})$. (From Ref. [53].)

there is another more important qualitative difference between the one- and the multi-loop calculation. The incoherent spectral weight on the low energy side of the quasihole peak in the spectral function Fig. 49 arises only from the coupling to mutiple spin-wave excitations. This incoherent part of the spectrum will be discussed again in more detail below in the context of the t–J model.

5.4.3. Hole motion in a quantum antiferromagnet

The problem of holes doped into a Heisenberg antiferromagnet is clearly one of the key issues that most of the theoretical work has focused on trying to understand the quasiparticle properties in the low doping region of cuprate superconductors. The majority of theoretical model calculations has been performed in one-band models for strong-coupling parameters. In order to contrast some of the related concepts to the SDW scheme discussed in the previous chapter we first consider an analogous polaron picture for the t–J model as earlier proposed by Schmitt-Rink et al. [351]. We choose to discuss this spin-polaron picture for a single hole in more detail because it has proven to give results which are in quantitative agreement with numerical diagonalization studies and allows for a physical description of the hole dynamics in the t–J model [200,255,252,236].

The basic idea in the spin-polaron picture is to treat the exchange interaction in the t–J model in linear-spin-wave (LSW) theory and to represent the hole in terms of a spinless fermion operator[7].

[7] For an outline of the important calculational steps we follow closely the derivation given by Martinez and Horsch [255].

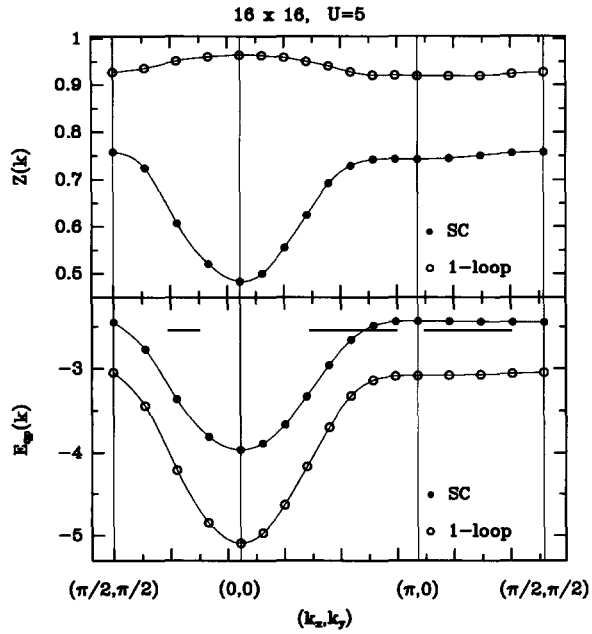

Fig. 51. Comparison of the quasiparticle properties resulting from a single iteration of Eq. (5.67), i.e. the one-loop level, versus the self-consistent non-crossing solution. (From Ref. [53].)

It is convenient to perform first a sublattice rotation on the, say, B sublattice of the antiferromagnet by 180° about the S_x axis. The spin operators on sublattice B are thereby transformed according to

$$S_j^{\pm} \to S_j^{\mp}, \qquad S_j^z \to -S_j^z, \qquad c_{j\sigma} \to c_{j-\sigma}, \quad j \in B, \tag{5.68}$$

creating a ferromagnetic spin alignment in the new reference frame. This removes the further necessity to distinguish between the two sublattices. After the sublattice rotation the t–J Hamiltonian takes the form

$$H_{tJ} = -t \sum_{\langle ij\rangle\sigma} [(1 - n_{i-\sigma}) c_{i\sigma}^{+} c_{j-\sigma} (1 - n_{j\sigma}) + \text{h.c.}]$$

$$+ J \sum_{\langle ij\rangle} [\tfrac{1}{2}\alpha (S_i^{+} S_j^{+} + S_i^{-} S_j^{-}) - S_i^z S_j^z - \tfrac{1}{4} n_i n_j]. \tag{5.69}$$

For later discussion Eq. (5.69) allows for an anisotropic exchange interaction controlled by the parameter α. The Heisenberg (Ising) limit is recovered by $\alpha = 1$ (0). Next, we introduce boson operators a_i^{+}, a_i by means of the Holstein–Primakoff transformation in the LSW approximation

$$S_i^{+} = \sqrt{(1 - a_i^{+} a_i)}\, a_i \sim a_i, \qquad S_i^{-} = a_i^{+} \sqrt{(1 - a_i^{+} a_i)} \sim a_i^{+}, \qquad S_i^z = \tfrac{1}{2} - a_i^{+} a_i. \tag{5.70}$$

Creation operators h_i^{+} for spinless holes, referred to as holons, are defined by $h_i^{+} = c_{i\uparrow}$. Similarly the original fermion operator $c_{i\downarrow}$ is expressed as a composite operator [351] by $c_{i\downarrow} = h_i^{+} S_i^{+}$. It is important to note that this introduction of boson and holon operators enlarges the original Hilbert space of the t–J model which contains only the three states $|\uparrow\rangle$, $|\downarrow\rangle$ and $|0\rangle$ at each site corresponding

to the occupation with a single up- or down-spin electron or a hole. Double occupancy is excluded in the t–J model. In spin-holon notation there is a spin at each site even in the presence of a hole. This is remedied by adding a constraint term to the Hamiltonian of the form

$$H_c = \lambda \sum_i h_i^+ h_i a_i^+ a_i \tag{5.71}$$

which with $\lambda \gg 1$ ensures that there is only one object on each site, either a spin or a hole.

Following these steps of the transformation the resulting Hamiltonian can be diagonalised if the density of holes δ is introduced on the mean-field level by replacing $h_i h_i^+ = (1 - h_i^+ h_i)$ by $(1 - \delta)$. After spatial Fourier transformation this leads to the spin-polaron Hamiltonian [351,200,252,255,236]

$$H_{s-p} = \frac{zt}{\sqrt{N}} \sum_{k,q} [h_k^+ h_k \alpha_q (u_q \gamma_{k-q} + v_q \gamma_k) + \text{h.c.}] + \sum_q \omega_q \alpha_q^+ \alpha_q + E_J^0, \tag{5.72}$$

where $\alpha_q = u_q a_q - v_q a_{-q}^+$ and E_J^0 is a constant energy shift. The spin-wave energy is

$$\omega_q = SzJ(1-\delta)^2 \nu_q = SzJ(1-\delta)^2 \sqrt{1 - (\alpha \gamma_q)^2} \tag{5.73}$$

for spin $S = 1/2$ and with the coordination number $z = 4$ of the square lattice. Eq. (5.73) also defines ν_q in terms of $\gamma_q = \frac{1}{2}(\cos q_x + \cos q_y)$. The coherence factors u_q and v_q are given by the usual expressions familiar from LSW theory:

$$u_q = \sqrt{\frac{1+\nu_q}{2\nu_q}}, \qquad v_q = -\operatorname{sgn} \gamma_q \sqrt{\frac{1-\nu_q}{2\nu_q}}. \tag{5.74}$$

Note that there is no bare kinetic energy term for the spinless fermions in the Hamiltonian Eq. (5.72), but otherwise it resembles closely the polaron Hamiltonian in the electron–phonon problem. The vertex function $M(\boldsymbol{k}, \boldsymbol{q}) = u_q \gamma_{k-q} + v_q \gamma_k$ in Eq. (5.72) describes the coupling of the holons to the spin-wave excitations.

In order to explore the holon properties Martinez and Horsch have calculated the Green's function for a single holon from [255]

$$G_h(\boldsymbol{k}, \omega) = \langle 0 | h_k \frac{1}{\omega - (H_{s-p} - E_J^0)} h_k^+ | 0 \rangle. \tag{5.75}$$

$|0\rangle$ is the vacuum state without holes and with respect to the spin wave operators it is the quantum Néel state

$$|0\rangle_{\text{spin}} = \exp\left(\sum_q \frac{v_q}{u_q} a_q^+ a_{-q}^+ \right) |N\rangle, \tag{5.76}$$

where $|N\rangle$ is the classical Néel state. (Note, however, that the holon Green's function is *not* identical to the Green's function of the original $c_{k\sigma}$ fermion operators. Only in the presence of the two-sublattice structure do the two bear a close resemblance. For a discussion of this issue see Ref. [255].)

The holon Green's function can be calculated self-consistently by the non-crossing diagrammatic series similar to the SDW polaron scheme in the previous chapter. As a result of this so-called

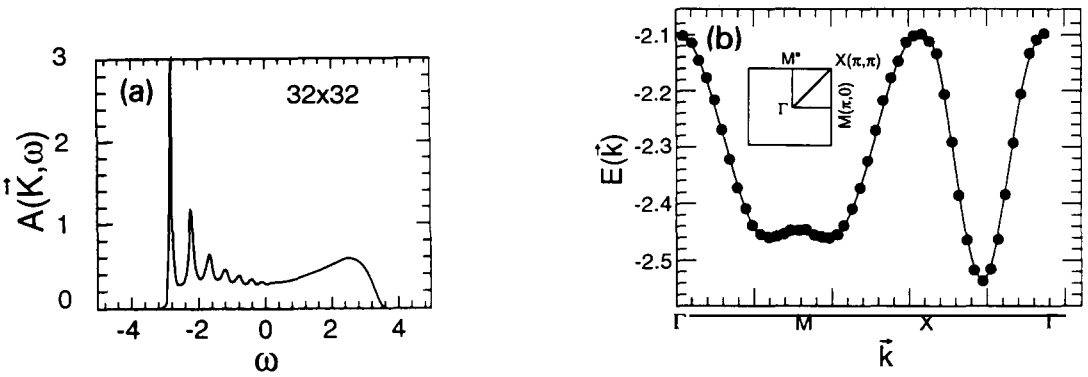

Fig. 52. (a) Single hole spectral function $A(\boldsymbol{k},\omega)$ for momentum $\boldsymbol{k} = (\pi/2,\pi/2)$ in the self-consistent Born approximation for the t–J model with $J/t = 0.1$ on a 32×32 lattice. (b) Hole dispersion for $J/t = 0.2$, plotted along the path $\Gamma \rightarrow M \rightarrow X \rightarrow \Gamma$ in the first Brillouin zone (see inset) of the square lattice. (From Ref. [236].)

self-consistent Born (SCB) approximation the holon self-energy at zero temperature is determined by the equation

$$\Sigma(\boldsymbol{k},\omega) = \frac{z^2t^2}{N}\sum_{\boldsymbol{q}} \frac{M^2(\boldsymbol{k},\boldsymbol{q})}{\omega - \omega_{\boldsymbol{q}} - \Sigma(\boldsymbol{k}-\boldsymbol{q},\omega-\omega_{\boldsymbol{q}})}. \tag{5.77}$$

Several authors have derived the self-consistency equation (5.77) for the holon self-energy and have considered its solution on finite lattices (see e.g. Refs. [255,351,200,236,252]). In the following we disscuss some of the results obtained for the spectral properties of a single hole in the t–J model.

A representative plot of the holon spectral function $A(\boldsymbol{k},\omega)$ is shown in Fig. 52a obtained from solving the SCB equation (5.77) on a 32×32 lattice. A pronounced quasihole peak is located at the low energy side of the spectrum indicating the coherence of the hole motion. The quasihole peak is separated from an incoherent part which is the analog of the spectral weight arising from multiple spin-wave excitations in the SDW based polaron scheme. The dispersion of the hole as obtained from the momentum dependence of the quasihole-peak in $A(\boldsymbol{k},\omega)$ can be modeled by a tight-binding form which includes hopping processes to first- and second-nearest neighbor sites on the same sublattice [255]. This corresponds to the most efficient way a hole can move (with the help of transverse spin fluctuations) leaving the magnetic order along its path undistorted. The minimum of the quasihole band is found to be located at $\boldsymbol{k}_p = (\pi/2,\pi/2)$ (see Fig. 52b). This result of the SCB approximation is in agreement with a series of other approximate analytical and numerical studies (see e.g. Refs. [427,364,342,93,313] and references therein). Despite the apparent agreement on the minimum of the quasihole dispersion from various single-hole model studies in the t–J model the true position of the minimum still remains a subtle quantitative issue. No conclusive answer has yet been obtained from numerical diagonalization studies. (For a discussion of this issue see Ref. [103]).

Useful insight into the physics of the t–J model is gained from the J dependence of the single-hole ground state energy E_{1h}. The result of the SCB calculation for a single hole with momentum $\boldsymbol{k} = (\pi/2,\pi/2)$ on a 4×4 lattice is best fit by the power law [255] $E_{1h}/t = -3.11 + 3.05(J/t)^{0.69}$ in the coupling range $0.1 \leq J/t \leq 1.5$. This result is very close to the exact diagonalization result [399,94] $E_{1h}/t = -3.17 + 2.83(J/t)^{0.73}$. The power law is very intriguing because it tells that the so-called *string* picture applies for the hole motion in quantum antiferromagnets (see also chapter

5.2.1).

This picture is most transparent in the Ising $t-J_z$ limit corresponding to $\alpha = 0$ in the Hamiltonian Eq. (5.69): Suppose a hole is created in an Ising antiferromagnet at a given site of the square lattice. The kinetic energy term in the Hamiltonian makes the hole hop some distance away from its initial position leaving behind a *string* of overturned spins. Pairs of misaligned spins are not healed by quantum fluctuations since S^+S^- terms are absent in the $t-J_z$ Hamiltonian. The number of misaligned spin pairs and therefore the magnetic energy cost grows linearly with the distance d from the hole's initial position creating an effective confining potential for the hole [365,115]. This problem can be solved numerically [365] giving a ground state energy for the hole of $E_{1h} = -2\sqrt{3} + 2.74(J_z/t)^{2/3}$. The energy of excited string states scale as $(J_z/t)^{2/3}$, too.

As we have discussed in chapter 5.2.1 this is not the whole story of the $t-J_z$ model since the more complicated spiraling Trugman-paths [427,428] allow the hole to escape the string potential [427]. Yet, Monte Carlo [28] and exact diagonalization studies [102] have given results for the single hole energy in excellent agreement with the 2/3 power law. Obviously the string picture alone does already contain the important physics for the hole's hopping motion. It is more surprising, though, that also for the t–J model the single hole energy is close to the 2/3 power law which means that even in the presence of transverse spin fluctuations the string picture works. For small J/t the hole can create and retrace a string path on a time scale set by $1/t$ before transverse spin fluctuations cut the string on the longer time scale $1/J$ [94]. Since the energy of the smaller peaks in the incoherent part of the spectral function in Fig. 52 scale with the same power law in J/t in the limit of small J/t, they have been identified as string excitations as well [236].

Finally, we mention the results for the quasihole spectral weight z_k and for the coherent bandwidth of the hole, both are shown in Fig. 53. In the strong coupling, i.e. small J/t, limit the weight of the quasihole peak in the spectral function is strongly suppressed. For $J \to 0$ z_k vanishes with a power law [255,236]. For $J = 0$, $z_k = 0$ and the hole motion is totally incoherent. In the strong coupling limit the holes acquire a large effective mass and the bandwidth for coherent hole motion is no longer proportional to t but rather proportional to J [94,428,314]. These results are important since they suggest that the quasiparticle pole strength of the propagator remains finite for all finite values of J. The holes, though heavily dressed by spin fluctuations, move coherently through the antiferromagnetic background and behave like ordinary quasiparticles with charge e and spin 1/2. Other scenarios have been suggested in favour of a vanishing z_k factor [365]. But they have not found support from the present results, neither from the polaron calculations nor from exact diagonalization studies on small clusters [97].

From the results obtained for a single hole doped into a quantum antiferromagnet one may attempt to describe the case of a finite but small hole density by a gas of noninteracting, spin fluctuation dressed holes in terms of a rigid band picture. This has been done in a first step by Trugman using only the renormalized quasihole dispersion to calculate the magnetic susceptibility and transport coefficients in the relaxation-time approximation [429]. The incoherent contributions to the single-hole propagator have been completely neglected. The temperature and doping dependence of the transport coefficients therefore arises solely from the Fermi surface topology. Inherent in this rigid band scheme is that at low hole concentrations, the Fermi surface in the first Brillouin zone forms four hole pockets centered around the minima of the hole dispersion at $\boldsymbol{k}_p = (\pm\pi/2, \pm\pi/2)$, as

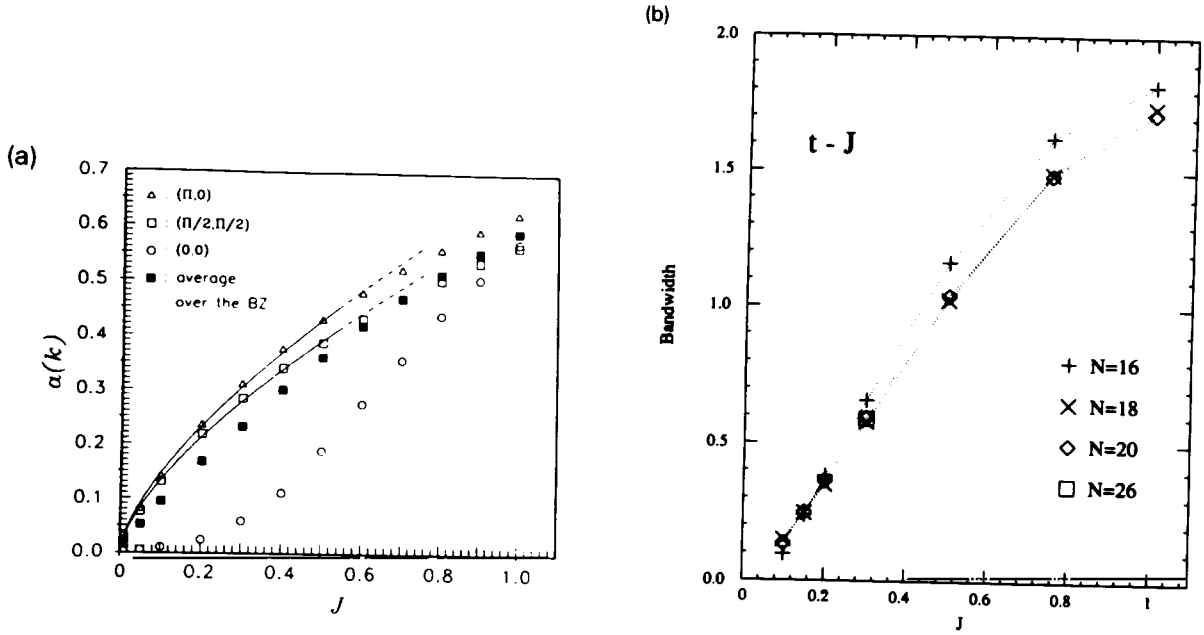

Fig. 53. (a) Quasihole spectral weight z_k [in the figure denoted by $a(k)$] at different k points on a 16×16 lattice in the strong coupling, small J/t regime as obtained from the self-consistent Born approximation. The solid lines represent power law fits $z_k \propto J^{\epsilon}$ with $\epsilon \sim 0.7$. (From Ref. [255].) (b) Coherent bandwidth W for a single hole in the t–J model as a function of J (with $t = 1$) from Lanzcos diagonalization studies for different cluster sizes. (From Ref. [314].)

shown in Fig. 54[8].

Clearly, in the case of hole pockets the Hall coefficient is positive, i.e. hole-like. With adding more holes the pockets grow until they touch at a filling of about 26% holes changing the Fermi surface into electron-like and the Hall coefficient changes sign [429]. Surprisingly, this result agrees qualitatively with the Hall effect data measured in $La_{2-x}Sr_xCuO_4$ [400]. This picture is appealingly simple and bears obviously some resemblance to experimental data, not only for the Hall coefficient but also for the doping dependence of the magnetic susceptibility and the thermopower [429]. Still, it remains dubious that the assumption of a gas of non-interacting holes is justified away from the very low density limit.

The possible appearance of hole pockets in the Fermi surface of the doped t–J model is a subtle and unresolved issue. Generally, in all calculations for the motion of a single hole in a quantum antiferromagnet the hole momentum is found to be $k_p = (\pi/2, \pi/2)$ (see also Refs. [113,428,174]). It is therefore expected that for low hole densities the holes will preferentially occupy momentum states in the vicinity of k_p, eventually forming pockets around k_p and the equivalent momenta in the Brillouin zone. High-temperature expansion studies for the momentum distribution function [378] and exact diagonalization studies with various numbers of holes [388] were, however, unable to detect any signature of hole pockets. Due to the relation of the t–J model to the strong coupling Hubbard model these results appear consistent with the QMC results on small Hubbard clusters [100,279]

[8] Note that the long range antiferromagnetic order is still assumed to be present at finite hole densities. The wave vector (π, π) is therefore a reciprocal lattice vector and the hole pockets appear in the extended magnetic zone scheme.

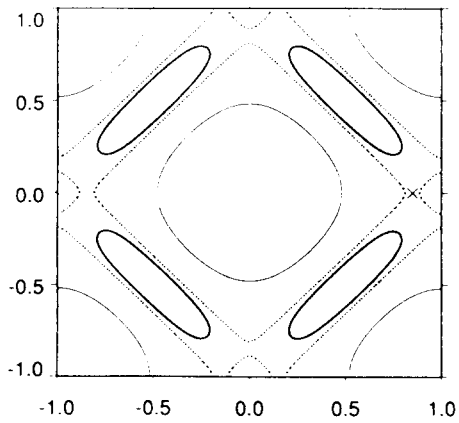

Fig. 54. Fermi surface in the repeated-zone scheme for a gas of non-interacting holes with a spin-fluctuation renormalized bandstructure calculated variationally in the $t-t'-J$ model as defined in chapter 4.2.2). As the hole doping x is varied the Fermi surface has three distinct topologies. For $x < x_1 = 0.26$ it consists of eccentric ellipses (heavy solid line) enclosing quasiholes, for $x_1 < x < x_2$ it consists of two disconnected parts (dashed lines for $x = 0.277$). For $x > x_2 = 0.31$ the Fermi surface is an ordinary closed curve centered at the origin (thin line for $x = 0.66$).(From Ref. [429].)

which show a Fermi surface barely distinguishable from the free tight-binding Fermi surface, which of course does not have any pockets. We will discuss these results in chapter 5.4.7. A similar conclusion has been drawn above from the SDW based polaron scheme.

It remains possible that the hole pockets do exist but are very shallow so that they rapidly merge at very low hole densities, forming a large electron-like Fermi surface. This, however, leaves the problem to explain the positive Hall constant observed in low doped cuprate materials. (For an early discussion of this problem see Ref. [223]). A possible solution to these conflicting issues has been suggested in the work of Dagotto, Nazarenko and Boninsegni [105]. From a Green Function Monte Carlo method for the t–J model they have obtained quasihole bands which are very flat for momenta near the Fermi surface. The near degeneracy of these momentum states provides a hidden small energy scale which is found responsible for a strongly temperature dependent and positive Hall coefficient.

5.4.4. Application to the optical conductivity

One of the outcomes of the model studies for hole motion in a quantum antiferromagnet is the large incoherent contribution in the spectral function arising from the coupling to spin-wave excitations. In turn, when the spin-wave renormalization due to the motion of holes in an antiferromagnet is considered, the incoherent part of the spectrum has been found responsible for a substantial spin-wave softening [207,172,310,141,214]. The magnitude of the softening compares favourably with neutron scattering data for spin-wave excitations in oxygen deficient 123 compounds [339,336]. It is significantly stronger than for the case of a finite density of static vacancies in a Heisenberg antiferromagnet as discussed in chapter 5.1.3.

In the present chapter we will discuss yet another example which underlines the significance of the incoherent part of the spectrum. We will show that it creates oscillator strength in the low-frequency regime of the optical conductivity. Due to the magnetic origin of the incoherent part of the spectrum we will argue that the spin fluctuations give rise to optical absorption for mid-infrared frequencies.

The conductivity describes the current response to an externally applied electromagnetic vector potential. We therefore consider the one-band Hubbard model in the presence of a time-dependent vector potential $A_x(\boldsymbol{r}, t)$ applied in the x-direction, $\boldsymbol{r}$ denotes a site on the square lattice. The presence of the vector potential modifies the hopping term $c^+_{i+x}c_{ix}$ in the kinetic energy by introducing a Peierls phase factor $\exp[ieA_x(\boldsymbol{r}, t)]$. Similarly to the derivation of the Raman scattering intensity in chapter 3.4 the kinetic energy is expanded to second order in $A_x(\boldsymbol{r}, t)$ (units are chosen such that $\hbar = c = 1$ and the lattice constant is set to 1),

$$H^{A_x}_{\text{kin}} = H^{A_x=0}_{\text{kin}} - \sum_i [j^p_x(i)A_x(i,t) + \tfrac{1}{2}e^2 h^x_{\text{kin}}(i)A^2_x(i,t)]. \tag{5.78}$$

Here, j^p_x is the x-component of the *paramagnetic* current-density operator

$$j^p_x(i) = iet\sum_\sigma (c^+_{i+x,\sigma}c_{i,\sigma} - c^+_{i,\sigma}c_{i+x,\sigma}), \tag{5.79}$$

and $h^x_{\text{kin}}(i)$ is the kinetic-energy density associated with the links along the x-direction,

$$h^x_{\text{kin}}(i) = -t\sum_\sigma (c^+_{i+x,\sigma}c_{i,\sigma} + c^+_{i,\sigma}c_{i+x,\sigma}). \tag{5.80}$$

The total physical current is then obtained from $\langle J_x\rangle = -\langle dH^{A_x}/dA_x\rangle$ and contains as usual both, the paramagnetic plus a diamagnetic contribution. The optical conductivity at frequency ω is defined by the linear response of the *total* current to an electric field $E_x(\boldsymbol{q}=0,\omega) = E^0_x e^{-i(\omega+i\delta)t} = i(\omega + i\delta)A_x(\boldsymbol{q}=0,\omega)$. Applying the standard linear response theory to the Hubbard Hamiltonian, containing the kinetic energy in the form Eq. (5.78), we obtain the formula for the complex, frequency-dependent conductivity

$$\sigma_{xx}(z) = (e^2/iz)[C^r_{xx}(z) + \langle H^x_{\text{kin}}\rangle], \qquad z = \omega + i\delta, \quad \langle H^x_{\text{kin}}\rangle = \left\langle (1/N)\sum_i h^x_{\text{kin}}(i)\right\rangle. \tag{5.81}$$

Here $\langle H^x_{\text{kin}}\rangle$ is the expectation value of the kinetic energy per site from hopping along the x-direction. $C^r_{xx}(\omega + i\delta)$ is the retarded current–current correlation function for the paramagnetic current operator $J^P_x = \sum_i j^p_x(i)$,

$$C^r_{xx}(\omega + i\delta) = \frac{i}{N}\int_0^\infty e^{i(\omega+i\delta)t}\,dt\,\langle [J^P_x(t), J^P_x(0)]_-\rangle, \tag{5.82}$$

which has to be evaluated for the Hubbard model in the absence of the external vector potential. The real part of the optical conductivity as obtained from Eq. (5.81) contains the two contributions

$$\operatorname{Re}\sigma_{xx}(\omega + i\delta) = D\delta(\omega) + \sigma_{\text{reg}}(\omega) \tag{5.83}$$

with the Drude weight

$$D = -\pi e^2 \operatorname{Re} C^r_{xx}(\omega \to 0 + i\delta) - \pi e^2\langle H^x_{\text{kin}}\rangle, \tag{5.84}$$

and the regular, finite-frequency part of the conductivity

$$\sigma_{\text{reg}}(\omega) = (e^2/\omega)\operatorname{Im} C^r_{xx}(\omega + i\delta). \tag{5.85}$$

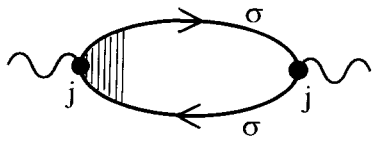

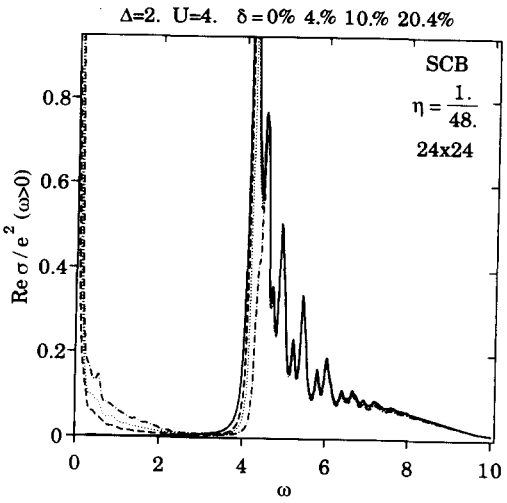

Fig. 55. Schematic diagram for the calculation of the current–current correlation function. Black circles indicate the coupling to the current and the set of vertical lines represents the current vertex function Γ_c.

Fig. 56. Regular part of the optical conductivity evaluated in the SDW based self-consistent polaron scheme extended to finite hole doping (see text). The different curves correspond to hole concentrations δ = 0% (solid line), 4% (dashed line), 10% (dotted line) and 20.4% (dashed-dotted line). This result has been obtained on a 24 × 24 lattice, with a finite imaginary part $i\eta = i/48$ added to the frequency ω for better convergence. (From Ref. [197].)

The regular part σ_{reg} of the conductivity is generally present in both metallic and insulating systems and arises from the electromagnetic field induced transitions to excited states. The Drude weight D of the δ-function at zero frequency is a consequence of the free acceleration of the quasiparticles. This is possible because the Hubbard model is purely electronic and contains no dissipative mechanism, which would e.g. arise in the presence of disorder or from a coupling to phonons (or at finite temperature). For an insulator $D = 0$; a *finite* Drude weight instead characterises a perfect metal or a superconductor [215,346]. $D > 0$ is, however, not sufficient for superconductivity, independently the existence of the Meissner effect has to be verified by evaluating the current response to a transverse static vector potential [346,352] (see also chapter 6.2.1).

We postpone the discussion of superconductivity to chapter 6 and focus now on the charge dynamics of the spin-fluctuation dressed quasiparticles. We begin again with the polaron quasiparticles in the SDW limit of the Hubbard model as introduced in chapter 5.4.2. We calculate the current–current correlation function C_{xx} for the renormalized SDW quasiparticles as represented by the general diagram in Fig. 55.

The result for the current correlator may be written in the form

$$C_{xx}(\omega) = i(1/N)\sum_{k\sigma}\int (d\nu/2\pi)\,\Gamma_c(k,\omega,\nu)$$

$$\times\{[G_\sigma^{11}(k,\nu)G_\sigma^{11}(k,\omega+\nu) + G_\sigma^{-1-1}(k,\nu)G_\sigma^{-1-1}(k,\omega+\nu)]n^2(k,k)$$

$$+ [G_\sigma^{11}(\boldsymbol{k}, \nu) G_\sigma^{-1-1}(\boldsymbol{k}, \omega + \nu) + G_\sigma^{-1-1}(\boldsymbol{k}, \nu) G_\sigma^{11}(\boldsymbol{k}, \omega + \nu)] m^2(\boldsymbol{k}, \boldsymbol{k})]\} \gamma(\boldsymbol{k}). \quad (5.86)$$

Here, $\Gamma_c(\boldsymbol{k}, \omega, \omega')$ is the current vertex function which includes the effects of repeated interactions between excited particle–hole pairs and $\gamma(\boldsymbol{k}) = \partial\epsilon(\boldsymbol{k})\,\partial k_x = 2t \sin k_x$. The coherence factors $m(\boldsymbol{k}, \boldsymbol{k}')$ and $n(\boldsymbol{k}, \boldsymbol{k}')$ are the same as introduced in chapter 5.2.1, Eq. (5.22). In Eq. (5.86) we have omitted already those terms which involve the interband Green's functions $G^{-1,1}$ and $G^{1,-1}$ because in the following we will use the SDW polaron results in the large U/t limit for which the Green's function matrix $G^{ll'}$ becomes diagonal. Furthermore, we will neglect vertex corrections which amounts to the replacement of $\Gamma(\boldsymbol{k}, \omega, \nu)$ by $\gamma(\boldsymbol{k})$. Assuming that the SDW order is approximately preserved for a small but finite hole density we introduce a finite chemical potential into the Green's functions G^{ll}. This is somewhat similar to a rigid band calculation, but we emphasize that the Green's functions contain the full incoherent background contributions from the spin-fluctuation dressing.

The results of this calculation are shown in Fig. 56 for the regular part of the optical conductivity at different hole doping concentrations δ. At half-filling, $\delta = 0$, there is a gap to optical excitations across the insulating energy gap of the renormalized SDW state. For finite δ oscillator strength appears inside the gap. The corresponding spectral weight is removed from the high-energy interband contributions and shifted to low frequencies. In fact, the optical absorption at low frequencies is entirely due to the spin fluctuation dressing of the quasiparticles, i.e. the incoherent part of the propagator. Coherent particle–hole excitations in the valence band at finite hole doping contribute only to the zero-frequency Drude weight. In a rigid band picture for the Hartree–Fock SDW quasiparticles the regular part of $\mathrm{Re}\,\sigma(\omega)$ would therefore contain only high-energy interband contributions. We may therefore directly identify the low frequency optical conductivity with the spin fluctuations accompanying the doped holes. The sharpness of the peak near $\omega = 0$ in Fig. 56 (which is *not* the Drude δ-function contribution omitted in this plot of σ_{reg} for frequencies $\omega > 0$) is a density of states effect and due to the flat quasiparticle dispersion along the magnetic Brillouin zone boundary (see the discussion in chapter 5.4.2 and Fig. 50).

To justify the qualitative relevance of these results to the measured optical conductivity in the normal state of lightly doped cuprates we show in Fig. 57a Uchida et al.'s data for the evolution of $\sigma(\omega)$ with doping in a sample series of $La_{2-x}Sr_xCuO_4$ between $x = 0$ and $x = 0.34$ [434]. Undoped La_2CuO_4 has a charge transfer gap of about $\sim$ 1.5–2 eV. For finite, small x the optical conductivity above $\sim$ 1.5 eV is reduced and a new feature grows at about 0.5 eV. This feature has been called the mid-infrared (MIR) band. The reported integrated conductivity in $La_{2-x}Sr_xCuO_4$ up to 4 eV remains approximately constant showing that oscillator strength is redistributed from the charge-transfer excitations to lower energies. At low x the MIR band is clearly distinct from a far-infrared Drude-like band peaked at $\omega = 0$. With increasing x the far infrared absorption increases rapidly and merges with the MIR band.

Similar MIR band absorption is observed in a number of other doped cuprates as well, as e.g. in the electron doped 214 compounds [434,90] or in the 123 materials [302,190]. (For a recent review on optical properties in cuprate superconductors see Ref. [414].) It is tempting to assume that the MIR band in the optical conductivity is common to all doped cuprate materials and related to the dressed, mobile charge carriers. However, it may often be masked by other sources for optical absorption in the infrared energy range. In this respect Uchida et al.'s data in Fig. 57a provide an exceptionally clean example for the MIR band and its evolution with doping.

A measure of the spectral weight transfer with doping in the optical conductivity used in the

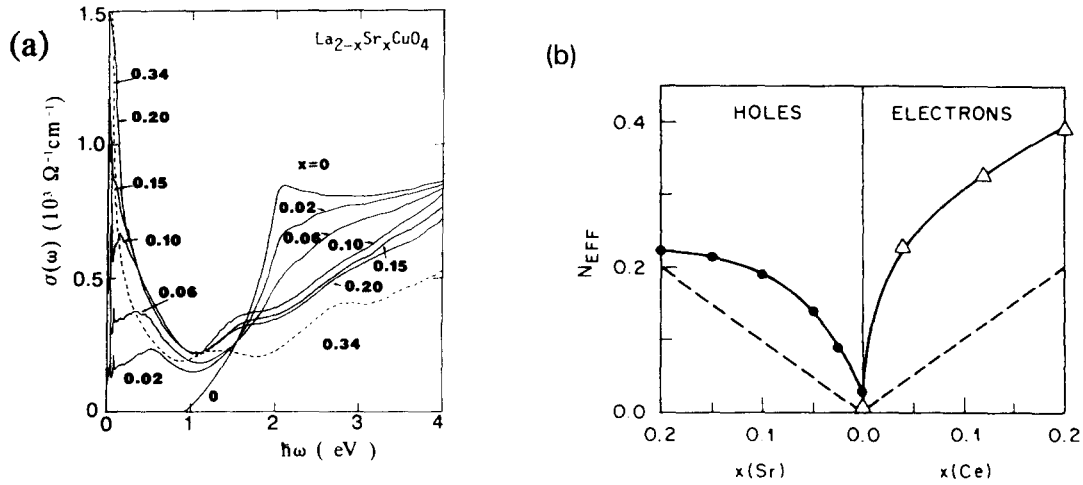

Fig. 57. (a) Frequency dependence of the optical conductivity for a sample series of $La_{2-x}Sr_xCuO_4$ at a temperature of 300 K obtained from the Kramers–Kronig transformation of $\boldsymbol{E} \perp \boldsymbol{c}$ spectra. (From Ref. [434].) (b) The total integrated spectral weights of the optical conductivities in both $Pr_{2-x}Ce_xCuO_4$ (△) and $La_{2-x}Sr_xCuO_4$ (•) up to $\omega = 1.5$ eV, plotted as a function of concentration x. N_{eff} is the effective carrier density as defined in the text below. The dashed lines represent the anticipated spectral weight contributions from Ce or Sr substitution alone, assuming an effective mass $m^* = m_e$ and that each Ce or Sr atom donates one mobile carrier/unit cell. (Figure taken from Ref. [90].)

analysis of experimental data [434,90] is a normalised effective carrier density N_{eff} defined by

$$N_{\text{eff}}(\omega) = \frac{2m_e V_{\text{cell}}}{\pi e^2} \int_0^{\omega} \text{Re}\,\sigma(\omega')\, d\omega', \tag{5.87}$$

where e and m_e are the bare electronic charge and mass, respectively, and V_{cell} is the unit cell volume. The significance of N_{eff} may be appreciated from the sum rule for the conductivity

$$\frac{2m_e}{\pi e^2} \int_0^{\infty} \text{Re}\,\sigma(\omega)\, d\omega = n \tag{5.88}$$

with n the total density of electrons. As shown in Fig. 57b N_{eff}, with $\sigma(\omega)$ integrated to the charge transfer gap edge ~ 1.5 eV has been found to rise more rapidly than expected from the doped carrier density alone in both electron- and hole-doped 214 compounds [434,90]. The excess contribution to N_{eff} is therefore a direct measure of the absorption in the MIR band which arises in addition to the Drude-like free carrier part in $\sigma(\omega)$ near $\omega = 0$.

The calculations of the conductivity from spin-fluctuation dressed quasiparticles are suggestive for a magnetic origin of the MIR band. This assertion has already been made earlier from exact diagonalization studies for the one-band Hubbard model [98] and the t–J model [355,387,280,312]. As an example we show in Fig. 58A results for the optical conductivity for the Hubbard model on a 4×4 lattice with $U/t = 10$ [98]. In particular the appearance of the MIR band in the t–J model is significant since this result ascertains that it is not related to charge excitations but results from the spin fluctuations. Importantly, the presence of the MIR band is a 2D effect since it is absent in the 1D t–J model [387].

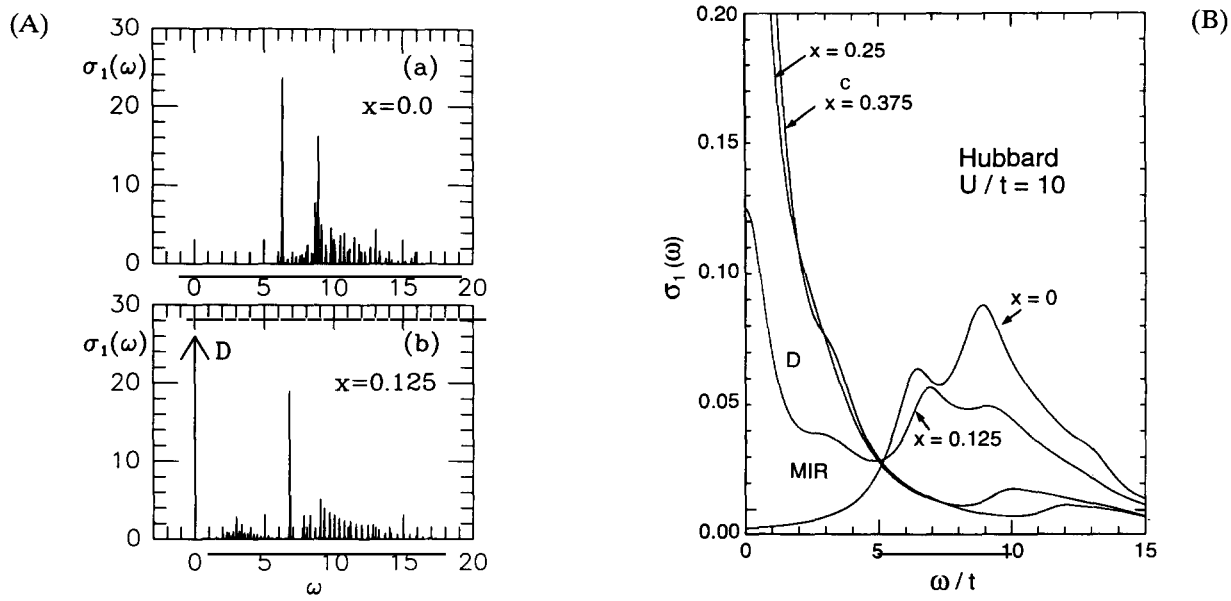

Fig. 58. (A) The real part of the optical conductivity $\sigma_1(\omega)$ for a 4×4 Hubbard cluster with $U/t = 10$ and band fillings (a) $x = 0$ (half-filled band) and (b) $x = 0.125$. A small shift from the real-frequency axis was used ($\delta = 0.01t$) to plot the individual δ-functions of the finite system. The Drude peak at $\omega = 0$ is included only for illustration, its intensity in the figure is *not* proportional to its real magnitude. The MIR band is clearly visible in the doped case, centered around $\omega \sim 3t$. (From Ref. [98].) (B) Same as in (A) for different hole doping concentrations but with a large broadening $\delta = t$. (From Ref. [103].)

The comparison of the exact diagonalization results to Uchida's experimental data becomes striking when the individual δ-functions in the spectrum are broadened to a width of the order of t. The corresponding result of Dagotto [103] for the optical conductivity is shown in Fig. 58B for different hole concentrations. For $U/t = 10$ the result resembles closely the experimental data for hole and electron doped 214 materials. In addition, the low-frequency part of $\sigma(\omega)$ has been found in this analysis to follow a power law $\sigma(\omega) \sim \omega^{-1}$ for $x = 0.25$ and $x = 0.375$ in the frequency range $t < \omega < 5t$. This agrees remarkably with the experimental observation that the decrease in the normal state conductivity is closer to ω^{-1} than to ω^{-2} as would be expected for a free carrier Drude contribution [335].

5.4.5. Pseudogap: RPA in the paramagnet

The preceding chapters have dealt with the problem of holes moving in an ordered (or nearly ordered) antiferromagnetic environment. As we have seen the specific spectral properties of doped holes arise from the coupling to strong spin fluctuations in the vicinity of the magnetic instability. On the other hand the spin-fluctuation dressing of quasiparticles or holes is expected to become less important in the large doping limit. In the present chapter we will take this weakly correlated limit as a starting point to ask how the growing magnetic correlations begin to influence the single particle properties when the electron density is increased to the vicinity of the magnetic instability [192,195].

Starting from the weak U and low density limit it is appropriate to consider the self-energy from

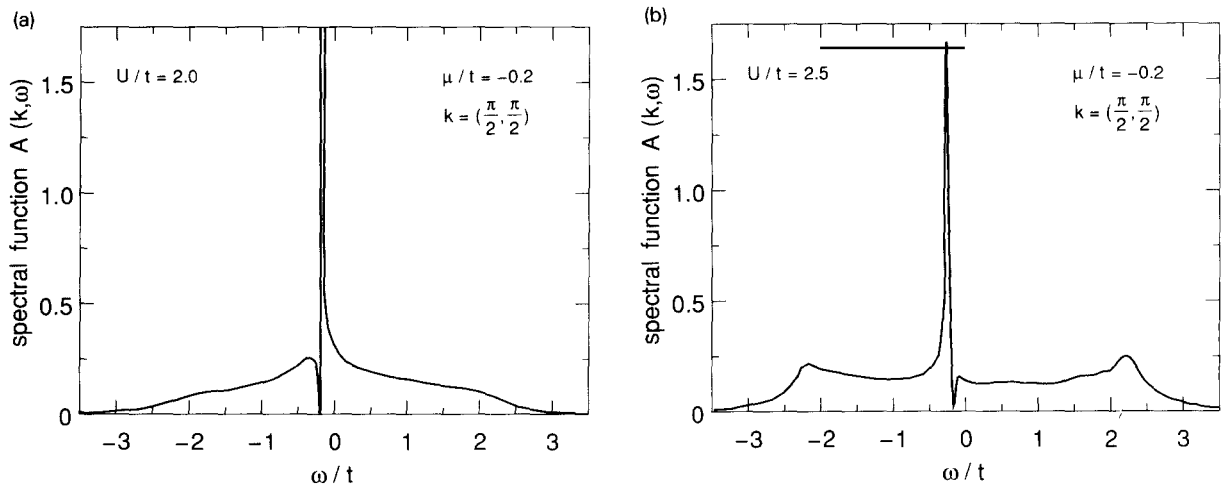

Fig. 59. Spectral function $A(\boldsymbol{k}, \omega)$ for the Hubbard model in the RPA approximation for the self-energy Eq. (5.89). The momentum is $\boldsymbol{k} = (\pi/2, \pi/2)$. For fixed chemical potential the spectral function is shown for (a) $U/t = 2$ and closer to the magnetic instability for (b) $U/t = 2.5$. (Note that the quasiparticle peak has moved below the chemical potential μ, an effect related to the omission of the Hartree term in the self-energy which will renormalize the value of μ.) (From Ref. [191].)

the RPA ladder and bubble diagram series in the paramagnetic state of the one band Hubbard model (here written without the Hartree term),

$$\Sigma(\boldsymbol{k}, \omega) = -i\frac{1}{N}\sum_{q}\int \frac{d\nu}{2\pi} G_0(\boldsymbol{k}-\boldsymbol{q}, \omega-\nu)\chi_{\mathrm{RPA}}(\boldsymbol{q}, \nu), \tag{5.89}$$

$$\chi_{\mathrm{RPA}}(\boldsymbol{q}, \nu) = \frac{U^2\chi_0(\boldsymbol{q}, \nu)}{1-U^2\chi_0^2(\boldsymbol{q}, \nu)} + \frac{U^3\chi_0^2(\boldsymbol{q}, \nu)}{1-U\chi_0(\boldsymbol{q}, \nu)}. \tag{5.90}$$

$G_0(\boldsymbol{k}, \omega)$ and $\chi_0(\boldsymbol{q}, \omega)$ are the free electron propagator and particle–hole bubble for the nearest-neighbor tight-binding dispersion, respectively, as introduced in previous chapters. We know that the RPA series carries an unphysical magnetic instability for finite U and electron densities away from half-filling. Yet, we may push the parameters in the RPA form of the self-energy Eq. (5.89) to near the instability by either changing the filling (or equivalently the chemical potential) or the coupling U/t and follow the changes in the single particle properties.

Fig. 59 shows the spectral function $A(\boldsymbol{k}, \omega) = (1/\pi)\mathrm{Im}|G(\boldsymbol{k}, \omega+\mu)|$ obtained with the RPA self-energy correction Eq. (5.89) for the propagator $G(\boldsymbol{k}, \omega) = [\omega - \epsilon_{\boldsymbol{k}} - \Sigma(\boldsymbol{k}, \omega)]^{-1}$. Away from the magnetic instability, the spectral function in Fig. 59a for $U/t = 2$ has the conventional Fermi liquid behavior with a dominant sharp quasiparticle peak near the Fermi energy and a featureless incoherent background. For the same fixed chemical potential Fig. 59b shows the corresponding spectral function for a larger value of U/t, i.e., closer to the magnetic instability. The quasiparticle peak has lost spectral weight, and in addition the incoherent background develops two broad peak structures nearly symmetrically above and below $\omega = 0$. This redistribution of spectral weight continues with further increasing U/t. The peak features in the incoherent part of the spectrum grow and will ultimately develop into the sharp quasiparticle peaks of the valence and conduction bands of the spin-density-

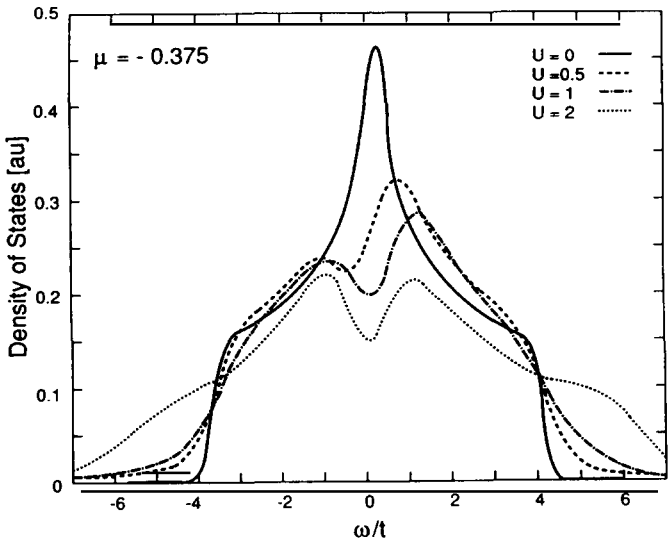

Fig. 60. Pseudogap formation in the density of states of the one-band Hubbard model calculated with the RPA self-energy correction Eq. (5.89) at fixed chemical potential $\mu/t = -0.375$ for different values of U/t. Plotted in this figure is $N(\omega+\mu)$. (Note that the logarithmic singularity for $U = 0$ is broadened due to a small finite imaginary part added to the frequency.) (From Ref. [192].)

wave state. Clearly, the RPA self-energy would be pushed too far to explore this most interesting regime near the Mott–Hubbard metal–insulator transition, but already on this level remarkable changes in the spectrum are observable.

The appearance of the broad peak structures in the spectral function and the accompanying redistribution of spectral weight leads to the development of a pseudogap in the density of states $N(\omega) = (1/N)\sum_{\boldsymbol{k}} A(\boldsymbol{k}, \omega)$ as shown in Fig. 60. This is an immediate consequence of the quasiparticles near the Fermi surface loosing spectral weight to the developing upper and lower SDW bands. The changes in the spectrum lead to a smooth evolution from Fermi liquid to pseudogap behavior. The source of these qualitative changes in the spectrum can be traced to the enhanced large momentum scattering from AF spin fluctuations near the magnetic instability where $\chi_{\mathrm{RPA}}(\boldsymbol{q}, \omega)$ develops a large peak near $\boldsymbol{Q} = (\pi, \pi)$ [192].

If the dynamic spin susceptibility $\chi(\boldsymbol{q}, \omega)$ varies slowly on the scale of the Fermi momentum and the Fermi energy – a situation appropriate for U small compared to the bandwidth – the familiar mass renormalization of Fermi liquid theory is obtained. As U increases χ becomes peaked as a function of $\boldsymbol{q}$ near $\boldsymbol{Q} = (\pi, \pi)$ and its characteristic frequency is reduced from the Fermi energy to the spin-fluctuation energy. It is in this regime when the one-particle spectral weight begins to develop the two new peak structures, rather than the one peak of conventional Fermi liquid theory whose weight vanishes as antiferromagnetic order sets in.

More about the qualitative details of the large momentum scattering has been learned from a model study [193] in which the RPA susceptibility is replaced by a Lorentzian centered at the AF wavevectors $\boldsymbol{Q} = (\pm\pi, \pm\pi)$. If χ is sharply peaked at $\boldsymbol{Q}$, "backward scattering" contributions to the self-energy dominate. They are positive for electrons and negative for holes. The resulting changes in the real part of the self-energy at frequencies away from the Fermi energy are found to be responsible

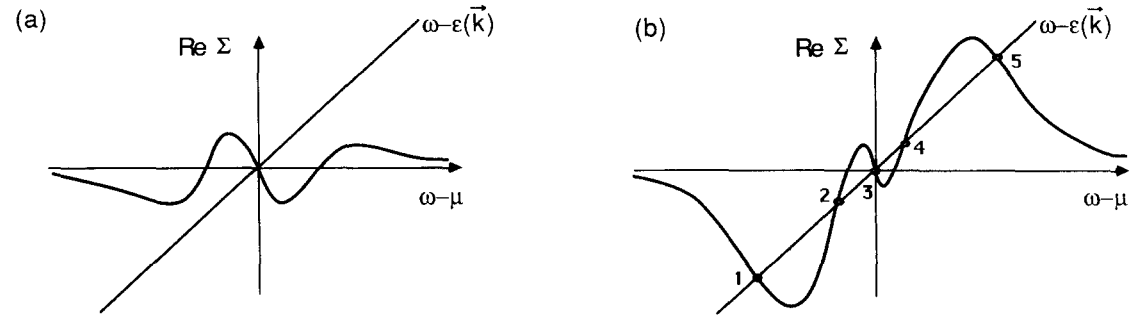

Fig. 61. Qualitative behavior of the real part of the self-energy in the (a) Fermi liquid and (b) the pseudogap regime. Indicated is also the graphical solution of the equation $\omega - \epsilon_k - \mathrm{Re}\,\Sigma(k,\omega) = 0$. (From Ref. [193].)

for the development of the two new peak structures in the spectral weight function. This is shown schematically in Fig. 61. In the conventional Fermi-liquid regime (Fig. 61a) we find one solution of $\omega - \epsilon_k - \mathrm{Re}\,\Sigma(k,\omega) = 0$ leading to a single quasiparticle peak in $A(k,\omega)$. In the pseudogap regime with finite range AF spin correlations changes in the self-energy lead to additional solutions of $\omega - \epsilon_k - \mathrm{Re}\,\Sigma(k,\omega) = 0$. Still, the spectral function evolves smoothly due to the presence of the imaginary part of Σ. In Fig. 61b the solutions 1 and 5 correspond to the developing valence and conduction band of the SDW state, solution 3 still describes the quasiparticle that was present in the weakly correlated Fermi liquid in Fig. 61a. The solutions 2 and 4 are accompanied by a large imaginary part of Σ and contribute only to the incoherent background of the spectral function.

Extended self-consistent calculations, using the RPA as well as the model susceptibility, have shown that the pseudogap development is weakened when dressed Green's functions are used in the calculation of the self-energy [191]. But we will see in following chapters that a pseudogap feature is also present in more elaborate calculational schemes. The pseudogap development may deserve more work in the future to clarify its role for the Hubbard model when doped slightly away from half-filling.

5.4.6. *Conserving approximations, FLEX*

One direction to improved results for the renormalized quasiparticle properties in the Hubbard model has been based on self-consistent conserving approximation schemes. These calculations follow a method which was originally devised by Baym and Kadanoff [35]. Conserving approximations guarantee that microscopic conservation laws for particle number, energy and momentum are automatically fulfilled. One such approximation scheme which has been found to be computationally tractable for the 2D Hubbard model is the fluctuation-exchange-approximation (FLEX) worked out in detail by Bickers and Scalapino [40]. The basic step in this approach is to derive the single-particle self-energy Σ or the irreducible vertex part Γ of two-particle correlation functions by functional differentiation of an approximate free energy functional $\Phi(G)$,

$$\Sigma = \delta\Phi/\delta G, \qquad \Gamma = \delta\Sigma/\delta G. \tag{5.91}$$

In the FLEX approximation the free energy functional Φ is taken as the sum of ring diagrams shown in Fig. 62 which account for the interaction of electrons with spin, density and two-particle fluctuations. The fermion lines in Fig. 62 represent fully dressed Green's functions which have to be determined

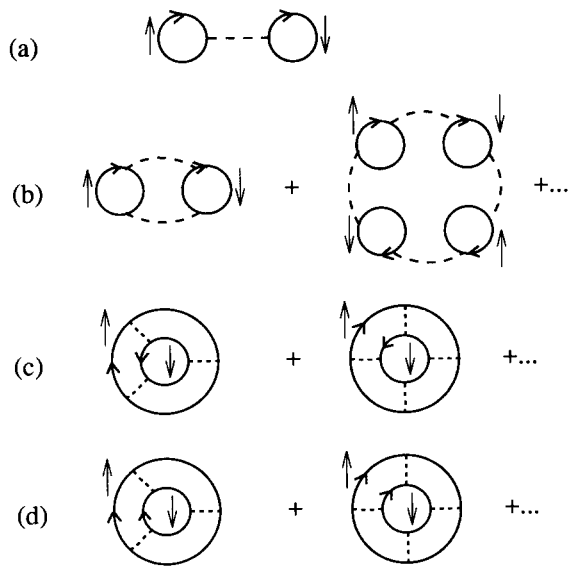

Fig. 62. Hubbard model diagrams for the fluctuation-exchange-approximation (FLEX). The interaction U is represented by a dashed line. (a) Lowest order Φ diagram, (b) Φ ring diagrams representing the interaction of longitudinal-spin and density fluctuations, (c) transverse spin fluctuations, and (d) particle-particle fluctuations. (Figure reproduced from Ref. [40].)

self-consistently. The Green's and correlation functions generated in this way are consistent with Luttinger's theorem and lead to Fermi liquid behavior at low temperatures (see also Ref. [356]).

The solution of the FLEX equations and their extensions [41,454,455,320] is very involved and relies heavily on computer power. As with the simple RPA calculations their accuracy is often judged from the comparison to available QMC results. One important outcome of the conserving approximation calculations by Wermbter and Tewordt [454] is that for weak to intermediate couplings vertex corrections give negligibly small corrections to the RPA spin susceptibility – supporting the conjecture discussed in chapter 5.3.2. However, the feedback effect of the self-energy correction on the RPA spin susceptibility is quite large. As mentioned in the previous chapter, this weakens the pseudogap formation, but a remnant of the pseudogap dip in the density of states has still been found to survive a self-consistent conserving approximation scheme [455].

5.4.7. Numerical results (QMC, Lanczos)

We close the chapter on single particle properties with a brief look on the spectrum obtained from finite cluster studies for the Hubbard model. Lanczos diagonalizations are restricted to 4×4 lattices, while quantum Monte Carlo (QMC) calculations have been extended to larger lattices of up to 16×16 sites. The finite temperature QMC algorithms provide results on the imaginary-time axis or equivalently on a discrete set of Matsubara frequencies for the measurement of Green's functions or susceptibilities, and they have to face the additional problem of the analytic continuation to the real frequency axis. While the recent application of the maximum entropy method [371] promises some progress to circumvent this problem, an annoying minus-sign problem still restricts the parameter sets for which reliable results are available with the presently existing computer power. Unfortunately,

this problem is most severe in the most interesting regime of low doping, strong coupling and low temperature. Small cluster studies, however, provide in principal exact results and have proved to be very valuable, in particular in the field of correlated electron theory where rigorous results in space dimensions $1 < D < \infty$ are rare. In this article we have not discussed the methods themselves or their limitations, but rather we have focused on the results they have provided for the Hubbard model and on the anticipated relevance for the physics of cuprate superconductors. In the remainder we will continue to do so and discuss numerical results for the spectrum of the single-band Hubbard model. (For recent comprehensive overviews on the QMC methods and their application to many-body problems we refer the reader to the review articles of von der Linden [231] and Dagotto [103] and the references therein.)

In order to avoid the complications still involved in the analytic continuation of QMC data we select for our discussion the exact results obtained from the diagonalization of 4×4 Hubbard clusters [100,236,126]. The Lanczos diagonalization method provides the exact eigenenergies $E_n^{N_e}$ and eigenfunctions $|\Psi_n^{N_e}\rangle$ for the system with N_e electrons. Or alternatively, the algorithm can be used to determine the coefficients of a continued fraction expansion of the single-particle Green's function (see e.g. Ref. [94]). The spectral functions – $A_\sigma^{(+)}(\boldsymbol{k}, \omega)$ for adding an electron with spin σ, momentum $\boldsymbol{k}$ and energy ω to the ground state and $A_\sigma^{(-)}(\boldsymbol{k}, \omega)$ for removing an electron from the ground state – are given by

$$A_\sigma^{(+)}(\boldsymbol{k}, \omega) = \frac{1}{N} \sum_n |\langle \Psi_n^{N_e+1} | c_{k\sigma}^+ | \Psi_0^{N_e} \rangle|^2 \, \delta(\omega - (E_n^{N_e+1} - E_0^{N_e})),$$

$$A_\sigma^{(-)}(\boldsymbol{k}, \omega) = \frac{1}{N} \sum_n |\langle \Psi_n^{N_e-1} | c_{k\sigma} | \Psi_0^{N_e} \rangle|^2 \, \delta(\omega + (E_n^{N_e-1} - E_0^{N_e})). \tag{5.92}$$

In angular resolved (AR) experiments, $A_\sigma^{(-)}(\boldsymbol{k}, \omega)$ is measured by photoemission (PES) and $A_\sigma^{(+)}(\boldsymbol{k}, \omega)$ by inverse photoemission spectroscopy (IPES), respectively. The corresponding densities of states (DOS) are obtained from summing over all momenta and spin

$$N^{\pm}(\omega) = (1/N) \sum_{k,\sigma} A_\sigma^{(\pm)}(\boldsymbol{k}, \omega). \tag{5.93}$$

Exact results of the DOS for $U/t = 8$ obtained by Dagotto, Ortolani and Scalapino for the 4×4 Hubbard cluster [100] are shown in Fig. 63. The particle–hole symmetric DOS at half-filling (Fig. 63a) shows the clear gap of the magnetically ordered, insulating ground state. The large structures near the gap edges result from the quasiparticles which form the upper and lower Hubbard band. The additional structure in the DOS above and below the quasiparticle band features results from the incoherent spin-fluctuation shakeoffs as discussed in the previous chapters.

Fig. 63b shows the corresponding DOS in the presence of two doped holes [100]. The effect of the doped holes amounts to a redistribution of spectral weight from the upper and lower Hubbard bands of the insulators to near the upper edge of the lower Hubbard band. New spectral weight has been created in the gap of the insulating state, but a pronounced pseudogap feature remains. The quasiparticle dispersion is found to follow closely the simple tight-binding form for nearest-neighbor hopping on the square lattice. The bandwidth of the quasiparticle bands is, however, strongly reduced by about 50%.

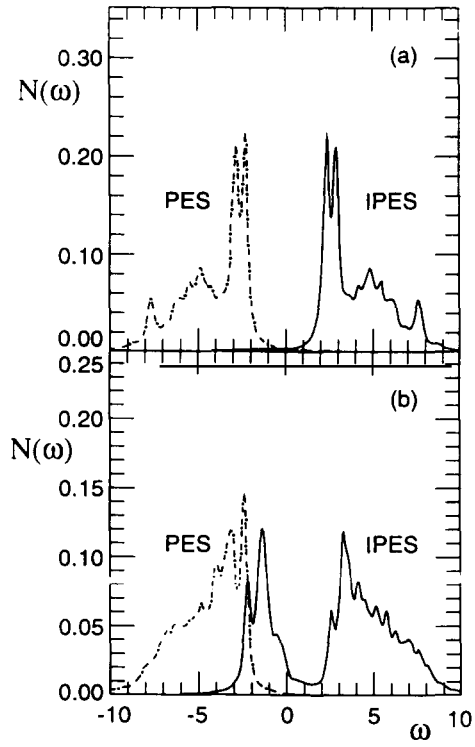

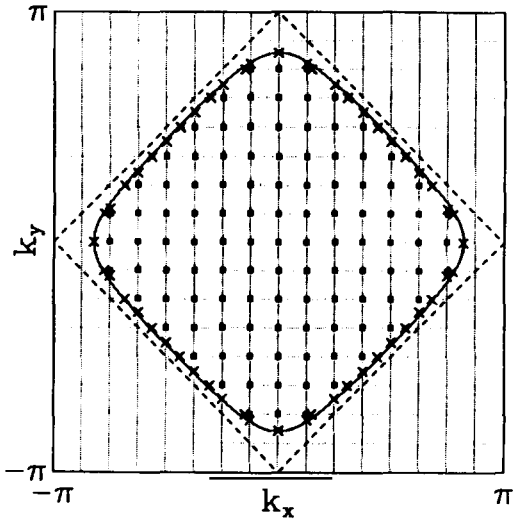

Fig. 63. Density of states from Lanczos calculations for the Hubbard model with $U/t = 8$ on a 4×4 lattice, at (a) half-filling, $\langle n \rangle = 1$ with the chemical potential at $\mu = 0$, and (b) for a hole-doped case, $\langle n \rangle = 0.875$ with $\mu/t = -2.4$. The solid and dashed–dotted lines mark the IPES and the PES parts of the spectrum, respectively. (Results from Ref. [100], figure taken from Ref. [103].)

Fig. 64. The figure shows the allowed $\boldsymbol{k}$ points in the Brillouin zone for a 16×16 lattice. The solid squares mark $\boldsymbol{k}$ points at which $\langle n_{\boldsymbol{k}} \rangle > 0.5$ for a band-filling of $\langle n \rangle = 0.87$ with $U/t = 4$ and $T = t/6$. Extrapolating the QMC data for $\langle n_{\boldsymbol{k}} \rangle$ on the 16×16-sites lattice to the points in the Brillouin zone where $\langle n_{\boldsymbol{k}} \rangle$ would equal 0.5 gives the crosses ($\times$). The solid line is the noninteracting ($U = 0$) Fermi surface for $\langle n \rangle = 0.87$ and the dashed line is the noninteracting Fermi surface for the half-filled band $\langle n \rangle = 1$. (From Ref. [279].)

The persisting approximate tight binding form of the dispersion in the presence of the interaction already implies that the Fermi surface remains essentially unchanged by the Hubbard interaction term, and agrees with the QMC results of Moreo et al. for the momentum distribution function [279]

$$\langle n_{\boldsymbol{k}} \rangle = T \sum_{n} \exp(-i\omega_n 0^-)\, G(\boldsymbol{k}, i\omega_n). \tag{5.94}$$

(0^- represents an infinitesimal number less than zero.) Note that $\langle n_{\boldsymbol{k}} \rangle$ does not suffer the analytic continuation problem and is obtained from the single-particle Green's function $G(\boldsymbol{k}, i\omega_n)$ at the discrete set of Matsubara frequencies $\omega_n = (2n + 1)\pi T$. The approximate form of the Fermi surface on a 16×16 lattice has been obtained [279] by mapping the momenta for which $\langle n_{\boldsymbol{k}} \rangle > 0.5$ (see Fig. 64). In particular, no indication of Fermi surface pockets has been found for $U/t = 4$.

Clearly, the redistribution of spectral weight in the DOS with doping is beyond the scope of any

rigid band approximation. The PES part of the spectrum in Fig. 63 has shrunk due to the reduced number of electrons. Importantly, the chemical potential has moved across the gap into the spectral range of the former lower Hubbard band. This is a significant result since there is no obvious way to reconcile this with some of the results of photoemission experiments. Photoemission data have found the chemical potential to remain pinned and hole doping to basically fill in spectral weight into the gap of the insulator [8,77,334]. Other sources, not included in the Hubbard model, may be responsible for the discrepancy with these experimental results. Contrary experimental results, however, have been reported from valence- and core-level spectroscopy which show instead a rather large shift of the chemical potential [440] which are much closer to the results for the one band-Hubbard model. The clarification of these problems remains a challenge for future work.

6. Pairing from antiferromagnetic spin fluctuations

In the final chapter we will discuss the possibility of a magnetic pairing mechanism for high-temperature superconductivity. In several instances in the previous chapters we have found that the 2D Hubbard model – one-band or three-band – appears to represent some of the essential features relevant to the physics of the CuO_2 planes in the cuprate superconductors. In particular, the Hubbard model is doing well in describing the magnetic properties. The obvious question to ask is whether the Hubbard model has a superconducting ground state, at least in some parameter range, despite the fact that it contains only repulsive interactions between the electrons. A lot of efforts have been devoted to answer this question, especially with powerful computational techniques. So far, no convincing quantum Monte Carlo evidence has been found for superconductivity in the Hubbard model. This may either mean that the electrons in the Hubbard model do not superconduct at all, or that the presently available numerical techniques are not accurate enough to find the presumably weak signals of superconductivity. The corresponding numerical results for the t–J model are more promising, in particular for electron densities and couplings in the vicinity of phase separation [101,102]. Generally in the one-band models, the dominant enhancement in the pair-field susceptibilities, as an indicator for superconducting correlations, occurs in the $d_{x^2-y^2}$ channel. As discussed in chapter 3.6, this symmetry for the gap function in the superconducting state has been found compatible with a number of experimental observations. This points to a possible electronic origin of high-temperature superconductivity and motivates the subsequent detailed discussion of the pairing correlations in the Hubbard model.

6.1. Spin-fluctuation-exchange mechanism

An early suggestion that AF spin fluctuations could give rise to singlet $d_{x^2-y^2}$-wave pairing in the cuprate superconductors was already made in 1987 by Bickers, Scalapino and Scalettar [39], i.e. one year after the pioneering discovery of Bednorz and Müller [36] was published. The early suggestion of d-wave pairing in the cuprates was based upon previously developed ideas of d-wave pairing near a spin-density-wave instability in heavy fermion superconductors [345]. Similar ideas were developed simultaneously by Miyake et al. [270]. The first calculations for this problem which hereafter took into account the full frequency and momentum dependence of the spin-fluctuation mediated pairing interaction were carried out based on the FLEX approximation to the Hubbard model (see chapter

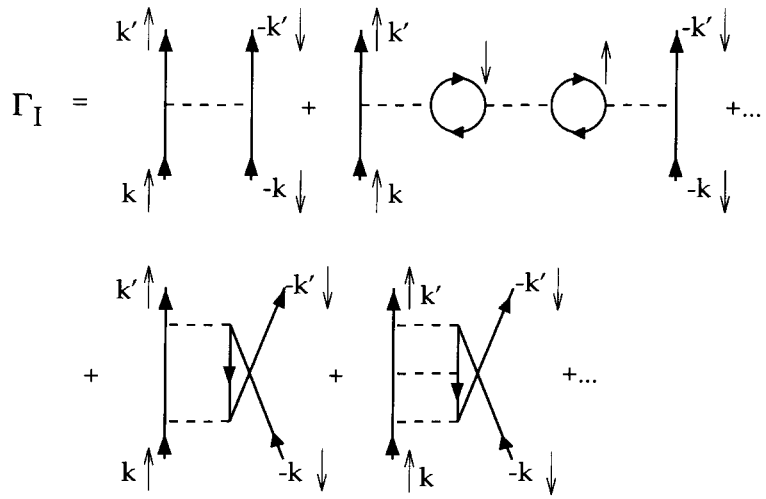

Fig. 65. Berk–Schrieffer diagrams for the single spin-fluctuation exchange interaction. The dashed line represents the bare Coulomb repulsion U.

5.4.6) [40]. These calculations gave a first estimate for a maximum $T_c \approx 0.015t$ from the magnetic pairing interaction. The continuing search for an instability towards superconductivity has since then focused on quantum Monte Carlo simulations, accompanied by diagrammatic studies for the Hubbard model, or exact diagonalization techniques for the t–J model.

6.1.1. Antiparamagnon exchange

As originally proposed by Berk and Schrieffer [38] the exchange of longitudinal and transverse spin fluctuations is described by the set of diagrams shown in Fig. 65. These diagrams contribute to the irreducible particle–particle interaction in the singlet channel. The Berk–Schrieffer diagrams lead to an effective interaction which in the zero center-of-mass momentum and zero-frequency channel is given by [38]

$$\Gamma_l^{\mathrm{SF}}(\boldsymbol{k}', \boldsymbol{k}) = U + \frac{U^2\chi_0(\boldsymbol{k}' + \boldsymbol{k}, 0)}{1 - U\chi_0(\boldsymbol{k}' + \boldsymbol{k}, 0)} + \frac{U^3\chi_0^2(\boldsymbol{k}' - \boldsymbol{k}, 0)}{1 - U^2\chi_0^2(\boldsymbol{k}' - \boldsymbol{k}, 0)}, \tag{6.1}$$

with χ_0 given by Eq. (5.19). Here, $\Gamma_l^{\mathrm{SF}}(\boldsymbol{k}', \boldsymbol{k})$ is used as a short notation for $\Gamma_l^{\mathrm{SF}}(\boldsymbol{k}', -\boldsymbol{k}'; \boldsymbol{k}, -\boldsymbol{k})$. At small doping away from half-filling χ_0 peaks at an incommensurate wavenumber $\boldsymbol{Q}^*$ near (π, π) which dominates the interaction Γ_l^{SF}, and the spin fluctuations are therefore referred to as antiferromagnetic paramagnons. As is obvious from Eq. (6.1) the effective particle–particle interaction is positive in the paramagnetic phase away from the RPA–Stoner instability. The exchange of a single paramagnon is therefore *repulsive*, and strong for large momentum transfer $\boldsymbol{q} = \boldsymbol{k} - \boldsymbol{k}'$ near (π, π).

One may wonder how pairing should come about if the interaction between the electrons is repulsive! The answer is hidden in the momentum dependence of the interaction. To see this it is instructive to examine the spatial Fourier transform of the interaction [345,110,109],

$$\Gamma_l^{\mathrm{SF}}(\boldsymbol{l}) \equiv \Gamma_l^{\mathrm{SF}}(l_x, l_y) = \frac{1}{N^2}\sum_{\boldsymbol{k}\boldsymbol{k}'} \exp[i(\boldsymbol{k} - \boldsymbol{k}')\cdot\boldsymbol{l}]\, \Gamma_l^{\mathrm{SF}}(\boldsymbol{k}', \boldsymbol{k}). \tag{6.2}$$

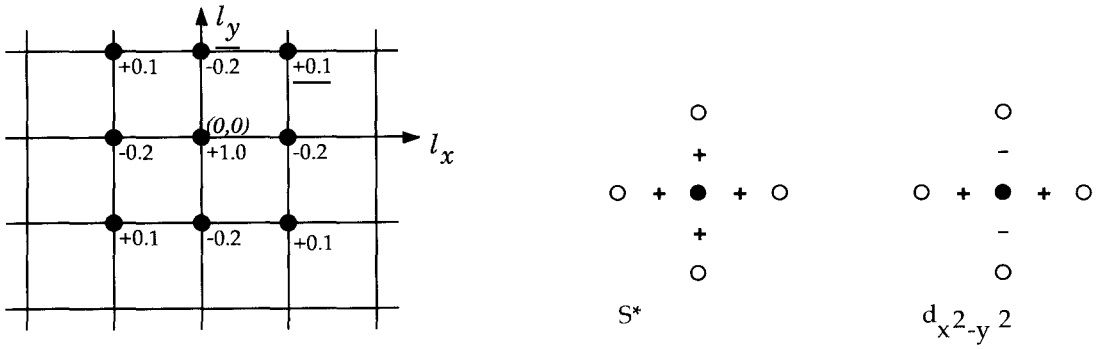

Fig. 66. Schematic picture for the spatial variation of $I_l^{SF}(l_x, l_y)$. The sign and the strength of the interaction are indicated at the lattice sites (l_x, l_y), the strength is given relative to the on-site interaction which has been arbitrarily set to 1. (From Ref. [109].)

Fig. 67. Extended s and $d_{x^2-y^2}$ pairing symmetry. The + and − signs are placed on the links that connect site l (•) with site $l+\delta$ (○), and they represent the values of the function $g_\alpha(\delta)$ in Eq. (6.3). (Reproduced from Ref. [282].)

Fig. 66 shows the sign and strength of the effective interaction near half-filling between two electrons of opposite spin separated by a lattice vector (l_x, l_y). It is not surprising that the interaction is repulsive if the electrons are sitting on the same site due to the Hubbard U term. But the interaction is attractive if the electrons are located on nearest-neighbor sites. At larger distances the interaction oscillates in sign and its strength weakens. The oscillatory spatial structure of the interaction has the character of a large Friedel oscillation. If two electrons can arrange themselves in an orbital state which takes advantage of the attractive spatial region of this interaction and avoid the repulsive regions, pairing can take place[9].

Singlet pairing correlations for superconductivity are measured by the correlation functions of the pair-field operators [344,282]

$$\Delta_\alpha^+ = \frac{1}{\sqrt{N}} \sum_l \Delta_\alpha^+(l) = \frac{1}{\sqrt{N}} \sum_l \sum_{\delta>0} g_\alpha(\delta) \tfrac{1}{2} (c_{l,\uparrow}^+ c_{l+\delta,\downarrow}^+ - c_{l,\downarrow}^+ c_{l+\delta,\uparrow}^+). \tag{6.3}$$

Here, $\delta = (\delta_x, \delta_y)$ with $\delta_x, \delta_y > 0$ runs over selected neighbors of the lattice site l, and $g_\alpha(\delta) = \pm 1$ specifies the symmetry of the electron pair field. From the spatial structure of the antiparamagnon exchange interaction we may already guess that there are the following two candidates for even-parity pair-field symmetries which can take the best advantage of the attraction,

$$\begin{aligned} \Delta_{s^*}^+(l) &= \tfrac{1}{2}(c_{l,\uparrow}^+ c_{l+x,\downarrow}^+ - c_{l,\downarrow}^+ c_{l+x,\uparrow}^+) + \tfrac{1}{2}(c_{l,\uparrow}^+ c_{l+y,\downarrow}^+ - c_{l,\downarrow}^+ c_{l+y,\uparrow}^+) \\ \Delta_d^+(l) &= \tfrac{1}{2}(c_{l,\uparrow}^+ c_{l+x,\downarrow}^+ - c_{l,\downarrow}^+ c_{l+x,\uparrow}^+) - \tfrac{1}{2}(c_{l,\uparrow}^+ c_{l+y,\downarrow}^+ - c_{l,\downarrow}^+ c_{l+y,\uparrow}^+), \end{aligned} \tag{6.4}$$

as is schematically shown in Fig. 67. These operators create electron pairs on nearest neighbor sites. In momentum space they correspond to the familiar forms

$$\Delta_{s^*} = \frac{1}{\sqrt{N}} \sum_k (\cos k_x + \cos k_y) c_{k,\uparrow}^+ c_{-k,\downarrow}^+, \qquad \Delta_d = \frac{1}{\sqrt{N}} \sum_k (\cos k_x - \cos k_y) c_{k,\uparrow}^+ c_{-k,\downarrow}^+, \tag{6.5}$$

[9] These arguments have been discussed in two recent lectures by D.J. Scalapino, see Refs. [110,109]

for extended s-wave and $d_{x^2-y^2}$ pair field operators, respectively.

Which one of these two pairing states will be preferentially selected by the single-paramagnon exchange interaction can be qualitatively argued [110,109] from the BCS weak coupling gap equation,

$$\Delta_k = -(1/N)\sum_{k'} \Gamma_l^{SF}(k,k')\Delta_{k'}/2E_{k'}, \quad E_k = \sqrt{\epsilon_k^2 + \Delta_k^2}. \tag{6.6}$$

Since from Eq. (6.1), $\Gamma_l^{SF}(k,k') > 0$, a solution of the gap equation requires that the gap function Δ_k must change sign on the Fermi surface. Among the two options we consider, this is fulfilled by the $d_{x^2-y^2}$-form of the gap function, $\Delta_k = \Delta_0(\cos k_x - \cos k_y)$. So we have to expect that if the electron–electron interaction in the Hubbard model is dominated by the Berk–Schrieffer single-paramagnon exchange, a pairing state with $d_{x^2-y^2}$ wave symmetry is the favourable candidate for superconductivity.

6.1.2. *Spin-bag pairing*

Beyond the repulsive single-spin-fluctuation exchange interaction there is a higher order *attractive* contribution to the pairing interaction Γ_l. The origin of this attraction was originally discussed by Schrieffer, Wen and Zhang (SWZ) [397,398] for holes doped into a spin-density-wave (SDW) environment. The arguments are based on the spin bag idea which suggests that holes sharing locally their regions of suppressed SDW amplitude experience an attractive potential. Since in this picture the reduced amplitude of the SDW in the vicinity of the hole is important for the pairing, SWZ have explored the interaction mediated by the exchange of longitudinal χ^{zz} spin fluctuations. Later on Frenkel and Hanke [133] have shown that the exchange of transverse χ^{+-} spin fluctuations is equally important and has to be included on equal footing for a complete picture of the spin-fluctuation induced pairing interaction in the SDW state.

In order to calculate the effective particle–particle interaction in the SDW state (see chapter 5.2.1) one considers a similar set of diagrams as for the Berk–Schrieffer interaction diagrams in Fig. 65. The difference is that the required spin susceptibilities have to be evaluated in the broken symmetry state of the SDW. This leads to the following expressions for the effective interaction between the valence band γ-quasiparticles at zero-energy transfer and in the singlet channel [398,133,441]

$$\begin{aligned}\Gamma_l^{+-}(k',k) &= V^{+-}(k'-k)n^2(k',k) - V^{+-}(k'-k-Q)p^2(k',k),\\ \Gamma_l^{zz}(k',k) &= V^{zz}(k'-k)l^2(k',k) - V^{zz}(k'-k-Q)m^2(k',k),\end{aligned} \tag{6.7}$$

with

$$V^{+-}(q) = U^2\frac{\bar{\chi}_0^{+-}(q,0)}{1-U\bar{\chi}_0^{+-}(q,0)}, \qquad V^{zz}(q) = U^2\frac{\bar{\chi}_0^{zz}(q,0)}{1-U\bar{\chi}_0^{zz}(q,0)}. \tag{6.8}$$

Here, n, p, l and m are the coherence factors and $\bar{\chi}_0^{zz}$ and $\bar{\chi}_0^{+-}$ are the intra-valence-band $(1,1)$ matrix elements of the non-interacting response functions as defined in chapter 5.2.1. SWZ have focused on the interaction Γ_l^{zz} which gives indeed rise to attraction for small momentum transfer $k' - k \sim 0$ as anticipated in the spin bag idea. The attraction is accompanied by a repulsion at large $q \simeq Q$ which is the analog of the repulsion arising from the exchange of one spin fluctuation in the paramagnetic phase. The antiperiodicity of the pairing potential, $\Gamma_l^{zz}(k',k) = -\Gamma_l^{zz}(k'+Q,k) = -\Gamma_l^{zz}(k',k+Q)$, implies that the solution of the corresponding superconducting gap equation satisfies $\Delta_k = -\Delta_{k+Q}$ which is e.g. fulfilled by the extended s-wave or the $d_{x^2-y^2}$-wave gap functions [see Eq. (6.5)].

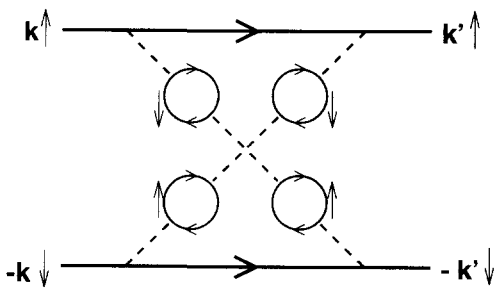

Fig. 68. Lowest-order spin-bag contribution to the irreducible pairing interaction in the paramagnetic state of the one-band Hubbard model. (From Ref. [192].)

Since the coherence factors $n(\boldsymbol{k}, \boldsymbol{k}')$ and $p(\boldsymbol{k}, \boldsymbol{k}')$ vanish for momenta on the Fermi surface of the non-interacting tight binding, Γ_I^{+-} appears to be less relevant for the interaction. However, the vanishing of $p(\boldsymbol{k}, \boldsymbol{k}')$ is cancelled by a pole in $V^{+-}(\boldsymbol{k}' - \boldsymbol{k} - \boldsymbol{Q})$ for $\boldsymbol{q} = \boldsymbol{k}' - \boldsymbol{k} \rightarrow 0$ as pointed out by Frenkel and Hanke [133]. In fact, in the large U/t limit one finds [133]

$$V^{+-}(\boldsymbol{q} + \boldsymbol{Q}) p^2(\boldsymbol{k} + \boldsymbol{q}, \boldsymbol{k}) \simeq 2U(q_x + q_y)^2/q^2. \tag{6.9}$$

Remarkably, this limit for the transverse spin-fluctuation channel leads to the same result for the pairing interaction as obtained in the context of a spiral phase for the t–J model [366]. This underlines again that strong coupling results can be smoothly connected to weak coupling RPA calculations for the Hubbard model in the SDW state. Interestingly, the spatial Fourier transform of Eq. (6.9) has a long range inverse power law contribution to the interaction. This long distance behavior is related to the spiral twist of the magnetic background as induced by the presence of the holes [366,133]. The spatial Fourier transform of the transverse Γ_I^{+-} interaction, however, shows that it does not lead to an attraction in the usual spin-antisymmetric channel [83].

The analysis so far presumed the existence of long range SDW order in the environment of the interacting electrons. As has been discussed by Schrieffer [353] and Kampf and Schrieffer [192] a pairing mechanism similar to the spin-bag attraction in the SDW state exists also in the paramagnetic metal phase of the doped one-band Hubbard model. It originates from the same effects which lead to the development of the pseudogap in the single-particle density of states (see chapter 5.4.5). Electrons mutually "help" each other to reduce their self-energy Σ_{SF} from the coupling to spin fluctuations. These self-energy effects enhance the energy of the electrons (or reduces the energy for holes) in the pseudogap regime. The suppression of Σ_{SF} due to the presence of another electron therefore lowers the energy of the electron and provides a source for an attractive contribution to the pairing potential. As described in detail in Ref. [192], this spin-bag effect in the paramagnetic phase is in lowest order $O(U^6)$ represented by the crossed-line diagram shown in Fig. 68. This diagram contains an attractive part for small momentum transfer $\boldsymbol{q} = \boldsymbol{k}' - \boldsymbol{k}$. It gives another contribution to the effective particle–particle interaction $\Gamma_I(\boldsymbol{k}', \boldsymbol{k})$ with a physical origin different from the single-paramagnon exchange, which is strongly repulsive at large $\boldsymbol{k}' - \boldsymbol{k} \simeq \boldsymbol{Q}$.

6.1.3. Effective particle–particle interaction

In order to test the relative importance of the Berk–Schrieffer single-spin fluctuation exchange and the crossed exchange spin-bag contribution to the irreducible particle–particle vertex Γ_I, Bulut et al. [66,67] have performed a comparison to QMC results obtained for the Hubbard model on a 8×8

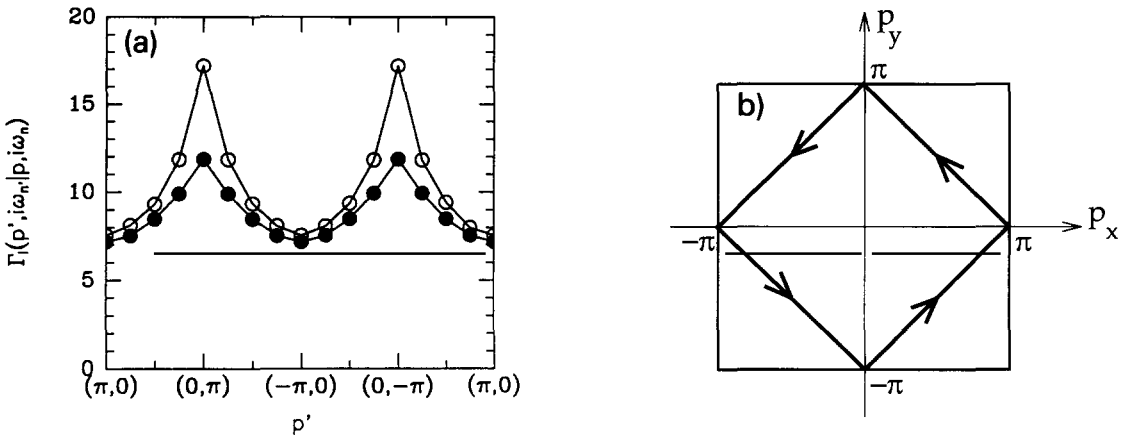

Fig. 69. (a) Quantum Monte Carlo results for the irreducible particle–particle interaction $\Gamma_l(\boldsymbol{p}', i\omega_{n'}; \boldsymbol{p}, i\omega_n)$ for $U/t = 4$, $\langle n \rangle = 0.87$ and $\omega_{n'} = \omega_n = \pi T$ on an 8×8 lattice at $T = 0.5t$ (•) and $T = 0.25t$ (○). The momentum $\boldsymbol{p}$ is kept fixed at $(\pi, 0)$ and $\boldsymbol{p}'$ is taken along the path shown in (b). The error bars are of order twice the size of the circles. (From Ref. [67].)

lattice doped away from half-filling. Fig. 69a shows QMC results for $\Gamma_l(\boldsymbol{p}', i\omega_{n'}; \boldsymbol{p}, i\omega_n)$ for the lowest Matsubara frequencies $\omega_{n'} = \omega_n = \pi T$, for fixed momentum $\boldsymbol{p} = (0, \pi)$, and with $\boldsymbol{p}'$ moving along the path shown in Fig. 69b. Note that the repulsive Γ_l peaks for large momentum transfers and that the strength of this peak increases as the temperature is lowered and short range AF correlations become stronger.

Corresponding diagrammatic results – which we denote by Γ_l^{SF} – for the single-spin fluctuation Berk–Schrieffer exchange and the crossed two-spin fluctuation exchange spin-bag contributions are presented in Fig. 70. The figure shows results in the singlet channel $\Gamma_{ls}^{\mathrm{SF}}$, obtained from the symmetrised Γ_l^{SF},

$$\Gamma_{ls}^{\mathrm{SF}}(\boldsymbol{p}', \boldsymbol{p}) = \tfrac{1}{2}[\Gamma_l^{\mathrm{SF}}(\boldsymbol{p}', \boldsymbol{p}) + \Gamma_l^{\mathrm{SF}}(-\boldsymbol{p}', \boldsymbol{p})]. \tag{6.10}$$

In the diagrammatic contributions the bare U has been replaced by an effective $\bar{U} = U/2$, a procedure which has proved to give a successful parametrisation of the QMC dynamic spin susceptibility by an RPA form of $\chi(\boldsymbol{q}, i\omega_n)$ [76,63,67] (see also chapter 5.3.2). The results in Fig. 70 have been obtained on a 128×128 lattice, $\boldsymbol{p}$ is kept fixed at $(p_F, 0)$ and $\boldsymbol{p}'$ is taken along a path on the Fermi surface.

Fig. 70a shows the single paramagnon exchange contribution which has a structure similar to the QMC result in Fig. 69, with a large peak near momentum transfer $\boldsymbol{p}' - \boldsymbol{p} = \boldsymbol{q} \sim (\pi, \pi)$ and a large constant background of order $5t$. The contribution from the sum of crossed two-spin fluctuation exchange diagrams, shown in Fig. 70b, exhibits the momentum structure proposed by Kampf and Schrieffer in the spin bag/pseudogap approach [194]; it is repulsive for momentum transfers $\boldsymbol{q} \sim (\pi, \pi)$ and attractive for $\boldsymbol{q} \sim (0, 0)$. But its magnitude is small relative to the single-paramagnon exchange in Fig. 70a. Similarly small are the contributions from additional vertex corrections [66]. The overall structure of the single-paramagnon exchange $\Gamma_{ls}^{\mathrm{SF}}$ resembles closely the QMC result. But a comparison of the magnitude to the symmetrised singlet QMC Γ_{ls} still shows that $\Gamma_{ls}^{\mathrm{SF}}$ underestimates the strength of the interaction.

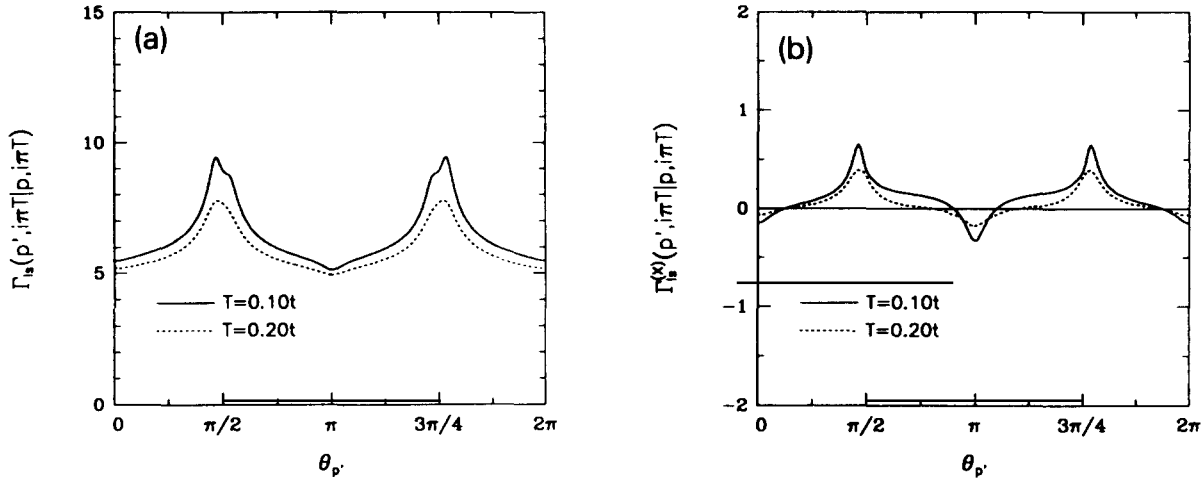

Fig. 70. (a) Momentum dependence of the irreducible particle–particle interaction $\Gamma_I(p',p)$ for the single-spin fluctuation exchange. Here, $p \equiv (\boldsymbol{p}, i\pi T)$ with $\boldsymbol{p} = (p_F, 0)$ and $p' \equiv (\boldsymbol{p}', i\pi T)$ with $\boldsymbol{p}'$ taken on the Fermi surface for a 128×128 lattice. Also, $\theta_{p'} = \tan^{-1}(p'_y/p'_x)$, $U/t = 4$, $\bar{U}/t = 2$ (see text), $\langle n \rangle = 0.87$ and $T/t = 0.1$ and $T/t = 0.2$. (b) Same as in (a) but for the crossed two-spin fluctuation exchange $\Gamma_{ls}^{(X)}(p',p)$. (From Ref. [66].)

Fair agreement with the QMC Γ_{ls} is obtained when the interaction is modeled by [111]

$$\Gamma_l^{\mathrm{SF}}(\boldsymbol{p}', i\omega_{n'}; \boldsymbol{p}, i\omega_n) = U + \tfrac{3}{2}g^2U^2\chi(\boldsymbol{p}' - \boldsymbol{p}, i\omega_{n'} - i\omega_n), \tag{6.11}$$

with QMC results inserted for the susceptibility $\chi(\boldsymbol{q}, \omega)$. The factor 3/2 is motivated by the Berk–Schrieffer interaction and arises from the two transverse and one longitudinal spin fluctuations. The factor g is introduced to account for the renormalization of U to an effective coupling gU (in Ref. [111] $g = 0.8$ has been used for QMC runs with $U/t = 4$). The success of this model form suggests that a properly renormalized single-spin fluctuation exchange interaction is capable of reproducing the basic features of the effective particle–particle interaction in the weak to intermediate coupling one-band Hubbard model [111].

6.2. *Pairing correlations from small cluster studies*

Having learned about the structure of the effective particle–particle interaction in the single-band Hubbard model we discuss in this chapter the results for pairing correlations obtained from numerical studies on small size clusters. It is not at all obvious what the appropriate measures in these small systems are to tell whether a superconducting state occurs at low temperatures and in the bulk limit. We therefore consider first different techniques which have been applied to the Hubbard model in searches for superconductivity. Separately we discuss numerical results for pairing correlations in the t–J model obtained by exact diagonalization or Green's function Monte Carlo studies.

6.2.1. *Criteria for superconductivity*

Pair-field susceptibilities. The clear indication for superconductivity in a bulk system is the finite expectation value for the pair-field operator Eq. (6.3) in a selected orbital symmetry. But for any

finite system $\langle \Delta_\alpha^+ \rangle$ vanishes identically, and one has to resort to measuring the equal-time pair-field correlation function [10]

$$P_\alpha(\boldsymbol{r}) = \sum_l \langle \Delta_\alpha^+(\boldsymbol{l}) \Delta_\alpha(\boldsymbol{r}+\boldsymbol{l}) \rangle, \tag{6.12}$$

and the pair-field susceptibility $\chi_\alpha^\Delta = \sum_r P_\alpha(\boldsymbol{r})$ [344,456,282]. Early studies by White et al. [456] for the one-band Hubbard model reported an enhancement at low temperatures in the $d_{x^2-y^2}$-wave channel of $\chi^\Delta(T)$, and a weaker enhancement also in the extended s-wave channel. Similar results have been reported for the pair-field susceptibilities in the three-band Hubbard model [347,108]. However, the distance dependence of the pair-field correlation function in the one-band model has revealed that the observed enhancement in $\chi^\Delta(T)$ is only a short distance effect, and none of the pairing channels has been found to develop pairing correlations beyond one lattice spacing down to the lowest temperature $T = t/6$ reached in these numerical simulations [282]. (For a similar conclusion see also the results of Imada in Ref. [175]).

One possible reason for the negative result for pairing correlations obtained from this method has been pointed out by Dagotto and Schrieffer [97]. The bare electron operators $c_{i\sigma}$ used to construct Δ_α^+ may have only a small overlap with the true physical quasiparticles, because the quasiparticle spectral weight factor z_k is small. The correlation functions $P_\alpha(\boldsymbol{r})$ are therefore suppressed by a factor z_k^2, which makes it difficult to detect superconducting pairing correlations in terms of c-fermion operators.

Bethe–Salpeter eigenvalues Another route to look for a superconducting instability is to consider the eigenfunctions $\phi_\alpha(p)$ and eigenvalues λ_α of the Bethe–Salpeter equation [40,67,68]

$$\lambda_\alpha \phi_\alpha(p) = -(T/N) \sum_{p'} \Gamma_l(p,p') G_\uparrow(p') G_\downarrow(-p') \phi_\alpha(p'), \tag{6.13}$$

where p is a short notation for $(\boldsymbol{p}, i\omega_n)$. QMC data have been used for the irreducible particle–particle interaction Γ_l and the single-particle Green's function $G_\sigma(p)$ in Eq. (6.13). As is well known, when the largest eigenvalue λ_α reaches 1, an instability to a superconducting state with the pair wavefunction $\phi_\alpha(p)$ occurs. The advantage of this approach is that it does not a priori select any pairing state by prejudice to be tested by numerical simulations, but rather the favoured pairing channel, its orbital symmetry and its spin state, are provided by the eigenfunction with the largest eigenvalue.

The results of this analysis by Bulut, Scalapino and White [68] for a half-filled 8×8 Hubbard lattice have shown that at low temperatures the pair eigenfunction with the largest eigenvalue has $d_{x^2-y^2}$ symmetry. Away from half-filling, at the lowest temperature, $T = t/4$, reached in the QMC simulations of Bulut et al. an odd-frequency s-wave triplet has the largest eigenvalue, but p- and $d_{x^2-y^2}$-wave singlet states grow the most rapidly with decreasing temperature and are expected to dominate at low temperatures [67].

Superfluid density. As we know the signature of superconductivity is the onset of the Meissner effect. A sufficiently weak magnetic field is expelled from a bulk superconductor except for a thin penetration depth λ. λ^{-2} is a measure for the superfluid density D_S [352]. For models of lattice electrons it has been shown by Scalapino et al. [346] that D_S is obtained from

[10] Note that we have used a singlet pair-field operator in Eq. (6.3) slightly different from the operators introduced in Ref. [282] which contain a combination of singlet and triplet pair-fields.

$$D_S/\pi e^2 = \langle -H^x_{\rm kin}\rangle - C_{xx}(q_x = 0, q_y \to 0, i\omega_m = 0), \tag{6.14}$$

where C_{xx} is given by the correlation function of the paramagnetic current-density operator along the bonds in the x-direction,

$$C_{xx}(\boldsymbol{q}, i\omega_m) = \frac{1}{N}\int_0^{1/T} d\tau\, e^{i\omega_m\tau}\,\langle j^p_x(\boldsymbol{q},\tau) j^p_x(-\boldsymbol{q},0)\rangle, \tag{6.15}$$

with $\omega_m = 2\pi m T$. As in the derivation of the optical conductivity in chapter 5.4.4, $\langle H^x_{\rm kin}\rangle$ is the kinetic energy per site along the x-oriented bonds. Crucial in Eq. (6.14) is the order in which q_y and ω_m are taken to zero. This accounts for the Meissner effect as the current response to a static transverse vector potential, with $\boldsymbol{q}\cdot\boldsymbol{A}(\boldsymbol{q},\omega = 0) = 0$. A superconductor is characterised by a finite superfluid density D_S and a finite Drude contribution $D\delta(\omega)$ in the conductivity [346]. This provides another criterion for superconductivity which does not specify the symmetry of the superconducting state.

QMC simulations have been applied to look for a finite superfluid density D_S in the one-band Hubbard model [346]. For $U/t = 4$ and down to temperatures $T = t/10$ the results suggest that the non-half-filled Hubbard model is metallic but not superconducting with a finite Drude weight $D > 0$ and $D_S \simeq 0$. This is consistent with a recent projector-QMC result of Assaad, Hanke and Scalapino [24] at $T = 0$ for quarter filling $\langle n\rangle = 1/2$. No signature of flux quantisation has been detected for the Hubbard model in a cylinder geometry threaded by a magnetic flux.

In summary, only negative results have so far been reported regarding superconductivity in the repulsive 2D Hubbard model. A parameter window between quarter and half-filling at low temperatures and strong coupling remains, however, still open where present day QMC studies are unable to reach a conclusive answer due to the unsolved fermionic sign problem. If there is superconductivity in the one-band Hubbard model, the numerical results suggest that it will most likely occur in the $d_{x^2-y^2}$ singlet pairing channel.

6.2.2. *Superconductivity in the t–J model*

In contrast to the Hubbard model there are stronger indications for superconductivity in the t–J model. A first indication of hole–hole attraction in the t–J model comes from the observation that in the two-hole ground state a bound state is formed between the holes [44,331,156,95,315] for couplings larger than a critical value which has been estimated to be $J_c/t \sim 0.27$ [46]. The internal symmetry of the bound state is $d_{x^2-y^2}$. The physical picture for the origin of binding is simple: Two holes added to a quantum antiferromagnet can minimize the magnetic energy cost by occupying nearest-neighbor sites. In this way only seven AF bonds are cut instead of eight, if the two holes were moving independently. In some sense this is similar to the spin bag pairing attraction in a SDW environment.

At larger couplings J/t it is well established that there is phase separation into hole-rich and hole-poor regions [118,318,99]. The region in the phase diagram in the vicinity of the phase separation boundary has been argued to be the most promising for a search of superconductivity, because in this regime the pair binding forces are strongest [101,102]. Furthermore, a signal for superconductivity should be favorably detectable for electron densities near quarter-filling $\langle n\rangle$ since for these fillings the number of electron or hole pairs available for pairing is maximised. Based on these ideas Dagotto and Riera have indeed observed for the first time positive evidence for a superconducting ground state with

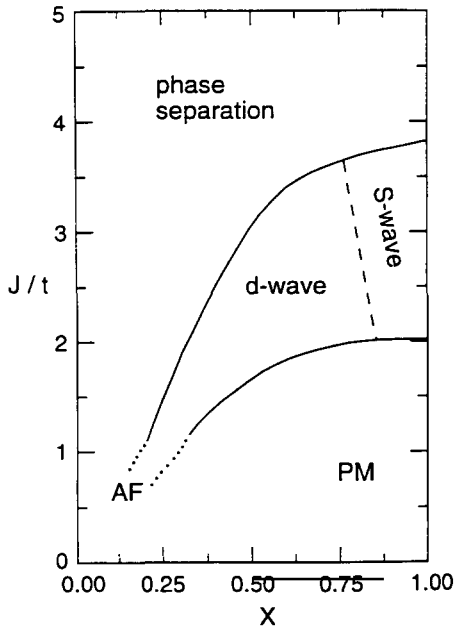

Fig. 71. Phase diagram for the 2D t–J model. d-wave denotes the phase where the $d_{x^2-y^2}$ correlations have been found to be strong in exact diagonalizations. s-wave denotes the regime where variational Monte Carlo studies have shown the presence of a stable s-wave condensate. The dashed line separating d-wave from s-wave is schematic since results have been obtained only at a small number of electronic densities. AF denotes the antiferromagnetic region close to half-filling where not enough accuracy has been reached to complete the phase diagram. PM denotes the paramagnetic metal state. (From Ref. [104].)

$d_{x^2-y^2}$-symmetry in the t–J model at quarter-filling and near phase separation [101,102,104]. This conclusion rests on the exact diagonalization results for the pair-field susceptibility, as well as flux quantisation, and a finite superfluid density [102]. These results of diagonalization and variational Monte Carlo studies are summarised in the schematic phase diagram shown in Fig. 71 for the t–J model as proposed by Dagotto et al. [104].

The slight caveat remains that the cleanest evidence for superconductivity has so far only been obtained in an unphysical parameter region at large values of J and for large doping near the phase separation boundary at quarter-filling. Superconductivity has still to be detected in the more realistic region of small J/t and densities near half-filling.

6.3. *Phenomenologies for d-wave pairing*

Given the as yet preliminary and unconclusive results of the numerical searches for superconductivity in the Hubbard or t–J models in the regime relevant to cuprate superconductors, one may follow another route for a theoretical discussion of the superconducting state. One possible way is to test various symmetries for the superconducting state against available experimental data. This may be done in the context of the BCS pairing theory appropriately extended to include magnetic correlations. Another approach has been chosen by Pines and coworkers which takes the experimentally determined dynamic spin susceptibility – as analysed in the NAFL phenomenology – as input into a

pairing theory based on the exchange of AF spin fluctuations. While the latter approach is destined to favor a d-wave pairing state due to the large momentum dominated pairing interaction (see the discussion in chapter 6.1.1), the former less biased attempts have reached similar conclusions. The subsequent two chapters will summarise some of these results and theoretical considerations for the superconducting pairing state.

6.3.1. NAFL superconductivity

Monthoux, Balatsky and Pines have suggested an effective model which assumes that the planar excitations in metallic cuprates form a nearly antiferromagnetic Fermi liquid (NAFL) made up of quasiparticles coupled to spin fluctuations [275]. Experimental NMR results for the normal state are used as input to fix the spectrum of the spin excitations and their coupling to the quasiparticles. The specific model Hamiltonian which has been considered by Monthoux et al. is given by [275]

$$H = \sum_{k,\sigma} \epsilon_k (c^+_{k,\sigma} c_{k,\sigma} + \text{h.c.}) + \frac{1}{\Omega} \sum_q g(q) s(q) \cdot S(-q), \quad s(q) = \tfrac{1}{2} \sum_{\alpha,\beta,k} c^+_{k+q,\alpha} \sigma_{\alpha\beta} c_{k,\beta}, \tag{6.16}$$

where $s(q)$ is the spin operator of the lattice quasiparticles. The dynamic properties of the "spin-fluctuation operator" $S(q)$ are determined by its susceptibility,

$$\chi_{ij}(q,\omega) = \delta_{ij} \frac{\chi_Q}{1 + \xi^2 (q - Q)^2 - i\omega/\omega_{SF}}, \tag{6.17}$$

where χ_Q is the static spin susceptibility at wave vector $Q = (\pi, \pi)$. The dynamic spin susceptibility Eq. (6.17) is of the MMP form [272] as discussed in chapter 4.1.2. The parameters χ_Q, ξ and ω_{SF} are determined such as to provide a quantitative fit to NMR experiments above T_c [272,273,289]; they are taken to be constant below T_c with the argument that the NMR data are suggestive for the AF spin correlations to become frozen in the superconducting state. The coupling functions $g(q, T)$ in Eq. (6.16) are adjusted appropriately for the different materials $123\,O_7$, $123\,O_{6.63}$, and $La_{1.85}Sr_{0.15}CuO_4$ to ensure the observed linear temperature dependence of the normal state resistivity in all three materials.

Having set up the model in this way Monthoux et al. have investigated first the linearised gap equation in the vicinity of T_c which in the singlet channel takes the approximate, simple form

$$\Delta(k) = -g^2_{\text{eff}}(T) \frac{1}{N} \sum_{k'} \text{Re}\, \chi(k - k', \epsilon_{k'} - \mu) \tanh\left(\frac{\epsilon_{k'} - \mu}{2k_B T}\right) (\epsilon_{k'} - \mu)^{-1} \Delta(k'). \tag{6.18}$$

Here, $g_{\text{eff}}(T)$ is an effective momentum averaged coupling constant, and the interaction is cut off in the frequency argument of $\text{Re}\,\chi$ when $\epsilon_{k'} - \mu \geq \omega_{SF}(\xi/a)^2$. The gap equation (6.18) leads uniquely to a solution $\Delta(k) = \Delta_0(\cos k_x - \cos k_y)$ with $d_{x^2-y^2}$ symmetry due to the strong, repulsive structure of the pairing interaction $Re\chi$ at large momenta $q \sim Q$. (The origin of this result has been discussed in chapter 6.1.1).

Besides the achieved high transition temperatures, two further principal results of the numerical solution of the gap equation as reported in Ref. [275] are the approximate formula for the transition temperature

$$T_c = \alpha \hbar \omega_{SF}(T_c) [\xi^2(T_c)/a^2] \exp[-1/\eta g^2_{\text{eff}}(T_c) \chi_0(T_c) N(0)], \tag{6.19}$$

and the temperature dependence of the maximum value $\Delta_0(T)$ of the gap function. The coefficients α, η in Eq. (6.19) are material dependent constants of order unity and $N(0)$ is the density of states at

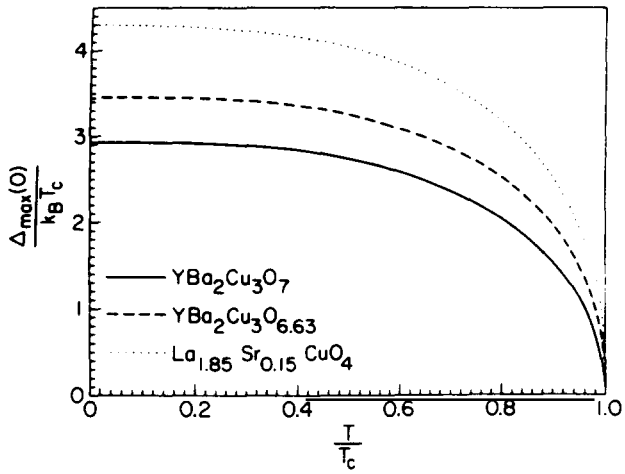

Fig. 72. The temperature dependence of the maximum value of the $d_{x^2-y^2}$ energy gap for the three high-T_c compounds $YBa_2Cu_3O_7$ (T_c = 95 K), $YBa_2Cu_3O_{6.63}$ (T_c = 60 K) and $La_{1.85}Sr_{0.15}CuO_4$ (T_c = 40 K) as obtained in the NAFL pairing theory of Monthoux, Balatsky and Pines. (From Ref. [275].)

the Fermi energy. The long-wavelength spin susceptibility $\chi_0(T)$ enters the MMP model susceptibility Eq. (6.17) as discussed in chapter 4.1.2. Although the coupling strength in this approach is weak to intermediate the energy gap opens up rapidly below T_c in agreement with the Knight shift experiments [30], reaching a maximum magnitude about two times larger than the BCS weak-coupling result $\Delta^{BCS}(T=0) = 1.76 k_B T_c$ (see Fig. 72).

Objections which may arise against this weak coupling treatment of superconducting pairing induced by the exchange of AF paramagnons have been subsequently addressed by Monthoux and Pines in a strong coupling calculation [276,277]. In the Eliashberg formalism this treatment includes in particular the lifetime effects from the quasiparticle scattering against spin fluctuations. It has proven that despite their short lifetime and despite the related, indeed severe, reduction of T_c, the quasiparticles can still take sufficient advantage of the spin-fluctuation induced pairing interaction to superconduct at high temperatures. Large coupling constants are necessary to obtain superconducting transition temperatures near 100 K. Even with the required large coupling constants the normal state properties in this model still compare reasonably well with experimental data on the resistivity and the optical conductivity [277]. To obtain high transition temperatures it has been found crucial to take into account the full momentum and frequency dependence of the effective interaction. In contrast, the standard Fermi-surface-restricted Eliashberg treatments generally lead to an order of magnitude lower T_c values [453,267,324].

The strong coupling calculations of Monthoux and Pines have shown that low- frequency spin fluctuations serve as a very effective candidate mechanism for high-temperature superconductivity. An unambiguous prediction of the theory of paramagnon induced superconductivity in a NAFL is the $d_{x^2-y^2}$ symmetry of the pairing state in $123\,O_7$ [277]. As the authors admit, if experiments prove a different pairing state to be realised in this 123 material, the NAFL pairing concept will have to be discarded as a valid theory for HTSC.

Doubts against d-wave pairing may be inferred from the apparent insensitivity to impurities in cuprate superconductors, since it is known that elastic scattering of quasiparticles from nonmagnetic

impurities gives rise to significant pair-breaking effects in a d-wave superconductor. However, Monthoux et al. have argued that the lifetime effects caused by impurity scattering are smaller than those attributed to the spin-fluctuation scattering [275] which have been included in their strong coupling calculations [276,277].

Besides the selected experiments discussed in chapter 3.6 some of the characteristic NMR results below T_c have in fact been favourably interpreted in terms of a $d_{x^2-y^2}$ pairing state. For example the absence of a Hebel–Slichter peak in the spin–lattice relaxation rates close below T_c is naturally obtained for a d-wave pairing state [287,63]. It offers an alternative explanation to the suggestion of an s-wave gap function together with a large temperature dependent pair-breaking rate and a large value for the ratio $2\Delta(0)/k_BT_c$ which equally leads to a suppression of the Hebel–Slichter peak [87,219,63]. Separately, the line nodes of the d-wave gap function on the Fermi surface lead to the development of a T^3 behavior of $1/T_1$ at low temperatures [287,63,65,416] as is observed in the oxygen and copper relaxation rate data of Martindale et al. [254]. As we will outline in the next chapter further analyses of the pairing state has been based on a phenomenological description of the dynamic spin susceptibility below T_c. This has allowed to derive useful predictions for different gap functions for a comparison to experimental results.

6.3.2. Phenomenological analysis of the pairing state

In order to obtain information about the symmetry of the gap function a simple phenomenological ansatz has been considered for the dynamic spin susceptibility below T_c which includes the effect of AF spin fluctuations on the RPA level. Explicitly, $\chi(\boldsymbol{q},\omega)$ in the superconducting state has been modeled in the form [63–65,69,227,228]

$$\chi(\boldsymbol{q},\omega)=\frac{\chi_0^{\mathrm{BCS}}(\boldsymbol{q},\omega)}{1-U_{\mathrm{eff}}\chi_0^{\mathrm{BCS}}(\boldsymbol{q},\omega)}, \tag{6.20}$$

with [352]

$$\begin{aligned}\chi_0^{\mathrm{BCS}}(\boldsymbol{q},\omega)=\frac{1}{N}\sum_{\boldsymbol{k}}\Bigg[&\frac{1}{2}\left(1+\frac{\xi_{\boldsymbol{k}}+\boldsymbol{q}\xi_{\boldsymbol{k}}+\Delta_{\boldsymbol{k}+\boldsymbol{q}}\Delta_{\boldsymbol{k}}}{E_{\boldsymbol{k}+\boldsymbol{q}}E_{\boldsymbol{k}}}\right)\frac{f(E_{\boldsymbol{k}+\boldsymbol{q}})-f(E_{\boldsymbol{k}})}{\omega-(E_{\boldsymbol{k}+\boldsymbol{q}}-E_{\boldsymbol{k}})+i\Gamma}\\&+\frac{1}{4}\left(1-\frac{\xi_{\boldsymbol{k}+\boldsymbol{q}}\xi_{\boldsymbol{k}}+\Delta_{\boldsymbol{k}+\boldsymbol{q}}\Delta_{\boldsymbol{k}}}{E_{\boldsymbol{k}+\boldsymbol{q}}E_{\boldsymbol{k}}}\right)\frac{1-f(E_{\boldsymbol{k}+\boldsymbol{q}})-f(E_{\boldsymbol{k}})}{\omega+(E_{\boldsymbol{k}+\boldsymbol{q}}+E_{\boldsymbol{k}})+i\Gamma}\\&+\frac{1}{4}\left(1-\frac{\xi_{\boldsymbol{k}+\boldsymbol{q}}\xi_{\boldsymbol{k}}+\Delta_{\boldsymbol{k}+\boldsymbol{q}}\Delta_{\boldsymbol{k}}}{E_{\boldsymbol{k}+\boldsymbol{q}}E_{\boldsymbol{k}}}\right)\frac{f(E_{\boldsymbol{k}+\boldsymbol{q}})-f(E_{\boldsymbol{k}})-1}{\omega-(E_{\boldsymbol{k}+\boldsymbol{q}}+E_{\boldsymbol{k}})+i\Gamma}\Bigg].\end{aligned} \tag{6.21}$$

This expression for χ_0^{BCS} contains inside the square brackets the usual coherence factors. The dispersion in the superconducting state is $E(\boldsymbol{k})=(\xi_{\boldsymbol{k}}^2+\Delta_{\boldsymbol{k}}^2)^{1/2}$ with $\xi_{\boldsymbol{k}}=\epsilon_{\boldsymbol{k}}-\mu$. The first term in Eq. (6.21) is due to the scattering of quasiparticles. At low temperatures it dominates the last two terms which arise from the creation and destruction of particle–hole pairs. Lifetime effects are incorporated by a scattering rate $\Gamma(T)$ which has been either set to a constant or has been modeled by a power law temperature dependence $\Gamma(T)=\Gamma_0+\Gamma_1(T/T_c)^n$. The specific choice of $\Gamma(T)$, however, does not qualitatively change the results and is only important near T_c where it controls logarithmic Hebel–Slichter divergences [65].

$\chi(\boldsymbol{q}, \omega)$ has been investigated in comparison to NMR and neutron scattering data for gap functions Δ_k with different symmetries such as

$$\Delta(\boldsymbol{k}) = \Delta_0(T), \quad \text{isotropic s wave},$$

$$\Delta(\boldsymbol{k}) = \Delta_0(T)(\cos k_x - \cos k_y), \quad d_{x^2-y^2} \text{ wave},$$

$$\Delta(\boldsymbol{k}) = \Delta_0(T) \sin k_x \sin k_y, \quad d_{xy} \text{ wave},$$

$$\Delta(\boldsymbol{k}) = \Delta_1(T) + i\Delta_2(T)(\cos k_x - \cos k_y), \quad \text{s + id state}. \tag{6.22}$$

The temperature dependence of the gap amplitudes $\Delta_{0,1,2}$ has been commonly assumed to follow the BCS behavior. The ratio for the maximum gap amplitude $2\Delta(0)/k_B T_c$ has been adjusted as a fit parameter.

In testing the different gap functions in Eq. (6.22) against experiments, also extensions of the RPA formula Eq. (6.20) have been considered which include band structure effects and a momentum dependent exchange coupling $J(\boldsymbol{q})$ instead of an effective U_{eff}, for a one-band model [416] as well as for a three-band model, the latter in the context of the *almost localised* Fermi liquid theory (see chapter 5.3.3) [473]. Most of the reported results have found a $d_{x^2-y^2}$ pairing state to be compatible with NMR and neutron data. A different conclusion has e.g. been reached by the authors of Refs. [227,228], which argue that only the s+id state [with $\Delta_2(T) = 2\Delta_1(T)$] is in qualitative agreement with both the Knight shift *and* the $1/T_1$ measurements.

Two particularly interesting examples for the RPA/BCS analysis of NMR data in the superconducting state are given in Fig. 73 as obtained by Bulut and Scalapino [65,64]. The figures show a comparison between the results for an isotropic s-wave and a $d_{x^2-y^2}$-wave gap function for the anisotropy ratio of the Cu spin–lattice relaxation rate ${}^{63}R = {}^{63}T_{1\perp}^{-1}/{}^{63}T_{1\parallel}^{-1}$ and the transverse spin–spin relaxation rate $1/T_{2G}$. (For a discussion of the corresponding experimental data see chapters 3.3.5 and 3.3.6, respectively.) These examples show clear qualitative differences in the temperature dependences for s- and d-wave gaps. The observed nonmonotonic behavior of the anisotropy ratio finds indeed a possible explanation in terms of a d-wave pairing state and the predicted only very weak temperature dependence of T_{2G} below T_c has been confirmed experimentally, too [184].

Still, it remains premature to argue that the correctness of the $d_{x^2-y^2}$ pairing description of the superconducting state in the high-T_c cuprates has been firmly established by experiments. (For a recent discussion of this issue see Ref. [225]). In particular, the pairbreaking effects of impurity scattering need to be further examined. But a decisive answer may soon be obtained e.g. by refined measurements of the phase differences of the superconducting order parameter on the Fermi surface by the SQUID experiments initiated by Wollman et al. [457] (see chapter 3.6.3).

7. Summary and conclusion

In this review we have tried to summarize results for the magnetic correlations in high-temperature superconductors. In the chapters on experimental work we have selected the results of experimental techniques which specifically probe the magnetic properties of insulating and metallic or superconducting cuprate materials. NMR measurements have provided very detailed information on the local,

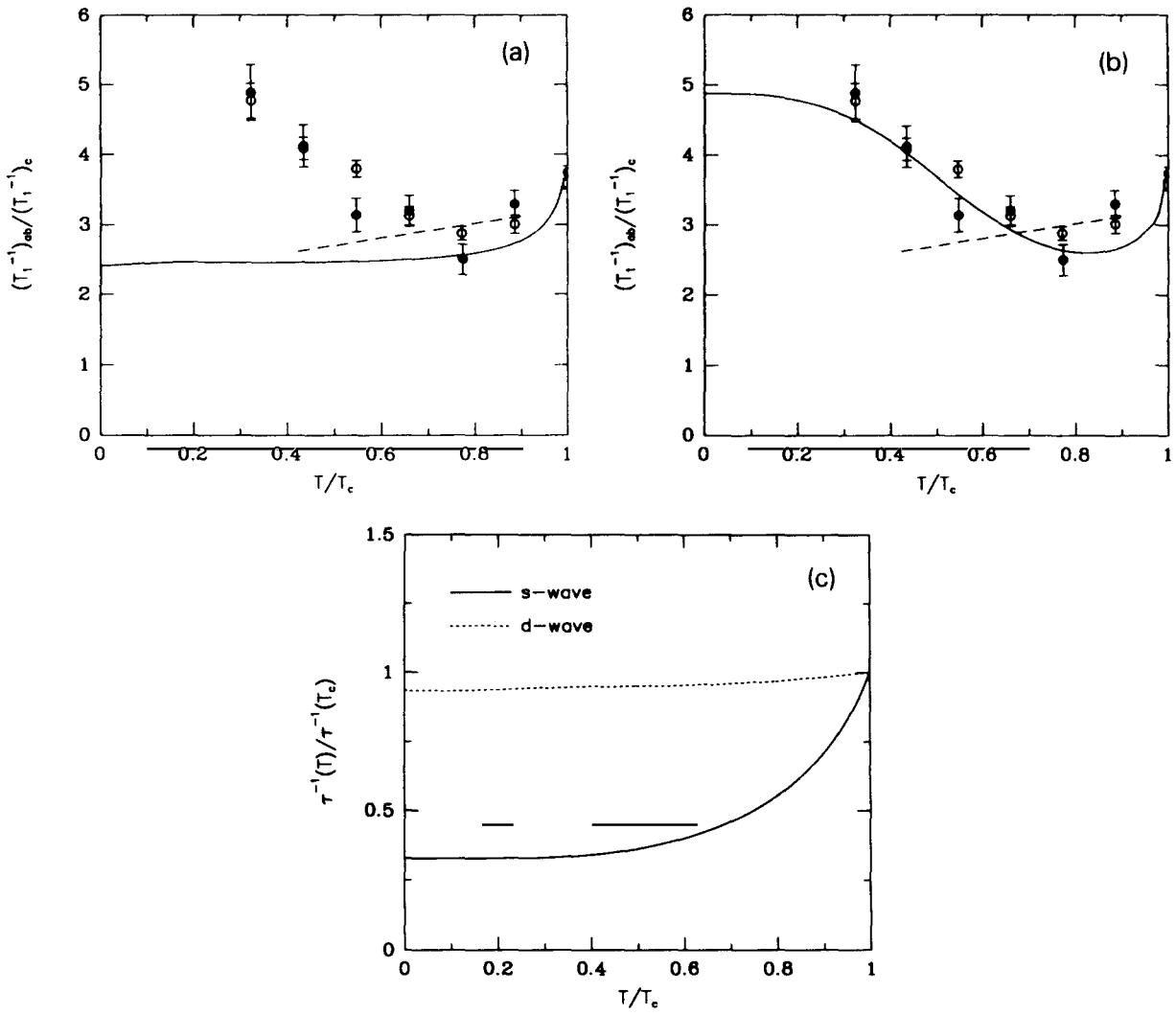

Fig. 73. The temperature dependence of the planar Cu anisotropy ratio for (a) an isotropic s-wave gap with $U_{\text{eff}}/t = 2$, $2\Delta(0) = 8k_BT_c$ and $\Gamma = 2.5T_c(T/T_c)^3$, and (b) for a $d_{x^2-y^2}$-wave gap with the same parameter set. The points are the experimental data of Takigawa et al. from Ref. [408], the dashed line represents the experimental data by Barrett et al. from Ref. [31]. (c) The temperature dependence of the transverse nuclear relaxation rate $1/T_{2G}$ (denoted by τ^{-1} in the figure) in the superconducting state for the isotropic s-wave (solid line) and the $d_{x^2-y^2}$-wave gap symmetries. (Figures a and b taken from Ref. [65], figure c taken from Ref. [64].)

low-frequency spin dynamics in the CuO_2 planes. Many features of NMR data have found a natural explanation in terms of strong antiferromagnetic spin fluctuations on the planar Cu sites. Still, there are mismatches to the results obtained from neutron scattering experiments which remain to be resolved. The quality of neutron scattering data continues to improve in a remarkable way and may soon further refine our present knowledge of the momentum, temperature and frequency dependence of the magnetic spin susceptibility, in particular for samples near optimum stoichiometry. Two-magnon light scattering has provided complementary information on the magnetic excitations in insulating

and metallic materials. Only few efforts on the theoretical side have so far been made to describe the magnetic light scattering in doped cuprates and the further development of tractable calculational schemes for electronic Raman scattering in correlated electron systems is very desirable.

We have included in this article also some of the experimental results which are suggestive of the important role that spin fluctuations play in the normal state properties of cuprate superconductors. For example the simultaneous appearance of a spin-excitation gap in the spin–lattice relaxation rate and a drop in the resistivity, or the mid-infrared band in the optical conductivity indicate the intimate coupling of the charge carrier dynamics and the spin fluctuations. Also the rapid drop of the quasiparticle scattering rate below T_c tells that the dominant source for scattering of charge carriers is electronic in origin. A Fermi-liquid picture of quasiparticles heavily dressed from the coupling to antiferromagnetic spin fluctuations may be adequate for a description of the normal state transport properties, with bandstructure effects included appropriately.

Microscopic Hubbard-type models, devised to describe the electronic correlations in the CuO_2 planes, have been the starting point to discuss theoretical results for the magnetic correlations as well as model calculations for the motion of holes in quantum antiferromagnets. At several instances we have given examples for qualitative agreement with experimental data for the magnetic properties. These results argue in favour of the 2D Hubbard models of various types to represent minimum models which contain the essential physics relevant to the electronic properties of cuprate superconductors.

Unanswered remains the question whether any of these models has a superconducting ground state for parameter sets which are supposed to describe the real materials. If the electrons in these models do indeed superconduct at low temperatures due to a magnetic pairing mechanism, the superconducting pairing state will most likely have $d_{x^2-y^2}$ symmetry. As we have emphasised in different chapters, the hypothesis of d-wave superconductivity in the cuprates would be compatible e.g. with the NMR relaxation rates or the linear temperature dependence of the London penetration depth, and would also naturally explain the peculiar paramagnetic Meissner effect observed in some granular samples.

From angular resolved photoemission data it seems established experimentally that the energy gap function is highly anisotropic. Again we emphasize the importance of the Wollman et al. SQUID experiments [457] on $YBa_2Cu_3O_7$ single crystals to determine the phase differences of the superconducting order parameter on the Fermi surface. If the superconducting state proves to have $d_{x^2-y^2}$ symmetry, this would be a strong impetus for theories which rely on the exchange of antiferromagnetic spin fluctuations as the pairing mechanism for high-temperature superconductivity.

Acknowledgements

The author benefited from enlightening and useful discussions with K. Bedell, N. Bonesteel, W. Brenig, B. Büchner, D. Coffey, A. Freimuth, M. Takigawa, P.C. Hammel, D.J. Scalapino, J.R. Schrieffer and G.T. Zimanyi during the course of writing this article. The author is particularly indebted to P.C. Hammel, E. Dagotto and D.J. Scalapino for helpful comments and careful reading of the manuscript. The author gratefully acknowledges the hospitality at the Center for Materials Science at Los Alamos National Laboratory and the opportunities to participate in the Correlated Electron Theory Program. Gratefully acknowledged is also the support through a habilitation scholarship of the Deutsche Forschungsgemeinschaft.

Apology

I wish to offer my apologies to all the many authors whose work – although relevant to the topic of this review article – I have felt unable to include or which has simply escaped my attention.

References

[1] A.A. Abrikosov and L.P. Gorkov, Zh. Eksp. Teor. Fiz. **39**, 1781, 1960 [Sov. Phys. JETP **12**, 1243, 1961].
[2] D. Achkir, M. Poirier, D.A. Bonn, R. Liang and W.N. Hardy, Phys. Rev. B **48**, 13184, 1993.
[3] G. Aeppli, S.M. Hayden, H.A. Mook, Z. Fisk, S.W. Cheong, D. Rytz, J.P. Remeika, G.P. Espinosa and A.S. Cooper, Phys. Rev. Lett. **62**, 2052, 1989.
[4] G. Aeppli, H.A. Mook, T.E. Mason, S.M. Hayden, A.D. Taylor, T.G. Perring, K.N. Clausen, P.B. Littlewood, S. W. Cheong and Z. Fisk, Lecture Notes for the Enrico Fermi School (Varenna, 1992), unpublished.
[5] I. Affleck and J.B. Marston, Phys. Rev. B **37**, 3774, 1988.
[6] A. Aharony, R.J. Birgeneau, A. Coniglio, M.A. Kastner and H.E. Stanley, Phys. Rev. Lett. **60**, 1330, 1988.
[7] R. Akis and J.P. Carbotte, Solid State Commun. **78**, 393, 1991.
[8] J.W. Allen, C.G. Olson, M.B. Maple, J.-S. Kang, L.Z. Liu, J.-H. Park, R.O. Anderson, W.P. Ellis, J.T. Markert, Y. Dalichaouch and R. Liu, Phys. Rev. Lett. **64**, 595, 1990.
[9] P.B. Allen and D. Rainer, Nature **349**, 396, 1991.
[10] P.B. Allen, Comments Cond. Mat. Phys. **15**, 327, 1992.
[11] H. Alloul, T. Ohno and P. Mendels, Phys. Rev. Lett. **63**, 1700, 1989.
[12] H. Alloul, P. Mendels, H. Casalta, J.F. Marucco and J. Arabski, Phys. Rev. Lett. **67**, 3140, 1991.
[13] H. Alloul, A. Mahajan, H. Casalta and O. Klein, Phys. Rev. Lett. **70**, 1171, 1993.
[14] See e.g. P.W. Anderson and Y. Ren, in: Proc. 1989 Los Alamos Symp. on High Temperature Superconductivity (Los Alamos, 1989), eds K.S. Bedell, D. Coffey, D.E. Meltzer, D. Pines and J.R. Schrieffer (Addison-Wesley, Reading, MA, 1990). p. 3;
P.W. Anderson, Phys. Rep. **184**, 195, 1989; Phys. Rev. B **42**, 2624, 1990; Phys. Rev. Lett. **67**, 2092, 1991; Prog. Theor. Phys. Suppl. **107**, 41, 1992.
[15] C. Almasan and M.B. Maple, in: Chemistry of High Temperature Superconductors, ed. C.N.R. Rao (World Scientific, Singapore, 1991).
[16] P.W. Anderson, J. Phys. Chem. Solids **11**, 26, 1959.
[17] P.W. Anderson, Phys. Rev. Lett. **64**, 1839, 1990.
[18] O.K. Anderson, A.I. Liechtenstein, O. Rodriguez, I.I. Mazin, O. Jepsen, V.P. Antropov, O. Gunnarson and S. Gopalan, Physica C **185-189**, 147, 1991.
[19] S.M. Anlage and D. Wu, J. Supercond. **5**, 395, 1992.
[20] J. Annett, N. Goldenfeld and S.R. Renn, Phys. Rev. B **43**, 2778, 1991.
[21] B. Arfi, Phys. Rev. B **45**, 2352, 1992.
[22] E. Arrigoni and G.C. Strinati, Phys. Rev. B **44**, 7455, 1991.
[23] F.F. Assaad, Phys. Rev. B **47**, 7910, 1993.
[24] F.F. Assaad, W. Hanke and D.J. Scalapino, Phys. Rev. Lett. **71**, 1915, 1993.
[25] A. Auerbach and D.P. Arovas, Phys. Rev. Lett. **61**, 617, 1988;
D.P. Arovas and A. Auerbach, Phys. Rev. B **38**, 316, 1988.
[26] A. Auerbach and B.E. Larson, Phys. Rev. B **43**, 7800, 1991.
[27] M. Bankay, M. Mali, J. Roos, I. Mangelschots and D. Brinkmann, Phys. Rev. B **46**, 11228, 1992.
[28] T. Barnes and G.J. Daniell, Phys. Rev. B **37**, 3637, 1988.
[29] T. Barnes, Int. J. Mod. Phys. **C2**, 659, 1991.
[30] S.F. Barrett, D.J. Durand, C.H. Pennington, C.P. Slichter, T.A. Friedmann, J.P. Rice and D.M. Ginsberg, Phys. Rev. B **41**, 6283, 1990.
[31] S.F. Barrett, J.A. Martindale, D.J. Durand, C.H. Pennington, C.P. Slichter, T.A. Friedmann, J.P. Rice and D.M. Ginsberg, Phys. Rev. Lett. **66**, 108, 1991.

[32] G. Baskaran and P.W. Anderson, Phys. Rev. B **37**, 580, 1988.
[33] B. Batlogg, in: Proc. 1989 Los Alamos Symp. on High Temperature Superconductivity (Los Alamos, 1989), eds K.S. Bedell, D. Coffey, D.E. Meltzer, D. Pines and J.R. Schrieffer (Addison-Wesley, Reading, MA, 1990), p. 37.
[34] B. Batlogg, in: Physics of High Temperature Superconductors, Springer Series in Solid State Sciences Vol. 106, eds S. Maekawa and M. Sato (Heidelberg, 1992), p. 219.
[35] G. Baym and L.P. Kadanoff, Phys. Rev. **124**, 287, 1961;
G. Baym, Phys. Rev. **127**, 1391, 1962.
[36] J.G. Bednorz and K.A. Müller, Z. Phys. B **64**, 189, 1986; Rev. Mod. Phys. **60**, 585, 1988.
[37] P. Bénard, L. Chen and A.-M.S. Tremblay, Phys. Rev. B **47**, 15217, 1993.
[38] N.F. Berk and J.R. Schrieffer, Phys. Rev. Lett. **30**, 1108, 1966
[39] N.E. Bickers, D.J. Scalapino and R.T. Scalettar, Int. J. Mod. Phys. **B1**, 687, 1987.
[40] N.E. Bickers, D.J. Scalapino and S.R. White, Phys. Rev. Lett. **62**, 961, 1989;
N.E. Bickers and D.J. Scalapino, Ann. Phys. (N.Y.) **193**, 203, 1989.
[41] N.E. Bickers and S.R. White, Phys. Rev. B **43**, 8044, 1991.
[42] R.J. Birgeneau and G. Shirane, in: D.M. Ginsberg, ed., Physical Properties of High Temperature Superconductivity, Vol. 1 (World Scientific, Singapore, 1989), p. 151.
[43] R.J. Birgeneau, R.W. Erwin, P.M. Gehring, M.A. Kastner, B. Keimer, M. Sato, S. Shamoto, G. Shirane and J. Tranquada, Z. Phys. B **87**, 15, 1992.
[44] J. Bonca, P. Prelovšek and I. Sega, Phys. Rev. B **39**, 7074, 1989.
[45] N.E. Bonesteel, Phys. Rev. B **47**, 11302, 1993.
[46] M. Boninsegni and E. Manousakis, Phys. Rev. B **47**, 11897, 1993.
[47] D.A. Bonn, P. Dosanjh, R. Liang and W.N. Hardy, Phys. Rev. Lett. **68**, 2390, 1992.
[48] D.A. Bonn, R. Liang, T.M. Riseman, D.J. Baar, D.C. Morgan, K. Zhang, P. Dosanjh, T.L. Duty, A. MacFarlane, G.D. Morris, J.H. Brewer, W.N. Hardy, C. Kallin and A.J. Berlinsky, Phys. Rev. B **47**, 11314, 1993.
[49] D.A. Bonn, S. Kamal, K. Zhang, R. Liang, D.J. Baar, E. Klein, and W.N. Hardy, Phys. Rev. B **50**, 4051, 1334.
[50] W. Brenig and A.P. Kampf, Phys. Rev. B **43**, 12914, 1991.
[51] W. Brenig, A.P. Kampf, H. Monien and J.R. Schrieffer, Phys. Rev. B **44**, 10381, 1991.
[52] W. Brenig and H. Monien, Solid State Commun. **83**, 1008, 1992.
[53] W. Brenig and A. P. Kampf, Europhys. Lett. **24**, 679, 1993; J. Low Temp. Phys. **95**, 329, 1994.
[54] W. Brenig, unpublished
[55] W.F. Brinkman and T.M. Rice, Phys. Rev. B **2**, 1324, 1970.
[56] P. Bourges, P.M. Gehring, B. Hennion, A.H. Moudden, J.M. Tranquada, G. Shirane, S. Shamoto and M. Sato, Phys. Rev. B **43**, 8690, 1991.
[57] W. Braunisch, N. Knauf, V. Kataev, S. Neuhausen, A. Grütz, A. Kock, B. Roden, D. Khomskii and D. Wohlleben, Phys. Rev. Lett. **68**, 1908, 1992.
[58] W. Braunisch, N. Knauf, G. Bauer, A. Kock, A. Becker, B. Freitag, A. Grütz, V. Kataev, S. Neuhausen, B. Roden, D. Khomskii, D. Wohlleben, J. Bock and E. Preisler, Phys. Rev. B **48**, 4030, 1993.
[59] B. Bucher, P. Steiner, J. Karpinski, E. Kaldis and P. Wachter, Phys. Rev. Lett. **70**, 2012, 1993.
[60] L.N. Bulaevskii, E.L. Nagaev and D.L. Khomskii, Zh. Eksp. Teor. Fiz. **54**, 1562, 1968 [Sov. Phys. JETP **27**, 1562, 1968]
[61] N. Bulut, D. Hone, D.J. Scalapino and E.Y. Loh, Phys. Rev. Lett. **62**, 2192, 1989.
[62] N. Bulut, D. Hone, D.J. Scalapino and N.E. Bickers, Phys. Rev. Lett. **64**, 2723, 1990; Phys. Rev. B **41**, 1797, 1990; J. Appl. Phys. **67**, 5097, 1990.
[63] N. Bulut, in: Proc. NATO Advanced Study Institute on Dynamics of Magnetic Fluctuations in High Temperature Superconductors, eds, G. Reiter, P. Horsch and G.C. Psaltakis (Plenum, New York, 1991).
[64] N. Bulut and D.J. Scalapino, Phys. Rev. Lett. **67**, 2898, 1991.
[65] N. Bulut and D.J. Scalapino, Phys. Rev. Lett. **68**, 706, 1992; Phys. Rev. B **45**, 2371, 1992.
[66] N. Bulut, D.J. Scalapino and S.R. White, Phys. Rev. B **47**, 2742, 1993.
[67] N. Bulut, D.J. Scalapino and S.R. White, Phys. Rev. B **47**, 6157, 1993.
[68] N. Bulut, D.J. Scalapino and S.R. White, Phys. Rev. B **47**, 14599, 1993.
[69] N. Bulut and D.J. Scalapino, Phys. Rev. B **47**, 3419, 1993.

[70] P. Burlet, C. Vettier, M.J. Jurgens, J.Y. Henry, J. Rossat-Mignod, H. Noel, M. Potel, P. Gougeon and J.C. Levet, Physica C **153-155**, 1115, 1988.
[71] C. Thomsen and M. Cardona, in: D.M. Ginsberg, ed., Physical Properties of High Temperature Superconductivity, Vol. 1 (World Scientific, Singapore, 1989), p. 409.
[72] C.M. Canali, S.M. Girvin and M. Wallin, Phys. Rev. B **45**, 10131, 1992.
[73] G.E. Castilla and S. Chakravarty, Phys. Rev. B **43**, 13687, 1991.
[74] S. Chakravarty, in: Proc. 1989 Los Alamos Symp. on High Temperature Superconductivity (Los Alamos, 1989), eds K.S. Bedell, D. Coffey, D.E. Meltzer, D. Pines and J.R. Schrieffer (Addison-Wesley, Reading, MA, 1990), p. 136.
[75] S. Chakravarty and R. Orbach, Phys. Rev. Lett. **64**, 224, 1990.
[76] L. Chen, C. Bourbonnais, T. Li and A.-M.S. Tremblay, Phys. Rev. Lett. **66**, 369, 1991.
[77] C.T. Chen, F. Sette, Y. Ma, M.S. Hybertsen, E.B. Stechel, W.M.C. Foulkes, M. Schluter, S.-W. Cheong, A.S. Cooper, L.W. Rupp, Jr., B. Batlogg, Y.L. Soo, Z.H. Ming, A. Krol and Y.H. Kao, Phys. Rev. Lett. **66**, 104, 1991.
[78] L. Chen and A.-M.S. Tremblay, Phys. Rev. B **49**, 4338, 1994.
[79] S.W. Cheong, J.D. Thompson and Z. Fisk, Phys. Rev. B **39**, 4395, 1989.
[80] S.W. Cheong, G. Aeppli, T.E. Mason, H. Mook, S.M. Hayden, P.C. Canfield, Z. Fisk, K.N. Clausen and J.L. Martinez, Phys. Rev. Lett. **67**, 1791, 1991.
[81] S. Chakravarty, B.I. Halperin and D. Nelson, Phys. Rev. Lett. **60**, 1057, 1988; Phys. Rev. B **39**, 7443, 1988.
[82] S. Chakravarty, B.I. Halperin and D. Nelson, Phys. Rev. B **39**, 2344, 1989.
[83] A.V. Chubukov and D.M. Frenkel, Phys. Rev. B **46**, 11884, 1992.
[84] D. Coffey, K.S. Bedell and S.A. Trugman, Phys. Rev. B **42**, 6509, 1990.
[85] D. Coffey, T.M. Rice and F.C. Zhang, Phys. Rev. B **44**, 10112, 1991.
[86] D. Coffey and L. Coffey, Phys. Rev. Lett. **70**, 1529, 1993.
[87] L. Coffey, Phys. Rev. Lett. **64**, 1071, 1990.
[88] R.T. Collins Z. Schlesinger, F. Holtzberg, C. Feild, U. Welp, G.W. Crabtree, J.Z. Liu and Y. Fang, Phys. Rev. B **43**, 8701, 1991.
[89] S.L. Cooper, M.V. Klein, B.G. Pazol, J.P. Rice and D.M. Ginsberg, Phys. Rev. B **38**, 7133, 1988.
[90] S.L. Cooper, G.A. Thomas, J. Orenstein, D.H. Rapkine, A.J. Millis, S.-W. Cheong, A.S. Cooper and Z. Fisk, Phys. Rev. B **41**, 11605, 1990.
[91] S.L. Cooper, D. Reznik, A. Kotz, M.A. Karlov, R. Liu, M.V. Klein, W.C. Lee, J. Giapantzakis and D.M. Ginsberg, Phys. Rev. B **47**, 8233, 1993.
[92] D.L. Cox and B.R. Trees, Phys. Rev. B **41**, 11260, 1990.
[93] E. Dagotto, A. Moreo and T. Barnes, Phys. Rev. B **40**, 6721, 1989.
[94] E. Dagotto, R. Joynt, A. Moreo, S. Bacci and E. Gagliano, Phys. Rev. B **41**, 9049, 1990; Phys. Rev. B **41**, 2585, 1990.
[95] E. Dagotto, J. Riera and A.P. Young, Phys. Rev. B **42**, 2347, 1990.
[96] E. Dagotto, Int. J. Mod. Phys. **B5**, 907, 1991.
[97] E. Dagotto and J.R. Schrieffer, Phys. Rev. B **43**, 8705, 1991.
[98] E. Dagotto, A. Moreo, F. Ortolani, D. Poilblanc, J. Riera, and D.J. Scalapino, Phys. Rev. B **45**, 10107, 1992.
[99] E. Dagotto, A. Moreo, F. Ortolani, D. Poilblanc and J. Riera, Phys. Rev. B **45**, 10741, 1992.
[100] E. Dagotto, F. Ortolani and D.J. Scalapino, Phys. Rev. B **46**, 3183, 1992.
[101] E. Dagotto and J. Riera, Phys. Rev. B **46**, 12084, 1992.
[102] E. Dagotto and J. Riera, Phys. Rev. Lett. **70**, 682, 1993.
[103] E. Dagotto, Rev. Mod. Phys., to be published.
[104] E. Dagotto, J. Riera, Y.C. Chen, A. Moreo, A. Nazarenko, F. Alcaraz and F. Ortolani, Phys. Rev. B **49**, 3548, 1994.
[105] E. Dagotto, A. Nazarenko and M. Bonisegni, Phys. Rev. Lett. **73**, 728, 1994.
[106] H.-Q. Ding and M.S. Makivić, Phys. Rev. Lett. **64**, 1449, 1990.
[107] I. Dzyaloshinskii, J. Phys. Chem. Solids **4**, 241, 1958; T. Moriya, Phys. Rev. **120**, 91, 1960
[108] G. Dopf, A. Muramatsu and W. Hanke, Phys. Rev. B **41**, 9264, 1990.
[109] D.J. Scalapino, to appear in: Proc. Enrico Fermi Summer School (Varenna, 1992).
[110] D.J. Scalapino, to appear in: Proc. Raymond L. Orbach Inauguration Symposium (World Scientific, Singapore).
[111] D.J. Scalapino, in: Proc. Cuprate and Heavy Fermion Superconductors (Cologne, September 1993); J. Low Temp. Phys. **95**, 169, 1994.

[112] M. Dzierzawa, Z. Phys. B **86**, 49, 1992.
[113] R. Eder and K.W. Becker, Z. Phys. B **78**, 219, 1990;
R. Eder, K.W. Becker and W. Stephan, Z. Phys. B **81**, 33, 1990.
[114] R.J. Elliott and R. Loudon, Phys. Lett. **A 3**, 189, 1963
[115] V. Elser, D. Huse, B. Shraiman and E. Siggia, Phys. Rev. B **41**, 6715, 1990.
[116] V.J. Emery, Phys. Rev. Lett. **58**, 2794, 1987.
[117] V.J. Emery and G. Reiter, Phys. Rev. B **38**, 11938, 1988; Phys. Rev. B **41**, 7247, 1990.
[118] V.J. Emery, S.A. Kivelson and H.Q. Lin, Phys. Rev. Lett. **64**, 475, 1990.
[119] Y. Endoh, K. Yamada, R.J. Birgeneau, D.R. Gabbe, H.P. Jenssen, M.A. Kastner, C.J. Peters, P.J. Picone, T.R. Thurston, J.M. Tranquada, G. Shirane, Y. Hidaka, M. Oda, Y. Enomoto, M. Suzuki and T. Murakami, Phys. Rev. B **37**, 7443, 1988.
[120] Y. Endoh, K. Yamada, K. Kakurai, M. Matsuda, K. Nakajima, R.J. Birgeneau, M.A. Kastner, B. Keimer, G. Shirane and T.R. Thurston, Physica B **174**, 330, 1991.
[121] H. Eskes and G.A. Sawatzky, in Electronic Properties of High T_c Superconductors and Related Compounds, eds H. Kuzmany, M. Mehring, and J. Fink (Springer, Berlin, 1990), p. 127
[122] H. Eskes and G. Sawatzky, Phys. Rev. B **43**, 119, 1991.
[123] H. Eskes and J.H. Jefferson, Phys. Rev. B **48**, 9788, 1993.
[124] W.E. Evenson, J.R. Schrieffer and S.Q. Wang, J. Appl. Phys. **41**, 1199, 1970.
[125] G. Fano, F. Ortolani and A. Parola, Phys. Rev. B **46**, 1048, 1992.
[126] G.S. Feng and S.R. White, Phys. Rev. B **46**, 8691, 1992.
[127] J.Fink, N. Nücker, H. Romberg, M. Alexander, S. Nakai, R. Manzke, T. Buslaps and R. Claessen, Springer Series in Solid State Sciences, Vol. **91**, eds H. Kuzmany, M. Mehring and S. Roth (Springer Berlin, 1989), p. 406
[128] M.E. Fisher, M.N. Barber and D. Jasnow, Phys. Rev. A **8**, 1111, 1973
[129] M.E. Flatté, S. Quinlan and D.J. Scalapino, Phys. Rev. B **48**, 10626, 1993.
[130] C.M. Varma, P.B. Littlewood, S. Schmitt-Rink, E. Abrahams, and A.E. Ruckenstein, Phys. Rev. Lett. **63**, 1996, 1989; Phys. Rev. Lett. **64**, 497(E), 1990.
[131] L. Forro, G.L. Carr, G.P. Williams, D. Mandrus and L. Mihaly, Phys. Rev. Lett. **65**, 1941, 1990.
[132] T. Freltoft, J.E. Fischer, G. Shirane, D.E. Moncton, S.K. Sinha, D. Vaknin, J.P. Remeika, A.S. Cooper and D. Harshman Phys. Rev. B **37**, 137, 1988.
[133] D.M. Frenkel and W. Hanke, Phys. Rev. B **42**, 6711, 1990.
[134] R. Frésard, M. Dzierzawa and P. Wölfle, Europhys. Lett. **15**, 325, 1991.
[135] R. Frésard and P. Wölfle, J. Phys. Condensed Mat. **4**, 3625 1992.
[136] B. Friedl, C. Thomsen and M. Cardona, Phys. Rev. Lett. **65**, 915, 1990.
[137] H. Fukuyama, O. Narikiyo and K. Kuboki, J. Phys. Soc. Jpn. **59**, 807, 1990.
[138] H. Fukuyama, Prog. Theor. Phys. **108**, 287, 1992.
[139] N. Furukawa and M. Imada, J. Phys. Soc. Jpn. **59**, 1771, 1990; **61**, 2048, 1992.
[140] N. Furukawa and M. Imada, J. Phys. Soc. Jpn. **61**, 3331, 1992.
[141] J. Gan, N. Andrei and P. Coleman, J. Phys. Condens. Matter **3**, 3537, 1991.
[142] P.M. Gehring, J.M. Tranquada, G. Shirane, J.R.D. Copley, R.W. Erwin, M. Sato and S. Shamoto, Phys. Rev. B **44**, 2811, 1991.
[143] V.B. Geshkenbein and A.I. Larkin, Pis'ma Zh. Eksp. Teor. Fiz. **43**, 306, 1986 [JETP Lett. **43**, 395, 1986]
[144] D.M. Ginsberg, ed., Physical Properties of High Temperature Superconductivity, Vol. 1 (World Scientific, Singapore, 1989).
[145] D.M. Ginsberg, ed., Physical Properties of High Temperature Superconductivity, Vol. 2 (World Scientific, Singapore, 1990).
[146] D.M. Ginsberg, ed., Physical Properties of High Temperature Superconductivity, Vol. 3 (World Scientific, Singapore, 1992).
[147] M. Grilli and G. Kotliar, Phys. Rev. Lett. **64**, 1170, 1990.
[148] M. Gurvitch and A.T. Fiory, Phys. Rev. Lett. **59**, 1337, 1987.
[149] R. Hackl, W. Gläser, P. Müller, D. Einzel and K. Andres, Phys. Rev. B **38**, 7133, 1988.
[150] B.I. Halperin and P.C. Hohenberg, Phys. Rev. **177**, 117, 1969.
[151] P.C. Hammel, M. Takigawa, R.H. Heffner, Z. Fisk and K.C. Ott, Phys. Rev. Lett. **63**, 1992, 1989.

[152] Z.P. Han, R. Dupree, A. Gencten, R.S. Liu and P.P. Edwards, Phys. Rev. Lett. **69**, 1256, 1992.
[153] W.N. Hardy, D.A. Bonn, D.C. Morgan, R. Liang and K. Zhang, Phys. Rev. Lett. **70**, 3999, 1993.
[154] A.B. Harris and R.V. Lange, Phys. Rev. **157**, 295, 1967;
K.A. Chao, J. Spalek and A.M. Oles, J. Phys.C **10**, L271, 1977.
[155] H. Hasegawa and T. Moriya, J. Phys. Soc. Jpn. **36**, 1542, 1974;
K. Nakayama and T. Moriya, J. Phys. Soc. Jpn. **56**, 2918, 1987.
[156] Y. Hasegawa and D. Poilblanc, Phys. Rev. B **40**, 9035, 1989.
[157] S.M. Hayden, G. Aeppli, H. Mook, D. Rytz, M.F. Hundley and Z. Fisk, Phys. Rev. Lett. **66**, 821, 1991.
[158] S.M. Hayden, G. Aeppli, R. Osborn, A.D. Taylor, T.P. Perring, S.W. Cheong and Z. Fisk, Phys. Rev. Lett. **67**, 3622, 1991.
[159] L.C. Hebel and C.P. Slichter, Phys. Rev. **107**, 901, 1957; Phys. Rev. **113**, 1504, 1959;
L.C. Hebel, Phys. Rev. **116**, 79, 1959
[160] J.E. Hirsch, Phys. Rev. Lett. **54**, 1317, 1985.
[161] J.E. Hirsch and S. Tang, Phys. Rev. Lett. **62**, 591, 1989.
[162] M.L. Horbach, F.L.J. Vos and W. van Saarloos, Phys. Rev. B **48**, 4061, 1993.
[163] P. Horsch and W. Stephan, in: Electronic Properties of High Temperature Superconductors, Proc. Inter. Winter School (Kirchberg, Austria), Springer Series of Solid State Sciences, eds. J. Fink, H. Kuzmany and M. Mehring; in: Dynamics of Magnetic Fluctuations in High Temperature Superconductors, eds G. Reiter, P. Horsch and G. C. Psaltakis (Plenum, New York, 1991), p. 175.
[164] M. Horvatić, T. Auler, C. Berthier, P. Butaud, W.G. Clark, J.A. Gillet and P. Ségransam, Phys. Rev. B **47**, 3461, 1993.
[165] A.P. Howes, R. Dupree, D.M. Paul and S. Male, Physica C **185-189**, 1137, 1991; Physica C **193**, 189, 1992.
[166] A.P. Howes, R. Dupree, Z.P. Han, R.S. Liu and R.P. Edwards, preprint, University of Warwick.
[167] M.S. Hybertsen, M. Schlüter and N.E. Christensen, Phys. Rev. B **39**, 9028, 1989.
[168] M.S. Hybertsen, E.B. Stechel, M. Schlüter and D.R. Jennison, Phys. Rev. B **41**, 11068, 1990.
[169] M.S. Hybertsen, E.B. Stechel, W.M.C. Foulkes and M. Schlüter, Phys. Rev. B **45**, 10032, 1992.
[170] M. Ishimura, M. Fujita and K. Nakao, J. Phys. Soc. Jpn. **61**, 2027, 1992.
[171] J. Igarashi and P. Fulde, Phys. Rev. B **45**, 10419, 1992.
[172] J. Igarashi and P. Fulde, Phys. Rev. B **45**, 12357, 1992.
[173] J. Igarashi, Phys. Rev. B **46**, 10763, 1992.
[174] J. Igarashi and P. Fulde, Phys. Rev. B **48**, 998, 1993.
[175] M. Imada, J. Phys. Soc. Jpn. **60**, 2740, 1991.
[176] T. Imai, T. Shimizu, H. Yasuoka, T. Takabatake, Y. Nakazawa, and M. Ishikawa, J. Phys. Soc. Jpn. **57**, 1771, 1988.
[177] T. Imai, T. Shimizu, H. Yasuoka, Y. Ueda, K. Yoshimura and K. Kosuge, J. Phys. Soc. Jpn. **57**, 2280, 1988.
[178] T. Imai, H. Yasuoka, T. Shimizu, Y. Ueda, K. Yoshimura and K. Kosuge, Physica C **162-164**, 169, 1989.
[179] T. Imai, J. Phys. Soc. Jpn. **59**, 2508, 1990.
[180] T. Imai, C.P. Slichter, K. Yoshimura and K. Kosuge, Phys. Rev. Lett. **70**, 1002, 1993.
[181] T. Imai, C.P. Slichter, A.P. Paulikas and B. Veal, Phys. Rev. B **47**, 9158, 1993.
[182] L.B. Ioffe and A.I. Larkin, Phys. Rev. B **39**, 8988, 1989; Int. J. Mod. Phys. **B2**, 203, 1988.
[183] T. Ito, K. Takenaka and S. Uchida, Phys. Rev. Lett. **70**, 3995, 1993.
[184] Y. Itoh, H. Yasuoka, Y. Fujiwara, Y. Ueda, T. Machi, I. Tomeno, K. Tai, N. Koshizuka and S. Tanaka, J. Phys. Soc. Jpn. **61**, 1287, 1992.
[185] Y. Iye, in: D.M. Ginsberg, ed., Physical Properties of High Temperature Superconductivity, Vol. 3 (World Scientific, Singapore, 1992), p. 285.
[186] C. Jayaprakash, H.R. Krishnamurty and S. Sarker, Phys. Rev. B **40**, 2610, 1989.
[187] D.C. Johnston, S.K. Sinha, A.J. Jacobson and J.M. Newsam, Physica C **153-155**, 572, 1988.
[188] D.C. Johnston, Phys. Rev. Lett. **62**, 957, 1989.
[189] J.D. Jorgensen, D.G. Hinks, P.G. Radaelli, S. Pei, P. Lightfoot, B. Dabrowski, C.U. Segre and B.A. Hunter, Physica C **185-189**, 184, 1991.
[190] K. Kamarás, S.L. Herr, C.D. Porter, N. Tache, D.B. Tanner, S. Etemand, T. Venkatesan, E. Chase, A. Inam, X.D. Wu, M.S. Hegde and B. Dutta, Phys. Rev. Lett. **64**, 84, 1990.
[191] A.P. Kampf, unpublished.

[192] A.P. Kampf and J.R. Schrieffer, Phys. Rev. B **41**, 6399, 1990; Physica B **163**, 267, 1990.
[193] A.P. Kampf and J.R. Schrieffer, Phys. Rev. B **42**, 7967, 1990.
[194] A.P. Kampf, Phys. Rev. B **44**, 2637, 1991.
[195] A.P. Kampf and J.R. Schrieffer, J. Phys. Chem. Solids **52**, 1321, 1991.
[196] A.P. Kampf and W. Brenig, Z. Phys. B **89**, 313, 1992.
[197] A.P. Kampf and W. Brenig, In: Proc.Cuprate and Heavy Fermion Superconductors (Cologne, September 1993); J. of Low Temp. Phys. **95**, 335, 1994.
[198] A.P. Kampf, unpublished.
[199] J. Kanamori, Prog. Theor. Phys. **30**, 275, 1963.
[200] C.L. Kane, P.A. Lee and N. Read, Phys. Rev. B **39**, 6880, 1989.
[201] C.L. Kane, P.A. Lee, T.K. Ng, B. Chakraborty and N. Read, Phys. Rev. B **41**, 2653, 1990.
[202] M.A. Kastner, R.J. Birgeneau, T.R. Thurston, P.J. Picone, H.P. Jensen, D.R. Gabbe, M. Sato, K. Fukuda, S. Shamoto, Y. Endoh, K. Yamada, and G. Shirane, Phys. Rev. B **38**, 6636, 1988.
[203] S. Katano, S. Funahashi, J.A. Fernandez-Baca, N. Môri, Y. Ueda and K. Koga, preprint JAERI-M 93-131
[204] B. Keimer, R.J. Birgeneau, A. Cassanho, Y. Endoh, R.W. Erwin, M.A. Kastner and G. Shirane, Phys. Rev. Lett. **67**, 1930, 1991.
[205] B. Keimer, A. Aharony, A. Auerbach, R.J. Birgeneau, A. Cassanho, Y. Endoh, R.W. Erwin, M.A. Kastner and G. Shirane, Phys. Rev. B **45**, 7430, 1992.
[206] B. Keimer, N. Belk, R.J. Birgeneau, A. Cassanho, C.Y. Chen, M. Greven, M.A. Kastner, A. Aharony, Y. Endoh, R.W. Erwin and G. Shirane, Phys. Rev. B **46**, 14034, 1992.
[207] G. Khaliullin and P. Horsch, Phys. Rev. B **47**, 463, 1993.
[208] J.H. Kim, K. Levin, A. Auerbach, Phys. Rev. B **39**, 11663, 1989.
[209] J.C. Kimball and J.R. Schrieffer, unpublished.
[210] J.R. Kirtley and D.J. Scalapino, Phys. Rev. Lett. **65**, 798, 1990.
[211] Y. Kitaoka, S. Hiramatsu, T. Kondo and K. Asayama, J. Phys. Soc. Jpn. **57**, 30, 1988.
[212] Y. Kitaoka, K. Ishida, S. Ohsugi, F. Fujiwara and K. Asayama, Physica C **185-189**, 98, 1991.
[213] M.V. Klein, S.L. Cooper, A.L. Kotz, R. Liu, D. Reznik, F. Slakey, W.C. Lee and D.M. Ginsberg, Physica C **185-189**, 72, 1991.
[214] D.Y.K. Ko, Phys. Rev. Lett. **65**, 116, 1990.
[215] W. Kohn, Phys. Rev. **133**, A171, 1964.
[216] G. Kotliar, Phys. Rev. B **37**, 3664, 1988.
[217] G. Kotliar, E. Abrahams, A.E. Ruckenstein, C.M. Varma, P.B. Littlewood and S. Schmitt-Rink, Europhys. Lett. **15**, 655, 1991.
[218] R. Kubo, Phys. Rev. **87**, 568, 1952
[219] Y. Kuroda and C.M. Varma, Phys. Rev. B **42**, 8619, 1990.
[220] F.V. Kusmartsev, Phys. Rev. Lett. **69**, 2268, 1992.
[221] Proc. 1989 Los Alamos Symp. on High Temperature Superconductivity (Los Alamos, 1989), eds K.S. Bedell, D. Coffey, D.E. Meltzer, D. Pines and J.R. Schrieffer (Addison-Wesley, Reading, MA, 1990).
[222] P. Lederer, D. Poilblanc and T.M. Rice, Phys. Rev. Lett. **63**, 1519, 1989.
[223] P.A. Lee, in: Proc. 1989 Los Alamos Symp. on High Temperature Superconductivity (Los Alamos, 1989), eds K.S. Bedell, D. Coffey, D.E. Meltzer, D. Pines and J.R. Schrieffer (Addison-Wesley, Reading, MA, 1990), p. 96.
[224] P.W. Leung, Z. Liu, E. Manousakis, M.A. Novotny and P.E. Oppenheimer, Phys. Rev. B **46**, 11779, 1992.
[225] B. Goss Levi, Physics Today **46**, 17, (May 1993)
[226] K. Levin, J.H. Kim, J.P. Lu and Q. Si, Physica C **175**, 449, 1991.
[227] Q.P. Li and R. Joynt, Phys. Rev. B **47**, 530, 1993.
[228] Q.P. Li, B.E.C. Koltenbah and R. Joynt, Phys. Rev. B **48**, 437, 1993.
[229] R.L. Lichti, C. Boekema, J.C. Lam, D.W. Cooke, S.F.J. Cox, S.T. Ting and J.E. Crow, Physica C **180**, 358, 1991.
[230] H.Q. Lin and J.E. Hirsch, Phys. Rev. B **35**, 3359, 1987.
[231] W. von der Linden, Phys. Rep. **220**, 53, 1992.
[232] P.B. Littlewood and C.M. Varma, J. Appl. Phys. **69**, 4979, 1991.
[233] P.B. Littlewood and C.M. Varma, Phys. Rev. B **46**, 405, 1992.
[234] P.B. Littlewood, in: Les Houches Lecture Notes, ed. B. Doucot (North-Holland, Amsterdam, 1992).

[235] P.B. Littlewood, J. Zaanen, G. Aeppli and H. Monien, Phys. Rev. B **47**, 487, 1993.
[236] Z. Liu and E. Manousakis, Phys. Rev. B **44**, 2414, 1991; Phys. Rev. B **45**, 2425, 1992.
[237] R. Liu, S.L. Cooper, M.V. Klein, W.C. Lee, S.W. Cheong and D.M. Ginsberg, Phys. Rev. B **47**, 8233, 1993.
[238] S.W. Lovesey, Theory of Neutron Scattering from Condensed Matter (Oxford University Press, Oxford, 1984); W. Marshall and R. Lowde, Rep. Prog. Phys. **31**, 705, 1968.
[239] J.P. Lu, Q. Si and K. Levin, Physica C **162-164**, 1465, 1989.
[240] J.P. Lu, Q. Si, J.H. Kim and K. Levin, Phys. Rev. Lett. **65**, 2466, 1990; Physica C **179**, 191, 1991.
[241] J.P. Lu, Q. Si, J.H. Kim and K. Levin, Physica C **179**, 191, 1991.
[242] J.P. Lu, Mod. Phys. Lett. B **6**, 547, 1992.
[243] K.B. Lyons, P.A. Fleury, J.P. Remeika, A.S. Cooper and T.J. Negram, Phys. Rev. B **37**, 2353, 1988.
[244] K.B. Lyons, P.A. Fleury, L.F. Schneemeyer and J.V. Waszczak, Phys. Rev. Lett. **60**, 732, 1988.
[245] K.B. Lyons, P.E. Sulewski, P.A. Fleury, H.L. Carter, A.S. Cooper, G.P. Espinosa, Z. Fisk and S.W. Cheong, Phys. Rev. B **39**, 9693, 1989.
[246] K.B. Lyons, P.A. Fleury, R.R.P. Singh and P. Sulewski, in Dynamics of Magnetic Fluctuations in High Temperature Superconductors, eds G. Reiter, P. Horsch and G.C. Psaltakis(Plenum, New York, 1991), p. 159.
[247] M.S. Makivić and H.Q. Ding, Phys. Rev. B **43**, 3562, 1991.
[248] A.A. Maksimov, A.V. Puchkov, I.I. Tartakovskii, D. Reznik, M.V. Klein, W.C. Lee and D.M. Ginsberg, JETP Lett. **56**, 570, 1992.
[249] E. Manousakis, Rev. Mod. Phys. **63**, 1, 1991.
[250] E. Manousakis, Phys. Rev. B **45**, 7570, 1992.
[251] J.T. Markert, T.W. Noh, S.E. Russek and R.M. Cotts, Solid State Commun. **63**, 847, 1987.
[252] F. Marsiglio, A.E. Ruckenstein, S. Schmitt-Rink and C.M. Varma, Phys. Rev. B **43**, 10882, 1991.
[253] J.A. Martindale, S.E. Barrett, C.A. Klug, K.E. O'Hara, S.M. DeSoto, C.P. Slichter, T.A. Friedmann and D.M. Ginsberg, Phys. Rev. Lett. **68**, 702, 1992; Physica C **185-189**, 93, 1991.
[254] J.A. Martindale, S.E. Barrett, K.E. O'Hara, C.P. Slichter, W.C. Lee and D.M. Ginsberg, Phys. Rev. B **47**, 9155, 1993.
[255] G. Martinez and P. Horsch, Int. J. Mod. Phys. **B5**, 207, 1991; Phys. Rev. B **44**, 317, 1991.
[256] L. Marville, Ph. D. thesis, MIT, 1992, unpublished.
[257] T.E. Mason, G. Aeppli and H.A. Mook, Phys. Rev. Lett. **68**, 1414, 1992.
[258] T.E. Mason, G. Aeppli, S.M. Hayden, A.P. Ramirez and H.A. Mook, Physica B **199/200**, 285, 1994.
[259] T.E. Mason, G. Aeppli, S.M. Hayden, A.P. Ramirez and H.A. Mook, Phys. Rev. Lett. **71**, 919, 1993.
[260] L.F. Mattheis, Phys. Rev. Lett. **58**, 1028, 1987; J. Yu, A.J. Freeman and J.H. Xu, Phys. Rev. Lett. **58**, 1035, 1987.
[261] M. Matsuda, K. Yamada, Y. Endoh, T.R. Thurston, G. Shirane, R.J. Birgeneau, M.A. Kastner, I. Tanaka and H. Kojima, Phys. Rev. B **49**, 6958, 1994.
[262] A.K. McMahan, R.M. Martin and S. Satpathy, Phys. Rev. B **38**, 6650, 1988.
[263] A.K. McMahan, J.F. Annett and R.M. Martin, Phys. Rev. B **42**, 6268, 1990.
[264] F. Mila and T.M. Rice, Physica C **157**, 561, 1989.
[265] F. Mila and T.M. Rice, Phys. Rev. B **40**, 11382, 1989.
[266] F. Mila, D. Poilblanc and C. Bruder, Phys. Rev. B **43**, 7891, 1991.
[267] A.J. Millis, Phys. Rev. B **45**, 13047, 1992.
[268] A.J. Millis and H. Monien, Phys. Rev. Lett. **70**, 2810, 1993; Phys. Rev. Lett. **71**, 210(E), 1993.
[269] A.J. Millis and H. Monien, preprint, unpublished.
[270] K. Miyake, S. Schmitt-Rink and C.M. Varma, Phys. Rev. B **34**, 6554, 1986.
[271] A.J. Millis and H. Monien, Phys. Rev. B **45**, 3059, 1992.
[272] A.J. Millis, H. Monien and D. Pines, Phys. Rev. B **42**, 167, 1990.
[273] H. Monien, P. Monthoux and D. Pines, Phys. Rev. B **43**, 275, 1991.
[274] H. Monien, unpublished.
[275] P. Monthoux, A.V. Balatsky and D. Pines, Phys. Rev. Lett. **67**, 3448, 1991; Phys. Rev. B **46**, 14803, 1992.
[276] P. Monthoux and D. Pines, Phys. Rev. Lett. **69**, 961, 1992.
[277] P. Monthoux and D. Pines, Phys. Rev. B **47**, 6069, 1993.
[278] H.A. Mook, M. Yethiraj, G. Aeppli, T.E. Mason and T. Armstrong, Phys. Rev. Lett. **70**, 3490, 1993.
[279] A. Moreo, D.J. Scalapino, R. Sugar, S. White and N.E. Bickers, Phys. Rev. B **41**, 2313, 1990.

[280] A. Moreo and E. Dagotto, Phys. Rev. B **42**, 4786, 1990.
[281] A. Moreo, E. Dagotto, T. Jolicoeur and J. Riera, Phys. Rev. B **42**, 6283, 1990.
[282] A. Moreo, Phys. Rev. B **45**, 5059, 1992.
[283] A. Moreo, 1993, unpublished.
[284] T. Morita, J. Math. Phys. **12**, 1744, 1971
[285] T. Moriya, Prog. Theor. Phys. **28**, 371, 1962.
[286] T. Moriya, Y. Takahashi and K. Ueda, J. Phys. Soc. Jpn. **59**, 2905, 1990; J. Phys. Soc. Jpn. **60**, 776, 1991.
[287] H. Monien and D. Pines, Phys. Rev. B **41**, 6297, 1990.
[288] H. Monien, D. Pines and C.P. Slichter, Phys. Rev. B **41**, 11120, 1990.
[289] H. Monien, D. Pines and M. Takigawa, Phys. Rev. B **43**, 258, 1991.
[290] A. Muramatsu, R. Zeyher and D. Schmeltzer, Europhys. Lett. **7**, 473, 1988.
[291] A. Muramatsu, Phys. Rev. Lett. **65**, 2909, 1990; C. Kübert and A. Muramatsu, Phys. Rev. B **47**, 787, 1993.
[292] N. Nagaosa and P. A. Lee, Phys. Rev. Lett. **64**, 2450, 1990; Phys. Rev. B **43**, 1223, 1991.
[293] Y. Nakazawa and M. Ishikawa, Physica C **158**, 381, 1989.
[294] D.M. Newns, P. Pattnaik, M. Rasolt and D.A. Papaconstantopoulos, Phys. Rev. B **38**, 7033, 1988.
[295] N. Nücker, P. Adelmann, M. Alexander, H. Romberg, S. Nakai, J. Fink, H. Rietschel, G. Roth, H. Schmidt and H. Spille, Phys. Rev. B **37**, 5158, 1988.
[296] M. Oda, T. Nakano, Y. Kamada and M. Ido, Physica C **183**, 234, 1991.
[297] M. Ogata and H. Shiba, J. Phys. Soc. Jpn. **57**, 3074, 1988.
[298] S. Ohsugi, Y. Kitaoka, K. Ishida and K. Asayama, J. Phys. Soc. Jpn. **60**, 2351, 1991.
[299] Y. Okabe and M. Kikuchi, J. Phys. Soc. Jpn. **57**, 4351, 1988; J. Phys. C **8**, 1393, 1988.
[300] N.P. Ong, in: D.M. Ginsberg, ed., Physical Properties of High Temperature Superconductivity, Vol. 2 (World Scientific, Singapore, 1990).
[301] C.G. Olson, R. Liu, D.W. Lynch, R.S. List, A.J. Arko, B.W. Veal, Y.C. Chang, P.Z. Jiang and A.P. Paulikas, Phys. Rev. B **42**, 381, 1990.
[302] J. Orenstein, G.A. Thomas, A.J. Millis, S.L. Cooper, D.H. Rapkine, T. Timusk, L.F. Schneemeyer and J.V. Wasczcak, Phys. Rev. B **42**, 6342, 1990.
[303] J.B. Parkinson, J. Phys. C **2**, 2012, 1969.
[304] C.H. Pennington and C.P. Slichter, in: D.M. Ginsberg, ed., Physical Properties of High Temperature Superconductivity, Vol. 2 (World Scientific, Singapore, 1990), p. 269.
[305] C.H. Pennington and C.P. Slichter, Phys. Rev. Lett. **66**, 3812, 1991.
[306] Special Issue: High Temperature Superconductivity, Physics Today Vol. **44**, No. **6**, 1991.
[307] W. E. Pickett, Rev. Mod. Phys. **61**, 433, 1989.
[308] W.E. Pickett, H. Krakauer and R.E. Cohen, Physica B **165/166**, 1055, 1990.
[309] W.E. Pickett, H. Krakauer, R.E. Cohen and D.J. Singh, Science **255**, 46, 1992.
[310] I.R. Pimentel and R. Orbach, Phys. Rev. B **46**, 2920, 1992.
[311] D. Pines, Physica B **163**, 78, 1990.
[312] D. Poilblanc, Phys. Rev. B **44**, 9562, 1991.
[313] D. Poilblanc, H.J. Schulz and T. Ziman, Phys. Rev. B **46**, 6435, 1992.
[314] D. Poilblanc, H.J. Schulz and T. Ziman, Phys. Rev. B **47**, 3268, 1993.
[315] D. Poilblanc, J. Riera and E. Dagotto, Phys. Rev. B **49**, 12381, 1994; D. Poilblanc, Toulouse preprint # LPQTH-93/01
[316] P. Prelovšek, Phys. Lett. A **126**, 287, 1988.
[317] N. Putilin, E.V. Antipov, O. Chmaissen and M. Marezio, Nature **362**, 226, 1993.
[318] W.O. Putikka, M.U. Luchini and T.M. Rice, Phys. Rev. Lett. **68**, 538, 1992.
[319] W.O. Putikka, R.L. Glenister, R.R.P. Singh and H. Tsunetsugu, Phys. Rev. Lett. **170**, 1994.
[320] R. Putz, B. Ehlers, L. Lilly, A. Muramatsu and W. Hanke, Phys. Rev. B **41**, 853, 1990.
[321] P.W. Anderson, Phys. Rev. **86**, 694, 1952
[322] P.W. Anderson, Phys. Rev. **115**, 2, 1959
[323] S.M. Quinlan, D.J. Scalapino and N. Bulut, Phys. Rev. B **49**, 1470, 1994.
[324] R.J. Radtke, S. Ullah, K. Levin and M.R. Norman, Phys. Rev. B **46**, 11975, 1992.
[325] J. Reger and A.P. Young, Phys. Rev. B **37**, 5978, 1988.
[326] L. Reven, J. Shore, S. Yang, T. Duncan, D. Schwartz, J. Chung, and E. Oldfield, Phys. Rev. B **43**, 10466, 1991.

[327] D. Reznik, A. Kotz, S.L. Cooper, M.V. Klein, W.C. Lee and D. M. Ginsberg, Physica C **185-189**, 1029, 1991.
[328] D. Reznik, M.V. Klein, W.C. Lee, D. M. Ginsberg and S.W. Cheong, Phys. Rev. B **46**, 11725, 1992.
[329] D. Reznik, S.L. Cooper, M.V. Klein, W.C. Lee, D.M. Ginsberg, A.A. Maksimov, A.V. Puchkov, I.I. Tartakovskii and S.W. Cheong, Phys. Rev. B **48**, 7624, 1993.
[330] T.M. Rice, in The Physics and Chemistry of Oxide Superconductors, Springer Proceedings in Physics Vol. 60, eds Y. Iye and H. Yasuoka (Springer, Berlin, 1992), p. 313
[331] J. Riera and A.P. Young, Phys. Rev. B **39**, 9697, 1989.
[332] G. Rietveld, N.Y. Chen and D. van der Marel, Phys. Rev. Lett. **69**, 2578, 1992.
[333] H. Romberg, N. Nücker, J. Fink, T. Wolf, X.X. Xi, B. Koch, H.P. Geserich, M. Dürrler, W. Assmus and B. Gegenheimer, Z. Phys. B **78**, 367, 1990.
[334] H. Romberg, M. Alexander, N. Nücker, P. Adelmann and J. Fink, Phys. Rev. B **45**, 8768, 1990.
[335] D. Romero, C. Porter, D. Tanner, L. Forro, D. Mandrus, L. Mihaly, G. Carr and G. Williams, Solid State Commun. **82**, 183, 1992.
[336] J. Rossat-Mignod, L.P. Regnault, C. Vettier, P. Burlet, J.Y. Henry and G. Lapertot, Physica B **169**, 58, 1991.
[337] J. Rossat-Mignod, L.P. Regnault, C. Vettier, P. Bourges, P. Burlet, J. Bossy, J.Y. Henry and G. Lapertot, Physica C **185–189**, 86, 1991.
[338] J. Rossat-Mignod, L.P. Regnault, C. Vettier, P. Bourges, P. Burlet, J. Bossy, J.Y. Henry and G. Lapertot, 180–181, 383, 1992.
[339] J. Rossat-Mignod, L.P. Regnault, J.M. Jurguens, P. Burlet, J.Y. Henry, G. Lapertot and C. Vettier, in Dynamics of Magnetic Fluctuations in High Temperature Superconductors, G. Reiter, P. Horsch and G.C. Psaltakis, eds (Plenum, New York, 1991), p. 35.
[340] L.D. Rotter, Z. Schlesinger, R.T. Collins, F. Holtzberg, C. Feild, U.W. Welp, G.W. Crabtree, J.Z. Liu, Y. Fang, K.G. Vandervoort and S. Fleshler, Phys. Rev. Lett. **67**, 2741, 1991.
[341] A.E. Ruckenstein and C.M. Varma, in Materials and Mechanisms of Superconductivity III, eds M. Tachiki, Y. Muto and Y. Syono (North-Holland, Amsterdam, 1991), p. 134.
[342] S. Sachdev, Phys. Rev. B **39**, 12232, 1989.
[343] Proc. Conf. on Lattice Effects in High T_c Superconductors (Santa Fe, 1992), eds Y. Bar-Yam, T. Egami, J. Mustre-De Leon and A.R. Bishop (World Scientific, Singapore, 1992).
[344] D.J. Scalapino, in: Proc. 1989 Los Alamos Symp. on High Temperature Superconductivity (Los Alamos, 1989), eds K.S. Bedell, D. Coffey, D.E. Meltzer, D. Pines and J.R. Schrieffer (Addison-Wesley, Reading, MA, 1990), p. 314.
[345] D.J. Scalapino, E. Loh, Jr. and J.E. Hirsch, Phys. Rev. B **34**, 8190, 1986; Phys. Rev. B **35**, 6694, 1987.
[346] D.J. Scalapino, S.R. White and S.C. Zhang, Phys. Rev. Lett. **68**, 2830, 1992; Phys. Rev. B **47**, 7995, 1993.
[347] R.T. Scalettar, Physica C **162-164**, 313, 1989.
[348] R.T. Scalettar, S.R. White, D.J. Scalapino and R.L. Sugar, Phys. Rev. B **44**, 770, 1991.
[349] A. Schilling, M. Cantoni, J.D. Guo and H.R. Ott, Nature **363**, 56, 1993.
[350] Z. Schlesinger, R.T. Collins, F. Holtzberg, C. Feild, S.H. Blanton, U. Welp, G.W. Crabtree, Y. Fang and J.Z. Liu, Phys. Rev. Lett. **65**, 801, 1990; Phys. Rev. B **41**, 11237, 1990.
[351] S. Schmitt-Rink, C.M. Varma and A.E. Ruckenstein, Phys. Rev. Lett. **60**, 2793, 1988.
[352] J.R. Schrieffer, Theory of Superconductivity (Addison-Wesley, Reading, MA, 1964).
[353] J.R. Schrieffer, unpublished notes.
[354] H.J. Schulz, Phys. Rev. Lett. **64**, 1445, 1990.
[355] I. Sega and P. Prelovšek, Phys. Rev. B **42**, 892, 1990.
[356] J.W. Serene and D.W. Hess, Phys. Rev. B **44**, 3391, 1991.
[357] S. Shamoto, M. Sato, J.M. Tranquada, B.J. Sternlieb and G. Shirane, Phys. Rev. B **48**, 13817, 1993.
[358] B.S. Shastry, Phys. Rev. Lett. **63**, 1288, 1989.
[359] B.S. Shastry and B. Shraiman, Phys. Rev. Lett. **65**, 1068, 1990; Int. J. Mod. Phys. **B5**, 365, 1991.
[360] Z.X. Shen, D.S. Dessau, B.O. Wells, D.M. King, W.E. Spicer, A.J. Arko, D. Marshall, L.W. Lombardo, A. Kapitulnik, P. Dickinson, S. Doniach, J. DiCarlo, A.G. Loeser and C.H. Park, Phys. Rev. Lett. **70**, 1553, 1993.
[361] G. Shirane, Y. Endoh, R.J. Birgeneau, M.A. Kastner, Y. Hidaka, M. Oda, M. Suzuki and T. Murakami, Phys. Rev. Lett. **59**, 1613, 1987.
[362] G. Shirane, J. Als-Nielsen, J.M. Tranquada, H. Chou, S. Shamoto and M. Sato, Phys. Rev. B **41**, 6547, 1990.

[363] G. Shirane, R.J. Birgeneau, Y. Endoh, P. Gehring, M.A. Kastner, K. Kitazawa, H. Kojima, I. Tanaka, T.R. Thurston and K. Yamada, Phys. Rev. Lett. **63**, 330, 1989.
[364] B.I. Shraiman and E.D. Siggia, Phys. Rev. Lett. **61**, 467, 1988.
[365] B.I. Shraiman and E.D. Siggia, Phys. Rev. Lett. **60**, 740, 1988.
[366] B.I. Shraiman and E.D. Siggia, Phys. Rev. Lett. **62**, 1564, 1989; Phys. Rev. B **40**, 9162, 1989.
[367] Q. Si, J.P. Lu, J.H. Kim and K. Levin, Physica C **162-164**, 1467, 1989.
[368] Q. Si, Y. Zha, K. Levin and J.P. Lu, Phys. Rev. B **47**, 9055, 1993.
[369] Q. Si, Int. J. Mod. Phys. B **8**, 47, 1994.
[370] M. Sigrist and T.M. Rice, J. Phys. Soc. Jpn. **61**, 4283, 1992.
[371] R.N. Silver, J.E. Gubernatis, D.S. Sivia and M. Jarrell, Phys. Rev. Lett. **65**, 496, 1990.
[372] R.R.J. Singh, Phys. Rev. B **39**, 9760, 1989; R.R.P. Singh and D. Huse, Phys. Rev. B **40**, 7247, 1989.
[373] R.R.P. Singh, P.A. Fleury, K.B. Lyons and P.E. Sulewski, Phys. Rev. Lett. **62**, 2736, 1989.
[374] A. Singh and Z. Tešanović, Phys. Rev. B **41**, 614, 1990; Phys. Rev. B **41**, 11457, 1990.
[375] R.R.P. Singh and M.P. Gelfand, Phys. Rev. B **42**, 996, 1990.
[376] R.R.P. Singh, Comments Cond. Mat. Phys. **15**, 241, 1991.
[377] A. Singh, Z. Tešanović and J.H. Kim, Phys. Rev. B **44**, 7757, 1991.
[378] R.R.P. Singh and R.L. Glenister, Phys. Rev. B **46**, 11871, 1992.
[379] F. Slakey, M.V. Klein, J.P.Rice and D.M. Ginsberg, Phys. Rev. B **43**, 3764, 1991.
[380] A. Sokol and D. Pines, Phys. Rev. Lett. **71**, 2813, 1993.
[381] S. Sorella, A. Parola, M. Parinello and E. Tosatti, Int. J. Mod. Phys. **B3**, 1875, 1989.
[382] W.P. Su, J.R. Schrieffer and A.J. Heeger, Phys. Rev. Lett. **42**, 1698, 1979; Phys. Rev. B **22**, 2099, 1980.
[383] T. Staufer, R. Hackl and P. Müller, Solid State Commun. **75**, 975, 1990.
[384] T. Staufer, R. Hackl and P. Müller, Solid State Commun. **79**, 409, 1991.
[385] T. Staufer, R. Nemetschek, R. Hackl, P. Müller and H. Veith, Phys. Rev. Lett. **68**, 1096, 1992.
[386] E.B. Stechel and D.R. Jennison, Phys. Rev. B **38**, 4632, 1988; Phys. Rev. B **38**, 8873, 1988.
[387] W. Stephan and P. Horsch, Phys. Rev. B **42**, 8736, 1990.
[388] W. Stephan and P. Horsch, Phys. Rev. Lett. **66**, 2258, 1991.
[389] W. Stephan and P. Horsch, in Dynamics of Magnetic Fluctuations in High Temperature Superconductors, G. Reiter, P. Horsch and G. C. Psaltakis, eds (Plenum, New York, 1991);
P. Horsch, W. Stephan, K. von Szczepanski, M. Ziegler and W. von der Linden, Physica C **162-164**, 783, 1989.
[390] B.J. Sternlieb, G. Shirane, J. Tranquada, M. Sato and S. Shamoto, Phys. Rev. B **47**, 5320, 1993.
[391] M.A. Subramanian, C.C. Torardi, J. Gopalakrishnan, P.L. Gai and A.W. Sleight, in Physics and Materials Science of High Temperature Superconductors, eds R. Kossowsky, S. Methfessel and D. Wohlleben, NATO ASI Series, Vol. 181 (Kluwer Academic, Dordrecht, 1990), p. 261
[392] S. Sugai, in: Mechanisms of High Temperature Superconductivity, eds H. Kamimura and A. Oshiyama (Springer, Berlin, 1989), p. 207
[393] S. Sugai, M. Sato, T. Kobayashi, J. Akimitsu, T. Ho, H. Takagi, S. Uchida, S. Hosoya, T. Kajitani and T. Fukuda, Phys. Rev. B **42**, 1045, 1990.
[394] S. Sugai, T. Ido, H. Takagi, S. Uchida, M. Sato and S. Shamoto, Solid State Commun. **76**, 365, 1990.
[395] S. Sugai and Y. Hidaka, Phys. Rev. B **44**, 809, 1991.
[396] Y. Suzumura, Y. Hasegawa and H. Fukuyama, J. Phys. Soc. Jpn. **57**, 2768, 1988.
[397] J.R. Schrieffer, X.G. Wen and S.C. Zhang, Phys. Rev. Lett. **60**, 944, 1988.
[398] J.R. Schrieffer, X.G. Wen and S.C. Zhang, Phys. Rev. B **39**, 11663, 1989.
[399] K.J. von Szczepanski, P. Horsch, W. Stephan and M. Ziegler, Phys. Rev. B **41**, 2017, 1990.
[400] H. Takagi, T. Ido, S. Ishibashi, M. Uota, S. Uchida and Y. Tokura, Phys. Rev. B **40**, 2254, 1989.
[401] H. Takagi, B. Batlogg, H.L. Kao, J. Kwo, R.J. Cava, J.J. Krajewski and W.F. Peck, Jr., Phys. Rev. Lett. **69**, 2975, 1992.
[402] M. Takano, Z. Hiroi, Y. Bando and M. Azume, in: Proc. Conf. "Materials and Mechanisms of Superconductivity, High Temperature Superconductors III" (Kanazawa, 1991), eds M. Tachiki, Y. Muto and Y. Syono (North-Holland, Amsterdam, 1991), p. 441; Physica C **176**, 441, 1991.
[403] M. Takigawa, unpublished.

[404] M. Takigawa, in: Proc. 1989 Los Alamos Symp. on High Temperature Superconductivity (Los Alamos, 1989), eds K.S. Bedell, D. Coffey, D.E. Meltzer, D. Pines and J.R. Schrieffer (Addison-Wesley, Reading, MA, 1990), p. 236.
[405] M. Takigawa, P.C. Hammel, R.H. Heffner, Z. Fisk, K.C. Ott, and J.D. Thompson, Phys. Rev. Lett. **63**, 1865, 1989.
[406] M. Takigawa, P.C. Hammel, R.H. Heffner and Z. Fisk, Phys. Rev. B **39**, 7371, 1989.
[407] M. Takigawa, A.P. Reyes, P.C. Hammel, J.D. Thompson, R.H. Heffner, Z. Fisk and K.C. Ott, Phys. Rev. B **43**, 247, 1991.
[408] M. Takigawa, J.L. Smith and L. Hults, Phys. Rev. B **44**, 7764, 1991; Physica C **185-189**, 1105, 1991.
[409] M. Takigawa, W. L. Hults and J.L. Smith, Phys. Rev. Lett. **71**, 2650, 1993.
[410] M. Takigawa, Phys. Rev. B **49**, 4158, 1994.
[411] T. Tanamoto, K. Kuboki and H. Fukuyama, J. Phys. Soc. Jpn. **60**, 3072, 1991.
[412] T. Tanamoto, H. Kohno and H. Fukuyama, J. Phys. Soc. Jpn. **61**, 1886, 1992; J. Phys. Soc. Jpn. **62**, 717, 1993.
[413] T. Tanamoto, H. Kohno and H. Fukuyama, J. Phys. Soc. Jpn. **62**, 717, 1993; J. Phys. Soc. Jpn. **62**, 1455, 1993.
[414] D.B. Tanner and T. Timusk, in: D.M. Ginsberg, ed., Physical Properties of High Temperature Superconductivity, Vol. 3 (World Scientific, Singapore, 1992).
[415] J.M. Tarascon, W.R. McKinnon, P. Barboux, D.M. Hwang, B.G. Bagley, L.H. Greene, G.W. Hull, Y. LePage, N. Stoffel and M. Girous, Phys. Rev. B **38**, 8885, 1988.
[416] D. Thelen, D. Pines and J.P. Lu, Phys. Rev. B **47**, 9151, 1993.
[417] D. Thelen and D. Pines, Phys. Rev. B **49**, 3528, 1994.
[418] T. Thio, T.R. Thurston, N.W. Preyer, P.J. Picone, M.A. Kastner, H.P. Jenssen, D.R. Gabbe, C.Y. Chen, R.J. Birgeneau and A. Aharony, Phys. Rev. B **38**, 905, 1988.
[419] C. Thomsen, in Topics in Applied Physics: Light Scattering in Solids, Vol. VI , eds M. Cardona and G. Güntherodt (Springer, Berlin, 1991), p. 285.
[420] T.R. Thurston, R.J. Birgeneau, M.A. Kastner, N.W. Preyer, G. Shirane, Y. Fujii, K. Yamada, Y. Endoh, K. Kakurai, M. Matsuda, Y. Hidaka and T. Murakami, Phys. Rev. B **40**, 4585, 1989.
[421] T.R. Thurston, M. Matsuda, K. Kakurai, K. Yamada, Y. Endoh, R.J. Birgeneau, P.M. Gehring, Y. Hidaka, M.A. Kastner, T. Murakami and G. Shirane, Phys. Rev. Lett. **65**, 263, 1990.
[422] T.R. Thurston, P.M. Gehring, G. Shirane, R.J. Birgeneau, M.A. Kastner, N.W. Preyer, Y. Endoh, M. Matsuda, K. Yamada, H. Kojima and I. Tanaka, Phys. Rev. B **46**, 9128, 1992.
[423] Y. Tokura, J.B. Torrance, T.C. Huang, A.I. Nazzai, Phys. Rev. B **38**, 7156, 1988.
[424] Y. Tokura, H. Takagi and S. Uchida, Nature **337**, 345, 1989.
[425] I. Tomeno, M. Yoshida, K. Ikeda, K. Tai, K. Takamuku, N. Koshizuka, S. Tanaka, K. Oka and H. Unoki, Phys. Rev. B **43**, 3009, 1991.
[426] J.B. Torrance, A. Bezinge, A.I. Nazzal, T.C. Huang, S.S.P. Parkin, D.T. Keane, S.J. LaPlaza, P.M. Horn and G.A. Held, Phys. Rev. B **40**, 8872, 1989.
[427] S.A. Trugman, Phys. Rev. B **37**, 1597, 1988.
[428] S.A. Trugman, Phys. Rev. B **41**, 892, 1990.
[429] S.A. Trugman, Phys. Rev. Lett. **65**, 500, 1990.
[430] J.M. Tranquada, D.E. Cox, W. Kunnmann, H. Moudden, G. Shirane, M. Suenaga, P. Zolliker, D. Vaknin, S.K. Sinha, M.S. Alvarez, A.J. Jacobson and D.C. Johnston, Phys. Rev. Lett. **60**, 156, 1988.
[431] J.M. Tranquada, W.J.L. Buyers, H. Chou, T.E. Mason, M. Sato, S. Shamoto and G. Shirane, Phys. Rev. Lett. **64**, 800, 1990.
[432] J.M. Tranquada, P.M. Gehring, G. Shirane, S. Shamoto and M. Sato, Phys. Rev. B **46**, 5561, 1992.
[433] N. Trivedi and D. Ceperley, Phys. Rev. B **40**, 2737, 1989.
[434] S. Uchida, T. Ido, H. Takagi, T. Arima, Y. Tokura and S. Tajima, Phys. Rev. B **43**, 7942, 1991.
[435] K. Ueda, J. Phys. Soc. Jpn. **43**, 1497, 1977.
[436] K. Ueda, T. Moriya and Y. Takahashi, in Electronic Properties and Mechanism of High T_c Superconductors, eds T. Oguchi, K. Kadowaki and T. Sasaki (Elsevier Science Publishers, Amsterdam, 1992).
[437] D. Vaknin, S.K. Sinha, D.E. Moncton, D.C. Johnston, J.M. Newsom, C.R. Safinya and H.E. King, Jr., Phys. Rev. Lett. **58**, 2802, 1987.
[438] C.M. Varma, S. Schmitt-Rink and E. Abrahams, Solid State Commun. **62**, 681, 1987.
[439] C.M. Varma, Int. J. Mod. Phys. **B3**, 2083, 1989.
[440] M.A. van Veenendahl, R. Schlatmann, G.A. Sawatzky and W.A. Groen, Phys. Rev. B **47**, 446, 1993.

[441] G. Vignale and K.S. Singwi, Phys. Rev. B **39**, 2956, 1989.
[442] G. Vignale and M.R. Hedayati, Phys. Rev. B **42**, 786, 1990.
[443] R.E. Walstedt, in: Proc. 1989 Los Alamos Symp. on High Temperature Superconductivity (Los Alamos, 1989), eds K.S. Bedell, D. Coffey, D.E. Meltzer, D. Pines and J.R. Schrieffer (Addison-Wesley, Reading, MA, 1990), p. 229.
[444] R.E. Walstedt and W.W. Warren, Science **248**, 1082, 1990.
[445] R.E. Walstedt, W.W. Warren, Jr., R.F. Bell, R.J. Cava, G.P. Espinosa, L.F. Schneemeyer and J.V. Waszczak, Phys. Rev. B **41**, 9574, 1990.
[446] R.E. Walstedt, R.F. Bell and D.B. Mitzi, Phys. Rev. B **44**, 7760, 1991.
[447] R.E. Walstedt, R.F. Bell, L.F. Schneemeyer, J.V. Waszczak, W.W. Warren, Jr., R. Dupree and A. Gencten, Phys. Rev. B **48**, 10646, 1993.
[448] W.W. Warren, Jr., R.E. Walstedt, G.F. Brennert, G.P. Espinosa, and J.P. Remeika, Phys. Rev. Lett. **59**, 1860, 1987.
[449] W.W. Warren, Jr., R.E. Walstedt, G.F. Brennert, R.J. Cava, R. Tycko, R.F. Bell and G. Dabbagh, Phys. Rev. Lett. **62**, 1193, 1989.
[450] B.O. Wells, Z.X. Shen, D.S. Dessau, W.E. Spicer, D.B. Mitzi, L. Lombardo, A. Kapitulnik and A.J. Arko, Phys. Rev. B **46**, 11830, 1992.
[451] X.G. Wen, F. Wilczek and A. Zee, Phys. Rev. B **39**, 11413, 1989.
[452] Z.Y. Weng and C.S. Ting, Phys. Rev. B **42**, 803, 1990.
[453] S. Wermbter and L. Tewordt, Phys. Rev. B **43**, 10530, 1991.
[454] S. Wermbter and L. Tewordt, Physica C **199**, 375, 1992.
[455] S. Wermbter and L. Tewordt, Phys. Rev. B **48**, 10514, 1993.
[456] S.R. White, D.J. Scalapino, R.L. Sugar, N.E. Bickers and R.T. Scalettar, Phys. Rev. B **39**, 839, 1989.
[457] D.A. Wollman, D.J. Van Harlingen, W.C. Lee, D.M. Ginsberg and A.J. Leggett, Phys. Rev. Lett. **71**, 2134, 1993.
[458] G. Xiao, M.Z. Cieplak, A. Gavrin, F.H. Streitz, A. Bakhshai and C.L. Chien, Phys. Rev. Lett. **60**, 1446, 1988.
[459] G. Xiao, A. Bakhshai, M.Z. Cieplak, Z. Tešanović and C.L. Chien, Phys. Rev. B **39**, 315, 1989.
[460] G. Xiao, M.Z. Cieplak and C.L. Chien, Phys. Rev. B **42**, 240, 1990.
[461] G. Xiao, M.Z. Cieplak, J.Q. Xiao and C.L. Chien, Phys. Rev. B **42**, 8752, 1990.
[462] K. Yamada, K. Kakurai, Y. Endoh, T.R. Thurston, M.A. Kastner, R.J. Birgeneau, G. Shirane, Y. Hidaka and T. Murakami, Phys. Rev. B **40**, 4557, 1989.
[463] H. Yasuoka, T. Shimizu, Y. Ueda and K. Kosuge, J. Phys. Soc. Jpn. **57**, 2659, 1988.
[464] H. Yasuoka, T. Imai and T. Shimizu, in: Strong Correlations and Superconductivity, eds H. Fukuyama, S. Maekawa and A.P. Malozemoff (Springer, Berlin, 1989), p. 254.
[465] R. Yoshizaki, N. Ishikawa, H. Sawada, E. Kita and A. Tasaki, Physica C **166**, 417, 1990.
[466] Y. Yoshinari, H. Yasuoka, Y. Ueda, K. Koga and K. Kosuge, J. Phys. Soc. Jpn. **59**, 3698, 1990.
[467] K. Yosida, Phys. Rev. **110**, 769, 1958.
[468] J.J. Yu, S. Massida, A.J. Freeman and D.D. Koelling, Phys. Lett. **A 122**, 203, 1987.
[469] R.C. Yu, M.B. Salamon, J.P. Lu and W.C. Lee, Phys. Rev. Lett. **69**, 1431, 1992.
[470] J. Zaanen, G.A. Sawatzky and J.W. Allen, Phys. Rev. Lett. **55**, 418, 1985.
[471] J. Zaanen and A.M. Oles, Phys. Rev. B **37**, 9423, 1988.
[472] J.F. Zasadzinski, in: Proc. U.S.–Japan Seminar on Electronic Structure and Fermiology of High T_c Superconductors (Sendai, 1992), to be published.
[473] Y. Zha, Q. Si and K. Levin, Physica C **212**, 413, 1993.
[474] F.C. Zhang and T.M. Rice, Phys. Rev. B **37**, 3759, 1988.
[475] F.C. Zhang and T.M. Rice, Phys. Rev. B **41**, 7243, 1990.
[476] G.T. Zimanyi and K.S. Bedell, Phys. Rev. B **48**, 6575, 1993.
[477] H. Zimmermann, M. Mali, D. Brinkmann, J. Karpinski, E. Kaldis and S. Rusiecki, Physica C **159**, 681, 1989.
[478] M.G. Smith, A. Manthiram, J. Zhou, J.B. Goodenough and J.J. Markert, Nature **351**, 549, 1991.